Méthodologie de remontée d'échelle pour la modélisation des batteries Li-ions

Oumaima Chaouachi

THÈSE

Pour obtenir le grade de

DOCTEUR DE L'UNIVERSITE GRENOBLE ALPES

Spécialité : MEP: **Mécanique des fluides Energétique, Procédés**

Arrêté ministériel : 25 mai 2016

Présentée par

Oumaima CHAOUACHI

Thèse dirigée par	**Yann BULTEL,**	**Professeur des universités,** Grenoble INP, UGA.
et co-encadrée par	**Marion CHANDESRIS,**	**Ingénieur-chercheur,** CEA Grenoble.
	Jean-Michel RETY,	**Ingénieur-chercheur,** Forsee Power Paris.

Préparée au sein du **Laboratoire LMP, CEA-LITEN, Grenoble**
dans **l'École Doctorale I-MEP2 - Ingénierie - Matériaux, Mécanique, Environnement, Energétique, Procédés, Production**

Up-scaling methodology for lithium-ion battery modelling

Thèse soutenue publiquement le **12 Mars 2021,** devant le jury composé de :

M. Vincent VIVIER Directeur de recherche,	Sorbonne Université,	Rapporteur
M. Guy FRIEDRICH Professeur des Universités,	Université de Technologie de Compiègne,	Rapporteur
M. Sylvain FRANGER Professeur des Universités,	Université Paris- Saclay,	Examinateur
Mme Delphine RIU Professeur des Universités,	Grenoble INP, UGA	Présidente
M. Yann BULTEL Professeur des Universités,	Grenoble INP, UGA	Directeur de thèse

Et des membres invités :

Mme Marion CHANDESRIS Ingénieur-chercheur,	CEA Grenoble,	Invitée
M. Jean-Michel RETY Ingénieur-chercheur,	Forsee Power Paris,	Invité

Remerciements

Tout d’abord, je tiens à remercier Monsieur Vincent VIVIER et Monsieur Friedrich GUY d’avoir accepté de rapporter mon travail de thèse. Je les remercie chaleureusement pour l'intérêt qu'ils ont porté à mon travail et pour leurs remarques constructives.

Je remercie vivement Madame Delphine RIU d’avoir accepté de présider mon jury de thèse, et Monsieur Sylvain FRANGER d’avoir accepté d’y participer.

Je remercie très chaleureusement Madame Marion CHANDERIS, Ingénieur-chercheur au CEA-Liten, pour son encadrement, sa compétence, sa rigueur scientifique et sa clairvoyance qui m’ont beaucoup appris. Ils ont été et resteront des moteurs de mon travail de chercheur.

Je remercie également Yann BULTEL, Professeur des Universités Grenoble Alpes, qui fut pour moi un directeur de thèse attentif et disponible malgré ses nombreuses charges, ses compétences, ses conseils avisés et son aide durant ces trois ans de thèse.

Je tiens aussi à faire part de la sincère gratitude que je ressens envers Monsieur Jean-Michel RÉTY, Ingénieur-chercheur à Forsee Power. Son expertise et sa rigueur ont apporté énormément de valeur de cette thèse.

Un grand merci pour Madame Sylvie GENIES, Ingénieur-chercheur, pour ses compétences, ses conseils avisés et son aide notamment dans les aspects expérimentaux. Je lui adresse ma reconnaissance la plus profonde pour m’avoir instruit efficacement et avoir contribuer à l’aboutissement de ce travail.

Mes remerciements seraient incomplets si je ne mentionnais pas l'ensemble des membres du département CEA/LITEN/DEHT qui m’ont accompagné lors de la réalisation de ces travaux et qui ont toujours trouvé du temps pour m’aider.

Je remercie également chaleureusement tous les collègues avec qui j’ai eu la chance d’échanger tout au long de ces trois années au sein du Forsee Power.

Je tiens à remercier l’Association Nationale de la Recherche Technologie (ANRT) pour avoir subventionné ces travaux dans le cadre d’une thèse CIFRE.

Un grand merci enfin à mes parents, mes sœurs, mon frère, mon fiancé et toute ma famille, pour leurs patiences et leurs investissements dans l’ombre.

Merci à vous tous…

Table of contents

List of figures

List of tables

Greek letters

Parameter	Symbol
Stoichiometry (-)	y
Symmetry factor of the charge transfer (-)	α
Ionic resistance ($ohm\ m$)	χ
Characteristic alternating current penetration depth in the electrode (m)	λ
Electronic conductivity ($S\ m^{-1}$)	σ_e
Electrode porosity (-)	ε
Empirical factor (V)	β_0
Overpotential (V)	η
Electrode density (Kg m^{-3})	ρ_i
Electronic potential at the interface (V)	φ_{int}
Ionic potential at the interface(V)	ψ_{int}
Characteristic time (s)	τ
Pulsation (rad s^{-1})	ω
Standard chemical potential (J mol^{-1})	μ_i^0
Stoichiometry coefficient	ν_i

Latin letters

Parameter	Symbol
Activity coefficient (-)	a_i
Capacitance (F m^{-2})	C
Double layer capacitance (F m^{-2})	C_{dl}
Concentration of the lithium ion at the interface in the electrolyte ($mol\ m^{-3}$)	C_l
Concentration of a specie i at the equilibrium ($mol\ m^{-3}$)	C_i^*
Concentration of the vacant site at the interface of the AM ($mol\ m^{-3}$)	$C_{<>}$
Concentration of the lithium atom in the AM ($mol\ m^{-3}$)	C_s
Diffusion coefficient of Lithium in the active material ($m^2\ s^{-1}$)	D_s
Diffusion coefficient of SEI through the SEI ($m^2\ s^{-1}$)	$D_{l_{SEI}}$
Equilibrium potential (V)	E^{eq}
Faraday's constant (96487$C\ mol^{-1}$)	F
Frequency (Hz)	f
Applied constant current during the pulse (A)	I_0

Exchange current density ($A\ m^{-2}$)	i_0
Double layer current ($A\ m^{-2}$)	i_{dl}
Faradaic current ($A\ m^{-2}$)	i_f
Interfacial current ($A\ m^{-2}$)	i_{int}
Electrode's thickness (m)	L
Capacity (Ah)	Q
Theorical capacity for graphite/NMC (Ah)	$Q_{th}^{Gr/NMC}$
Reversible capacity for graphite/NMC in CC design (Ah)	$Q_{rev}^{CC,Gr/NMC}$
Irreversible capacity for graphite/NMC in CC design (Ah)	$Q_{irrev}^{CC,Gr/NMC}$
Reversible capacity for graphite/NMC in pouch design (Ah)	$Q_{rev}^{Pouch,Gr/NMC}$
Irreversible capacity for graphite/NMC in pouch design (Ah)	$Q_{irrev}^{Pouch,Gr/NMC}$
Reversible capacity for graphite/NMC in pouch design (Ah)	$Q_{rev}^{Pouch,Gr/NMC}$
Lithium loss during cycling (Ah)	Q_{LLi}
SEI capacity (Ah)	Q_{sei}
Gas constant (8.314 $J\ mol^{-1}K^{-1}$)	R
Capacity of loading (Ah)	$Q_{loading}$
Charge transfer resistance ($ohm\ m^2$)	R_{ct}
Ohmic resistance ($ohm\ m^2$)	R_{ohm}
SEI resistance ($ohm\ m^2$)	R_{SEI}
Average particle size (m)	r_{50}
Exchange area (m^2)	S_{AM}
Geometric area (m^2)	S_g
Temperature (K)	T
Cationic transference number (-)	t_+
Molar volume($m^3\ mol^{-1}$)	V_M
Area-specific impedance of the electrochemical reaction taking place at the interface ($ohm\ m^2$)	Z_{int}
Warburg impedance ($ohm\ m^2$)	Z_W
TLM impedance ($ohm\ m^2$)	Z_{TLM}
SEI Warburg impedance ($ohm\ m^2$)	Z_W^{SEI}
SRL Warburg impedance ($ohm\ m^2$)	Z_W^{SRL}
Number of electrons exchanged during the (de)-insertion reaction (-)	z_i

Abbreviation

Name	Symbol
Active material	AM
Butler-Volmer	BV
Beginning of life	BOL
Coin cell	CC
Check-up	CU
Dimethyl carbonate	DMC
Electrochemical impedance spectroscopy	EIS
Ethylene carbonate	EC
Equivalent electric circuit model	EEC
Ethyl methyl carbonate	EMC
End of life	EOL
Galvanostatic Intermittent Titration Technique	GITT
Lithium-ion battery	LIB
lithium iron phosphate	LFP
lithium titanate	LTO
Lithium loss	LLi
Negative electrode	NE
Open circuit potential	OCP
Positive electrode	PE
PolyVinyliDene Fluoride	PVDF
Potentio-Electrochemical Impedance Spectroscopy	PEIS
Reference electrode	REF
$LiNi_{0.6}Mn_{0.2}Co_{0.2}O_2$	NMC622
State of charge of the cell	SOC
Solid Electrolyte Interphase	SEI
Surface reconstruction layer	SRL
Scanning electron microscopy	SEM
Transmission line model	TLM
Vapor Grown Carbon Fibers	VGCF-H

Chapter I : Introduction

Table of contents

This research project is part of partnership set up between the Innovation Laboratory for the Technologies of the renewable energy and the nanomaterials (LITEN-CEA) and Forsee Power, via a CIFRE grant.

LITEN is an institute of the division of the technological research at the Atomic Energy and Alternative Energy (DRT-CEA), located

in Grenoble and Chambéry. Its main lines of research are linked to energy diversification in housing, transport, and nomadic technologies. LITEN, with approximately 1,200 employees and a portfolio of more than 800 patents, generates a turnover of approximately 150 million Euros. Its researches are currently focusing on solar and building energy, high-energy processes, electric vehicles, and advanced energy materials [1].

Forsee Power is an industry specialized in the design of batteries, energy management and integration systems for the portable and mobile equipment, electric transport and energy storage markets. The company was formed through the merger of Uniross Industrie, Ersé, EnergyOne and Dow Kokam France. It has 500 employees worldwide, and has commercial and industrial establishments in Europe, China and the USA [2].

The aim of this collaboration is to optimize Forsee Power module design and improve the prediction of its products lifetime. Indeed, CEA expertise in battery characterization, assembly and modelling will be exploited to meet Forsee Power expectations.

The following sections provide the survey of context and topics related to the thesis research.

I.1 Energy context and electrochemical storage for mobility

Given the decline in fossil fuel storage, the increase in oil prices and the undeniable effects of global warming, research is intensively active in implementing innovative solutions to reduce greenhouse gas emissions in industry, housing and transportation. Renewable energy sector is increasingly becoming a potential substitute for fossil fuels in view of recent progress in the fields of solar and wind energy [3, 4]. In this context, demands for high-capacity/power energy storage, to address the exploitation of intermittent energies, electromobility, and development of "smart-grids", have been identified and have led to a strong interest in the development of new energy storage systems. Indeed, renewable energy sources cannot be

directly used in their primary form. They should be transformed in electrical energy, which is considered as the most common energy vector, and we need efficient rechargeable storage systems. These storage systems are designed to address four main issues: the recovery of excess energy production compared to current demand, the supply of energy to make up for shortfalls due to the intermittent nature of the source, the supply of energy to meet occasional peaks in demand and finally the supply of energy in the case of an electrical system or grid interruption. For thirty years now, storage energy systems allow powering devices for small electronic applications, like portable electronic, and large-scale applications for the transport. In fact, in the automotive sector, a major change is currently taking place with the development of Hybrid Electric Vehicles (HEVs), all-Electric Vehicles (EVs) and Plug-in Hybrid Electric Vehicles (PHEVs). Thus, energy transition is essential to meet climate targets [5].

Electrochemical secondary batteries are among the most promising technologies in storage energy systems. In fact, electrochemical energy storage systems are devices for storing electrical energy in chemical form. This form of storage takes advantage of the fact that electrical and chemical energy share the same vector, the electron. This advantage limits losses related to the conversion of energy from one form to another. Such technologies include lead acid batteries, nickel/cadmium or nickel/metal hydride batteries and lithium-ion batteries. For transportation, there are several alternatives among which Li-ion technology (LIB) is known to be the most efficient one. It is the technology used by Forsee Power to develop battery solutions for various applications.

Nevertheless, many challenges remain in terms of optimizing performance, durability and security in order to accelerate the marketing of LIB technologies. Indeed, Li-ion battery system conception must ensure the lowest decrease of performances along with ageing. To that end, models are used to estimate the evolution of accumulator's performance as function of time and finally to optimize the design. In this context, to control its commercialized battery module Flex 7, Forsee Power relied on real-time empirical models. To develop these models, it required a significant data acquisition and adjustment time. Furthermore, the approach is also time consuming and expensive to be applied for other accumulators. Indeed, Forsee Power integrates different accumulators with different electrochemistry and design for diverse applications, which impact the aging mechanisms of the cell. For that, an adjusted oversizing of the pack has been adopted as a solution. Today, the challenge for Forsee Power is to improve the prediction of its products lifetime and consequently to optimize the battery sizing. To achieve these

challenges, an EEC model for real time application was developed in this Ph-Doctoral work via an up-scaling methodology.

I.2 Lithium-ion battery

Lithium-ion batteries (LIB) have been proposed in the 1970s by M. S. Whittingham using lithium metal as an anode [6] and metal disulfide (such as TiS2 or MoS2) for the cathode In 1981, this anode has been replaced by a graphite material which has been considered as a good alternative to the lithium metal. At the same time, material development research has been performed offering an intercalated positive electrode based on cobalt as suggested by Goodenough [7]. The development of these two electrodes was achieved by proposing a LIB combining them and thus based on $LiC_6/LiCoO_2$. The LIB based on this technology have been considered as a technological and commercial success since their first commercialization by SONY in 1991. Due to their advantageous characteristics such as their high energy density and power capability, this technology is equipping a growing number of applications ranging from small-scale electronic gadgets to automotive vehicles [8].

Principles of lithium-ion battery

The lithium-ion battery is based on the reversible exchange of lithium ions between a positive and a negative electrode (Figure I-1). These electrodes have an overall potential difference that depends on the chemical nature of the two electrode materials. Each electrode has a support that serves as a metallic current collector, usually an aluminum collector for the positive electrode and a copper collector for the negative one. The electrode consists of active materials (>80%), an electronic conductor (carbon black) and a polymer binder. The metal collectors are connected to the external circuit, their role being to ensure the circulation of electrons. It should be noted that a separator is placed between the two electrodes in order to avoid any internal short circuit. It is a porous separator whose role is to allow the passage of ions between the two electrodes without allowing electron conduction. The two electrodes with the separator are immersed in an electrolyte, which ensures the transport of lithium ions from one electrode to the other.

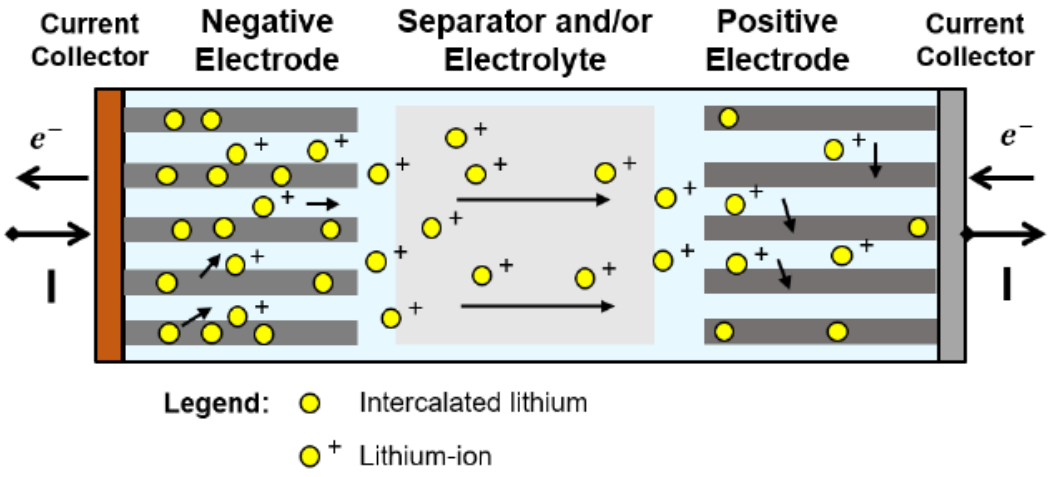

Figure I-1 *: Principles of lithium-ion battery during discharge* [9]

Positive electrodes

The positive electrode is most of the time made of an intercalated material where lithium ions are inserted in the crystallographic structure. This structure is able to supply lithium ions. It should assure a high ionic and electronic conductivity. The active material (AM) should be able to intercalate a large lithium quantity with minor structural changes to ensure a high reversibility. Moreover, AM should not dissolve in the electrolyte, must be abundant and available at low cost. The intercalation process in these compounds should take place at high potentials, higher than 3 V vs Li+/Li [10, 11], to increase the stored energy, but not too high, to remain in the stability window of the electrolyte. Several active materials can be used to play this role. Lithiated metal oxides $LiMO_2$ (M = Co, Ni), such as $LiCoO_2$ (LCO), $LiMn_2O_4(LMO)$, $LiNi_xMn_yCo_xO_2(NMC)$... are commonly used. They can be classified according to their lattice structure: layered similar to LCO, spinal similar to LMO. LCO is well-known and was used because of its high capacity. However, cobalt is expensive and unstable. To enhance safety, it has been replaced by other materials such as manganese (Mn) [12], which is clearly much cheaper than Co, resulting in the appearance of the LMO technology with a spinel structure. Although, it has a good capacity, LMO suffers from manganese dissolution causing SEI growth on the negative electrode and capacity losses [12] [13]. More recently, NMC active materials have been elaborated to enhance the stability of the crystallographic structure [12]. Regardless the percentage of each metallic components, NMC is widely used in EV applications [14]. It can suffer from nickel (Ni) migration which can block lithium vacant sites and form Surface Reconstruction Layer (SRL) [12]. Another highly common active

material is lithium iron phosphate $LiFePO_4(LFP)$, which has an olivine structure. It is known for its thermal stability and high-power capability [15]. However, it has a low electrical conductivity which has been partially solved by adding carbon coating on the particles. It also suffers from a lower average potential and theorical capacity (around 140-160 mAh.g^{-1}) compared to NMC (theoretical capacity of 200 mAh.g^{-1}), which reduces the available energy [12].

In the scope of this thesis, NMC622 has been used as active material for the positive electrode and graphite for the negative one. NMC provides a good compromise between safety and power density. It presents 25% from the available commercialized positive electrodes in 2016 (2nd place behind lithium-iron-phosphate).

Negative electrodes

Negative electrodes should be stable at low potential and offer a huge reservoir of lithium to store the charges. Lithium metal has been the first developed negative electrodes, with its extremely high theoretical specific capacity of 3860 mAh.g^{-1}. However, it has an unstable surface leading to dendrites formation increasing short-circuit problems. Nowadays, graphite is the most commonly used negative electrode material. It can intercalate lithium at very low potentials between 0.5 V and 1 mV vs Li+/Li, close to the potential of metallic lithium and it has a theoretical specific capacity of 372 mAh.g^{-1} . In addition to that, it has an excellent electronic conductivity, is rather abundant and available at a low price. The crystallographic structure of the graphite is lamellar with two dimensional layers sheets [16]. It requires a stable passivation layer to protect graphite particles from further degradation mechanisms. However, this layer formation induces lithium losses. Lithium- titanate, $LiTi_5O_{12}(LTO)$, is another type of negative active material commonly used. This material has a high stability and does not require the formation of any passivation layer on its surface. It has a spinel configuration similar to LMO electrodes. The only weakness of this electrode type is the cost of titane (Ti), the reduced cell voltage and its lower capacity (175 mAh.g^{-1} theoretical) [15]. Silicon (Si) active material is studied since the 90s due to its huge theoretical specific capacity (around 4200 mAh.g^{-1}) and low electrode potential (i.e. 0.2V vs Li+/Li) [17]. However, it suffers from volume expansion that can reach +300% from its initial volume causing a huge irreversibility and premature aging. Therefore, the application of this type of negative electrode is still limited, even though it starts to be introduced in limited amount in recent cells, around 2 to 5% blended

with graphite. For the graphite, it constitutes 90% of the negative electrodes in the market. Therefore, it will be used as a negative electrode in the present study.

I.3 Li-ion battery models

Nowadays, mathematical models are a useful tool to decouple and quantify the different mechanisms, and to understand their evolution along the lifetime of the battery. A huge research effort devoted to battery modeling started in the 60s with different approaches such as Electric Equivalent Circuit (EEC) models [18], but also electrochemical ones like the so called porous electrode model approach introduced by Newman and Tiedeman in 1975 [19, 20] and applied on LIB in the 90s [21]. On one hand, EEC models, considered as semi-empirical models, simplify the multi-physics behavior of the cell to obtain a representation with an electric circuit, which makes them easy to implement in a Battery Management System (BMS). On the other hand, physics-based models take into account the complex mechanism occurring in the porous electrode.

Electric Equivalent Circuit (EEC) models

Electric Equivalent Circuit models are famous empirical models, which are fitted to experimental data without direct relations to the physicochemical mechanisms occurring inside the LIB. They over-simplify the electrochemical behavior of the battery, thereby, they have a simpler construction and a faster computation time. Among their various applications, they can be employed in Battery Management System (BMS), where computational resources are limited, or for the sizing of modules or battery packs with specific requirements. However, since these models are adjusted from experimental data, they are often poor predictor of the battery behavior under different operating conditions and specially, cannot be extrapolated to other cells or LIB technologies. Moreover, EEC models are also often used to interpret the Electrochemical Impedance Spectroscopy (EIS) results. However, for the same system, many different EEC models have been suggested in the literature depending on the researcher interpretations and visions based on the time constants. Among EEC models, the Transmission Line Model (TLM) has been introduced by De Levi in 1964 [22] based on a physical approach, as it takes into account the porous nature of the electrode. It is commonly applied and developed on porous electrode to analyze EIS spectra, by considering electronic and ionic paths through the solid phase and the electrolyte in the pores respectively [23], [24].

Electrochemical models

Electrochemical models are physics-based, describing the physical phenomena in the cell *via* mathematical equations. In these models, different physics are coupled such as electrochemical reactions, transport equations and thermal effects. Local conditions inside the cell, such as local potentials or concentrations, and global physical variables of the electrochemical cell are thus accessible. These models have been developed by Newman's group on a cell model based on lithium anode, a solid polymer electrolyte and an insertion composite cathode material [19]. Due to its success, several researchers used similar electrochemical models for Li-ion batteries to analyze and then optimize the performance and the design of the battery. Since then, many approaches have been presented in the literature such as, the Pseudo two–Dimensional (P2D) model [25] and the single particle one (SPM) [26]. Although, these models allow to predict the behaviour of the system, they require the knowledge of many physical parameters not provided by cell manufacturers and have non-negligible computational time.

Upscaling methodology

The main objective of an up-scaling methodology is to get the link between local physical phenomena taking place in the battery impedance to get a physics-based EEC model. In fact, it allows to define the different EEC model components as function of the physical parameters at the electrode scale.

This approach has been presented in several forms. Meyers *et al.* [27] were among the first research groups to present an analytic impedance of a single particle electrode model with all the interfacial physics but neglecting the diffusion in the liquid phase (Figure I-2).

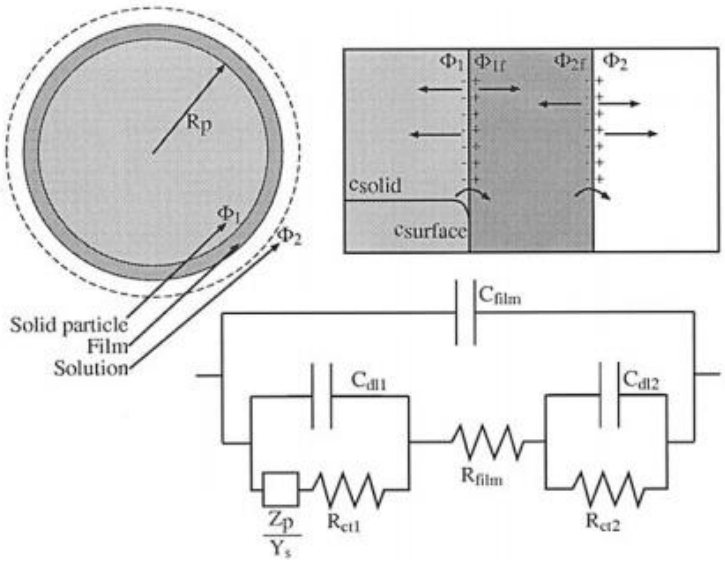

Figure I-2 *: Presentation of Meyers et al. model* [27]

An analytic EEC model for all the battery considering a porous electrode has also been proposed by Doyle *et al.* [28] taking in consideration the diffusion in the liquid phase. For the last years, many studies have been presented to enrich these up-scaling approaches with respect to the physics proposed by Newman for a porous electrode model. These include the work proposed Sikha *et al.* [29], Huang *et al.* [30], Gruet *et al.* [8]… These models can identify the origin of different constant times in the frequency domain. However, they do not look for representing the Warburg, the diffusion impedance, with real electric components (LRC). In general, this step is performed in the real time model domain as suggested in many studies [31]. They use a mathematical development to linearize the Warburg expression without looking to define all the electric components as function of the physical parameters.

I.4 Topic of the current thesis

To the best of my knowledge, we developed for the first time an up-scaling methodology to bridge the gap between the physical and geometrical parameters from physics-based models at the electrode scale, and the empirical parameters from EEC models used for batteries. Our methodology is established in two stages. First, the physical equations are solved in the frequency domain to obtain the corresponding impedance model. Then, this impedance model is mathematically simplified in a series of RC elements (in parallel), using a mathematical development. The obtained formulation is adapted to real-time applications since it involves only RC type elements. The proposed upscaling methodology has been developed at the

beginning of life of the battery and during its entire life. Graphite vs NMC622 cell configuration has been selected to validate the different steps of the methodology.

In the second chapter of this manuscript, the experiments carried out in this thesis are presented. These experiments have been conducted to extract the physical parameters and to validate the final models. These experiments include characterization at the beginning of life of the battery and also aging experiments. The experimental designs, protocols, and result analyzing are detailed. The experimental results presented in this chapter are then used in the two other chapters of the manuscript to validate the different steps of the up-scaling methodology.

In the third chapter, the up-scaling methodology developed in this thesis is applied at the beginning of life of the battery. The different physical assumptions are presented. The developed two-steps approach has been applied and discussed for the positive and the negative electrodes. The analytic and real-time models are compared to the experimental results and discussed.

Finally, the aging mechanisms of the graphite and NMC622 electrodes observed in our experiments are discussed in chapter four. In this latter, the upscaling methodology is applied to the aged cell at different state of health. The goal is to propose an EEC model able to account for the evolution of the cell with aging. The evolution of the different physical parameters related to electrodes, such as, diffusions inside active material, diffusion within the passivation layer, passivation layer thickness, exchange areas…, during the cell lifetime are deduced and discussed. Besides, characteristic frequencies and times of the different physical process are identified.

Chapter II : Experimental and material characterization of Li-ion cell

Table of contents

The investigation of the properties of LIB components is crucial to validate the model and to check the evolution of the physical parameters of the single cell battery during its entire lifetime. In this chapter, we propose two different time domains for battery characterization. The first one, at beginning of life, in which experimental tests protocols were suggested to identify the model parameters and the reference state of the battery. The second one is about following the evolution of the battery during its lifetime. The different active materials, electrodes and cell designs employed in this analysis are described and detailed. For this study, NMC622 *vs* graphite battery system is selected to be studied and characterized in the aim to validate the developed models.

II.1 Active materials and electrodes

In this section, a presentation of the different electrodes employed in the scoop of the thesis is proposed. Active materials (AM), choice of binders and conductive additive with the manufacturing protocols for the positive, negative and reference electrodes are described. Then, a characterization of the AM and of the electrolyte conductivity are suggested.

II.1.1 Positive electrode

A NMC-based positive electrode (PE) was prepared by coating on an aluminum foil a dispersion of a polycristalline LiNi0.6Mn0.2Co0.2O2 (from Umicore), Super P65 (from Imerys) with an exchange surface area of 65m²/g, VGCF-H (Vapor Grown Carbon Fibers) from Showa Denko as carbon conductive additive and PolyVinyliDene Fluoride (PVDF) as a binder with 92:2:2:4 weight ratio, respectively. The average particle size of the NMC powder $\boldsymbol{r_{50}}$ is around 6.6µm. It has been measured by laser granulometry (Figure II-1 .a). This electrode was prepared using a laboratory in house process [32]. The components were mixed using a planetary mixer, using NMP solvent. The slurry was then coated onto the current collector. A custom reverse roll coater installed in dry room with 1.5 m drying oven was used to dry the electrode, which was then calendared to reach the desired porosity. The positive electrode was manufactured considering a loading of 18.2 mg/cm² corresponding to 3.43 mAh/cm² with a porosity of 24%. Scanning electron microscopy (SEM) was used for preliminary observation of the NMC electrode to see the well-defined spherical morphology of the particles (Figure II-1 .b)

(a)

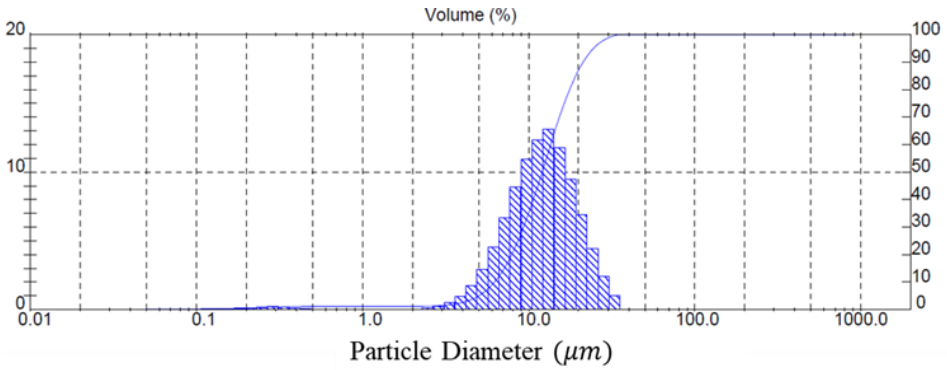

(b)

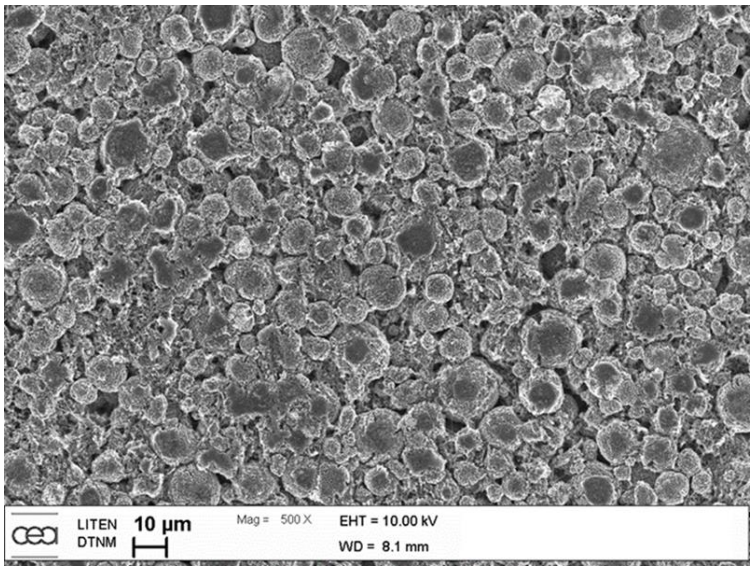

Figure II-1*: Positive electrode geometric characterization: (a) Particle size distributions of NMC622 powder measured by laser granulometry (b) SEM images of a pristine NMC electrode.*

II.1.2 Negative electrode

The graphite-based negative electrode (NE) was prepared similarly, by using a mixture of spherical graphite with CMC (from Ashland), SBR (from BASF) binders (acronyms of Sodium Carboxymethyl Cellulose and Styrene Butadiene Rubber) with 97.4:1.3:1.3-weight ratio, respectively, coated on a copper foil. The average particle size of the graphite powder, r_{50} , was measured by a granulometry and it is around 7.88μm (*Figure II-2*.a). Similar to the positive electrode, the negative electrode was manufactured using the same laboratory in house process, but using deionized water as solvent. The negative electrode was manufactured

considering a loading of 10.8 mg/cm² corresponding to 3.78 mAh/cm², with a porosity of 26%. A visual inspection of the SEM image (*Figure II-2*.b) shows a well define spherical geometry of the graphite.

(a)

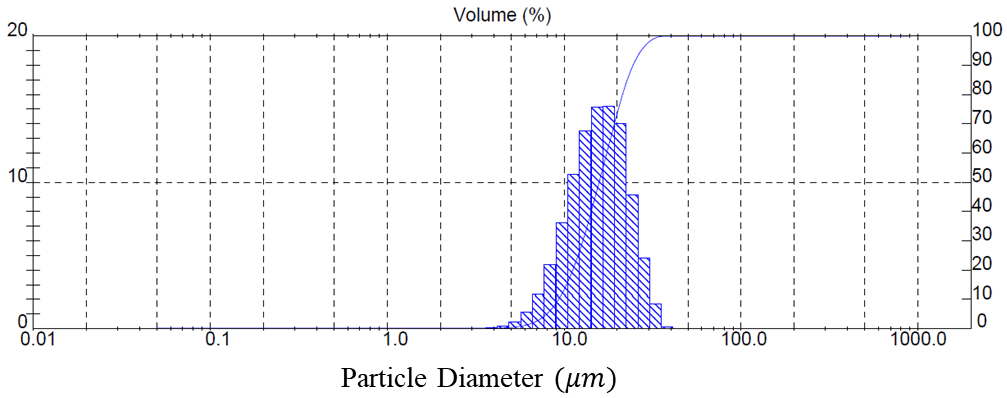

(b)

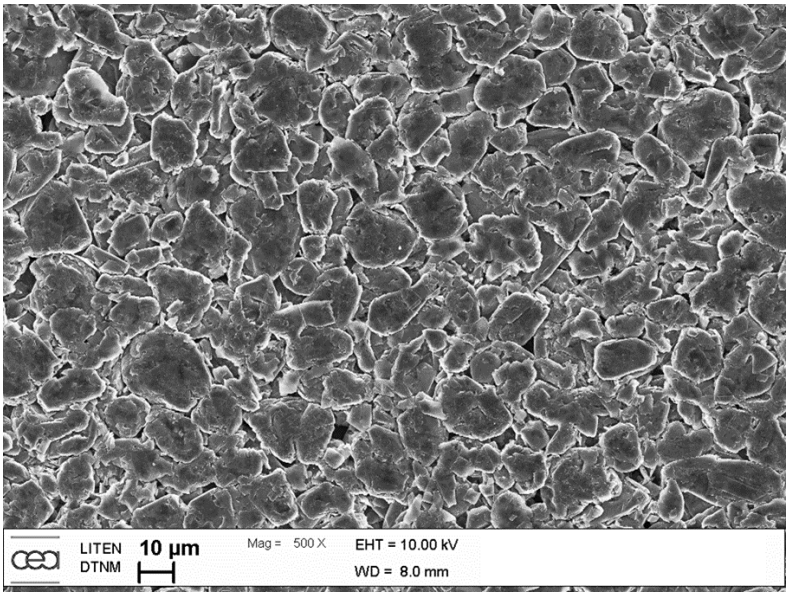

Figure II-2 *: Negative electrode geometric characterization: (a) Particle size distributions of graphite powder measured by laser granulometry (b) SEM images of a pristine graphite electrode.*

II.1.3 Reference electrodes

In this work two references electrodes were elaborated. The first one is a lithium foil-based electrode. It was employed for the Galvanostatic Intermittent Titration Technique (GITT) measurements to have access to the equilibrium potential of the active materials inside the pouch cell. In fact, lithium foil reference electrode for the beginning of life tests presents a good stability and has been employed in previous studies [33]. It was prepared by deposing a lithium chip on fine copper mesh with pressing before sealing it on the copper collector.

For Electrochemical Impedance Spectroscopy (EIS) measurements, lithium foil reference electrode suffers from a too low stability [34] and can also cause artificial EIS response detected in Nyquist plots as a "spiral" type behavior, leading to a lack of reproducibility [35]. These effects make them non-efficient for investigations during aging or impedance measurements. Alternative solutions are proposed in the literature to limit these effects. As reference electrodes must have a stable potential over a large SOC range, lithium titanate (LTO: $Li_4Ti_5O_{12}$) and lithium iron phosphate (LFP: $LiFePO_4$) have recently attracted considerable attentions as reference electrodes for EIS [36], [23], [37], [38], [39], [40]. For the present work, LFP is manufactured as an alternative solution to lithium electrode, to follow the electrodes potential and the impedance spectra evolution during aging tests. This reference electrode is prepared by mixing a commercial $LiFePO_4$ active material from BeLife with Super P65 as carbon conductive additive and PVDF as binder before a coating on an aluminum mesh.

II.1.4 Estimation of the Electrode geometric parameters

The thickness (E) and the weight (m) of the different electrodes with the separator and the collectors have been measured using numerical dispositive. The electrodes characteristic have been used to re-calculate the porosity and the exchange area of each electrode active material. For the porosity, the following relation is used:

$$\varepsilon = 1 - \frac{m}{SE}\sum x_i \rho_i \qquad \text{(II.1)}$$

Where x_i is the mass fraction of one electrode component, ρ_i the correspondent density and S the electrode surface. Assuming spherical active material geometry, the active material exchange surface can be estimated as following:

$$\boldsymbol{S_{AM}} = (1-\varepsilon)\frac{3}{r_{50}}ES \qquad \text{(II.2)}$$

II.1.5 Electrolyte

In this study the employed electrolyte consisting of 1M of lithium hexafluorophosphate salt ($LiPF_6$) in 1:1:1 weight proportion of ethylene carbonate (EC), ethyl methyl carbonate (EMC), and dimethyl carbonate (DMC). Its conductivity dependences to the concentration and the temperature have been estimated (*Figure II-3*) using Bernardi relation [33] and Arrhenius law respectively. In fact, Bernardi *et* al. presented in their work an empirical polynomial

equation to express the conductivity of an electrolyte, similar to the one that we use in the scoop of this thesis, as function of the concentration and the temperature. Therefore, at T=20°C, the standard conductivity can be expressed as:

$$\sigma_0(T = 20°C, C) = 2.72C^3 - 14.67C^2 + 22{,}15C \quad \text{(II. 3)}$$

To get the variation within the temperature, the following Arrhenius law was respected:

$$\sigma(C,T) = \frac{T_0}{T}\sigma_0(C = 1, T = 20°C)e^{-\frac{Ea}{R}[\frac{1}{T}-\frac{1}{T_0}]} \quad \text{(II. 4)}$$

Where T_0 is the standard temperature equals to 20°C, C the concentration, Ea the activation energy equals to 15510,6 ($J.mol^{-1}$) and R the ideal gas constant.

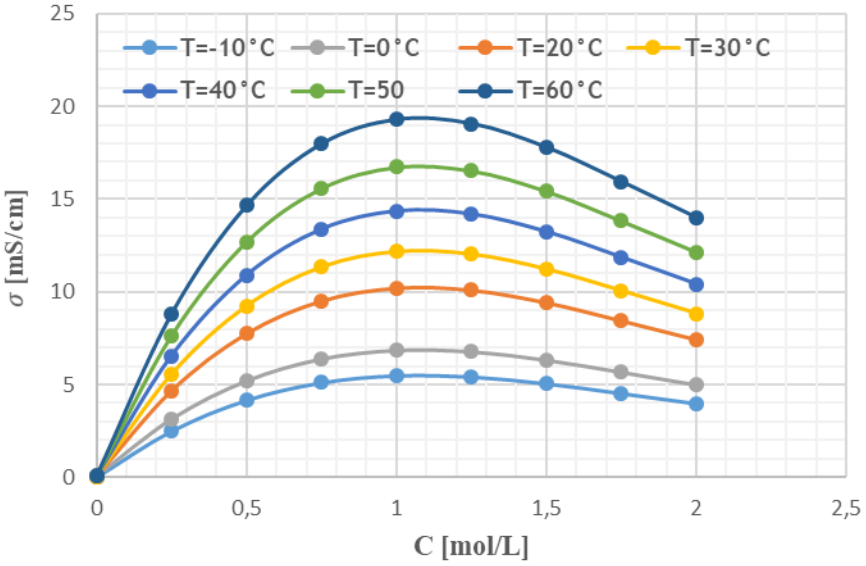

Figure II-3 : *Estimated conductivity of the electrolyte as function of the concentration and the temperature.*

II.2 Cell designs

In this paragraph, the two cell designs employed for the cell characterization are presented. The details of the design's assembly with the different components and materials are described. The first design is a coin cell design used for beginning of life tests and post-mortem analysis. The second one is a pouch cell design employed for beginning of life and aging tests.

II.2.1 Coin cell design

The first design is a so-called half-cell design in coin cell (CC) format. It is a CR2032 coin cell made of stainless steel and it consists of a top cover, bottom container spacer and spring. An illustrative schema is shown in *Figure II-4*. The assembly of the CC is carried out as described in *Figure II-4* from the positive cap to the negative one. Counter and working electrode disks used are separated by a separator with appropriate dimensions to guarantee the safety and avoid short circuit by contact on the edge of the electrodes. The separator is a 25 µm thick monolayer (PP) Celgard 2400. This design consists of an assembly of the tested active materials electrode as working electrode (graphite in case of the NE and NMC 622 in case of the PE) with a 14mm diameter and a lithium foil as counter electrode, with a 16mm diameter. For postmortem analysis, symmetric CC design is elaborated consisting on Gr *vs* Gr and NMC *vs* NMC. It was employed to perform EIS measurements at the end of life of both electrodes.

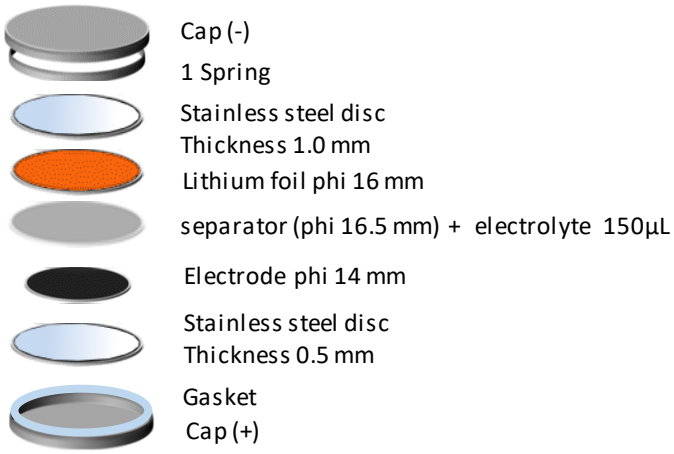

Figure II-4 *: An illustrative schema of coin cell components in the order of their assembly.*

II.2.2 Pouch cell designs

The pouch cell design used in this work is a pouch cell containing the two tested electrodes (graphite for the NE, $LiNi_{0.6}Mn_{0.2}Co_{0.2}O_2$ for the PE) with a lithium foil reference electrode inserted between the PE and the separator an covered with an extra separator to avoid short circuit, as described Figure II-5a and *Figure II-6*. An aluminum tab is ultrasonically welded to the positive electrode, while a nickel one is welded to the negative. The pouch cells are assembled in a dry room (-20°C dew point) and filled with electrolyte in an Argon filled glove box. The pouch cells are put under partial vacuum and are sealed using a heat sealer. The electrode surface areas $\boldsymbol{S_g}$ are for the positive electrode 10.24 cm² (3.2x3.2 cm) and for the

negative 12.25 cm² (3.5x3.5 cm). These dimensions are chosen to ensure a good coverage of the positive electrode by the negative one, while trying to keep this mismatch as low as possible. Indeed, this mismatch implies an increase of the irreversible capacity with lithium ions consumed at the negative electrode during its first lithiation due to SEI formation. This area mismatch leads to a lower utilization of the anode with, at the cell scale, an electrode capacity ratio N/P of 1.3 instead of the "face to face" N/P ratio of 1.1. The exchange surface areas $\boldsymbol{S_{AM}}$ for this pouch cell design are estimated from the knowledge of $\boldsymbol{r_{50}}$ giving a value around 22.03m² for the $LiNi_{0.6}Mn_{0.2}Co_{0.2}O_2$ and 22.28m² for the graphite (Summary in table 1). As we have mentioned before, for EIS measurements, LFP reference electrode was employed. This reference electrode is inserted inside the 4-electrode pouch cell design presented Figure II-5b. The Li reference electrode is kept in the system to control the potential of the electrodes. A partial delithiation of $LiFePO_4$ is performed *in situ* once the cell is assembled and charged at a C/50 rate to reach the 3.424V *vs* Li^+/Li potential plateau that corresponds to a stoichiometry of around 0.5.

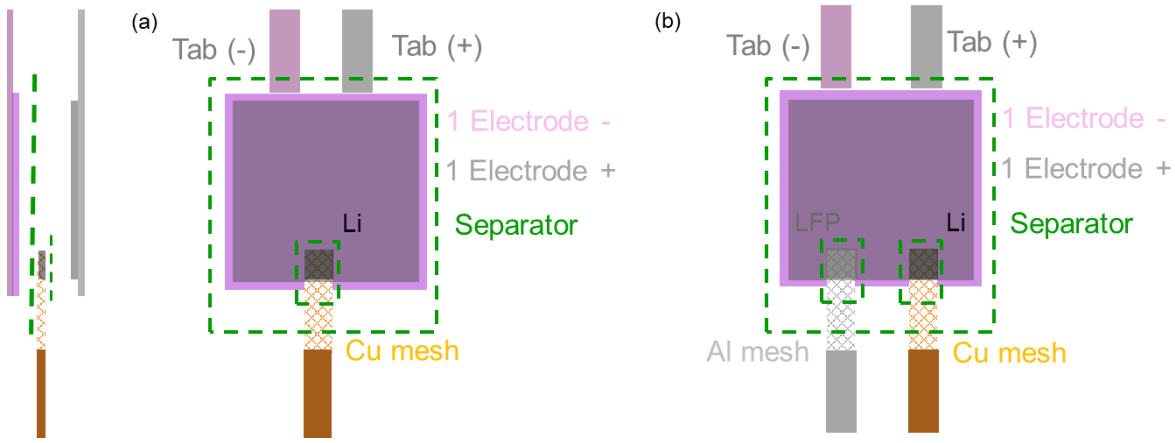

Figure II-5: *Schematic description of (a) the 3-electrodes pouch cell design and (b) the 4-electrodes pouch cell design from top view.*

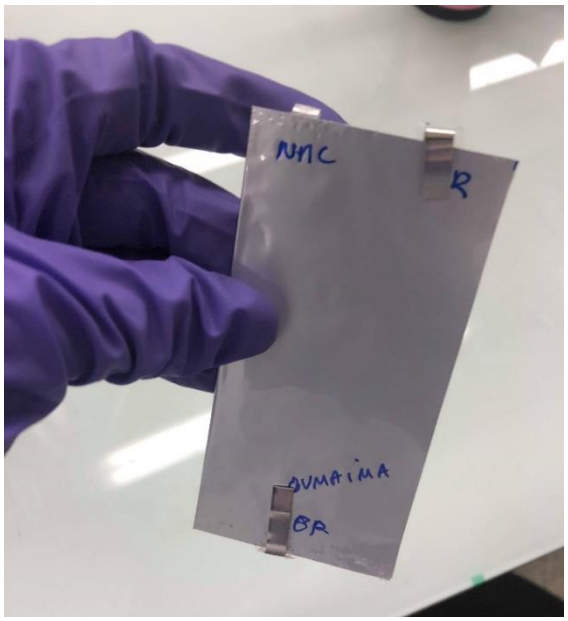

Figure II-6*: a real photo of the 3-electrodes pouch cell design.*

II.3 Beginning of life experiments

In this section, the different experimental protocols used to characterize the cell at beginning of life are presented. This part aims to propose an experimental strategy to extract the different parameters of the electrodes. In the present work, three important protocols have been applied [41]:

- Formation protocols are performed depending on the active material type to to check that the expected specific capacity is well obtained and also, in the case of the NE, to form the Solid Electrolyte Interphase (SEI) on the graphite particles
- Electrochemical impedance spectroscopy (EIS) protocol is done to deduce the exchange current density, i_0, and the different resistance of the electrode.
- Galvanostatic Intermittent Titration Technique protocol (GITT) is first used to measure the equilibrium potential of the electrode with CC and pouch cell designs in order to have an empirical law of the variation of the OCV as a function of either SOC or the two electrode stoichiometries. Second, the diffusion solid coefficient, D_s, is estimated for each electrode.

II.3.1Experimental protocols

II.3.1.1 **Formation protocols**

In this work, two types of formation protocols were performed. The first one for NMC *vs* Li coin cells consists of two full charge/discharge cycles between 2.6 and 4.3V at C/20. The second type was applied for the graphite vs. Li coin cells and all the pouch cell designs. It consists of one cycle at C/20 (one discharge/charge cycle for graphite vs. Li coin cells or one charge/discharge for the pouch cells) followed by 3 others cycles at C/5 applied between 10mV and 1V and 2.5 and 4.2V respectively. This second protocol is performed to ensure the formation of a stable Solid Electrolyte Interphase (SEI) on the graphite particles.

II.3.1.2 **Electrochemical Impedance Spectroscopy (EIS)**

Electrochemical Impedance Spectroscopy has been considered as a standard method to estimate fundamental physical properties, to investigate reaction mechanisms and to characterize cells [8], [42], [43], [44]. It is an effective tool to follow concurrently the resistive, capacitive and the inductive behaviors of the system. The exploitation of the EIS results can help to figure out many physical phenomena such as solid phase diffusion, charge transfer kinetics and ion transport by using their frequency dependent characteristics. Moreover, in the literature, EIS measurements have been used to study electrode/electrolyte interface [45], electrolyte performance [46], and to evaluate the aging by following the SEI resistance [47], [48]. It has been also used to study the kinetics of charge transfer in Li-ion batteries and evaluate precisely the exchange current density i_0. Generally, a simple R-C element model is implemented to extract i_0 from an impedance spectrum [49].

During an EIS measurement, alternative sinusoidal potential excitations are applied to the electrochemical cell at various frequencies, while measuring the resulting currents. These current signals are analyzed at the different frequencies to obtain the cell impedance spectrum. This measurement is performed by using an excitation signal with a small amplitude to obtain the pseudo-linear response of the cell. In this study, Potentio-Electrochemical Impedance Spectroscopy (PEIS) measurements were performed at different SOC on the pouch cell with LFP reference electrode. The measurements were done with a voltage amplitude of 5mV. The frequency range was set to 200 kHz-10 mHz with 8 points per decade. Impedance spectra were measured at room temperature. To reach the desired SOC, a galvanostatic discharge at C/10 is applied during 1h, followed by a rest period of 1h to reach equilibrium before the PEIS measurement. This protocol is repeated 10 times to complete the electrochemical processes. It

is applied in discharge after the cell formation protocol and a first charge of the cell until the cut off voltage of 4.2V.

II.3.1.3 **Galvanostatic Intermittent Titration Technique (GITT)**

GITT experiment consists of series of current pulses at a fixed value followed by rest periods. This sequence is repeated until the battery is fully charged and discharged and it used to extract information about the equilibrium potential and lithium diffusion coefficient of active materials [50], [51], [52]. In this study, a series of pulses is applied to the cell at a fixed current of C/10 during 12 minutes, followed by a 4h relaxation time. The sequence is repeated 50 times until complete charge or discharge of the cell. GITT tests were performed on NMC *vs.* Li and graphite *vs.* Li coin cells, as well as in the pouch cell design with a Li reference electrode. During the pulse period, data are recorded at every voltage increment/decrement of 1 mV. The GITT protocol is applied after formation of the cells and is performed in both charge and discharge. It is started in charge for NMC vs. Li and full cell configurations, and in discharge for graphite vs. Li.

II.3.2 Experimental results

II.3.2.1 **Equilibrium potential**

Equilibrium potential, E_q of an active material inside an electrode is reached when the chemical potentials of lithium in both phases, *i.e.* at the interface between the active material and the electrolyte, are equal. Using GITT method, E_q is identified at the end of each relaxation period [53]. For the coin cell designs, *i.e.* working electrode vs. Li, the measured open circuit potential (OCP) corresponds to the equilibrium potential of the studied material. The results obtained for NMC and graphite in both lithiation and delithiation are shown Figure II-7 as function of the material stoichiometry, together with the averaged value.

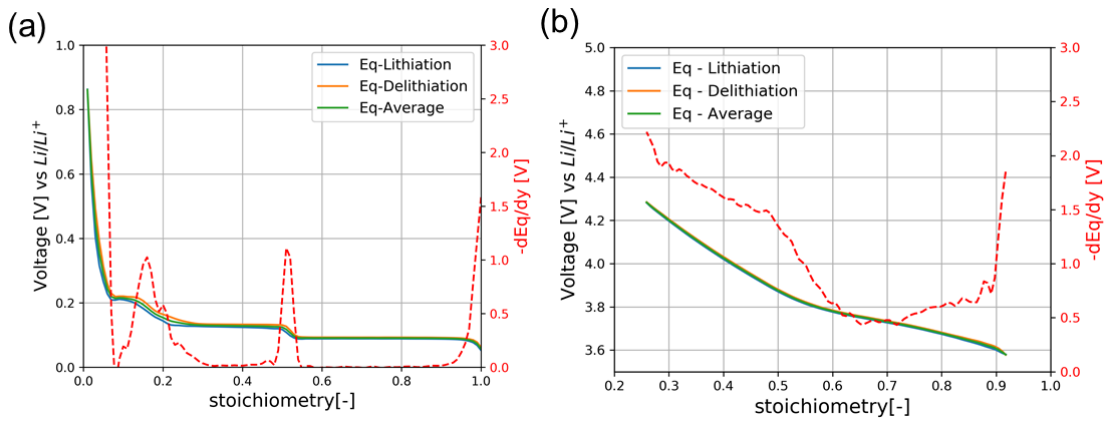

Figure II-7 *: Equilibrium potentials measured in half-cell configuration (CC cell) in lithiation and delithiation together with the average value and its derivative versus stoichiometry (a) Graphite vs Li (b) NMC vs Li.*

For the graphite (*Figure II-7*a), the stoichiometry range is defined by assuming that, at the end of the first lithiation the material stoichiometry, $y_{max}^{CC,Gr}$ is equal to one, and by using the subsequent delithiation to determine the reversible capacity $Q_{rev}^{CC,Gr}$, which is reached in our case at 356 mAh/g with a first irreversible capacity ($Q_{irrev}^{CC,Gr}$) of 28 mAh/g. This latter value is slightly lower than the theoretical capacity Q_{th}^{Gr}equals to 372 mAh/g. This theoretical capacity is used to calculate the minimum stoichiometry ($y_{min}^{CC,Gr}$) corresponding to the delithiated graphite to obtain a value of 0.045 with the following equation:

$$y_{min}^{CC,Gr} = \frac{Q_{th}^{Gr} - Q_{rev}^{CC,Gr}}{Q_{th}^{Gr}} \quad \text{(II. 5)}$$

For the graphite (*Figure II-7*a), the three classical potential plateaus are observed with a slope close to zero and two transitions regions for stoichiometry around 0.17 and 0.5. A slight difference between the lithiation and delithiation curves is observed, but only during these transition regions. The potential plateaus correspond to coexistence of two-phases in the solid material, while only one phase exists in the transition regions [54]. The derivative of the equilibrium potential versus stoichiometry, obtained from the average value, is also presented and highlights the variation of the potential during the transition regions.

For the NMC 622, the stoichiometry range is calculated considering the theoretical value (Q_{th}^{NMC}) of 276.7 mAh/g and by assuming that the material is fully lithiated before formation. The measured reversible capacity ($Q_{rev}^{CC,NMC}$) of 184 mAh/g is determined from the lithiation step, by taking into account the first irreversible capacity ($Q_{irrev}^{CC,NMC}$) of 21 mAh/g. The

maximum and minimum stoichiometries of $LiNi_{0.6}Mn_{0.2}Co_{0.2}O_2$ in lithiation $y_{max}^{CC,NMC}$ and delithiation $y_{min}^{CC,NMC}$ are respectively given by:

$$y_{max}^{CC,NMC} = \frac{Q_{th}^{NMC} - Q_{irrev}^{CC,NMC}}{Q_{th}^{NMC}} \quad \text{(II. 6)}$$

$$y_{min}^{CC,NMC} = \frac{Q_{th}^{NMC} - (Q_{rev}^{CC,NMC} + Q_{irrev}^{CC,NMC})}{Q_{th}^{NMC}} \quad \text{(II. 7)}$$

leading to a variation range of [0.259 – 0.92].

As presented in (*Figure II-7*b), there is almost no difference between lithiation and delithiation measurements, which confirms that the equilibrium state is reached at the end of the relaxation periods. The equilibrium potential for $LiNi_{0.6}Mn_{0.2}Co_{0.2}O_2$ steadily decreases when the stoichiometry increases with a higher slope at low stoichiometry. It is highlighted on the derivative of the average equilibrium potential that the slope is almost constant for a stoichiometry above 0.65.

II.3.2.2 **Stoichiometry of the electrodes**

The investigation of the different parameters of the positive and the negative electrodes inside a pouch cell design requires the knowledge of their stoichiometry as function as the SOC of the cell. For that reason, the identification of this correlation has been carried out by combining of the CC and the pouch cell experimental results. To get that, OCP curves measured with the reference electrode for the NMC 622 and the graphite on the pouch cell are superposed with the ones obtained with the CC design (Figure II-8.a). As the masses of the AM employed in the CC and the pouch cell designs are different, therefore, to perform this comparison, the capacities of NMC and graphite measured per masse of active material in the CC design, are multiplied by the masses of active material used in the pouch format. Finally, the “computed CC OCP” are then shifted to be superposed with the pouch cell results. A very good superposition is obtained. These operations allow having a first overview of the stoichiometry ranges used for the two electrodes in the pouch cell design. We can notice that with the present one, only 56% of the negative electrode capacity is used. Indeed, as shown in Figure II-8.a, the two upper plateaus of the graphite are fully used and a small portion of the lower one with the pouch format.

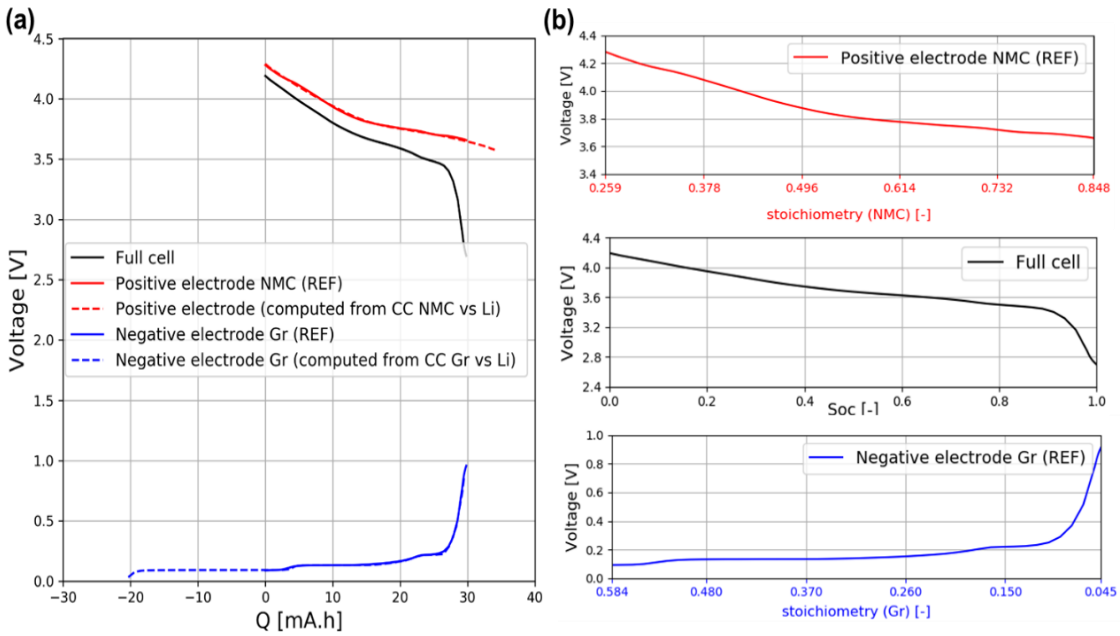

Figure II-8 : *(a) Pouch cell OCP curves as function of the cell capacity with the positive and the negative electrodes potentials measured with the reference electrode (labeled REF) compared to the positive and negative electrodes potentials computed from the coin cells (CC) measurements, (b) OCP curves of the full cell and positive and negative electrodes as function of the cell SOC and active materials stoichiometry.*

For *the positive electrode*, the maximum stoichiometry in the pouch design is calculated considering the theoretical capacity and the irreversible capacity of the pouch formation as:

$$y_{max}^{Pouch,NMC} = \frac{Q_{th}^{NMC} - Q_{irrev}^{pouchNMC}}{Q_{th}^{NMC}} \quad \text{(II. 8)}$$

Since, the irreversible capacity $Q_{irrev}^{pouch,NMC}$ expressed as function of positive active material is higher in the pouch cell format due to SEI formation on the negative electrode, $Q_{irrev}^{pouch,NMC} = 42$ mAh/g, it leads to a maximum stoichiometry of 0.848, which is lower than in the coin cell format. The minimum stoichiometry $y_{min}^{Pouch,NMC}$ is determined considering the first delithiation step leading to a minimum stoichiometry of 0.259 equals to the value obtain in the coin cell format.

For *the negative electrode*, the amount of used capacity in the pouch format is only 29.8mAh, much lower than the 53 mAh available capacity. It corresponds to a reversible capacity $Q_{rev}^{Pouch,Gr}$ equals to 205 mAh/g. Assuming that the minimum stoichiometry for graphite in the

pouch cell format is the same than in the coin cell format ($y_{min}^{Pouch,Gr} = 0.045$), the value of the full lithiation in the case of pouch system is expressed as:

$$y_{max}^{Pouch,Gr} = y_{min}^{Pouch,Gr} + \frac{Q_{rev}^{Pouch,Gr}}{Q_{th}^{Gr}} \quad \text{(II. 9)}$$

It leads to a value of 0.598, lower than the one in CC format.

Finally, the stoichiometry of the active material in each electrode can be related to every SOC of the cell (*Figure II-8*b) using the following relations:

$$y_{NMC} = -\left(y_{max}^{Pouch,NMC} - y_{min}^{Pouch,NMC}\right) SOC + y_{max}^{Pouch,NMC} \quad \text{(II. 10)}$$

$$y_{Gr} = \left(y_{max}^{Pouch,Gr} - y_{min}^{Pouch,Gr}\right) SOC + y_{min}^{Pouch,Gr} \quad \text{(II. 11)}$$

II.3.2.3 **Solid diffusion coefficient**

The chemical diffusion coefficient is determined from the transient voltage responses during the pulses at constant current of the GITT experiment in coin cell design. To that end Eq. ((II. 12)), developed in [53], [50], [8] from the analytical solution of diffusion processes in a planar geometry, is used. For this geometry, the solution of the diffusion problem can be expressed as an infinite series of error functions. For the spherical geometry, the analytical solution is developed in the literature only in Fourier series [55], which do not converge rapidly for short time. Nevertheless, Smith *et* al. [56] have shown, by using an empirical development of the Fourier series at short time, that the development proposed to estimate the diffusion coefficient for the planar geometry, is also valid for the spherical one.

$$D_s = \frac{4}{\pi}\left(\frac{V_M I_0}{S_{AM} F z_i}\right)^2 \left[\frac{dE_q}{dy} \Big/ \frac{dE}{d\sqrt{t}}\right]^2 \qquad t \ll {r_s}^2 \Big/ D_s \quad \text{(II. 12)}$$

Where I_0 is the applied constant current during the pulse, V_M the active material molar volume, z_i the number of electron exchanged during the (de)-insertion reaction, and equals to 1, F the Faraday constant and S_{AM} the exchange area in CC design between the electrolyte and the active material particles. $\frac{dE_q}{dy}$ is the slope of the equilibrium potential vs. the stoichiometry y. Equation

12 assumes a diffusion Fick's law, a small diffusion length compared to the dimension of the particle as well as a negligible volume changes.

Note that $\frac{dE}{d\sqrt{t}}$ can be obtained from the plot of the transient voltage versus the square root of time during the constant current pulse. To choose the right time domain, the linearity of the transient voltage versus the square root of time has been checked for each pulse. For the positive electrode, Figure II-9.a shows the typical transient voltage response obtained during one of the pulse at C/10 as function of time for the first 250s of the pulse. At beginning of the pulse, the voltage varies linearly with the square root of time, as illustrated Figure II-9.b. A similar behavior is obtained for the negative electrode in the single-phase regions, as illustrated Figure II-10. This confirms that the diffusion coefficient values obtained by GITT for these stoichiometries are accurate and that the slope from the fitted curve can be used in Eq. (II. 12) [57] [58] [53]. The physical parameters used in the data treatment are summarized (Table II-1). The values obtained for the diffusion coefficients for both active materials are displayed Figure II-11 as function of the stoichiometry of each electrode.

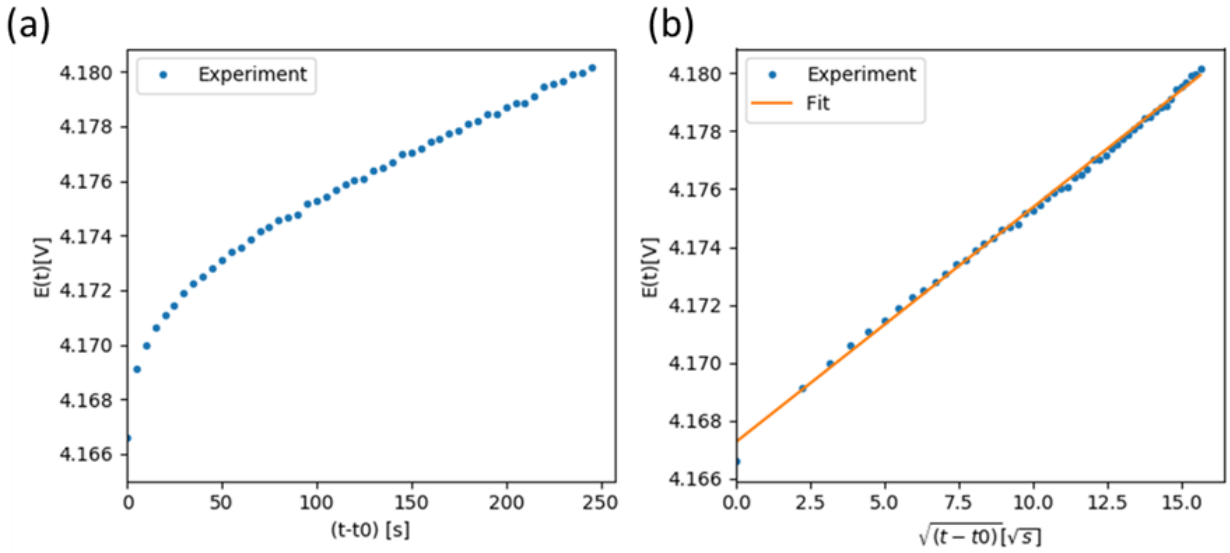

Figure II-9 : *$LiNi_{0.6}Mn_{0.2}Co_{0.2}O_2$ vs. Li GITT experiment (a) Cell voltage as a function of time during a charging current pulse (b) Cell voltage vs square root time for the same charging current pulse with the corresponding linear fit.*

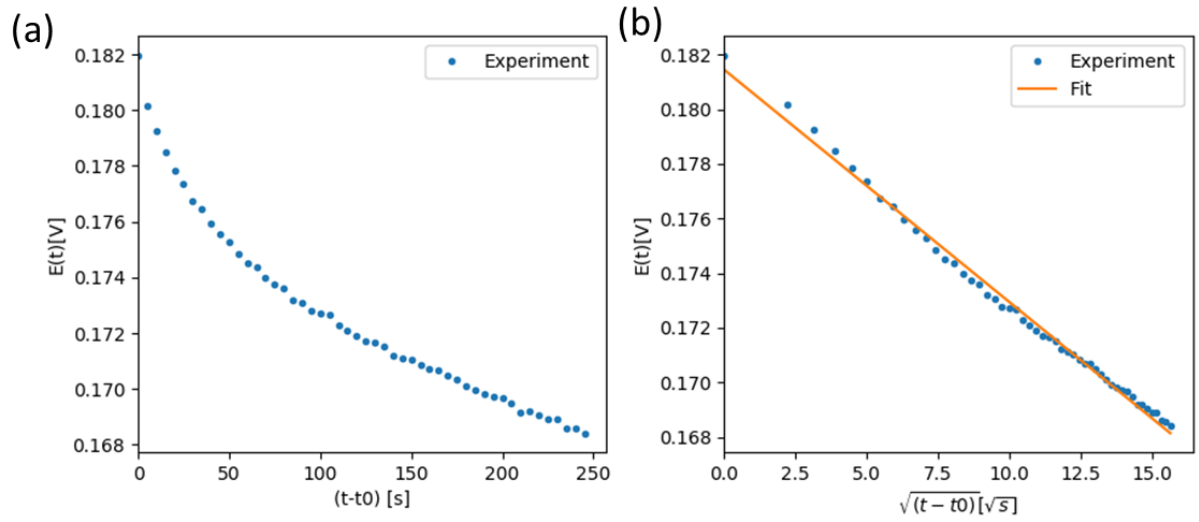

Figure II-10*: Graphite vs. Li GITT experiment (a) Cell voltage as a function of time during a discharging current pulse (b) Cell voltage vs square root time for the same discharging current pulse with the corresponding linear fit.*

Table II-1: Parameters used to extract the graphite and $LiNi_{0.6}Mn_{0.2}Co_{0.2}O_2$ diffusion coefficients (CC design) and exchange current densities (Pouch design)

Parameter	**Value**			
	Graphite	$LiNi_{0.6}Mn_{0.2}Co_{0.2}O_2$	Source	Error
$\boldsymbol{I_0(A)}$ **during pulse**	5.50E-04	4.60E-04	calculated	-
$\boldsymbol{V_M(m^3.mol^{-1})}$	5.31E-04	12.35E-04	calculated	-
$\boldsymbol{r_{50}(m)}$	7.88E-06	6.60E-06	Measured	± 1.8µm
$\boldsymbol{L\ (m)}$	72.00E-06	60.00E-06	Measured	± 1µm
$\boldsymbol{S_g(m^2)}$ **in CC design**	1.54E-04	1.54E-04	calculated	-
$\boldsymbol{S_{AM}(m^2)}$ **in CC design**	2.68E-04	3.31E-04	calculated	-
$\boldsymbol{S_g(m^2)}$ **in pouch design**	12.25E-04	10.24E-04	calculated	-
$\boldsymbol{S_{AM}(m^2)}$ **in pouch design**	22.28E-04	22.03E-04	calculated	-

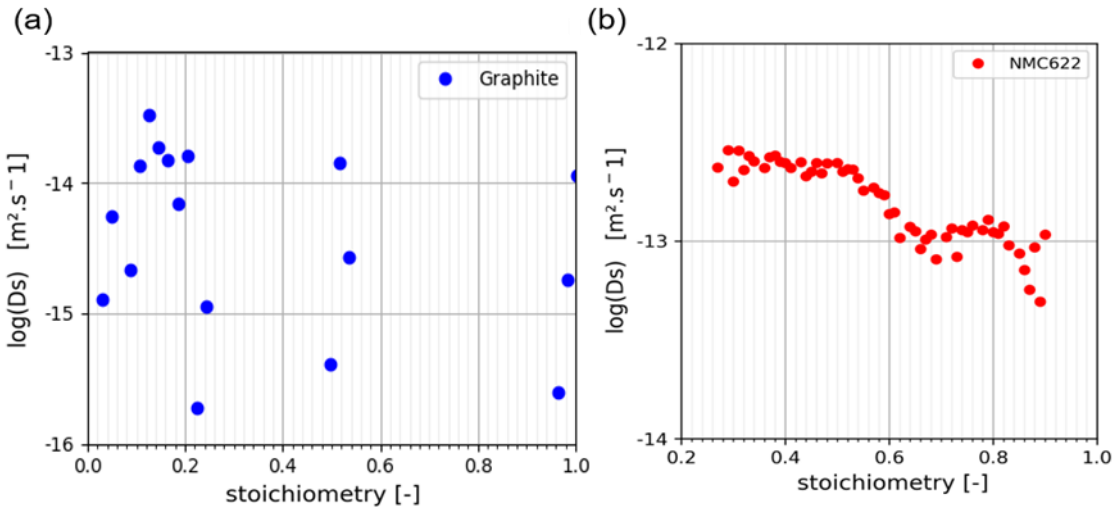

Figure II-11*: Base 10 logarithm of the diffusion coefficient vs stoichiometry: (a) graphite, (b) $LiNi_{0.6}Mn_{0.2}Co_{0.2}O_2$.*

The diffusion coefficient measured with this technique is a function of the derivative of the potential with respect to the stoichiometry, $\frac{dE_q}{dy}$. The interpretation of the measurement relies on Fick's law, which accounts for diffusion in one phase. For the graphite electrode, two phases can co-exist, which leads to a plateau in the equilibrium potential of graphite (See *Figure II-7*.a) where $\frac{dE_q}{dy}$ is almost zero. As the present technique is not adequate to extract diffusion coefficients in these two-phase regions, we choose to not display the points obtained on the plateaus on Figure II-11.a, but only those corresponding to the transition regions. For the three regions (stoichiometries below 0.25, stoichiometries around 0.5 and stoichiometries above 0.95), the values are between 1E-15 and 1E-14 $m^2.s^{-1}$ without a clear tendency regarding the dependence on the stoichiometry. The order of magnitude and the overall tendencies are nevertheless coherent with results reported in the literature for graphite, whose values are in the range [1.00E-15 – 1.00E-13] $m^2 . s^{-1}$ in [59], or [3.00E-15 and 1.00E-12] in [60].

For $LiNi_{0.6}Mn_{0.2}Co_{0.2}O_2$, a regular monotone decrease of the diffusion coefficient can be observed in Figure II-11.b. D_s values are varying between 1E-13 and 5E-13$m^2.s^{-1}$ over the entire stoichiometry compared to the values proposed in the literature [1E-16 – 1E-11] $m^2 . s^{-1}$ [61]. An almost constant value around 5E-13$m^2 . s^{-1}$ is obtained for stoichiometry below 0.49, while a slight decrease is observed until stoichiometry of 0.64, with a subsequent stabilization at a value around 1E-13 $m^2 . s^{-1}$ for the highest stoichiometry values. These three domains might be related to the structure changes of the $LiNi_{0.6}Mn_{0.2}Co_{0.2}O_2$ active material [62] [63]. This material undergoes phase transition from pristine hexagonal H1 phase to subsequent

hexagonal H2 and H3 phases. Although *ex-situ* and operando XRD measurements have been reported recently [63], the cognition of the structural difference between these phases and their precise stoichiometry range remains not fully understood. In our measurements, the domain of stoichiometry above 0.64 could related to the region where H1 and H2 structures coexist and the second domain [0.49 – 0.64] to a region where only the H2 structure is existing, while the last domain [0.26 – 0.49] to a region where a transition between H2 and H3 structures manifests.

II.3.2.4 **Electrochemical impedance spectra**

Electrochemical impedance spectra have been measured to characterize the cell at beginning of life with the protocol described above (section II.3.1.2) using the 4-electrodes design pouch cell.

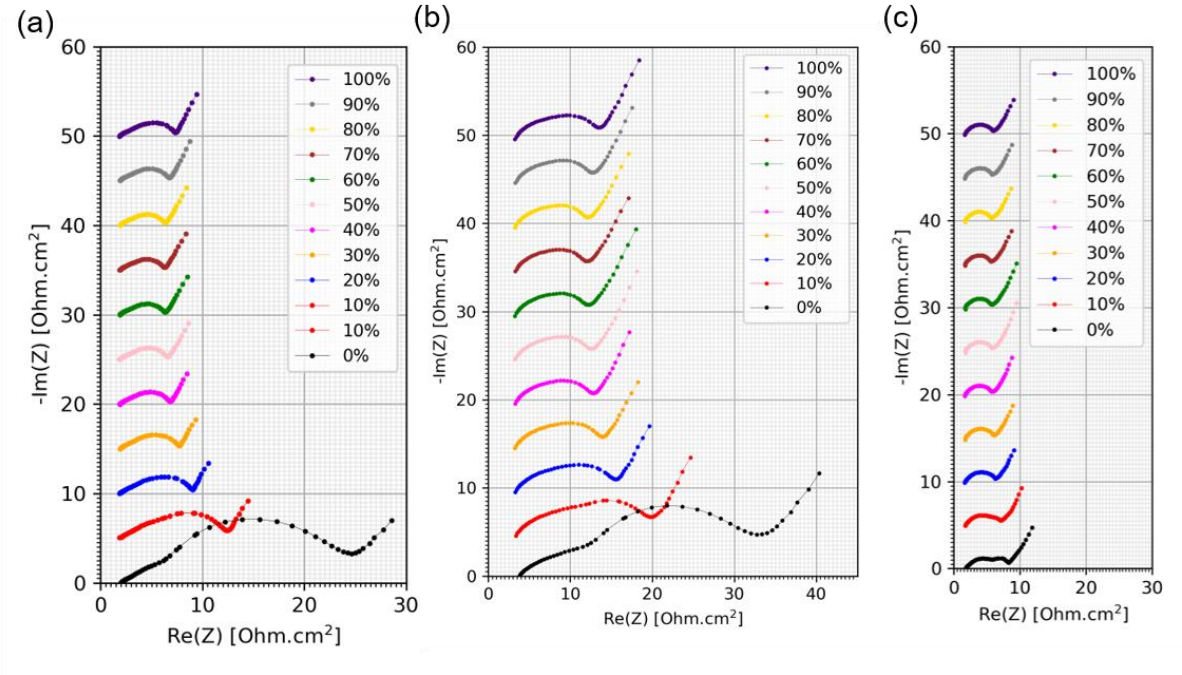

Figure II-12 *EIS spectra of the 4-electrode pouch cell in Nyquist plot at different SOC with an appropriate shift to have a clear presentation: (a) negative electrode (graphite), (b) full cell and (c) positive electrode (NMC 622).*

Figure II-12 displays the Nyquist plots of the EIS obtained for the negative electrode (a), full cell (b) and positive electrode (c) at the different states of charge of the cell. Whatever the system, the Nyquist plots consist of an out-of-shaped semicircle alike in appearance of a half ellipse in high and intermediate frequency ranges and a straight line inclined at a constant angle to the real axis in the lower frequency range. The first capacitive arc is related for a part to the charge transfer phenomenon from where the i_0 values for the two electrodes can be fitted. The

flattened shape can be observed in the case of porous electrodes with limited electronic or ionic conductivities [27]. The straight-line in the low frequency limit is due to diffusion phenomena that can be described with a Warburg contribution. For a better identification of the different physical domain in the spectra, a representation of the imaginary part of the impedance vs. frequency is shown in Figure II-13 for the two electrodes. This figure allows to determine the characteristic frequency of the charge transfer (f_{max}), which corresponds to the highest point of the semi-circle in the Nyquist plots. The second identified characteristic frequency is the one corresponding to the minimum value of the imaginary part of the impedance while going to low frequency ($f_{\min}$). This frequency represents the limit between the interfacial phenomena (charge transfer resistance) and the bulk phenomena (lithium transports in particles and electrolyte).

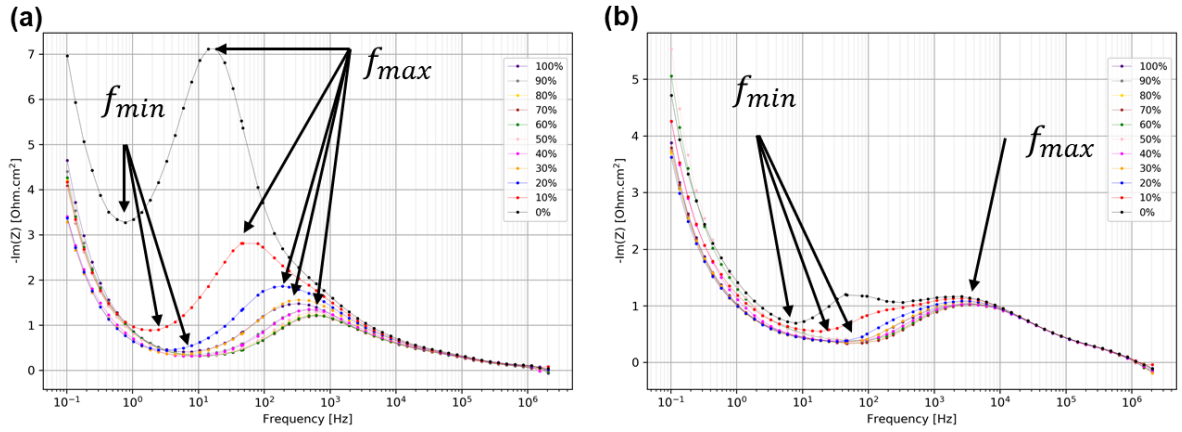

Figure II-13 *: EIS spectra of the 4-electrode pouch cell at different SOC represented with -Im(Z) vs frequency: (a) negative electrode (graphite), (b) positive electrode (NMC622).*

For the graphite, the physical phenomenon representing the AM/electrolyte interface in the EIS diagrams is in the intermediate to high frequency domain. As shown in *Figure II-12*a, the magnitude of the flattened semi-circle corresponding to the charge transfer resistance decreases when the SOC of the cell increases. For a SOC higher than 20%, f_{max} and $f_{\min}$ are rather constant as can be seen *Figure II-13*a, which reflects a stable interface electrochemistry. However, for a SOC between 20% and 0%, $f_{\min}$ decreases a lot, going from values around 260 Hz for SOC of 100% to values around 19 Hz at 0% SOC (*Figure II-13*a) suggesting a slower charge transfer for a lower SOC [37].

For NMC 622 (Figure II-12c), EIS spectra are quite similar to the negative ones, but with an overall lower magnitude. For a SOC higher than 30%, all the diagrams have the same flattened semicircles shape with a constant width. Conversely, two flat semicircles shape can be distinguished with a width increase when the SOC decreases from 20% to 0%. As presented in

Figure II-13b, f_{max} and $f_{\min}$ are the same over a large SOC range of [30%- 100%]. However, they increase from 20% to 0%. The same behavior, for a SOC below 30%, was reported for other materials similar to NMC 622, like $LiMn_2O_4$ [23] and $LiNi_{0.8}Co_{0.15}Al_{0.005}O_2$ [41]. In these works, the high frequency arc was associated to the Li^+ migration through the oxide layer film and the second one between the higher and middle frequency to the charge transfer resistance.

II.3.2.5 **Exchange current density**

In the literature, many approaches have been adopted to extract the exchange current density of the active materials. One of them is to exploit the impedance spectra at different state of charge of the cell. To reach this goal, the capacitive arc of the different spectra should be analyzed quantitatively by using EEC model. In general, a simple R-C element model is implemented to extract i_0 from an impedance spectrum [49]. However, this model assumes a semi-circle shape for the charge transfer resistance in the impedance spectra, which is not observed in the present case (see *Figure II-12*). In fact, porous electrodes have a potential gradient along the electrode thickness .Thus, Transmission Line Model (TLM) [64], [24] is more appropriate to take into account the non-semicircle shape of the impedance spectra in the middle to high frequency range that porous electrode may cause. TLM considers the electronic and ionic paths through the solid phase and the electrolyte in the pores respectively [23], [24]. For porous LIB electrodes, the electronic conductivity is much higher than the ionic one. Therefore, electronic resistance can be neglected, and the TLM [65] impedance is reduced to:

$$Z_{TLM} = \lambda\chi \coth\left(\frac{L}{\lambda}\right) \quad \text{(II. 13)}$$

The resistance per unit length χ related to the ionic path is defined as:

$$\chi = \frac{1}{\sigma_e} \quad \text{(II. 14)}$$

The ionic conductivity σ_e is equal to 1 mS/cm at 25°C for the studied electrolyte. This model takes into account the charge transfer at the interface between active materials and the electrolyte, via the introduction of λ, the characteristic alternating current penetration depth in the electrode defined by:

$$\lambda = \sqrt{\frac{Z_{int}\, L}{\chi}} \tag{II. 15}$$

The values of the electrode thickness L are provided in table 1 for the positive and negative electrodes respectively. The area-specific impedance Z_{int} of the electrochemical reaction taking place at the interface is modeled as a simple parallel combination between the charge transfer R_{ct} and a constant phase element (CPE) [64]:

$$Z_{int} = \frac{R_{ct}}{1 + (i\omega R_{ct} C)^n} \tag{II. 16}$$

where the charge transfer resistance is given:

$$R_{ct} = \frac{RTS_g}{Fi_0 S_{AM}} \tag{II. 17}$$

Where S_g is the geometric area in the pouch design, S_{AM} the AM exchange area in the pouch design (see *Table II-5*), *R* gas constant, *T* the temperature, *F* the Faraday's constant and i_0 the exchange current density. A procedure was adopted to fit, with this TLM model, the capacitive arc of the experimental EIS spectra (*Figure II-12*a/c) corresponding to the charge transfer phenomenon for each value of the SOC in the frequency range between f_{min} and 200kHz. The used parameters are presented in Table 1. This method allows us to extract the values of i_0 for each stoichiometry value for both PE and NE, *via* Eq. (II. 6).

The obtained results are presented Figure II-14.a. as function of the active material stoichiometries. For the graphite, the experimental curve of exchange current density is asymmetric, with values ranging between 0.8 and 8.4 A/m², which is consistent with the values reported in the literature [66], [67] that show large variation: between 0.5 and 35 A/m². For the NMC622, the experimental curve has a more symmetric shape compared to the graphite. The exchange current densities obtained as function of the stoichiometry are in the range of 2.3-4.8 A/m², in agreement with the values proposed in the literature that are in the range [0.1-6] A/m² [59], [68]. In earlier studies on lithium iron phosphate (LFP) [69], [70], it has been reported that the variation of the exchange current density with the stoichiometry is different from the Butler-Volmer approach classically used in porous electrode theory [71]. This discrepancy is also observed in the present study for the positive and the negative electrodes as shown in Figure II-14.b, where the dimensionless measured exchange current densities are compared to the Butler-Volmer results using $\alpha = 0.5$. This can be related to the non-ideal behavior of the active materials due to the molecular interaction (repulsive or attractive) inside.

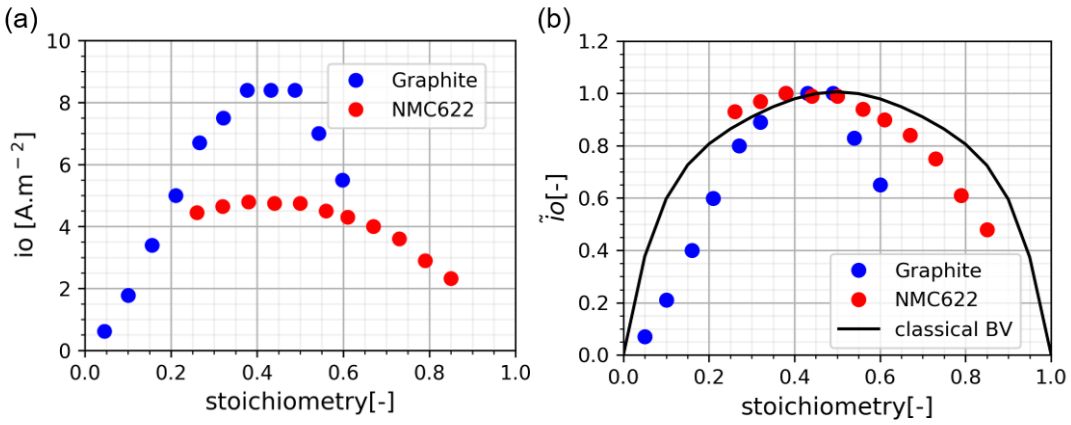

Figure II-14: *Exchange current density vs. Stoichiometry: (a) for NMC and graphite, (b) dimensionless version for comparison with the Butler-Volmer relation using* $\alpha = 0.5$ *(classical BV)* [72].

II.4 Aging experiments

In this section, the results of the experimental campaigns during aging and postmortem analysis are discussed. These results are used to develop, supply with the physical parameters and validate the aging models presented in chapter 4. In the scoop of this thesis, a cycling aging protocol is presented with the different check-up protocols during which, the effective capacity of the electrodes is measured. Moreover, from the impedance check-up, the degradation mechanisms evolution during the lifetime of the cell is deduced.

The *post mortem* analysis in the end of this section is implemented to deeper insight and a coherent interpretation of the obtained results.

II.4.1Experimental protocols

The aging test plan has been conducted on the pouch cell design. To check the reproducibility, three cells have been aged for each operating condition, two without references electrodes and one with the 4-electrode design. This strategy was adopted to ensure that the reference electrode does not affect the measurements. Besides, aging cycling tests are time consuming that can last four to five months. Therefore, to avoid redoing the same measure, especially in the middle of the cycling, because of any accident that can damage the cell, two

pouch cells without reference electrode were also elaborated. In the following *Table* , the cells aged by cycling at different temperatures are summarized.

Table II-2 : *Overview of cells and aging conditions*

Cell type	**Aging cycling temperature: 25°C**	**Aging cycling temperature: 45°C**
2-electrode design cell (i.e. without reference electrode)	2	2
4-electrode design cell (i.e. with reference electrode)	1	1

II.4.1.1 **Formation protocol**

After assembly, pouch cells are put in a mechanical homemade design, where a homogeneous force of roughly 100N is applied, which corresponds to a pressure of 1bar on the 10 cm² surface. A formation protocol is performed, similar to the one applied for the characterization at beginning of life for pouch cell designs (see section II.3.1.1).

II.4.1.2 **Aging operating conditions**

As we have mentioned in *Table* , two temperatures have been selected for aging operating: T=25°C and T=45°C. However, the regular check-up protocols have been performed at room temperatures to be able to compare them.

As presented in *Table II-3*, for the tests carried out under a temperature of 25°C, a check-up protocol was applied to the three cells every 50 cycles. For the cell with a reference electrode, an EIS measurement was performed at the beginning of life and after 200 and 600 cycles (*Table II-4*). During EIS measurements, the 2-electrode design cells (i.e. without reference electrode) are in standby. For the tests carried out under temperature of 45°C, the check-up protocol under temperature of 25°C was applied every a higher number of cycles as detailed in *Table II-3*. In fact, this was adopted to facilitate the test procedure at this temperature of 45°C considering the fact of the cells have to be taken out the cells from the oven 4h before each check-up. Similar to the test carried out at 25°C, an EIS measurement was done for the cell with reference electrode at the beginning of life and after 250 and 600 cycles, (*Table II-4*) while the other cells are in standby at a temperature of 25°C.

Table II-3 *:* An overview of the different number of cycles and electrochemical check-up moments for two aging cycling temperature

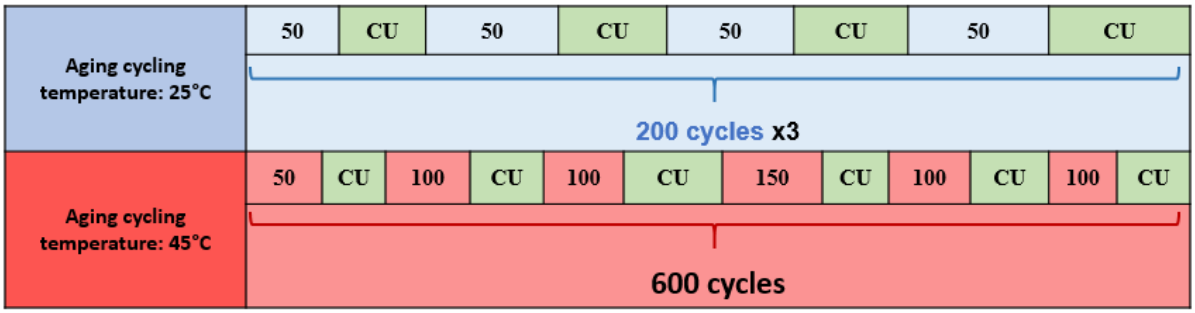

Table II-4 *:* An overview of the different number of cycles and EIS check-up moments for two aging cycling temperature

Aging cycling temperature: 25°C	**0**	**EIS**	**200**	**EIS**	**600**	**EIS**
Aging cycling temperature: 45°C	**0**	**EIS**	**250**	**EIS**	**600**	**EIS**

II.4.1.3 **Cycle aging protocol**

As we have specified in the previous paragraph two experimental series have been launched: the first one at 25°C and the second one with a temperature of 45°C. The cycling aging tests were conducted for 600 cycles.

The cells have been cycled according to the following protocol. Cells are firstly charged at a C/2 rate, up to 4.2 V. Then, a floating step is carried out by keeping the potential at 4.2 V until the current drops below C/50. Then, after a 15-minutes breakoff rest, cells are discharged at a 1C rate, up to 2.5 V. A 15 minutes rest is repeated before a new cycle begins. This cycle operation is performed as many times as possible depending on the temperature operating condition.

II.4.1.4 **Check-up protocol**

The check-up consists on a cycle at low C-rate followed by a cycle including pulses. The first check-up cycle corresponds to a full charge at C/10 up to 4.2V, 15-minutes of rest. The cell potential is kept at 4.2V until the current drops below C/50, which is referred as the floating step in the following. Then after a 15-minutes of rest, C/10 discharge up to 2.5V and another 15-minute of rest. For the check-up cycle including pulses, a full charge at C/5 up to 4.2V

flowed by a floating step by keeping the potential at 4.2 V until the current drops below C/50 is performed to estimate the capacity of the cell Qn. Then, after 15-minutes of rest, the pulse check-up starts. It is a discharge pulse sequence composed of 10s current pulses at 1D rate, followed by a discharge of 10% of the measured cell capacity Qn at C/5 followed by a 30-minute break before the next pulse. This procedure allows to measure a direct current resistance every 10% of the cell SOC.

II.4.1.5 **Electrochemical Impedance Spectroscopy (EIS) protocol**

As mentioned before, EIS measurement during aging was performed to follow the cell performance evolution and the losses during the aging of the cell. In order to understand and have an access to aging mechanisms of each electrode, pouch cell with 4-electrode design was used to perform the EIS measurement. The EIS protocol applied for the characterizations during the aging tests is similar to the one presented in the section II.3.1.2. In particular, the protocol is applied after a CCCV discharge at C/10 until 2.5V. The measurements are obtained by discharging the cell at a constant current. A rest period of 1h is applied to reach equilibrium before the PEIS measurement. This protocol is repeated until to attend a potential of 2.5 V to complete discharge of the cell.

II.4.2 Experimental result

In this section, we present the results of capacity fade and EIS measurements after applying the previous experimental aging protocols. For the cells cycling at 25°C, one cell with 2-electrodes design after 100 cycles was lost. Therefore, in this part, the results for one cell with 4-electrodes design and one cell with 2-electrodes design are presented. For the cells cycling at 45°C, all the cells completed the aging protocols. Thus, we will discuss the results obtained with three cells: one with 4-electrodes design and two with 2-electrodes design.

II.4.2.1 **Check-up capacity for cycle aging**

Aging at 25°C

The discharge capacity at 1D together with discharge check-up capacity at D/10 is displayed as function of the cycle number in Figure II-15 for the cells cyclied at a temperature of 25°C. The discharge capacities measured during the CU can be distinguished from the discharge capacities at 1D, as they are higher, leading to a peak in the figure. The capacity evolution is very similar

for the two cells (4-electrodes design cell and two electrodes design one) with closed capacities values. The dip and fluctuation seen in the discharge capacities of the 2 electrodes design cell between 100 and 200 cycles havs been caused by an electrical contact problem in the dispositive test. During the first 400 cycles, an important and regular drop in the discharge capacities can be observed . This corresponds to a capacity fade of roughly 65% compared to the capacity of 35 mAh measured during the first check-up. Up to the 600 cycles, the discharge and the check-up capacities are similar and around an average value of 10 mA.h.

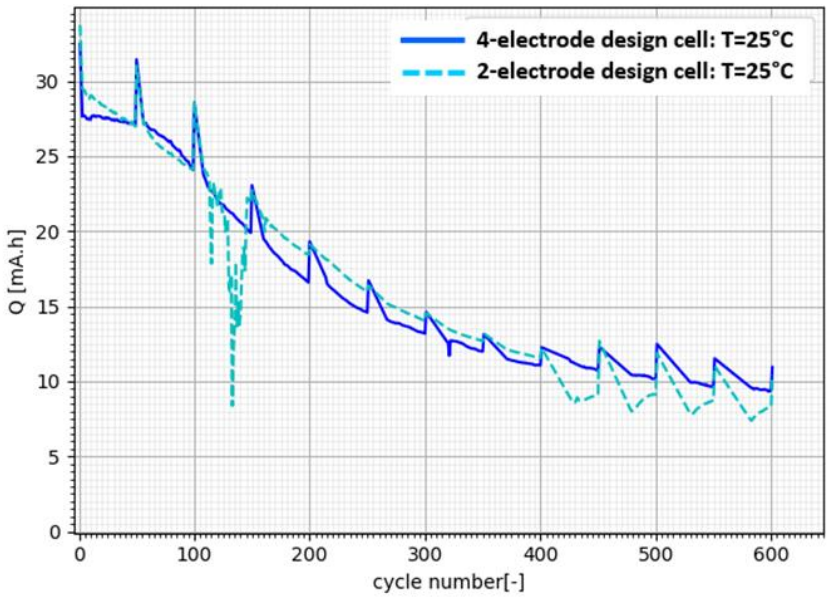

Figure II-15*: Discharge capacity of pouch cells during C/2 – 1D cycling at 25°C [2.5-4.2V]*

Aging at 45°C

Figure II-16 displays the corresponding results obtained for the cells cycled at a temperature of 45°C. As mentioned in the previous paragraph, the discharge capacities measured at D/10 during the check-up can be distinguished from the discharge capacities during cycling with the presence of peaks of higher capacities. The amplitude of the peak is much higher than for the cells aged at 25°C.

For the tests performed at 45°C, three cells were elaborated and aged. Two cells are with the 2-electrode design and one cell with the four-electrode design. From a global visual inspection, the profiles of the three cells have a similar shape with an important capacity fade during the first 300 cycles, which then seems to stabilize. However, one of the 2-electrodes design cell (2-electrode design cell n°1: T=45°C) has an irregular behaviour between 300 cyles and 400 cycles. Furthermore, its capacity has been slightly increased after a standby of twenty days at

25°C before the 400 cycles check-up measurment. The other cells have not been affected by this rest time.

Similar to the cycling at 25°C, during the first 200 cycles, an important and regular drop in the discharge capacities can be observed for the two designs. This leads to a capacity fade of 62% from the fresh one measured at 33 mAh during the first check-up. Up to the 600 cycles, three cells degradation is similar and around an average value of 10 mA.h.

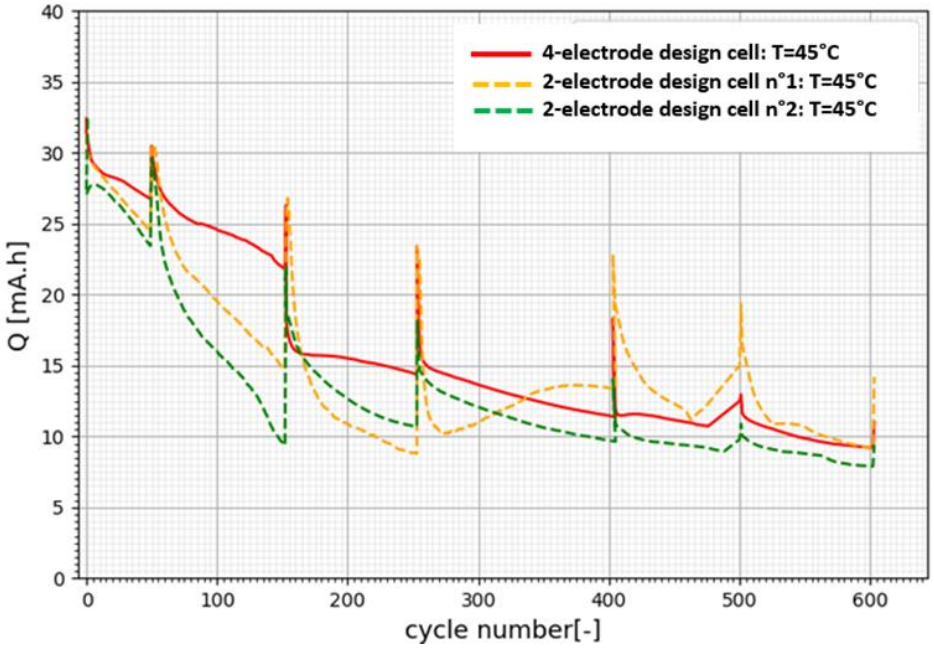

Figure II-16*: Discharge capacity of pouch cells during C/2 – 1D cycling at 45°C [2.5 – 4.2V]*

Comparison between test at 25°C and 45°C

Figure II-17 presents a comparison of the discharge capacities measured for the cells cycled at the two temperatures (25°C and 45°C). This figure shows a similar global behavior for all the cells with a capacity fade around 70%. A closer look to the discharge capacities measured during the regular check-up and presented in Figure II-18 shows a slower capacity drop during the first 400 cycles for the 2 electrode designs cycled at 45°C compared to the other cells. In order to validate that, post mortem experiments were performed for the cell with 4-electrode design cycled at 25°C.

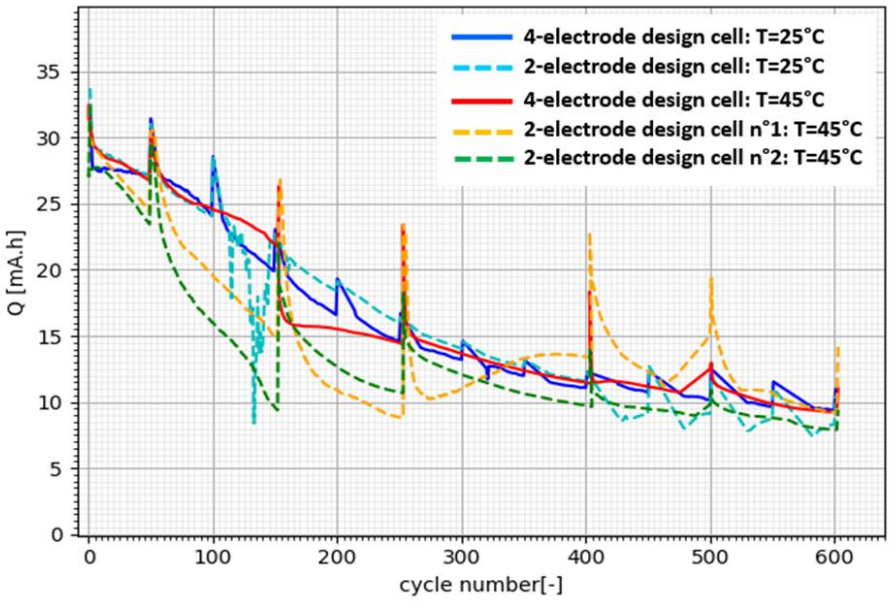

Figure II-17*: A comparison of discharge capacities fade through cycling between cells cycled at 45°C and 25°C.*

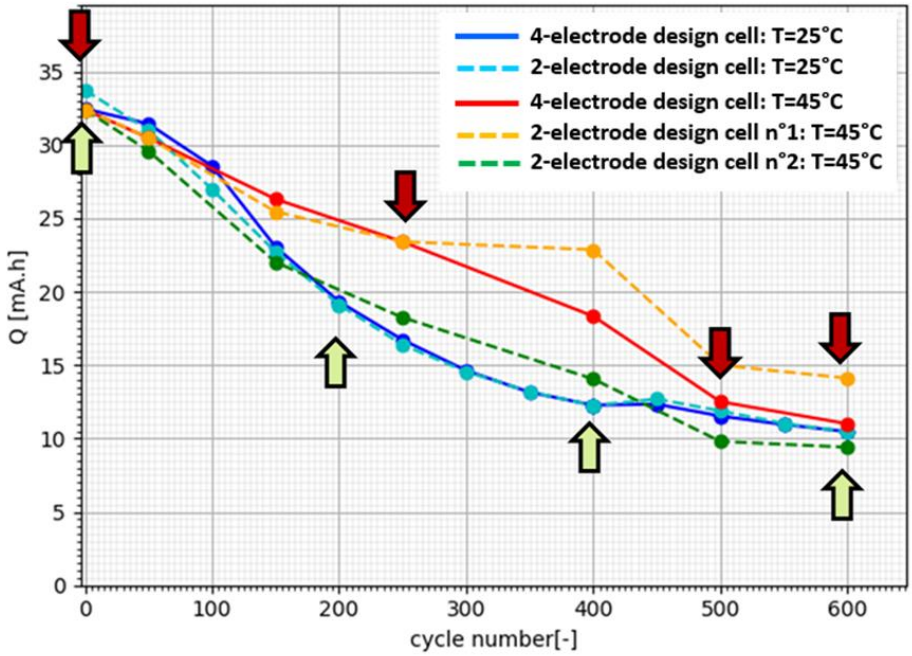

Figure II-18: *A comparison of check-up capacities between cells cycled at 45°C and 25°C*

II.4.2.2 **Impedance spectra after check-up**

EIS measurements were performed at different cycling time to have a better and clear idea about the cell evolution during the aging and to validate the analytic model developed in the scoop of this thesis. These measurements had been done for cells with 4-electrode design at 25°C and

45°C. In this paragraph, the different impedance spectra obtained for the full cell and each electrode are presenting at different cycling time during aging.

Full cell results

The different impedance spectra measured for the full cell cycled at 25°C and the other one cycled at 45°C are presented in Figure II-19 and Figure II-20 respectively. The obtained results with the 4-electrodes design cycled at 25°C, shows the presence of two apparent modifications in the impedance spectra with the aging of the cell. The first one is the appearance of a semi-circle at high frequencies, which is usually attributed to SEI growth at the surface of the graphite particles and which becomes significant after 600 cycles. The second modification observed is an increase the slope size at the high frequency domain which becomes increasingly visible with the cycling. For the results obtained with the 4 electrodes design cycling at 45°C, similar behaviors are observed. However, it seems that a bigger SEI semi-circle is observed. This result confirms the effect of temperature on the aging process. Higher temperature is known to favor the formation of SEI. This phenomenon has been studied and verified in the literature with Li-ion cells cycled at a temperature higher than 40°C [73]. To have a clear idea about the different aging mechanisms, which contributed, to the cell performance degradation, a diagnostic study of each electrode is recommended and presented in the next paragraph.

(a)

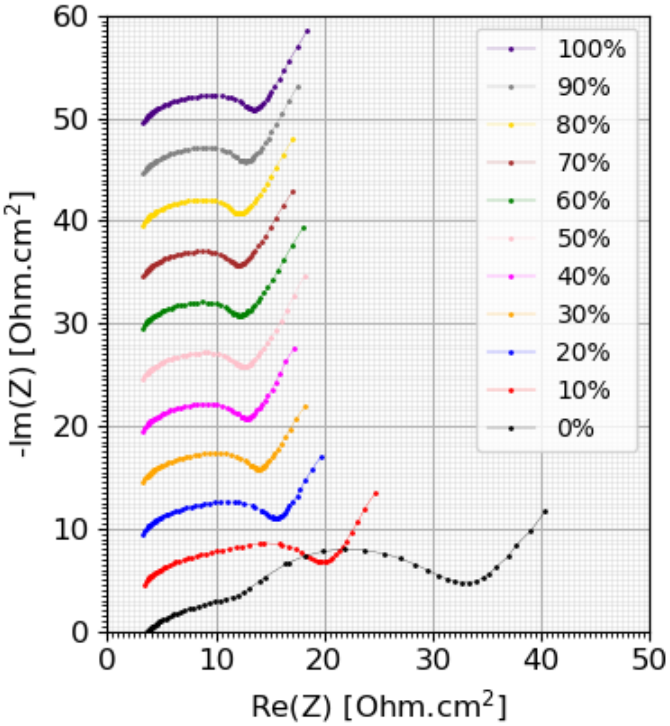

(b)

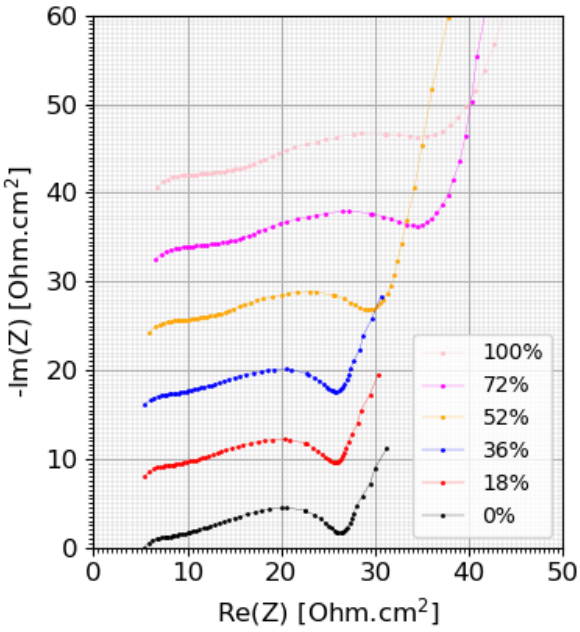

(c)

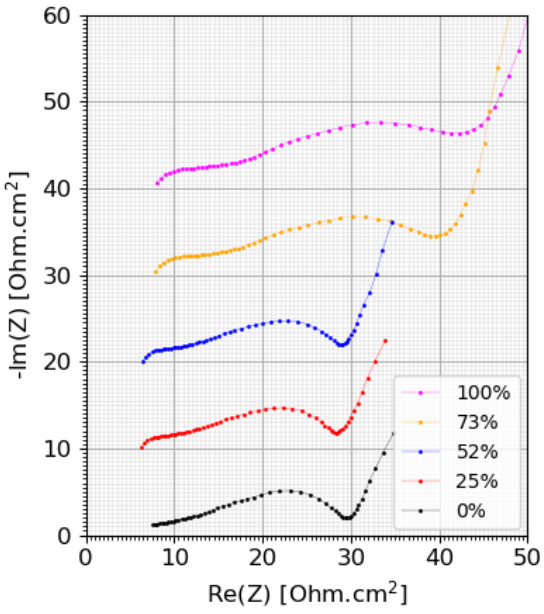

Figure II-19*: Full cell EIS spectra of the 4-electrode pouch cell in Nyquist plot at different SOC cycled at 25°C, shift between two successive SOC is adjusted with an appropriate to get a clear representation: (a) beginning of life , (b) after 200 cycles (c) after 600 cycles.*

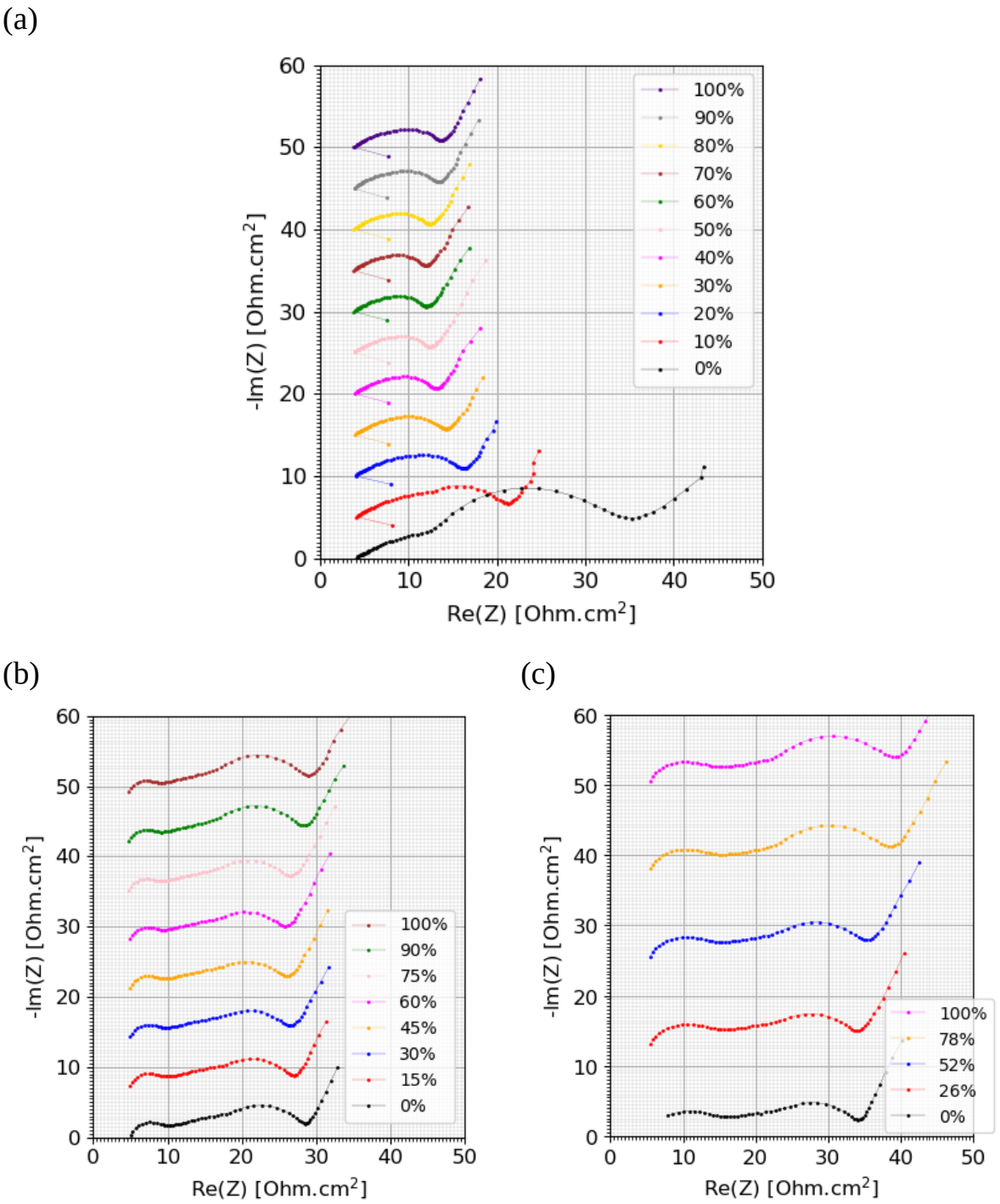

Figure II-20*: Full cell EIS spectra of the 4-electrode pouch cell in Nyquist plot at different SOC cycled at 45°C, shift between two successive SOC is adjusted with an appropriate to get a clear representation: (a) beginning of life, (b) after 250 cycles, (c) after 600 cycles.*

Positive electrode

EIS spectra of the positive electrode with the two cells cycled at 25°C and 45°C, are presented in *Figure II-21* and *Figure II-22* respectively. A visual deformation in the different impedance spectra within the aging is noticed. Indeed, the spectra became increasingly flattened with cycling. This behavior can be attributed in the literature to the oxide layer formed at the surface of the crystallographic structure [37] of the NMC from the beginning of life of the electrode. For NMC622 this layer is sometimes referenced as SRL [74] for Surface Restriction Layer. It is caused by a migration of the Ni^+ ions of the NMC structure to the lithium vacant sites leading to a modification of the crystallographic structure of the active materials at its surface. In this study, the presence of this film and the diffusion of the lithium atoms within will be considered to build the aging model.

(a)

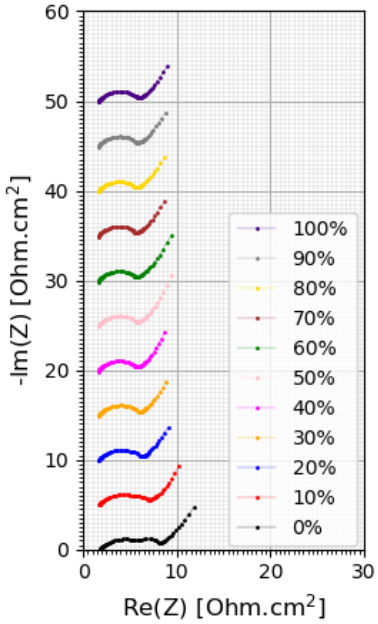

(b)

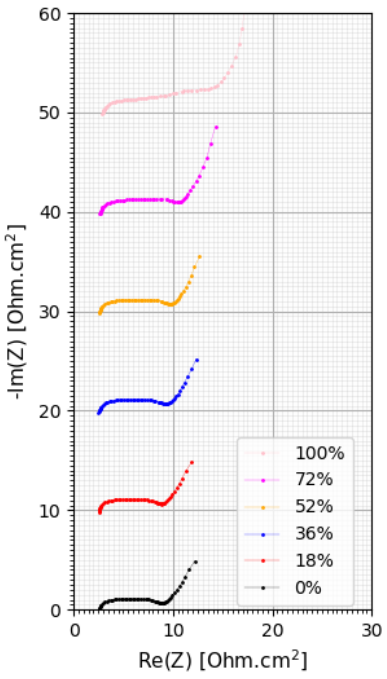

(c)

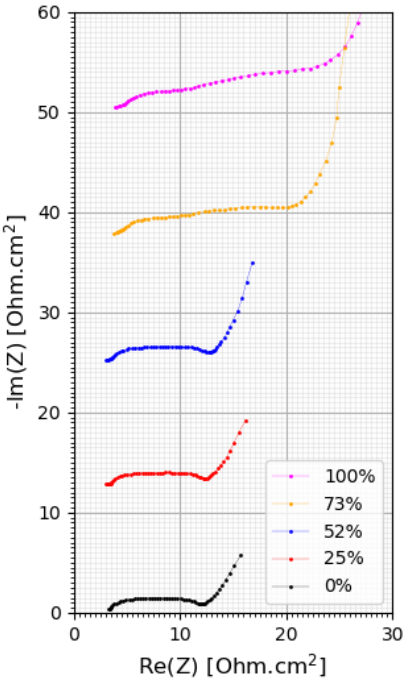

Figure II-21*: Positive electrode EIS spectra of the 4-electrode pouch cell in Nyquist plot at different SOC cycled at 25°C: shift between two successive SOC is adjusted with an appropriate to get a clear representation: (a) beginning of life, (b) after 200 cycles, (c) after 600 cycles.*

(a)

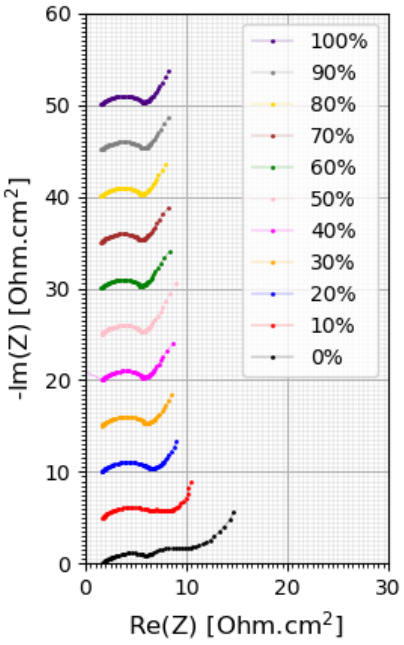

(b)

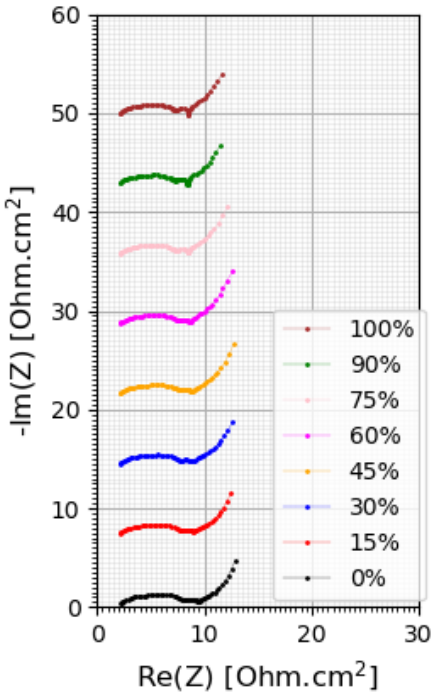

(c)

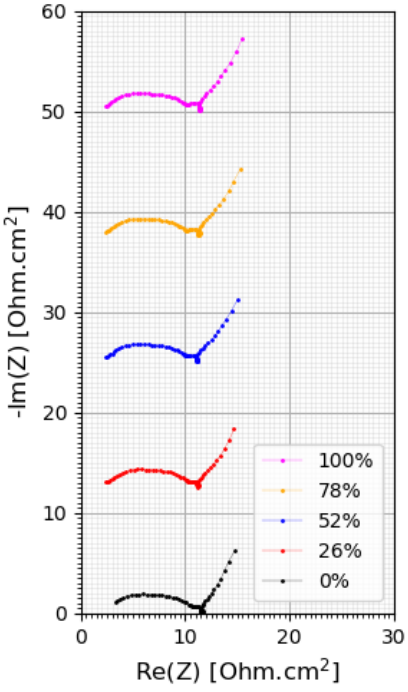

Figure II-22*: Positive electrode EIS spectra of the 4-electrode pouch cell in Nyquist plot at different SOC cycled at 45°C shift between two successive SOC is adjusted with an appropriate to get a clear representation: (a) beginning of life, (b) after 250 cycles, (c) after 600 cycles.*

Negative electrode

Figure II-23 and Figure II-24 represent the different impedance spectra for the two designs cycled at 25°C and 45°C respectively. In a general overview, the evolution of the first semi-circle with the slope, at high frequency domain is increasingly important within the cycling. In fact, the first semi-circle is due to the solid electrolyte interphase (SEI) film at surface of the graphite resulting from a reduction of the electrolyte at typical working potentials. Although this phenomena has been approved in the literature, and the origin of the slope of the high frequency domain is also discussed [75]. In this study, this slope is related to the diffusion of the lithium ion through this SEI. These two physics will be considered in the development of the aging model for the graphite.

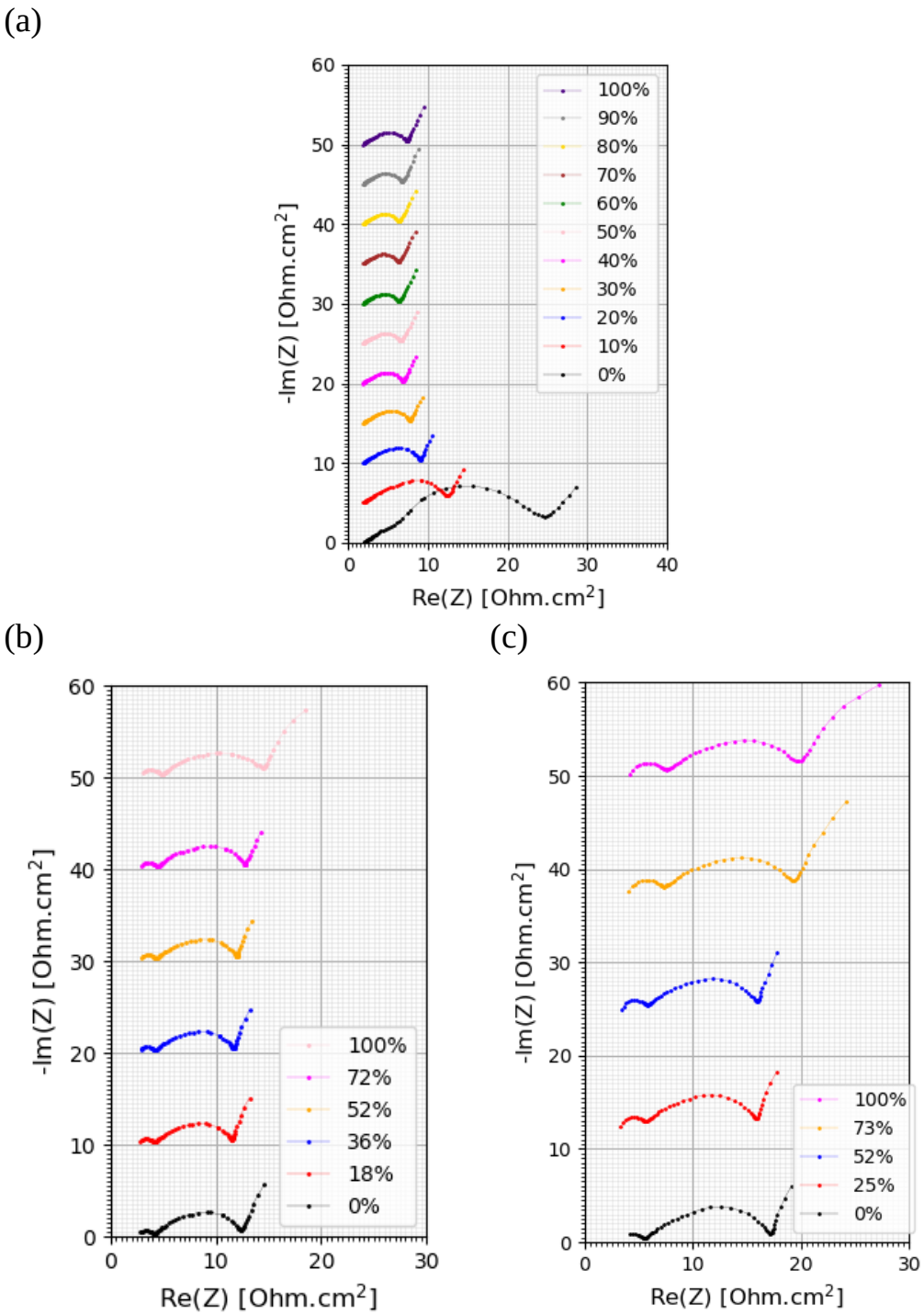

Figure II-23: *Negative electrode EIS spectra of the 4-electrode pouch cell in Nyquist plot at different SOC cycled at 25°C shift between two successive SOC is adjusted with an appropriate to get a clear representation: (a) beginning of life, (b) after 200 cycles ,(c) after 600 cycles.*

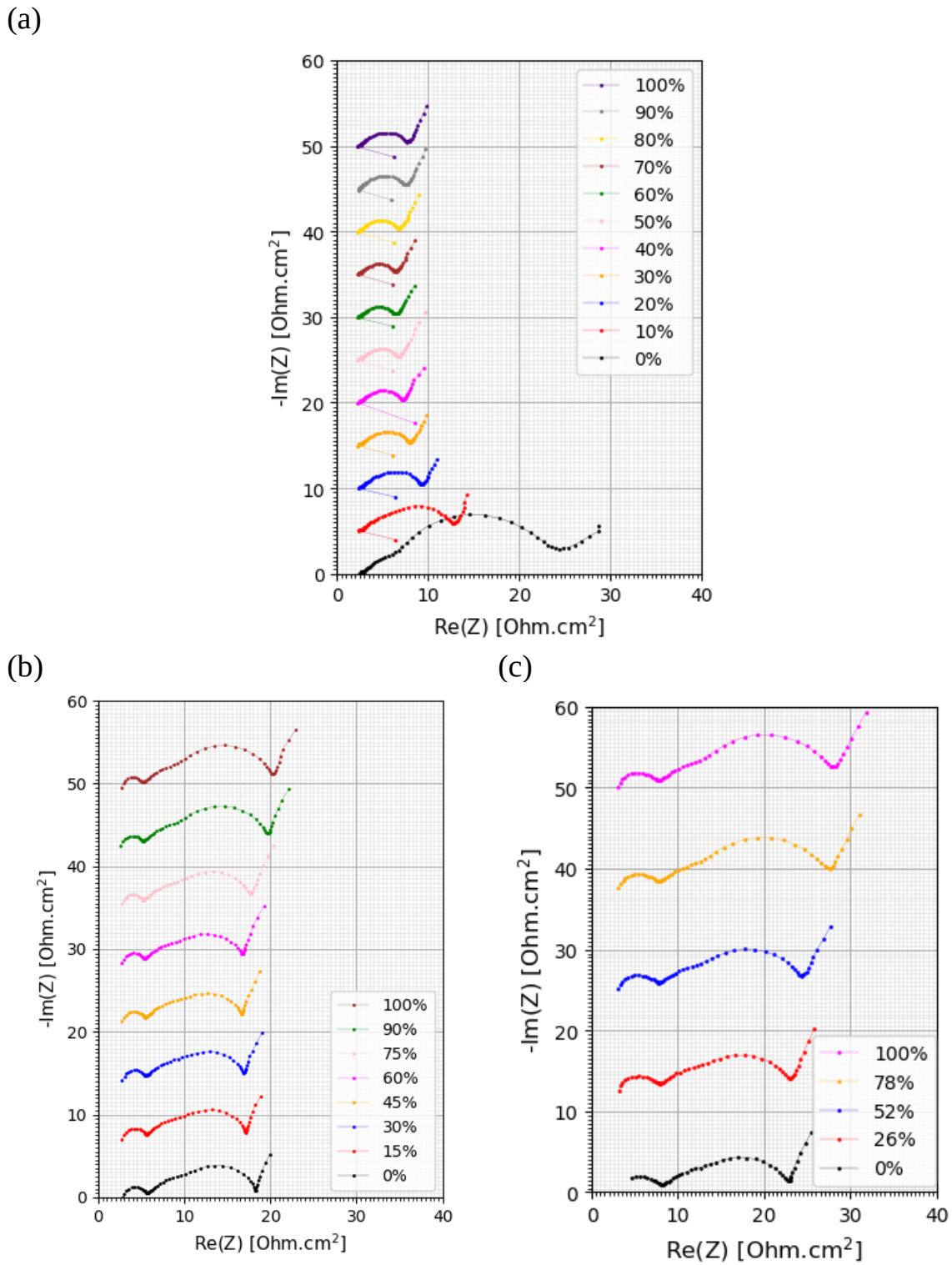

Figure II-24*: Negative electrode EIS spectra of the 4-electrode pouch cell in Nyquist plot at different SOC cycled at 45°C shift between two successive SOC is adjusted with an appropriate to get a clear representation: (a) beginning of life, (b) after 250 cycles, (c) after 600 cycles.*

II.4.2.3 **Post mortem analysis**

In order to select the degradation mechanisms leading to battery aging, *post mortem* analysis is crucial. In this work, visual inspection of the aged electrode samples with electrochemical analyses using half-cells by assembling coin cells were done. The 4-electrode design cell cycled at a temperature of 25°C has been chosen for this *post mortem* analysis. Furthermore, a cell opening and a visual inspection has been conducted on the 2-electrode design cell.

Protocol of cell opening

The cell was discharged to 2.5V followed by a CV step for 10 h to ensure a complete lithium extraction from the anode. Then, the cell was dismantled and opened (Figure II-25) in an argon-filled glove box (H_2O < 1 ppm; O_2 < 1 ppm). After disassembly, the electrodes were harvested and a couple of coin cells were assembled from the positive and negative electrodes to perform the electrochemical analyses.

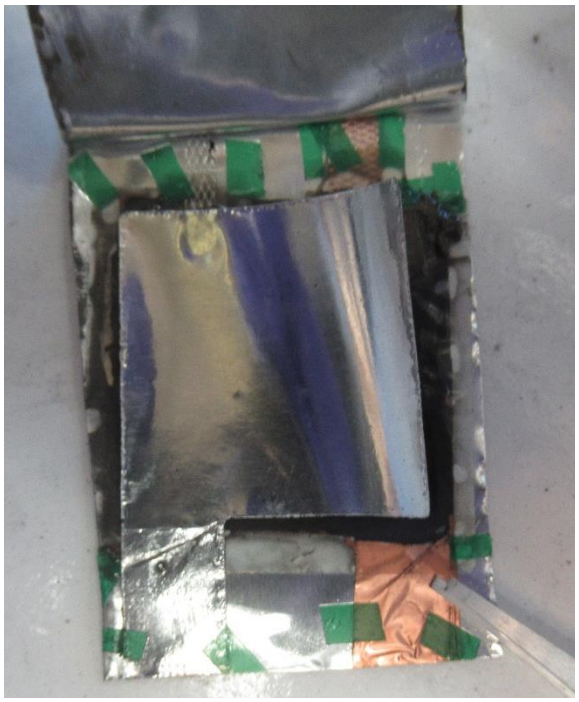

Figure II-25*: Sandwich of the dismantled 4-electrode design cell.*

Protocol of electrochemical analysis

For the NMC 622 vs Li coin cells, the electrochemical analysis consists on a first lithiation at a C-rate of C/10 to quantify the lithium consumed during the cycling, also referred as Q_{LLi} for loss of lithium. It is followed by two charge/discharge cycles at C/10 before a last lithiation at a C-rate of C/10 to deduce the reversible capacity of the positive electrode after the cycling. For the other coin cells based on graphite *vs* Li the protocol of the electrochemical analysis consists

in a first delithiation until 1.5V to verify that no lithium is trapped reversibly in the electrode after the complete cell discharge. It is followed by three charge/discharge cycles at C/10 before a last delithiation at C-rate of C/10. The first delithiation was to check the residual capacity, which should be very small; however, the last one is to deduce the reversible capacity and then the loss of AM. At the end of this check-up, the different CC samples are lithiated at C-rate of C/10 to 40% from their available capacities. Then, they were dismantled and opened in an argon-box (H_2O < 1 ppm; O_2 < 1 ppm) in order to be assembled in two symmetric coin cells: NMC *vs* NMC and Gr *vs* Gr for last EIS measurements.

Results and discussing: visual inspection

Visual inspection is a simple test whose aim is to identify the inhomogeneities in the aged electrodes and the stability of the reference electrodes by comparing them with fresh ones. It is carried out with a human eye without needs of sophisticated instruments. It provides a rapid insight of the dominating degradation phenomena in the various components before going further with electrochemical tests. As presented in Figure II-26, the AM of the positive electrode remained stuck on the collector. However, parts of the AM of the negative electrode are disconnected from the collector, on the boarder of the surface and close to the reference electrode. In fact, graphite sheet is fragile and can be readily fractured during cell opening especially in the presence of a thick SEI film.

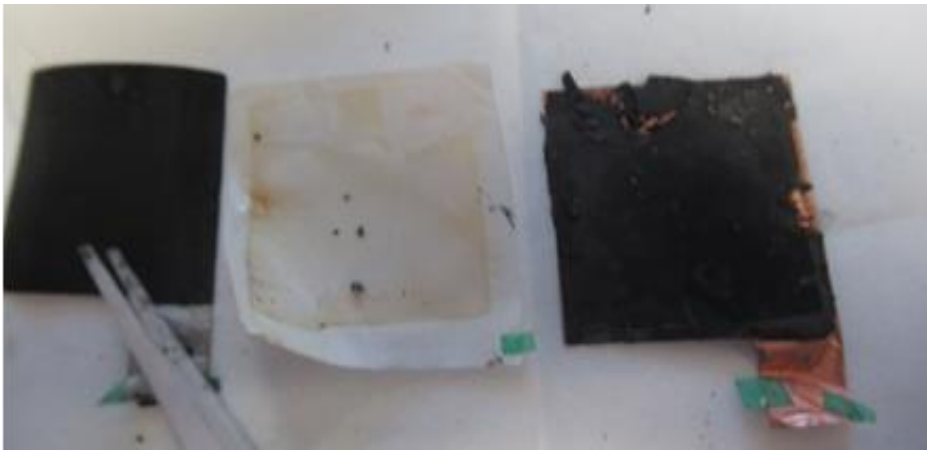

Figure II-26*: 4-electrode design cell disassembly result: In the left: positive electrode, the middle: the separator, the right: negative electrode.*

For the other cell with 2-electrode design cycled at 25°C, the different components are presented in Figure II-27. The visual inspection is very similar. It shows a disconnection of the AM of the negative electrode from the collector, especially on the border, which are lodged on the separator surface. For the positive electrode, the AM remained stuck on the collector.

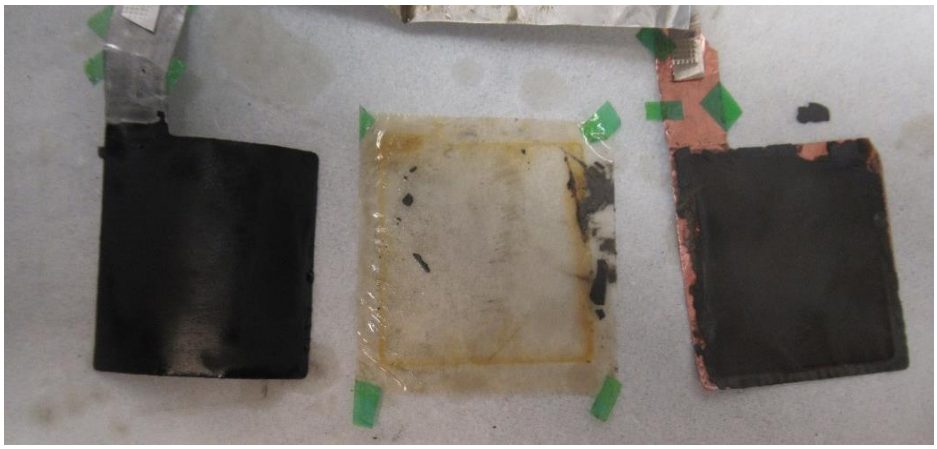

Figure II-27*:2-electrode design cell disassembly result: In the left: positive electrode, the middle: the separator, the right: negative electrode.*

For both negative electrodes, no deposit linked to lithium plating are visually present, that has to be confirmed by SEM observation.

Electrochemical analyses: Results and discussion

The disks of negative electrodes have been sampled in a not delaminated area on the electrode, close to the terminal. For the positive electrode, identically, the disks have been sampled on the electrode, close to the terminal to be in a comparable area.

With the electrochemical cycling, the quantity of the lithium consumed during the 600 cycles can be deduced from the first lithiathion of the NMC 622 $Q_{lithiation}^{CC,NMC}$. In general, this capacity is the sum SEI capacity Q_{sei} consumed during graphite electrode formation plus the lithium loss during cycling Q_{LLi} [76]:

$$Q_{1^{rst}lithiation}^{CC,NMC} = Q_{LLi} + Q_{sei} \quad \text{(II. 18)}$$

Q_{sei} is the capacity lost during the first formation cycle due to the SEI first formation on graphite active material particles. It can be estimated from the irreversible capacity measured for the graphite electrode $Q_{irrev}^{CC,Gr}$, section II.3.2.2, which is equal to 7% from the graphite available capacity. Considering a loading, $Q_{loading}$, of 10.8 mg/cm^2 and the CC electrode area Q_{sei} can be estimated by using the flowing equation:

$$Q_{sei} = Q_{irrev}^{CC,Gr} * Q_{loading} * S_g^{cc} \quad \text{(II. 19)}$$

The obtained results are summarized in *Table II-5* for the two samples tested from the positive electrode. The second important parameter is the reversible capacity after cycling for the NMC $Q_{reversible}$. This value can be deduced from the last lithiation of the NMC. It allows to quantify the AM lost during the 600 cycles by comparison with the reversible capacity of the positive electrode at beginning of life, which was 184 mAh/g. The obtained results are presented in *Table II-5* for the two samples tested from the positive electrode. The experimental results for the first and the second samples are nearly the same. This confirms that we have a very homogenous positive electrode, even after ageing. The *LLi* capacities for the first and second samples are equal to 3.35 mAh and 3.51 mAh respectively. It is a very high, non-expected value, corresponding to a capacity fade of 68% similar to the capacity fade observed during the check-up at low C-rate of the aging cycling. The NMC AM loss is very small around 4%. The capacity loss seems therefore dominated by a non-stable SEI. To confirm this point, we need to verify the AM loss of the graphite electrode. This information can be deduced from the last delithiation of the two Gr vs Li CC samples, by comparison with the reversible capacity of the electrode at beginning of life which is 356 mAh/g. As mentioned in *Table II-5* the graphite AM loss is around 10% for the two samples, which is of the order of expected values after 600 cycles.

Table II-5 : Post-mortem electrochemical analysis results

NMC vs Li	Sample 1	Sample2
$Q_{sei}\ (mA.h)$	0.46	0.46
$Q^{CC,NMC}_{1^{rst}lithiation}\ (mA.h)$	3.81	3.99
$Q_{reversible}(mA.h)$	4.9	4.91
$Q_{LLi}\ (mA.h)$	3.35	3.51
$Q^{CC,NMC}_{rev}$(mAh/g)	184	184
% of NMC AM loss	4.2%	4.02%
Gr vs Li	Sample 1	Sample2
$Q_{rev}(mA.h)$	5.45	5.33
% of Gr AM loss	10%	9.6%
$Q^{CC,Gr}_{rev}$(mAh/g)	356	356

For further analysis of the origin of these high *LLi* values, EIS measurements in symmetric cells were performed. The impedance spectra obtained for the CC made of Gr vs Gr, Figure II-28.a, show a very big first semi-circle related to the SEI. This result confirms the hypothesis of having a growth of a very thick SEI film during aging. The SEI resistance is bigger than the one obtained with aging check-up. In fact, because of the confinement (Covid-19) the different CC used to measure the EIS in symmetry has been stored in an argon-box for 3 months after a full delithiation to avoid SEI growth. This storage may be the raison of this huge difference.

For the NMC vs NMC a classical shape has been obtained. In fact, as shown in Figure II-28.b, a small semicircle appears for the very high frequency domain. In the literature, this semicircle, named CSEI, can be caused by the formation of passivation layer due to the reduction of dissolved active material at the interface [77]. However, after cycling, the NMC spectra impedances does not show a significant modification at the high frequency domain. Therefore, it can be explained by a continue degradation of the electrodes during the storage in the argon-box for 3 months before performing this EIS spectra after a full lithiation. The spectra shape deformations have been appeared at a low frequency domain corresponding to the diffusion in the active material. Therefore, this hypothesis of passivation layer will not be considered in the chapter of upscaling model. However, the presence of two-phase diffusion domains due to nickel migration and SRL formation discussed before will be considered.

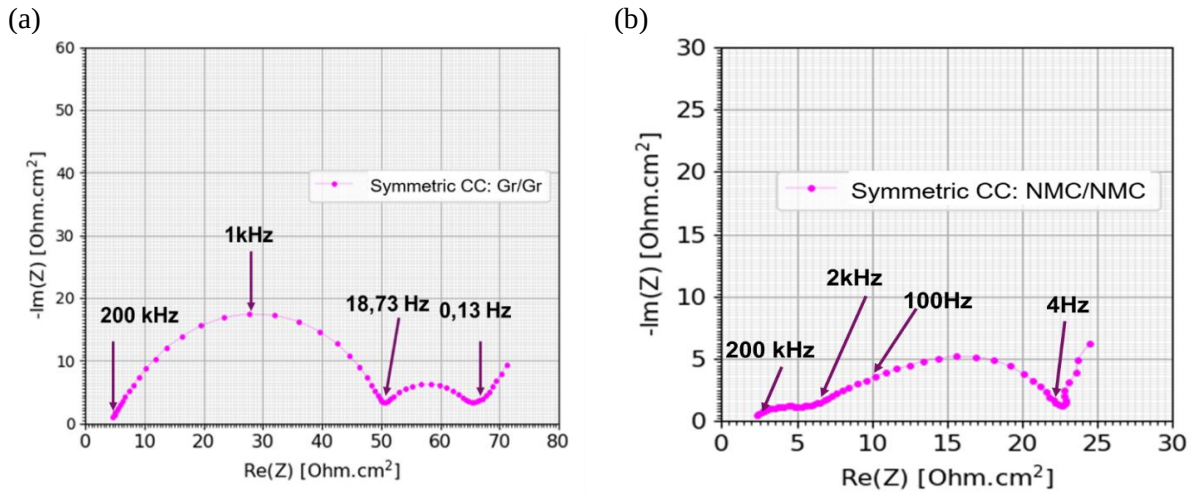

Figure II-28*: EIS spectra obtained from symmetric CC: (a) Gr vs Gr, (b) NMC vs NMC.*

MEB results

As we have mentioned before, SEM was adopted to get a clear information about the surface topology. Assuming a high Q_{LLi} quantities measured via the electrochemical post mortem analysis discussed in the previous paragraph, a thick SEI film should be the origin of this lithium loss. With symmetric EIS measurements, the resistance corresponding to the SEI is very important which can be the origin of the high Q_{LLi} obtained. Therefore, imagery with SEM technique has been performed in a graphite sample electrode at the end of life and compared to fresh electrodes. As presented in *Figure II-29*.b, graphite particles seem to be smooth on the surface compared to fresh electrode (*Figure II-29*a). Moreover, for the porosity (*Figure II-29*d)., it decreases with aging as presented with Ning *et* al. [78]. Lithium plating can been

seen in (*Figure II-29*d) between the particles. It is dispersed over the electrode surface and covers the AM pores.

(a) (b)

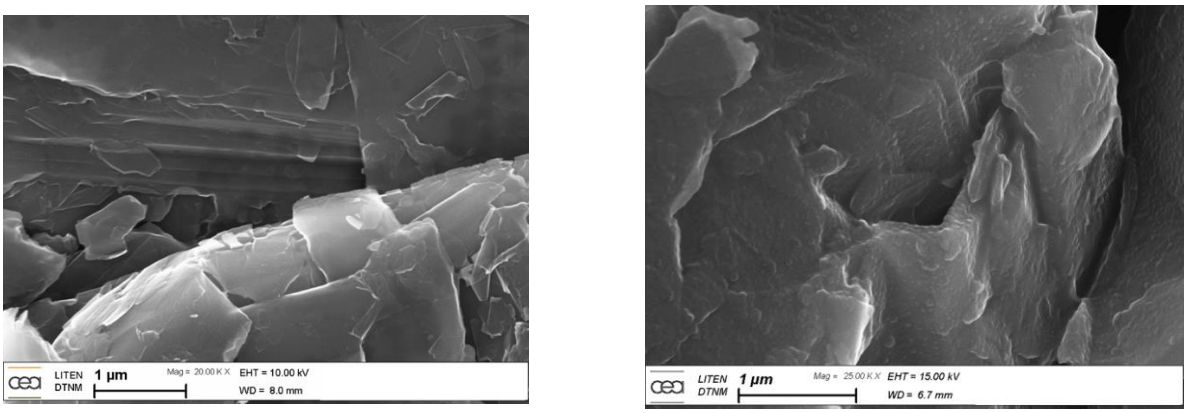

(c) (d)

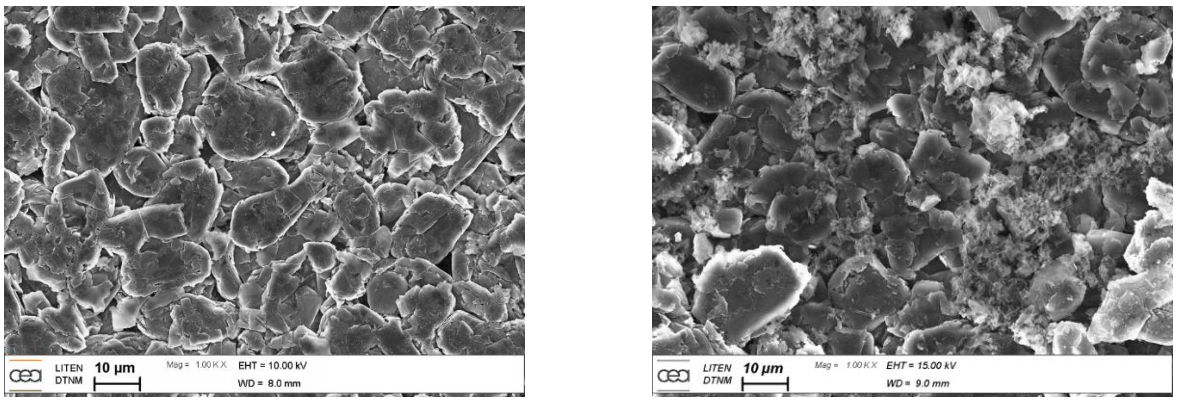

Figure II-29 *: SEM observation for graphite electrode: (a) Pristine electrode X 20K(c) Pristine electrode, X 1K (b) Aged electrode samples X 25K (d) Aged electrode samples X 1K.*

II.5 Conclusion

In this chapter, an investigation of the different active materials properties of a NMC 622 / graphite system and their evolution during lifetime of the batteries are presented. The results of the different experimental protocols proposed in this chapter have been exploited to have sufficient inputs for the model development and to validate the results. The different methods employed to analyze the experiments have been detailed and discussed. During this thesis, an in-depth analyze of the variation of the different parameters of the active material with the SOC has been performed. For the NMC thermodynamic models have been proposed for the OCP, $D_s$and i_0. This study has been published in Electrochemica Acta journal 2021(Annex).

The cell aging with a reference electrode is an excellent strategy to have a clear insight of the cells electrode evolution during aging. It allows us to fix the aging physics to study in the end of life upscaling methodology chapter (chapter 4). In fact, for the graphite, the appearance of the SEI with the diffusion with it will be considered. However, for the NMC 622, the presence for an SRL with the diffusion through it will be studied. Finally, having some post-mortem analysis results helped us to understand the origin of the large capacity fade observed during cycling. For the next chapters, the EIS spectra will be involved to validate the up-scaling methodology developed in this thesis.

Chapter III : Up-scaling methodology for Beginning of Life

Table of contents

In this chapter, a description of the up scaling methodology applied to model the performance of the cells at their beginning of life is presented. The up-scaling methodology is developed in order to bridge the gap between the physical and geometrical parameters of physics-based models at the electrode scale and the empirical parameters of equivalent electric circuit EEC models used for battery sizing and/or management. Our methodology is established in two stages. First, the physical equations are solved in the frequency domain to obtain the corresponding impedance model. Then, this impedance model is mathematically simplified in a series of R-C elements (in series), using a mathematical development in series. The obtained formulation is well adapted to real-time applications since it involves only R-C type elements.

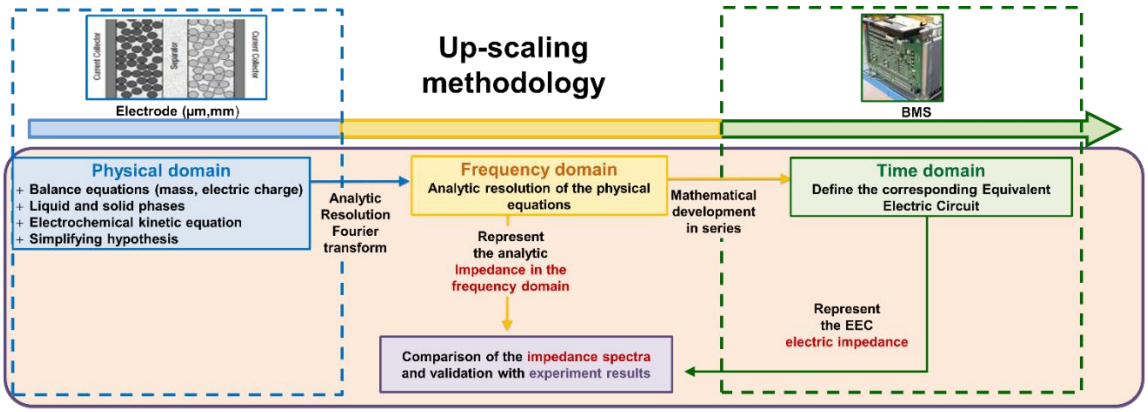

Figure III-1 : *presentation of the up-scaling methodology.*

Two general steps are followed to establish the up-scaling methodology (*Figure III-1*). The first one consists in considering a simplified single particle model. We show that this configuration leads to the well-known Randles impedance model [79]. The second one is about enhancing the impedance model results to adopt it with the EIS experiment measurements for the positive electrode (NMC622) and the negative one (graphite) presented in Chapter II. This enhancement has been performed by considering a Constant Phase Element (CPE) and a Transmission Line Model (TLM). CPE is a good alternative to consider the non-ideal character of the double layer capacity. TLM employment allows to consider the effect of the ionic resistance inside a thick electrode such as the type of graphite studied in this work.

In the first section of this chapter, a presentation of the different physics and assumptions will be detailed. Then the first up-scaling step will be demonstrated and discussed by comparing

with experiments. Finally, the second up-scaling step will be established and compared to the experimental results.

III.1 Physicochemical phenomena of the battery

Electrical modeling of batteries is essential for predicting their performance and operation throughout their lifetime. Indeed, the equivalent electrical circuit model must be able to correctly reproduce the battery's voltage response, represents its state of charge, ohmic losses... In fact, the model has to be robust so that it can be tested under different operating conditions. This requires a good knowledge of the physico-chemical principles of operation of batteries, but also an identification of the parameters to calibrate the model and obtain a satisfactory modeling.

Therefore, in this part a presentation of the different physics within the battery is detailed with the associated assumptions.

III.1.1 Potential of insertion electrode

Nernst equation:

At the electrolyte-active material (AM) interface, the charge transfer reaction corresponding to the insertion and disinsertion of the lithium ion can be written as follows:

$$Li^+ + e^- + <> \leftrightarrow Li_s$$

Where <> refers to the vacant site available in the active material and Li_s is the lithium inserted inside the active material. In general, the chemical potential of a species *i*, is defined in as a function of its thermodynamic activity Eq. (III. 1).

$$\mu_i = \mu_i^0 + RTlna_i \qquad \text{(III. 1)}$$

Where μ_i^0 and a_i are the standard chemical potential and the activity coefficient respectively of a species, *R* and T are the gas constant, ($R = 8.314\ Jmol^{-1}K^{-1}$) and the operating temperature (K) respectively. In order to consider the effect of the electric field gradient on the charged

species present in solution, Butler and Guggenheim [72] introduced the concept of electrochemical potential, which can be expressed as:

$$\mu_i = \mu_i^0 + RTlna_i + Z_iF\phi \quad \text{(III. 2)}$$

$Z_iF\phi$ being the work required to transfer one mole of a neutral species to a charged one with Z_i the charge number, F the Faraday constant ($F = 96500C$) and ϕ the electrostatic potential.

The free enthalpy variation ΔG is the thermodynamic driving force of a chemical reaction that can be expressed as a function of the electrochemical potentials of the species present in the reaction concerned as:

$$\Delta G = \sum \nu_i \mu_i \quad \text{(III. 3)}$$

Where ν_i, represents the stoichiometry coefficient of the reactants and the products of the reaction.

Moreover, according to the Nernst equation, the reversible potential of an electrode is related to the free enthalpy variation of the oxidation-reduction reaction considered as follows:

$$\Delta G = -n\mathrm{FE} \quad \text{(III. 4)}$$

Where n is the number of electrons exchanged in an electrochemical reaction, F is Faraday's constant and E is the potential of an electrode. At equilibrium, the Nernst Equation is deduced from Eq. (III. 3) and Eq. (III. 4) considering the charge conservation ($Z_{Li_s} - Z_{Li^+} - n = 0$) and stoichiometric coefficients equal to 1:

$$E^{eq} = E_0^{eq} + \frac{RT}{F} ln \frac{a_{Li^+}}{a_{Li_s}} \quad \text{(III. 5)}$$

Where E_0^{eq} is the standard equilibrium potential of the reaction. In this study, the electrode is a very good electronic conductor. Therefore, the modeling of the electron chemical potential, which is not as straightforward, is neglected [80].

Equilibrium potential of a lithium-ion battery electrode:

The activity coefficient can be modeled using two contributions, an ideal and a non-ideal one a leading to non-ideal behavior contributions, V_{int} [81] in the equilibrium potential expression. It is the consequence of interactions between the host material and the inserted species and the repulsive ones between the same species inside the active material. Thus, the equilibrium potential can be modeled as following:

$$E^{eq} = E_0^{eq} + \frac{RT}{F}\ln\left(\frac{1-y_i}{y_i}\right) + V_{int}(y_i) \qquad \text{(III. 6)}$$

Where, y_i represents the stoichiometry of the inserted element. It is defined as the ratio of the inserted lithium quantity over the maximal theoretical quantity that can be inserted Cs/Csmax. Redlich-Kister model given by the following relation is one the empirical models used to account for this non ideal-behavior. As it has been presented by Karthikeyana *et al* [82], this empirical model shows a better agreement with experiment data compared to other models.

$$V_{int}(y_i) = \sum_{k=0}^{k_i} A_{i,k}\left[(2y_i-1)^{y+1} - \frac{2y_i k(1-y_i)}{(2y_i-1)^{1-k}}\right] \qquad \text{(III. 7)}$$

The linearization of the Nernst equation (Eq. (III. 6) around y=0.5 and considering only the first order expansion for Redlich-Kister model ($k = 0$), gives:

$$E^{eq} = E_0^{eq} + \frac{4RTC_0}{nF}\left(\frac{1}{2} - y\right) - \beta_0 + C_0\beta_1 y \qquad \text{(III. 8)}$$

Where β_0 and $\beta_1$are empirical factors deduced from the non-ideal energies of the system.

III.1.2 Polarizable electrodes

III.1.2.1 **Double layer current**

When a metal or a solid surface is introduced into solution, the properties of the phases at the interface are changed. A capacitor is created at the metal-electrode interface, with a dielectric thickness of a few tens of nanometer. In this manner, at the interface between an inert electrode material such as graphite, NMC, LFP… and an electrolyte, a charge separation occurs. This interface is referred to as the electrochemical double layer. It develops at the interface due to the potential drop across it. This phenomenon is purely electrostatic and does not require any chemical changes inside the solid phase of the electrode. At this interface, it is possible to define a double layer charging current density, which can be modeled using the following equation of an ideal capacitor [27, 72, 83]:

$$i_{dl} = \frac{\partial q}{\partial t} = C_{dl}\frac{\partial(\psi_{int}^{+/-} - \varphi_{int}^{+/-})}{\partial t} \quad \text{(III. 9)}$$

Where $\varphi_{int}^{+/-}$ is the electronic potential (positive or negative electrode) at AM/electrolyte interface and $\psi_{int}^{+/-}$,is the ionic one (positive or negative electrode) at AM/electrolyte, while q is the charge of the capacitor and C_{dl} the double layer capacity.

III.1.2.2**Faradaic current**

The faradaic process corresponds to the electron transfer reaction and involves the reduction or oxidation of the materials.

$$Li^+ + e^- + <> \leftrightarrow Li_s$$

In general, this intercalation kinetic can be modeled with the Butler-Volmer equation to quantify the current density of intercalation, i_f as [84, 72]:

$$i_f = i_0[\frac{C_l}{C_l^*}\exp\left(\alpha_r \frac{F}{RT}\eta\right) + \frac{C_{<>}}{C_{<>}^*}\exp\left(\alpha_r \frac{F}{RT}\eta\right) - \frac{C_s}{C_s^*}\exp\left((\alpha_r - 1)\frac{F}{RT}\eta\right)] \quad \text{(III. 10)}$$

Where α_r is the electron transfer symmetry factor (α_r =0.5), i_0 the exchange current density, and η the surface overpotential due to irreversible physical phenomena inside the system. Note

that C_l, $C_{<>}$ and C_s are the concentration of the lithium ion at the interface in the electrolyte, the concentration of the vacant site at the interface of the AM and the concentration of the lithium atom in the AM respectively. C_i^* represents concentration of a specie i at the equilibrium. The overpotential, η, is defined as:

$$\eta = (\varphi_{int} - \psi_{int}) - E^{eq} \quad \text{(III. 11)}$$

It is considered as the additional potential implied to drive a reaction at a specific rate [72]. The linearization of the Butler Volmer equation as leads to a simple linear relation between the overpotential and the faradic current:

$$\eta = \frac{RT}{nF}\left(\frac{C_l}{C_l^*} + \frac{C_{<>}}{C_{<>}^*} - \frac{C_s}{C_s^*} + \frac{i_f}{i_0}\right) \quad (12)$$

III.1.3 Ohmic phenomena

Ohmic drops or ohmic losses depend on the electronic circuit and the ion circuit. Indeed, the electrons find an opposition to their movement when they are transported from/toward the particles of active material, through the path made by binders to/from the current collector. At the same time, the lithium ions exchanged at the surface of the active material particles of one electrode are transported through the electrolyte from/to the active material particles of the other electrode. Thus, the ohmic resistance is related to electrons and ions transport in the electrodes and electrolyte. They depend on many parameters as the temperature, porosity and tortuosity of the electrodes. Given that the contribution of ionic resistivity is more significant than that of electronic one [85], ohmic losses decrease when the temperature increases. Indeed, when the temperature increase, ionic conductivity increase. These ohmic losses are usually modeled using Ohm's law, which relates the potential gradient to the flux of charge via the conductivity of the material:

$$i_s = -\sigma_{s,AM} \nabla \phi_s \quad \text{(III. 13)}$$

Where $i_s$the flux of charge, ϕ_s the potential and $\sigma_{s,AM}$ is the conductivity of the material.

III.1.4 Ion transport

Mass transport takes place within the electrolyte and the active material particles. The flux density N_i of species i can be driven by different phenomena, namely convection, diffusion and migration:

$$N_i = \underbrace{C_i V}_{convection} - \underbrace{D_i \nabla C_i}_{diffusion} + \underbrace{C_i v_i z_i F \nabla \varphi}_{migration} \quad \text{(III. 14)}$$

Where C_i is the concentration of species i, V the velocity of the fluid, D_i the diffusion coefficient of species i and v_i the mobility of a charged species i of charge z_i. Inside the lithium-ion batteries, ion can move by diffusion or migration. The convection is null in the solid active materials and can be neglected in the electrolyte. In fact, the convection in electrolyte can be avoided by preventing stirring and vibration [72].

Transport in the electrolyte:

The diffusion transport involves the movement of matter under the effect of a chemical potential gradient, i.e. from the most concentrated zone to the least concentrated. Considering the migration, the transport in the electrolyte can be defined :

$$\frac{\partial c_l}{\partial t} = \nabla . (D_l \nabla C_l - \frac{t_+}{F} i_l) \quad \text{(III. 15)}$$

Where

$$i_l = -\sigma_l \nabla \phi_l + \sigma_l \frac{RT}{F} \frac{(1 - t_+)}{C_l} (1 + \frac{\partial ln \gamma_l}{\partial ln C_l}) \nabla C_l \quad \text{(III. 16)}$$

σ_l, is the electrolyte conductivity, ϕ_l, the ionic potential, t_+, the cationic transference number and $\frac{\partial ln \gamma_l}{\partial ln C_l}$ the activity coefficient.

This phenomenon may become preponderant compared to charge transfer when the electrode deviates from its equilibrium potential (when charges or discharges are carried out at high currents). Moreover, when an electric potential exists in a solution, e.g. in electrochemical cells, cations (positive ions) will be attracted to the negative electrode and anions (negative ions) to the positive electrode: this is referred to as migration. According to Karthikeyan *et* all. [82], in most lithium-ion batteries, diffusion can be neglected compared to migration within the electrolyte. In the scope of this thesis, the diffusion in the electrolyte is neglected.

Transport in the active material:

Inside the active material, the mass transport is governed by the diffusion and the migration is neglected. In fact, the active materials are rather good electronic conductors in Li-ion batteries. For that reason, the electric potential gradient is negligible. The transport inside the active material is only controlled by the concentration gradient and can be described by Fick law as:

$$\frac{\partial c_s}{\partial t} = \nabla . D_s \nabla c_s \tag{III. 17}$$

Where c_s is the ion concentration inside the active material, *t* is the time variable, and D_s is the chemical diffusivity of ions in the active material. For one-dimensional mass transfer along the x-axis of a plane active material geometry, and assuming a constant chemical diffusivity, Eq. (III. 17) can be written as:

$$\frac{\partial C_s(x,t)}{\partial t} = D_s \frac{\partial^2 C_s(x,t)}{\partial x^2} \tag{III. 18}$$

In spherical coordinates for a one-dimensional mass transfer along the r-axis, Eq. (III. 17), can be presented as following [71] [86]:

$$\frac{\partial C_s(r,t)}{\partial t} = \frac{D_s}{r^2}\frac{\partial}{\partial r}\left(r^2 \frac{\partial C_s(r,t)}{\partial r}\right) \tag{III. 19}$$

III.2 Up-scaling methodology: From the physics to the analytical impedance models

In the previous section, we have presented the physical phenomena of a battery that are important at the electrode scale. In this part, these equations will be solved in the frequency domain to determine analytically the impedance model of the battery with a clear link to the different physics. From this point of view, the equivalent circuit model is built in the frequency domain by considering physics laws and a given number a simplification.

III.2.1 Introduction to the model electrode configuration

In a lithium ion-battery, an electrode can be presented *via* three important domains: a single particle (representative of the active material), an electronic conductor and an ionic one (Figure III-2). The electrons are transported in the solid phase composed of the active materials and electronic conductors. In the liquid phase, which consist of the electrolyte and is an ionic conductor domain, the transport of the lithium ion is performed from/to the AM/electrolyte interfaces of each electrode. The electrochemical reaction at the interface ensures the reduction/oxidation of the lithium ion before/after diffusing inside the solid phase of the AM.

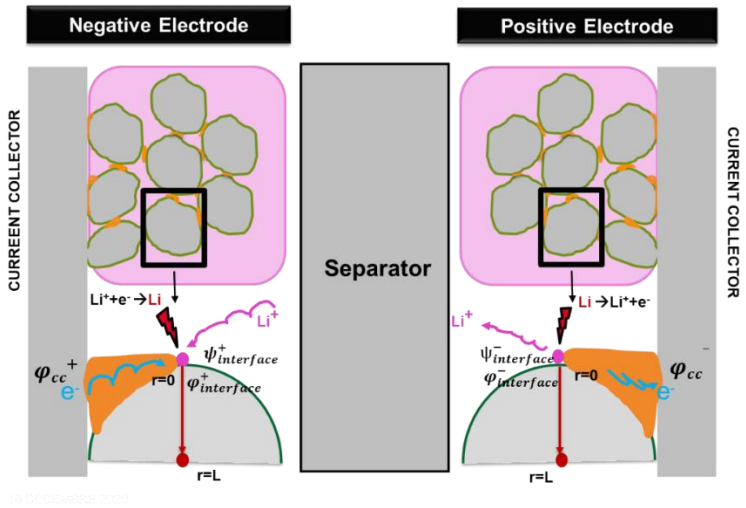

Figure III-2: *cell presentation.*

The cell electric potential difference is defined as the electronic potential difference between the two current collectors:

$$U_{cell} = (\varphi_{cc}^{+} - \varphi_{cc}^{-}) \qquad \text{(III. 20)}$$

The *Figure III-2* allows defining this cell voltage with the different electric and ionic potentials inside the cell, presenting the electrical path.

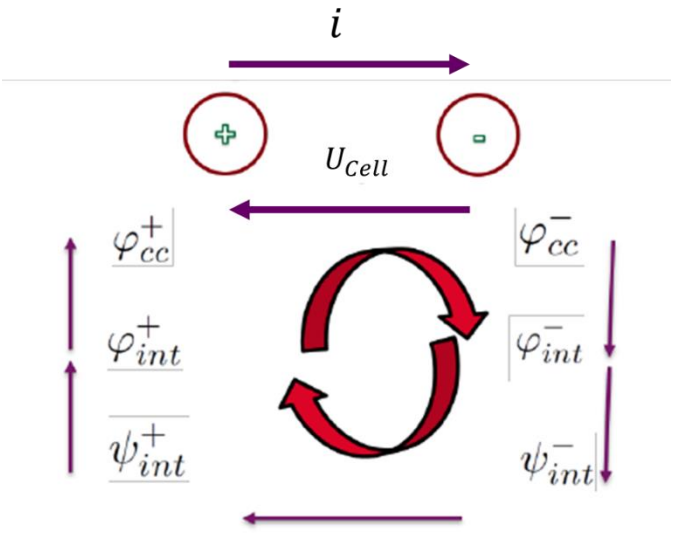

Figure III-3: *Electrical path.*

As a positive current is considered in charge, the cell potential can be divided as following:

$$U_{cell} = (\varphi_{cc}^{+} - \varphi_{int}^{+}) + (\varphi_{int}^{+} - \psi_{int}^{+}) + (\psi_{int}^{+} - \psi_{int}^{-}) + (\psi_{int}^{-} - \varphi_{int}^{-}) + (\varphi_{int}^{-} - \varphi_{cc}^{-}) \quad \text{(III. 21)}$$

Where:

$\varphi_{int}^{+/-}$: Electronic potential (positive or negative electrode) at AM/electrolyte interface.

$\psi_{int}^{+/-}$: Ionic potential (positive or negative electrode) at AM/electrolyte.

$\varphi_{cc}^{+/-}$: Electric potential at the (positive or negative) current collector.

The electric potential difference between the collector and the AM ($\varphi_{cc}^{+/-} - \varphi_{int}^{+/-}$) is due to the electron transport within the solid phase and can be related to the ohmic resistance, $R_{ohm,electronic}^{+/-}$, as following:

$$\varphi_{cc}^{+/-} - \varphi_{int}^{+/-} = R_{ohm,electronic}^{+/-} i_{tot} \quad \text{(III. 22)}$$

Where i_{tot} is the total current passing throw the cell defined as the sum of the capacitive and the faradic ones:

$$i_{tot} = i_{dl} + i_f \quad \text{(III. 23)}$$

Similarly, the ionic potential difference between the two electrodes is related to the ionic resistance, $R_{ohm,ionic}^{+/-}$, resulting from the ion transport:

$$\psi_{int}^{+} - \psi_{int}^{-} = R_{ohm,ionic}^{+/-} i_{tot} \quad \text{(III. 24)}$$

For the potential differences between the ionic at the electronic potentials at the AM/electrolyte interface, they can be expressed as the sum of the overpotential ($\eta_{p/n}$) and the equilibrium potentials at each interface ($E_{eq}^{p/n}$):

$$\psi_{int}^{+/-} - \varphi_{int}^{+/-} = \eta_{p/n} - E_{eq}^{p/n} \quad \text{(III. 25)}$$

Thus, considering these definitions and Eq. (III. 22,III. 24,III. 25), the cell potential can be expressed as:

$$U_{cell} = E_{eq}^{p} - E_{eq}^{n} + \eta_p - \eta_n + R_{ohm} i_{tot} \quad \text{(III. 26)}$$

Where R_{ohm} is the sum of the ionic and electric ohmic resistances.

III.2.2 Introduction to cell impedance

The electrical impedance is representative of the physico-chemical phenomena and components present in the environment. As a first approximation, electrical circuits based on elementary components, such as resistance, capacitance or inductance, can be used to model these phenomena. This first approximation is often insufficient. Therefore, more complex elements, whose correspondence in the physical domain is less trivial, are employed to improve the correspondence between model and reality. For instance, components, such as the constant phase element (CPE), as well as non-linear elements (charge transfer resistance, Warburg impedance) become necessary in order to represent all the dynamics inside the electrode, leading to a better fit of the impedance spectra measurements. The impedance of the cell is obtained with Electrochemical Impedance Spectra (EIS) measurements (see chapter II). These experimental results are used in this chapter to validate the developed models. Applying a small perturbation during the measurements allows obtaining a linear answer, which is supposed to be at the same frequency. To go more into the mathematical developments, , each variable X is presented as the sum of a steady-state contribution and a second term related to the perturbation signal at the pulsation ω as follows [87] [88] [84]:

$$X = \overline{X} + \Delta\check{X}\exp(j\omega t) \quad \text{(III. 27)}$$

Where $\overline{X}$ is the steady state term, $\widetilde{\Delta X}$ the amplitude of the sinusoidal part of the signal, $\omega = 2\pi f$ the pulsation and f the frequency and $j^2 = -1$. The Fourier transformation of the perturbation is noted $\Delta\check{X}$. It is a complex number containing the magnitude and the phase of the perturbation.

Remember that the impedance noted Z is defined by:

$$Z = \frac{d\Delta\widetilde{U}_{cell}}{d\Delta\tilde{\imath}_{tot}} \quad \text{(III. 28)}$$

Where $\tilde{\imath}_{tot}$ is the current passing through the cell and $\widetilde{U}_{cell}$ is the potential of the cell. Using the expression of the cell voltage (Eq. (III. 26)), and the steady state solution, the cell impedance can be expressed as:

$$Z = \frac{d\Delta\tilde{E}_{eq} + d\Delta\tilde{\eta}}{d\Delta\tilde{\imath}_{tot}} + R_{ohm} \quad \text{(III. 29)}$$

In the following sections, the interfacial impedance of the electrode presented in the previous equation (Eq. (III. 29)) related to the overpotential and the equilibrium potential will be detailed.

III.2.3 Local interface impedance

The lithium-ion reduction/oxidation takes place at the surface of the particle before/after diffusion of the lithium ions inside the active material. So that, interfacial impedance consists of a faradaic contribution related to the kinetic of the electrochemical reaction and non-faradaic process due to the double layer capacitance. The total current density at the MA/electrolyte interface is defined as following, using Fourrier-transformed variables (section III.2.1):

$$\tilde{\imath}_{tot} = \tilde{\imath}_f + \tilde{\imath}_{dl} \quad \text{(III. 30)}$$

The capacitive current density can be presented in the frequency domain using the definition (Eq. (III. 9)) and surface difference potential definition (Eq. (III. 25)) as:

$$\Delta\tilde{\imath}_{dl} = j\omega C_{dl}(\Delta\tilde{\eta} + \Delta\tilde{E}_{eq}) \quad \text{(III. 31)}$$

Thus, using the previous Eq. ((III. 30,) (III. 31)), the cell impedance can be expressed as:

$$Z = \frac{1}{\frac{1}{Z_c} + \frac{1}{Z_f}} + R_{ohm} \quad \text{(III. 32)}$$

Where Z_f is the faradaic impedance of the electrode:

$$Z_f = \frac{d\Delta\tilde{U}_{OCV} + d\Delta\tilde{\eta}}{d\Delta\tilde{\imath}_f} \quad \text{(III. 33)}$$

And Z_c is the capacitive impedance of the electrode:

$$Z_c = \frac{1}{j\omega C_{dl}} \quad \text{(III. 34)}$$

Following Randles and Graham [79, 89] , the double layer current and the Faradaic one at the active material/electrolyte interface follow an independent parallel arrangement.

As presented in the previous section, the equilibrium potential and the overpotential depend on the stoichiometry at the surface of the active material. Therefore, the faradaic impedance can be decomposed as:

$$Z_f = \underbrace{\left.\frac{d\Delta\tilde{\eta}}{d\Delta\tilde{\imath}_f}\right|_{soc}}_{R_{ct}} + \underbrace{\left[\left.\frac{\partial\Delta\tilde{\eta}}{\partial\Delta\tilde{y}}\right|_{\tilde{\imath}_f} + \left.\frac{\partial\Delta\tilde{U}_{OCV}}{\partial\Delta\tilde{y}}\right|_{\tilde{\imath}_f}\right]\frac{d\Delta\tilde{y}}{d\Delta\tilde{\imath}_f}}_{Z_W} \quad \text{(III. 35)}$$

Where y represent the stoichiometry of the inserted lithium atom at the surface of the active material:

$$y = \frac{{C_s}^{surface}}{C_{max}} \quad \text{(III. 36)}$$

Where C_{max} is the maximum lithium concentration inside the active material. R_{ct} is the charge transfer resistance. It is deduced from the linearized Butler Volmer equation (Eq.(12)) and it is expressed as:

$$R_{ct} = \frac{RT}{nFi_0} \quad \text{(III. 37)}$$

Z_W , the Warburg impedance can be simplified using the overpotential expression (Eq.(12)) and the equilibrium potential relation (Eq. (III. 8)):

$$Z_W = -\left[\frac{RT}{nFi_0}\left(\frac{1}{C^*_{<>}} + \frac{1}{C^*_s}\right) + \left(\frac{4RT}{nF} - \beta_1\right)\right]\frac{d\Delta\tilde{c}_s{}^{surface}}{d\Delta\tilde{\imath}_f} \quad \text{(III. 38)}$$

Where $\tilde{C}_s{}^{surface}$is the concentration of lithium inserted at the surface of the active material while $C^*_{<>}$and C^*_s represent the reference concentration of the vacant site and the lithium atom inserted at the steady state. They can be defined as function of the stoichiometry as:

$$C^*_{<>} = (1 - \bar{y})C_{max} \quad \text{(III. 39)}$$

$$C^*_s = \bar{y}C_{max} \quad \text{(III. 40)}$$

To get the general form of the Warburg impedance, an expression for $\tilde{c}_s{}^{surface}$ should be provided. In the next section, this concentration is determinate by studying the diffusion inside the active material.

III.2.4 Diffusion impedance

The diffusion impedance is determined by considering the concentration change inside the active materials as function of the perturbing signal and frequency. Therefore, Eq. (III.17) presenting the general Fick law can be rewritten using Fourrier transformation as:

$$\frac{\partial\Delta\tilde{c}_s}{\partial t} = D_s\nabla^2\Delta\tilde{c}_s \quad \text{(III. 41)}$$

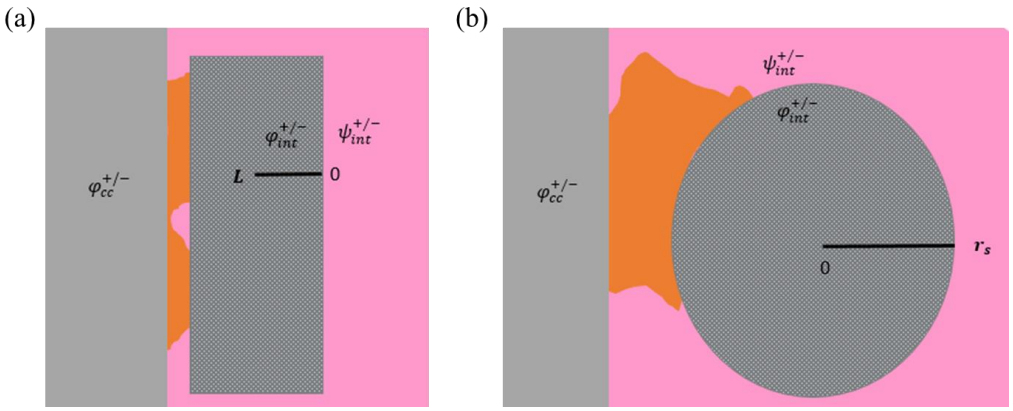

Figure III-4 *: Schematic presentation of the diffusion boundary conditions: (a) plane geometry, (b) spherical geometry.*

For the plane geometry, let us start by applying the Laplace transformation to Eq. (III. 18):

$$j\omega\Delta\tilde{c}_s = D_s \frac{\partial^2 \Delta\tilde{c}_s(x,t)}{\partial x^2} \tag{III. 42}$$

As presented in *Figure III-4*(a) the boundary conditions considered are:

$$\left.\frac{\partial \Delta\tilde{c}_s}{\partial x}\right|_{x=0} = \frac{\Delta\tilde{\imath}_f}{D_s F} \tag{III. 43}$$

$$\left.\frac{\partial \Delta\tilde{c}_s}{\partial x}\right|_{x=L} = 0 \tag{III. 44}$$

Where L is the electrode mid-thickness. The first condition, Eq. (III. 43), presents the flux density of lithium intercalated inside the solid active material at the electrolyte/AM interface. The second one (Eq. (III. 44)) prohibits the mass flow diffusion through the second limit of solid state by considering a symmetry in the center of the particle. This differential equation is solved using the two boundary conditions leading to:

$$\Delta\tilde{c}_s{}^{surface} = -\frac{\Delta\tilde{\imath}_f\, L}{nD_s F} \frac{\coth\left(\sqrt{j\tilde{\omega}}\right)}{\sqrt{j\tilde{\omega}}} \tag{III. 45}$$

Where $\tilde{\omega} = \omega \frac{L^2}{D_s}$ and ω is the pulsation.

For the spherical geometry, applying the Laplace transformation on Eq. (III. 19) gives:

$$j\omega\Delta\tilde{c}_s = \frac{D_s}{r^2}\frac{\partial}{\partial r}\left(r^2\frac{\partial\Delta\tilde{c}_s(r,t)}{\partial r}\right) \quad \text{(III. 46)}$$

To solve this equation, two boundary conditions are employed (*Figure III-4*b). The first one is about supposing symmetry at the center the spherical particle:

$$\left.\frac{\partial\Delta\tilde{c}_s}{\partial r}\right|_{r=0} = 0 \quad \text{(III. 47)}$$

The second condition accounts for the flux density of lithium intercalated inside the solid active material at the electrolyte/AM interface applying Faraday's law:

$$\left.\frac{\partial\Delta\tilde{c}_s}{\partial r}\right|_{r=R_p} = -\frac{\Delta\tilde{\imath}_f}{D_s F} \quad \text{(III. 48)}$$

The differential Eq. (III. 46) is solved using the previous boundary conditions. The equilibrium potential of the faradaic intercalation reaction is a function of the concentration of the lithium atoms called intercalant at the particle/electrolyte interface. Thus, we define $\Delta\tilde{c}_s|_{r=R_p} = \Delta\tilde{c}_s{}^{surface}$ and we obtain:

$$\Delta\tilde{c}_s{}^{surface} = \frac{\Delta\tilde{\imath}_f}{nD_s F}\frac{R_p}{\left(1-\sqrt{j\widetilde{\omega}}\coth\left(\sqrt{j\widetilde{\omega}}\right)\right)} \quad \text{(III. 49)}$$

Where $\widetilde{\omega} = \omega\frac{{R_p}^2}{D_s}$ and ω is the pulsation.

The Warburg impedance for the planar and spherical geometries can be determined replacing the expression of $\Delta\tilde{c}_s{}^{surface}$ (Eq. (III. 45) and Eq. (III. 49) respectively) in Eq. (III. 38)).

$$Z_W{}^{plan} = \left[\frac{RT}{nFi_0}\left(\frac{1}{(1-\bar{y})}+\frac{1}{\bar{y}}\right)+\left(\frac{4RT}{nF}-\beta_1\right)\right]\frac{L}{nC_{max}D_s F}\frac{\coth\left(\sqrt{j\widetilde{\omega}}\right)}{\left(\sqrt{j\widetilde{\omega}}\right)} \quad \text{(III. 50)}$$

$$Z_W{}^{spherical} = \left[\frac{RT}{nFi_0}\left(\frac{1}{(1-\bar{y})}+\frac{1}{\bar{y}}\right)+\left(\frac{4RT}{nF}-\beta_1\right)\right]\frac{R_p}{nC_{max}D_sF}\frac{1}{\left(\sqrt{j\widetilde{\omega}}\coth\left(\sqrt{j\widetilde{\omega}}\right)-1\right)} \quad \text{(III. 51)}$$

For the planar geometry, a similar solution has been presented in the literature. However, the hypothesis of considering the dependency of the OCP with the electrode stoichiometry is not discussed in many reviews [87]. This assumption has been considered with Schönleber *et al.* [90] and leads to an analytic expression of the diffusion within the planar geometry electrode similar to Eq. (III. 50). For the spherical geometry, similar expression has been presented [87] considering an empirical factor to express the derivative of the OCP with the stoichiometry [84] [91]. For Eq. (III. 51) , the dependency of the OCP with the electrode stoichiometry, similar to the one used with planar geometry, has been considered.

In the scoop of this thesis, the active materials particles for the two studied electrodes are assumed spherical. Therefore, in the presented up-scaling methodology we only consider the diffusion impedance solution for the spherical geometry.

III.2.5 Cell impedance: Results and discussion

The cell impedance was calculated in this work considering the following hypothesis: the Fick law has been considered for the diffusion inside the active material and the diffusion in the electrolyte is neglected. A kinetic reaction of insertion and de-insertion is considered at the active material/electrolyte interface. In this section, the analytic cell impedance (Eq.(III. 29)) is compared with experimental results for both the positive and the negative electrodes. A part of physical parameters used in this study has been measured in the chapter II. For the rest, they have been identified via model fitting, with experiments, in the Nyquist and Bode presentations.

Single particle model

As shown before, the analytic model has been determined assuming a single particle electrode model. The analytic impedance (Eq. (III. 32)) can be written using the faradaic impedance, Z_f, as:

$$Z = \frac{1}{j\omega C_{dl} + \frac{1}{Z_f}} + R_{ohm} \quad \text{(III. 52)}$$

Where:

$$Z_f = R_{ct} + Z_W \quad \text{(III. 53)}$$

Z_W being the Warburg impedance (Eq. (III. 51) and R_{ct} the charge transfer resistance detailed in the previous paragraph (Eq. (III. 37). The ohmic resistance, the charge transfer resistance and the diffusion phenomena occur in different frequency domains. Thus, their contributions can be presented separately considering the following equivalent electric circuit model:

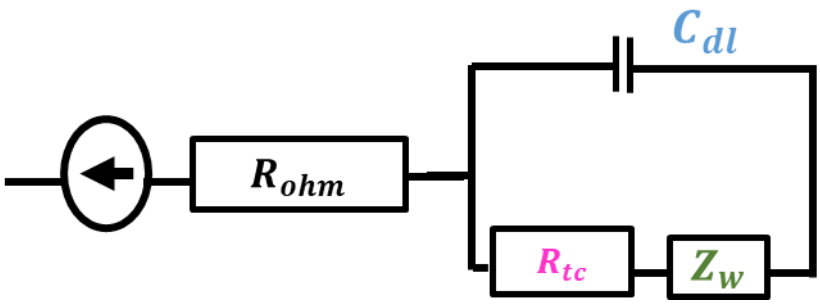

Figure III-5: *Analytic EEC representation for the analytic impedance of the electrode.*

To simulate the analytical model, we use the physical parameters for the graphite and the NMC622 active materials presented in Table III-1. Figure III-6 and Figure III-7 show the impedance spectra in Nyquist diagram and Bode plot. The presented results are compared to EIS experimental measurements, detailed in chapter II, at the BOL for a cell SOC of 50%.

The single particle model proposed consists of a Warburg diffusion impedance Z_W in series with the charge transfer resistance R_{ct}, connected in parallel with an ideal capacity standing for the double layer capacitor C_{dl} (See Figure 4). This ideal capacity leads to a semi-circle shape in the Nyquist plot and is obtained for both the graphite and NMC622 electrodes (Figure III-6 and Figure III-7a). This semi-circle does not agree with the real shape of the impedance spectra for the graphite and the NMC. Regarding the lower frequencies (below 1Hz) which corresponds to the Warburg part of the EEC, the diffusion slope fits very well the experiment results for the two electrodes.

To be more confident with the hypothesis implemented and the physical parameters measured, a comparison with Bode representation is recommended. It can compensate the limitations inherent to the Nyquist plot by showing explicitly the frequency dependence of the different physics described in the battery system. Indeed, Figure III-6b and Figure III-7b show a good agreement between the model and the experiment data for frequency domain lower than 1 Hz for the two electrodes. However, for frequencies higher than 1 Hz, the model doesn't fit the experiment data for the two electrodes. This domain is controlled by the charge transfer and the type of the double layer capacitor implemented. In fact, using an ideal capacitor does not allow representing the behavior of the battery electrodes. Therefore, in the next section, we suggest to replace the ideal capacitor by a constant phase element (CPE) [92] component.

Table III-1 : Parameters used in the Single Particle model

Parameter	Graphite	NMC622	Source
$D_s(m^2.\ s^{-1})$	7.00E-13	5.00E-14	Measured
$R_p\ (m)$	8.00E-06	6.00E-06	Measured
$i_0(A.m^2)$	5.00E+00	2.20E+00	Measured
$C_{dl}(F)$	6.40E+02	1.70E+02	Measured
$L\ (m)$	7.80E-05	6.00E-05	Measured
$\sigma_e(S.m^{-1})$	7.00E-02	1.00E-01	Calculated
$C_0\ (mol.m^{-3})$	3.07E+04	4.90E+04	Calculated
$F\ (C.mol^{-1})$	9.65E+04	9.65E+04	-
$R\ (J.mol^{-1}.K^{-1})$	8.31E+00	8.31E+00	-
$T(k)$	2.98E+02	2.98E+02	-
$R_{ohm}(\Omega)$	1.60E-04	1.80E-04	Calculated
$S\ (m^2)$	1.00E-03	1.20E-03	Measured
$n\ (-)$	1.00E+00	1.00E+00	-

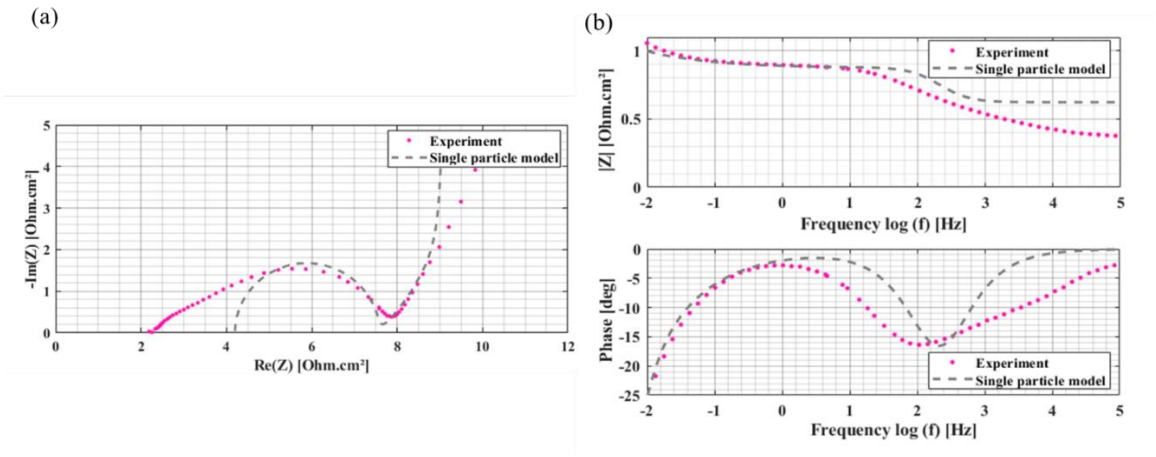

Figure III-6*: A comparison between experiment measurements and single particle model result for the graphite electrode at full cell SOC=50%: (a) EIS spectra in Nyquist representation (b) EIS spectra in BODE representation, log10 scale for the magnitude plot and linear scale for the phase plot.*

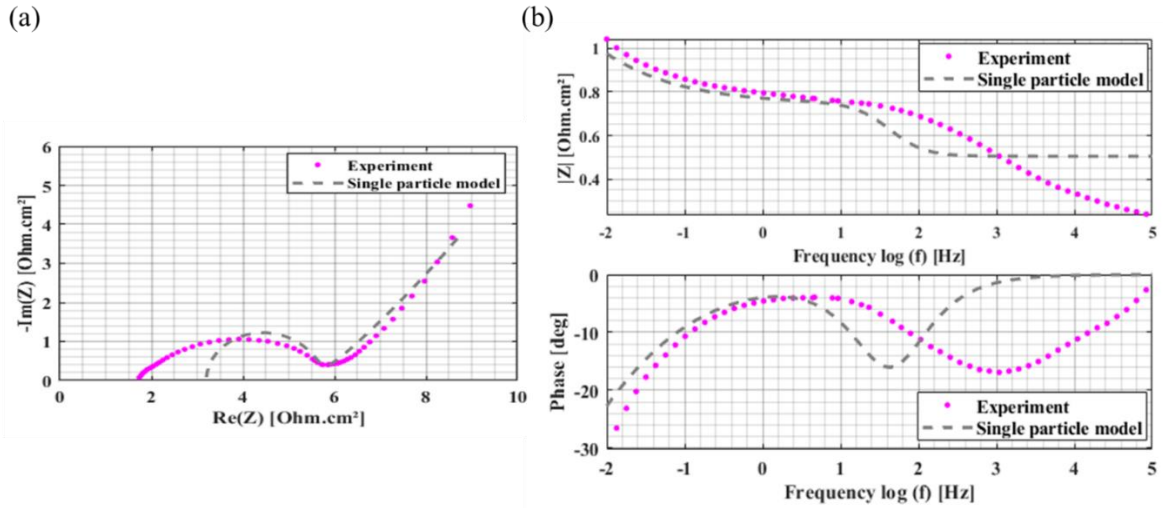

Figure III-7: *A comparison between experiment measurements and single particle model result for the NMC622 electrode at full cell SOC=50%: (a) EIS spectra in Nyquist representation (b) EIS spectra in BODE representation, log10 scale for the magnitude plot and linear scale for the phase plot.*

CPE approximation

A CPE is implemented to model the electric field between the electrode and the electrolyte. This model allows to account for the non-ideal behavior of the double-layer capacity. The analytic impedance (Eq. (III. 52) becomes:

$$Z_{Cell,CPE} = \frac{1}{\frac{1}{Z_{c,CPE}} + \frac{1}{Z_f}} + R_{ohm} \quad \text{(III. 54)}$$

Where $Z_{c,CPE} = \frac{1}{(j\tilde{\omega}C_{dl})^{\alpha}}$ with $0 \leq \alpha \leq 1$.

The depression factor of the CPE, α, accounts for the non-ideality of the capacitor. Once α=1, the system can be considered as an ideal capacitor. For the simulations, the value of α for the graphite was around 0.8 compared to 1 for an ideal capacitor. Figure III-8 shows the resulting EIS impedance spectra with CPE approximation for the graphite electrode compared to the experiment result using les parameters presented in Table III-1. As shown in Figure III-8a, the CPE model allows to fit very well the flattened part of the semicircle shape for the all the frequency domain from 10 mHz to 1000Hz. However, for very high frequencies, the model does not fit very well the experiment data. This disagreement is due to the presence of another physic controlling this domain in the case of a thick electrode, as the graphite one studied in this work. Therefore a TLM model will be introduced in the next section as an alternative to take into account the impact of the electronic and the ionic path through the solid phase and the electrolyte in the pores respectively [93] [22].

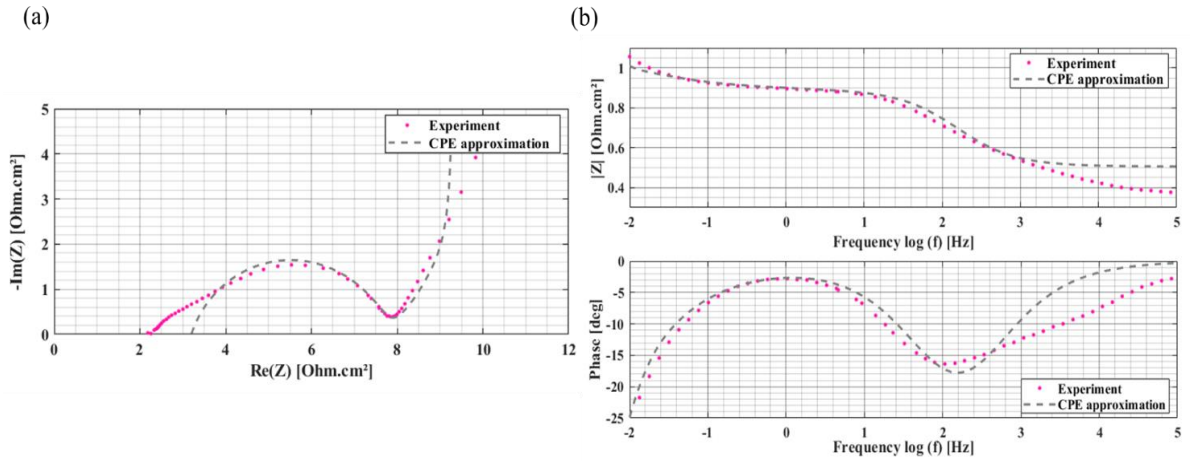

Figure III-8: *A comparison between experiment measurements and CPE approximation model result for the graphite electrode at full cell SOC=50%: (a) EIS spectra in Nyquist representation (b) EIS spectra in BODE representation, log10 scale for the magnitude plot and linear scale for the phase plot.*

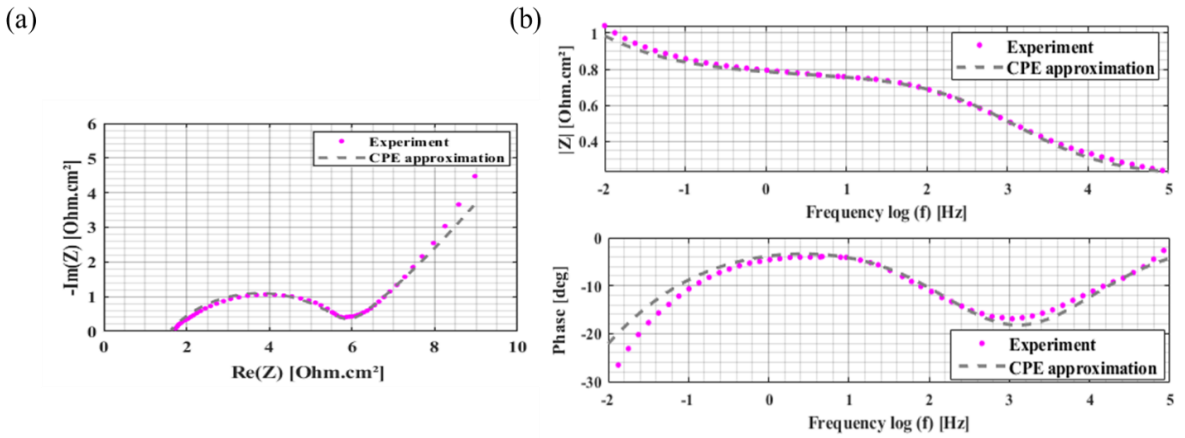

Figure III-9: *A comparison between experiment measurements and CPE approximation model result for the NMC622 electrode at full cell SOC=50%: (a) EIS spectra in Nyquist representation (b) EIS spectra in BODE representation, log10 scale for the magnitude plot and linear scale for the phase plot.*

For the positive electrode, the model with the CPE approximation is well adapted as can be seen Figure III-9 . A depression CPE factor of 0.6 has been used to fit the flattened semicircle shape. As presented in Figure III-9, CPE approximation fits very well the EIS spectra in the Nyquist plot and the Bode representation. Thus, for the NMC positive electrode, the single particle model with the CPE approximation allows to describe the different physics inside the electrode.

TLM approximation

TLM approximation is applied using the general definition presented in the first chapter of state of art as:

$$Z_{TLM} = \lambda\chi \coth\left(\frac{L}{\lambda}\right) \quad \text{(III. 55)}$$

Where the resistance per unit length, χ, related to the ionic path is defined as:

$$\chi = \frac{1}{\sigma_e} \quad \text{(III. 56)}$$

σ_e being the effective ionic conductivity of the electrolyte provided in Table III-1. This model takes into account the charge transfer at the interface between active materials and the

electrolyte, via the introduction of λ, the characteristic alternating current penetration depth in the electrode defined by:

$$\lambda = \sqrt{\frac{Z_{int,CPE} L}{\chi}} \quad \text{(III. 57)}$$

Where

$$Z_{int,CPE} = \frac{1}{\frac{1}{Z_{CPE}} + \frac{1}{Z_f}} \quad \text{(III. 58)}$$

The values of the electrode thickness L are provided in Table III-1 for the positive and negative electrodes, respectively. The impedance taking place at the interface, $Z_{int,CPE}$, corresponds to the analytic impedance developed in the previous section for a single particle electrode model with a CPE approximation (Eq. (III. (III. 54). Hence, the cell impedance considering a TLM approximation is:

$$Z_{cell,TLM} = R_{ohm} + Z_{TLM} \quad \text{(III. 59)}$$

The results obtained with this model are compared to the experimental ones (Figure III-10 Figure III-11) showing very a good agreement for both the graphite and the NMC622 electrodes. Therefore, the TLM approximation is a good alternative to account for the different physics, which are dominating in the electrode.

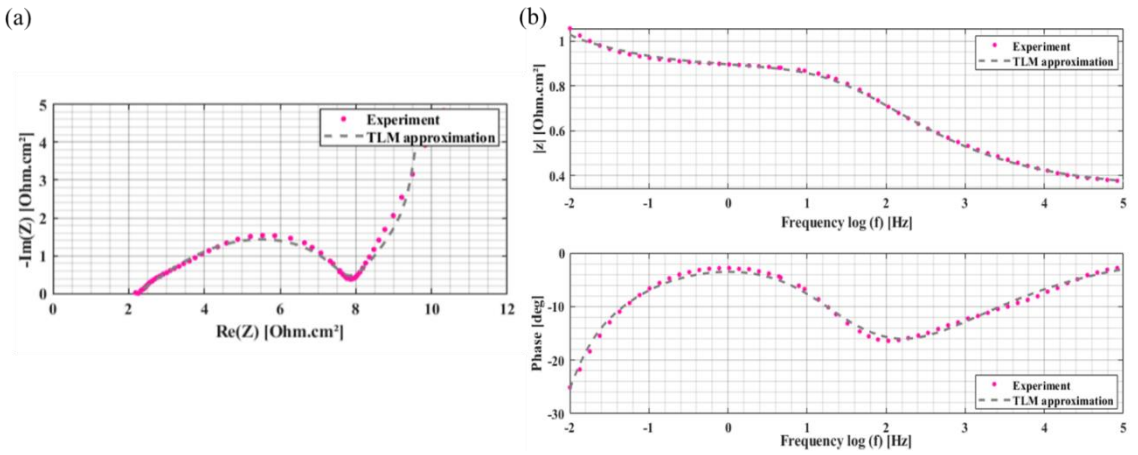

Figure III-10 : *A comparison between experiment measurements and TLM approximation model result for the graphite electrode at full cell SOC=50%: (a) EIS spectra in Nyquist representation (b) EIS spectra in BODE representation, log10 scale for the magnitude plot and linear scale for the phase plot.*

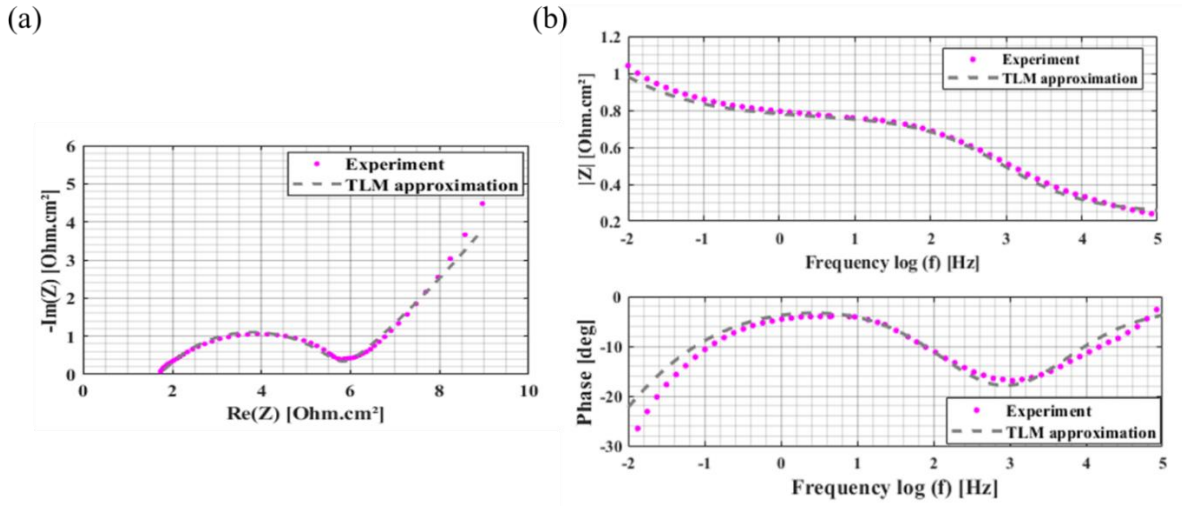

Figure III-11: *A comparison between experiment measurements and TLM approximation model result for the NMC622 electrode at full cell SOC=50%: (a) EIS spectra in Nyquist representation (b) EIS spectra in BODE representation, log10 scale for the magnitude plot and linear scale for the phase plot*

For the NMC622, the previous results have shown that a CPE approximation is sufficient to present the different physics controlling the chosen frequency domain. To have a better idea about the impact of the ionic resistance, we have calculated the ionic path (Eq.(III. 57)). To have real number $Z_{int,CPE}$ is replaced byR_{Ct}, assuming that this domain is controlled by charge transfer. For NMC622, λ is equal to 50E-6m, corresponding to 90% from entire thickness of the electrode. This result explain the fact that in Figure III-10 the slope of 45°is not significant.

In the other hand, for the graphite, λ is equal to 35e-6m, referring to 45% of the total thickness of the electrode. For that reason, as shown in Figure III-11, the slope of 45° is more significant and explain why, in the graphite, it is more difficult to penetrate through the total thickness.

For a very low frequency, regardless of the involved approximation, a non-perfect agreement between the experiment EIS spectra in the Nyquist and Bode representation is observed for both the graphite and the NMC 622 electrodes. This disagreement could be explained by neglecting the diffusion in the electrolyte for the current developed model.

In the following section, the TLM and the CPE corresponding approximating models are developed to find the corresponding temporal EEC of the electrodes. This corresponds to the second step of our up-scaling methodology as described Figure III-1.

III.3 Up scaling methodology: From the analytical impedance models to the temporal EEC models

In the previous section, analytic equivalent circuit models have been developed in the frequency domain. However, to have an online battery diagnostic, a temporal CEE model should be developed. In the following paragraphs, an up-scaling methodology is proposed to determine in a rigorous way a CEE in the temporal domain from the analytic impedance model.

III.3.1 Cell EEC temporal model

An equivalent electric circuit model in the temporal domain is composed of only resistance, capacitor and inductor elements. To get that, an analytic development of the Warburg expression is required. In the next section, this decomposition is detailed.

III.3.1.1 Development for the Warburg expression

The obtained analytic EEC model in the previous section (Figure III-5) has a Warburg impedance, which represents part of the complex dynamics of the battery. This latter term has an expression only in the frequency domain and should be approximated by a series of RC elements to be used in the temporal domain. To perform this approximation in a rigorous way, a mathematical development in series following by RC identification [31] have to be done. The mathematical development, of the Eq. (III. 51) is presented as following:

$$Z_W = \frac{P}{(s\coth(s) - 1)} \quad \text{(III. 60)}$$

Where $s = \sqrt{j\tilde{w}}$ and P:

$$P = \left[\frac{RT}{nFi_0}\left(\frac{1}{(1-\bar{y})} + \frac{1}{\bar{y}}\right) + \left(\frac{4RT}{nF} - \beta_1\right)\right]\frac{R_p}{nC_0D_sF} \quad \text{(III. 61)}$$

Therefore, the Warburg impedance is presented as rational fraction of two complex polynomials. A partial decomposition of Eq. (III. 60) based on Mittag-Leffler's theorem [31] [94] has been performed. This decomposition leads to present the Warburg function as series of simple elements. This final model structure is known in the literature as Foster structure [31] [95]. The simplified solution of the mathematical decomposition derives from solving $x_n = tan(x_n)$ and $x_n \cong (n + \frac{1}{2})\pi$ and gives:

$$Z_W = \frac{3P}{s^2} + \sum_{n=1}^{\infty} \frac{1}{\frac{s^2}{2P} + (n + \frac{1}{2})^2\pi^2\frac{1}{2P}} \quad \text{(III. 62)}$$

Foster structure, Eq. (III. 62) can be presented as function of series of admittances Y_n and impedance Z_n presenting by capacitor and resistance respectively as:

$$Z_W = Y_0 + \sum_{n=1}^{\infty} \frac{1}{Y_n + \frac{1}{Z_n}} \quad \text{(III. 63)}$$

Where,

$$Y_0 = C_0 s^2 \quad \text{(III. 64)}$$

$$Y_n = C_n s^2 \quad \text{(III. 65)}$$

And the impedance of each RC is given by:

$$Z_n = R_n \quad \text{(III. 66)}$$

Within this representation, the Warburg impedance can be presented as a capacitor connected to a series of RC elements. By identification, the first capacitor is a function of the factor P as:

$$C_0 = \frac{1}{3P} \tag{III. 67}$$

The different capacitors of the RC series are constant and does not depend of the number of RC implemented in the EEC model. It depends on the different physical parameters of the electrode contained in the factor P expression (Eq. (III. 61)):

$$C_n = \frac{1}{2P} \tag{III. 68}$$

However, the resistance of the EEC elements depends on the factor P and the number of elements n used to express the Warburg:

$$R_n = \frac{2P}{(n+\frac{1}{2})^2\pi^2} \tag{III. 69}$$

Thanks to this development, the corresponding EEC model in the temporal domain can be presented in the case of a single particle model with a CPE as displayed in Figure III-12.

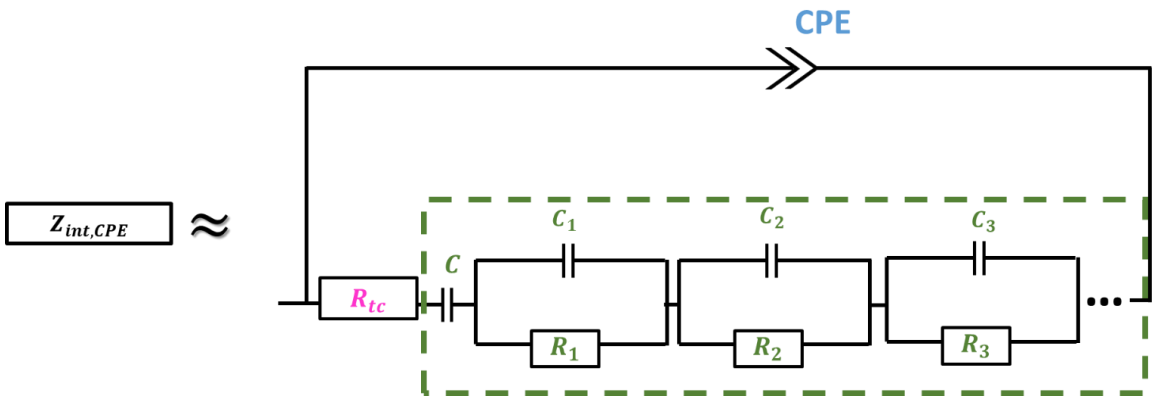

Figure III-12: *Representation of the EEC model for the interfacial impedance model corresponding to a single particle with a CPE approximation.*

III.3.1.2 **Development for the TLM expression**

As, we have mentioned before, for the graphite at the beginning of life, a TLM model is implemented to take in consideration the effect of the ionic resistance of the thick electrode. The general equation of the TLM impedance (Eq. (III. 55) can be expressed as:

$$Z_{TLM} = \frac{P}{x}\coth(x) \tag{III. 70}$$

Where $P = R_i$ representing the ionic resistance($R_i = \chi L$) and $x = \frac{L}{\lambda}$. Similar to the previous section, Mittag Leffer [31] [94] expansion has been applied to express the $\coth(x)$ as:

$$\coth(x) = \frac{1}{x} + \sum_{n=1}^{\infty} \frac{2x}{x^2 + n^2\pi^2} \tag{III. 71}$$

Therefore, the TLM impedance can be rewritten as:

$$Z_{TLM} \simeq Z_{int,CPE} + \sum_{n=1}^{\infty} \frac{1}{\frac{1}{2Z_{int,CPE}} + \frac{n^2\pi^2}{2R_i}} \tag{III. 72}$$

Following the Foster structure, Eq. (III. 72) can be represented as function of CPE impedance in series with series of parallel ionic resistance/CPE impedance. Therefore, the EEC corresponding model can be described by *Figure III-13*.

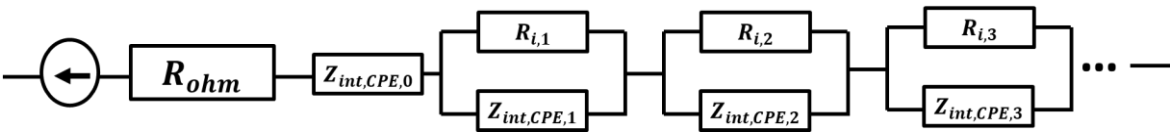

Figure III-13: *Representation of the EEC model for a single particle with a TLM approximation.*

In the next section, the EEC model impedance results obtained with these mathematical developments are computed with the same physical parameters of the positive and the negative electrodes as in the previous section (See Table III-1) to assess the validity of the approximation.

III.3.2 Results and discussions

Figure III-14 shows the comparison between the electric equivalent circuit model, the analytic model in the frequency domain and the EIS measurements. For the graphite, the simulated EEC model contains 9R-Z elements to account for the single particle model with the TLM approximation. The Warburg element contained in the Z element is developed with 3RC. A good agreement between the EEC model and the experimental measurements is obtained for the two representations of the impedance spectra: Nyquist and Bode. The TLM approximation allows performing a good fit of the high frequency slope related to the thick electrode. The charge transfer is correctly captured thanks to the use of the adopted CPE to express the flattened semicircle shape. However, at very low frequencies the model is not perfect due to the limited number of RC used to express the Warburg. The value of the different electric components of the Warburg part of the EEC model are presented in Table *III-2*.

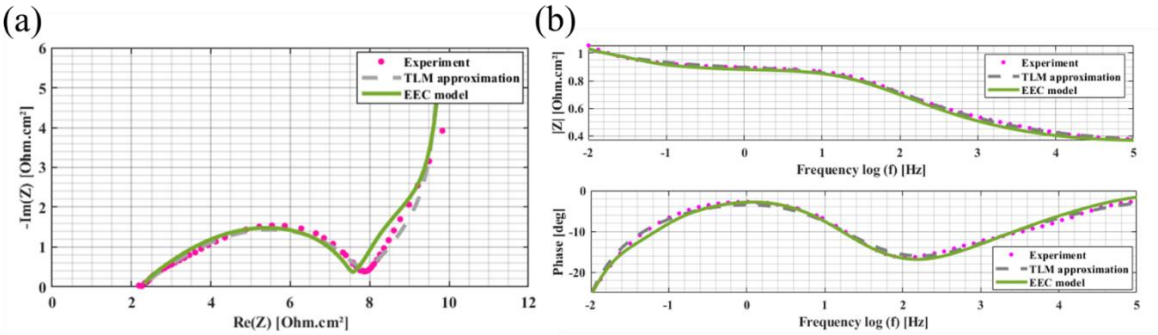

Figure III-14: *Comparison between experimental measurements and temporal EEC model developed from TLM approximation model result for the Graphite electrode at full cell SOC=50%: (a) EIS spectra in Nyquist representation (b) EIS spectra in BODE representation, log10 scale for the magnitude plot and linear scale for the phase plot.*

The same behavior is observed for the NMC electrode where 3RC elements are used to express the Warburg diffusion impedance. For the NMC electrode, the TLM model is not used. The developed EEC model is based on the single particle model with the CPE approximation. As shown in *Figure III-13*, a good agreement between the temporal model and the experiment EIS measurements especially in the high and middle domain frequencies. As for graphite, the value of the different electric components of the EEC model are presented in Table *III-2*.

The no perfect result at the very low frequency may be due to various hypotheses. In fact, this current model is to implement an up-scaling methodology developed to take in consideration the most important physics that can limit the response of the battery the temporal domain. From the first step, the diffusion in the electrolyte has been neglected. In the literature, this physic

can contribute from a frequency lower than 1Hz [96]. Besides, NMC622 active material suffers from a phase separation in the crystallographic structure due to the migration of the nickel particles leading to a two-frequency diffusion domain inside the AM. This hypothesis will be studied in the next chapter dedicated to the aging study. Therefore, in the beginning of life of a NMC 622 electrode, an EEC model with 3RC to express the Warburg can be good enough to explain the different physical mechanisms.

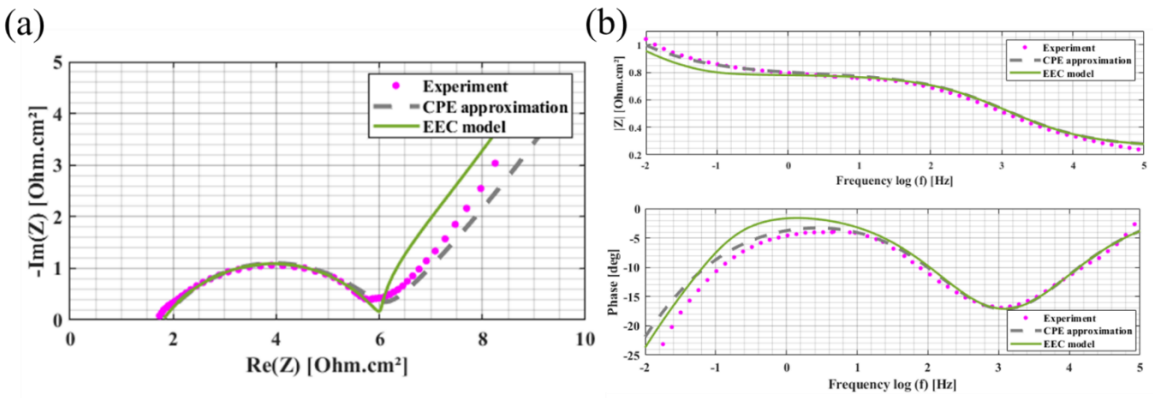

Figure III-15: *A comparison between experiment measurements and temporal EEC model developed from CPE approximation model result for NMC electrode at full cell SOC=50%: (a) EIS spectra in Nyquist representation (b) EIS spectra in BODE representation, log10 scale for the magnitude plot and linear scale for the phase plot.*

Table III-2: Resulting values for components used with Foster structure to represent the EEC model representing single particle model with CPR approximation

Parameter	Graphite	NMC622
P ($\Omega.cm^2$)	7.80E+00	2.90E+01
CPE ($F.cm^{-2}$)	5.80E-03	2.00E-03
$R_1(\Omega.cm^2)$	2.47E+00	4.22E+00
C ($F.cm^{-2}$)	3.48E+01	1.10E+01
$C_{i=1.2.3}(F.cm^{-2})$	5.22E+01	1.66E+01
$R_1(\Omega.cm^2)$	7.00E-01	2.64E+00
τ_1 (s)	3.66E+01	4.39E+01
$R_2(\Omega.cm^2)$	2.53E-01	9.50E-01
τ_2 (s)	1.31E+01	1.58E+01
$R_3(\Omega.cm^2)$	1.10E-01	4.80E-01
τ_3 (s)	5.74E+00	7.98E+00

To have a better fit of the low frequency domain corresponding to the Warburg diffusion inside the active material, a model enhancement is proposed. To achieve that, the impact of RC elements number is discussed. In fact, when the number of RC element increases the number of degrees of freedom rises too. Therefore, an RC model with 3RC, 5RC and 10 RC have been modeled and compared in *Figure III-16* with experimental result. The increase of RC element number from 3 to 10 leads to a finest fit of experimental spectra. The different RC element characteristic time, $\boldsymbol{\tau_i}$,is presented in Table III-3. For n higher than 3, the variation of this factor is not significant. Therefore, giving that, the impact of this enhancement is not so significant and the limit RC elements number to be implemented in a BMS, will be limited to 3RC elements.

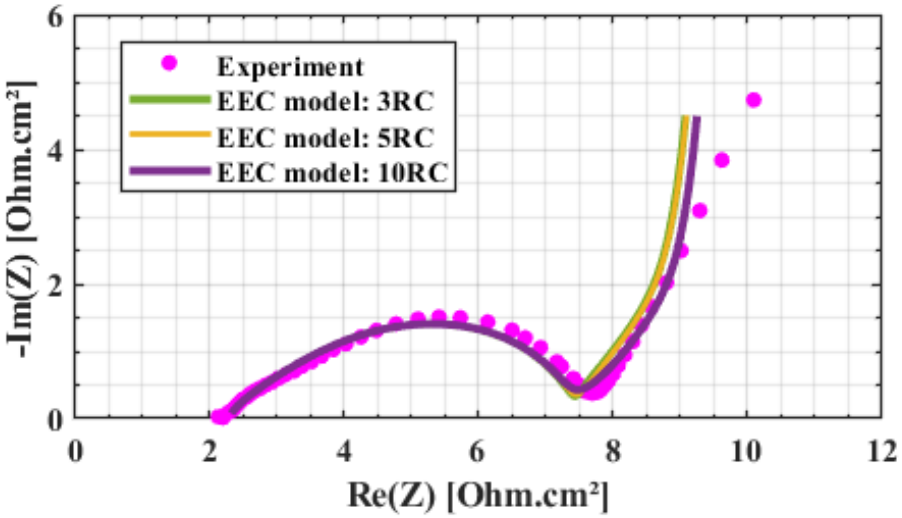

Figure III-16 : *A comparison between experimental result and EEC models with 3RC, 5RC and 10RC: Applied on graphite electrode at cell SOC =50%*

Table III-3 : value of components for EEC model applied on Graphite electrode

Parameter	Graphite
P ($\Omega.cm^2$)	7.80E+00
CPE ($F.cm^{-2}$)	5.80E-03
$R_1(\Omega.cm^2)$	2.47E+00
C ($F.cm^{-2}$)	3.48E+01
$C_{i=1,2...,10}(F.cm^{-2})$	5,22E+01
$R_1(\Omega.cm^2)$	7.00E-01
τ_1 (s)	3.66E+01
$R_2(\Omega.cm^2)$	2.53E-01
τ_2 (s)	1.31E+01
$R_3(\Omega.cm^2)$	1.10E-01
τ_3 (s)	5.74E+00
$R_4(\Omega.cm^2)$	4.00E-02
τ_4 (s)	3.66E+00
$R_5(\Omega.cm^2)$	5.00E-02
τ_5 (s)	2.61E+00
$R_6(\Omega.cm^2)$	3.00E-02
τ_6 (s)	1.57E+00
$R_7(\Omega.cm^2)$	2.00E-02
τ_7 (s)	1.04E+00
$R_8(\Omega.cm^2)$	2.00E-02
τ_8 (s)	1.04E+00
$R_9(\Omega.cm^2)$	1.70E-02
τ_9 (s)	8.90E-01
$R_{10}(\Omega.cm^2)$	1.40E-02
τ_{10} (s)	7.30E-01

III.4 Conclusion

In this chapter, an up-scaling methodology has been established and developed to determine an equivalent electric circuit model from on the physics at the electrode scale. This methodology has been developed in two steps. At first, the different physics at the electrode scale with the corresponding assumptions have been identified. From these physics, an electrode impedance model has been determined at the beginning of life of the cell using Fourier transformation. In this thesis, a battery based on graphite vs NMC622 system is considered. A model validation and enhancement have been performed for each electrode. This was accomplished through a comparison with the experimental EIS measurements presented in the chapter 2. A single particle model with a CPE approximation illustrates perfectly the limiting physics of the NMC622 electrode. However, for the studied graphite electrode, a single particle model with a TLM approximation is recommended to take into account the ionic resistance of the thick electrode. In the next chapter, the presence of the SEI at the graphite surface and the

diffusion within must be accounted during the electrode aging. In fact, experimental results highlight a semi-circle corresponding to SEI resistance evolving along with aging. The effect of the ionic path (considered with TLM) at a very high frequency domain is neglected and the CPE for the medium to the low frequency domain will be considered. The second step consists in simplifying the analytic impedance model in the frequency domain in order to obtain an EEC model in the temporal domain. This up-scaling step is performed rigorously using a mathematical development in series. From these results, we have shown that an EEC model with 3RC for the diffusion impedance was sufficient to describe the NMC 622 electrode. Similarly, for the graphite a 3RC element was employed to model the Warburg diffusion impedance. Moreover, 9R-Z, representing TLM impedance, is implemented to fit the impedance spectra of the graphite. Within this model, the physics of the two electrodes has been identified with the adequate EEC model. More importantly, the different electric element of the EEC in the temporal domain are expressed as function of the physics parameters at the electrode scale.

Chapter IV : Up scaling methodology for the End of Life

Table of content

In this chapter, the up-scaling methodology developed in the previous chapter is applied to the cells during their aging.

The up-scaling methodology developed in the scope of this chapter takes into consideration the aging phenomena at the positive and negative electrodes. The evolution of the different physical parameters implemented in the previous chapter *(e.i* Up-scaling methodology for the beginning of life) are also considered.

Similar to chapter 3, this methodology aims to bridge the gap between the physical and geometrical parameters from physics-based models at the electrode scale during aging, and the empirical parameters from equivalent electric circuit EEC models used for battery. The methodology is established in two stages. First, the physical equations are solved in the frequency domain to obtain the corresponding impedance model. Then, this impedance model is mathematically simplified in a series of R-C elements, using the mathematical structure of Foster. The obtained formulation is well adapted to real-time application since it involves only R-C type elements.

Since the aging phenomena differs from an active material to another and as we consider graphite active material for the negative electrode and NMC622 for the positive one, the approach was developed for these two types of AM. At the end an EEC model is proposed for the positive and the negative electrodes taking into account their aging.

IV.1 Physicochemical phenomena of battery degradation

Electrical modeling of batteries is essential for predicting their performance and operation. For this reason, it is important to develop an electric model taking in consideration the aging mechanisms in the different components of the battery. These phenomena have already been widely studied over the last period to develop batteries dedicated to stationary and automotive applications [97] [98] [99] [100]. Several articles studied and identified the different aging phenomena. Some of them are detailed in Figure IV-1 and can be classified as quantifiable and non-quantifiable. In the first category we can cite passivation layer on the negative and positive electrodes, lithium plating on the negative electrode, transition metal dissolution for the positive electrode, etc... For the non-quantifiable or difficult to be, we find the loss of electronic and

conductive path in the solid phase of the electrode or with the current collector, micro-cracking of the active material, etc [101].

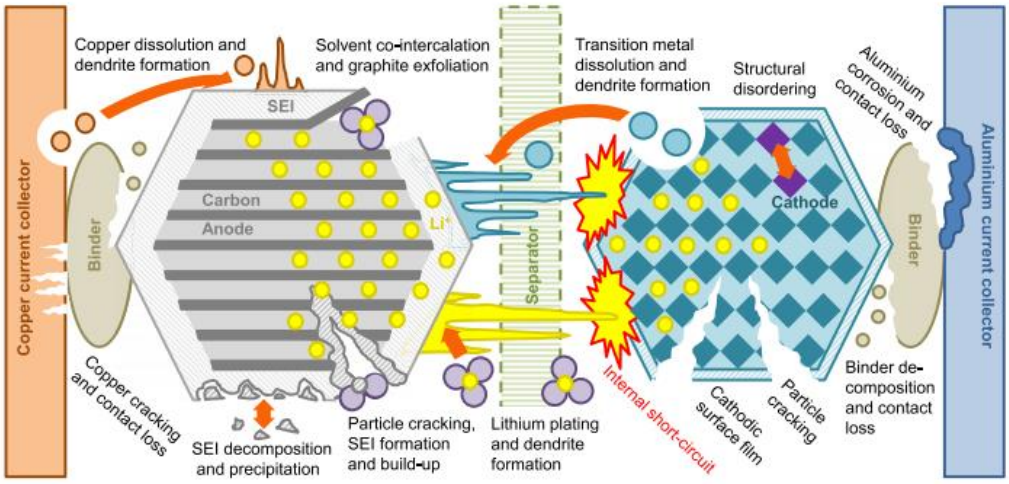

Figure IV-1 *: Degradation mechanisms in Li-ion cells (From Birkl et al.* [101]*).*

In the present work, aging mechanisms in the positive and negative electrodes will be taken into account. To that end, a literature research of the degradation phenomena in each electrode is detailed.

IV.1.1 Aging mechanism at the negative electrode

As we have already mentioned in the scope of this thesis, graphite active material has been chosen for the negative electrode. Lithium plating and non-stable passivation layer (SEI) are considered as aging factors in the graphite. In fact, during formation cycle, the passivation layer (SEI) should be stable to protect the graphite. When it is not stable, it can cause a mechanical aging factor due to the exfoliation of the graphite or a chemical one due to the isolation of the AM particles. In this paragraph the origin of the SEI and its aging factors *(i.e.* exfoliation with isolation) with the lithium metal plating will be detailed.

a) Solid Electrolyte Interphase Layer (SEI)

Origin of the SEI formation:

The SEI layer is formed at the negative electrode due to the electrolyte degradation which is not stable at the graphite operating potential [102]. This layer contains both organic and inorganic compounds. The organic part of the SEI is saturated with electrolyte. It is, thus, the transport medium of the lithium ions. The inorganic part represents the stable compounds which protects the SEI film by resisting to the electrolyte degradation. Indeed, it is seen as a selective sieve, only permeable to lithium ions [103]. SEI degradation becomes worse when the electrolyte contains ethylene carbonate (EC) due to its simple dissociation compared to other electrolyte components such as Dimethyl carbonate (DMC) or propylene carbonate (PC). In general, adding a polymer adjuvant to protect the SEI formed during the formation step is important. In fact, in the absence of this polymer, the SEI film components dissociate allowing continuous decomposition reactions of the electrolyte leading to further SEI film.

SEI growth and exfoliation of graphite

The cracks in the SEI layer present an important aging factor allowing the appearance of non-protected graphite surface zones. In fact, the electrolyte solvents having diffused within the SEI can also interact with the graphite and create the gas, which is the origin of these cracks [104]. On one hand, these non-covered graphite surfaces enhance the electrolyte reduction, reduce the quantity of cyclable lithium and participates to the SEI growth. On the other hand, the solvent at the surface of the particle can co-intercalate inside the particles, leading to a partial exfoliation of the graphite, forming cavities between the graphite sheets.

Particle isolation

Because of the reconstruction of the SEI film, the different particles can become disconnected and isolated [105]. In general, propylene carbonate (PC) reduction produces at the graphite interface a solid film with propylene gaz. With the aging, the pressure increases and the graphite particles crack. Therefore, new isolated particles surface are exposed to the electrolyte and become electrically disconnected from the AM because of the SEI film reconstructed. In general, this phenomenon can be experimentally deduced from cell resistance by the ohmic drop increase during cycling [106].

b) Lithium metal plating

Lithium metal plating consists of lithium metal deposition on the graphite electrode surface. It causes cyclable lithium loss and can be detected during a postmortem analysis via visual inspection. It corresponds to the presence of light color zones at the electrode surface. This phenomenon is particularly present when the battery is operated at low temperatures (due to the decrease of lithium conductivity with low temperature) or at high charging rates. It depends on the characteristics of the electrolyte and if it contains SEI stabilizer or not [107]. In general, SEI stabilizer, such as Vinylene carbonate (VC) [108] [109], Fluoroethylene carbonate (FEC) [108], Polysulfide [110]… limit the lithium plating. In fact, these additives lead to a more rigid SEI film and avoid channels formation in which lithium metal plating can be deposed. Deposed lithium metal tends to grow in the form of dendrites, which can cause a risk of a short circuit if the dendrites reach the positive electrode. The low potential of the lithium metal causes a reaction with the electrolyte which results in the formation of additional SEI and more cyclable lithium loss.

IV.1.2 Aging mechanism at the positive electrode

In general, positive electrode suffers from the dissolution of transition metals, phenomenon which has been identified to be the subject of the loss of the active materials. This dissolution is a well-known aging mechanism in the LMO positive electrode with spinel structure, and results in a loss of sites for Li-ions storage. Studies have been conducted to study the effects of this transition metal's dissolution in the electrolyte and the SEI contamination. This phenomenon leads to increase the cyclable lithium loss by enhancing SEI growth [111], due to the catalytic activity of transition metals such as the manganese when it reaches the negative electrode. In addition to manganese, using non-pure iron in LFP active materials, which has an olivine structure, may increase the SEI growth after the dissolution of the contained impurities [112]. To avoid this problem of metal dissolution, using active materials with lamellar arrangement like NMC type is suggested. However, it has been reported recently that they can also suffer from dissolution but not as much as the spinel electrode types. In this latter case, the dissolution of the active material causes two aging effects for the positive electrode: a modification of the active material structure at its surface called Surface Reconstruction Layer (SRL) and the formation of a passivation layer at the AM surface.

a. SRL

The reconstruction layer is a thin region that appears at the surface of the active material of a positive electrode because of the metal transition instability. This phenomenon is increased in Ni-rich electrodes. It is due to the low energy barrier for Ni migration. The Ni atoms will tend to occupy the vacant sites of the lithium at the interface. Thus, new surfaces impermeable to lithium are constructed with some open diffusion channels in between [113].

b. Passivation layer formation

The passivation layer in the positive electrode is formed after electrolyte oxidation at a higher potential [97]. Similar to the SEI in the graphite, this film is permeable to lithium ions but impermeable to electrons and electrolyte components. This layer is important because it protects the electrolyte from further degradation under specific conditions and limits the metal dissolution [114]. For the LFP electrodes without transition metals, Kim *et all* [115] show that the interfacial resistance increases during cycling to form LiF film. This passivation layer is the product of the LFP active material reacted with HydroFluoric acid (HF) contained in the electrolyte salt ($LiPF_6$).

IV.2 Up-scaling methodology for aging: From the physics to the analytical impedance models

In this part, the up-scaling methodology developed in the chapter III is adapted to take into account some of the aging phenomena presented above. From this point of view, the equivalent circuit model is built considering the SEI formed at the negative electrode and the SRL for the positive one. Besides the different assumptions employed in the frequency domain to simplify the obtained results.

IV.2.1 Graphite electrode

IV.2.1.1 **Model configuration for aging**

In a LIB, a graphite electrode can be presented *via* three important domains: the active material, the SEI film and the electrolyte domain (Figure IV-2).

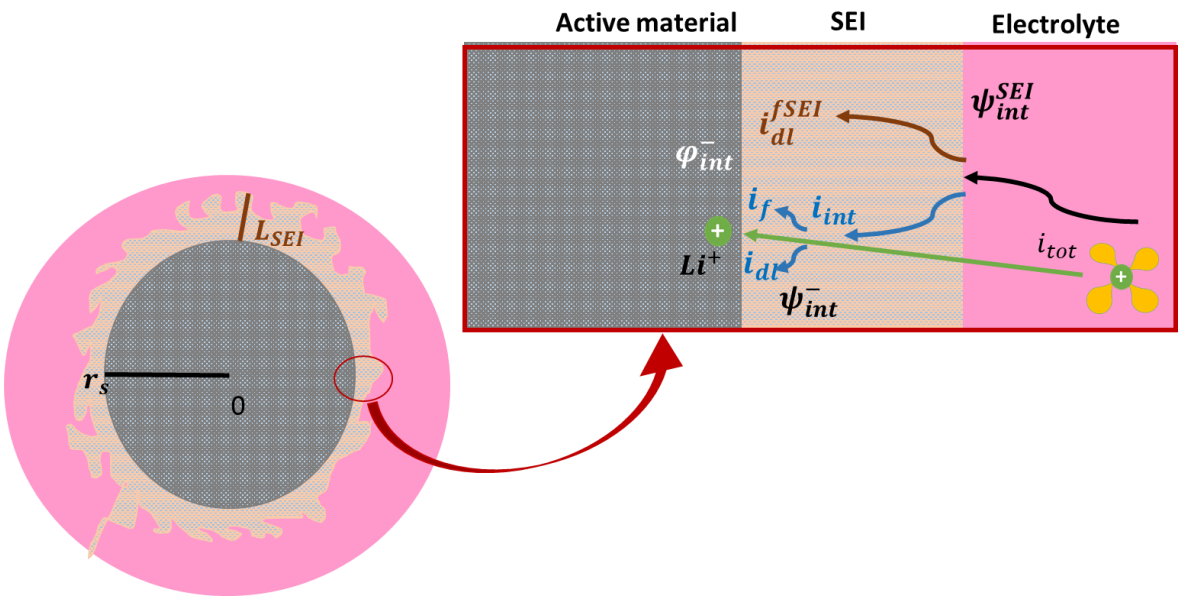

Figure IV-2*: Transfer phenomena at the surface of a graphite particle at the negative electrode.*

The different transfer phenomena in the AM and electrolyte domains have been detailed and discussed in the chapter 3. The SEI domain is added to take in consideration the aging effect in the graphite electrode *due to* the SEI layer growth. This SEI layer is supposed to conduct only the ion and not the electron. Therefore, only the ionic potential is defined in this domain. The negative electrode potential is then decomposed as follows:

$$U_{half\ cell} = (\varphi_{cc}^{-} - \varphi_{int}^{-}) + (\varphi_{int}^{-} - \psi_{int}^{-}) + (\psi_{int}^{-} - \psi_{int}^{SEI}) + (\psi_{int}^{SEI} - \psi_{int}^{sep}) \qquad \text{(IV. 1)}$$

Where:

φ_{cc}^{-}: Electric potential at the current collector.

φ_{int}^{-}: Electronic potential of the negative electrode at the active material surface.

ψ_{int}^{-}: Ionic potential of the negative electrode at the active material /SEI interface

ψ_{int}^{SEI}: Ionic potential of the SEI layer at the SEI/electrolyte interface.

ψ_{int}^{sep}: Ionic potential of the electrolyte in the separator far away from the SEI surface.

$(\varphi_{cc}^{-} - \varphi_{int}^{-})$ and $(\varphi_{int}^{-} - \psi_{int}^{-})$ have been defined in the previous chapter and can be expressed as follows:

$$\varphi_{cc}^{-} - \varphi_{int}^{-} = R_{ohm,electronic}^{-} i_{tot} \quad (\text{IV. 2})$$

$$\varphi_{int}^{-} - \psi_{int}^{-} = \eta_n + E_{eq}^{n} \quad (\text{IV. 3})$$

$R_{ohm,electronic}^{-}$ being the ohmic resistances resulting from the electron transport and the second equation being related to the lithium insertion inside the active material

The ionic potential difference inside the SEI between the graphite active material surface and the SEI/electrolyte interface is related to the ionic SEI resistance, R_{SEI}, as following:

$$\psi_{int}^{-} - \psi_{int}^{SEI} = R_{SEI} i_{int} \quad (\text{IV. 4})$$

Where i_{int}, the total interfacial current passing through the cell, is defined as the sum of the capacitive and the faradic ones (Figure IV-2):

$$i_{int} = i_{dl} + i_f \quad (\text{IV. 5})$$

And for the ionic potential difference in the electrolyte between the SEI/electrolyte interface and the separator, we have:

$$\psi_{int}^{SEI} - \psi_{int}^{sep} = R_{ohm,ionic}^{-} i_{tot} \quad (\text{IV. 6})$$

Where, $R_{ohm,ionic}^{-}$ is the ohmic resistance resulting from the ionic transport.

Thus, considering the previous definitions, the negative electrode potential can be presented as:

$$U_{Gr} = E_{eq}^{n} + \eta_n + R_{SEI} i_{int} + R_{ohm} i_{tot} \quad (\text{IV. 7})$$

Where i_{tot} presents the total current passing through the whole negative electrode. It can be divided on two paths as detailed on Figure IV-2.

$$i_{tot} = i_{int} + i_{dl}^{fSEI} \quad (\text{IV. 8})$$

The first current density (on the right side of the equation) corresponds to the interfacial current presented in the previous chapter i_{int}. This latter is the sum of the double layer current i_{dl} and the faradaic one, i_f, at the surface of the active material while the second one represents the double layer current density due to the SEI film presence, i_{dl}^{fSEI}.

I.4.1.1 Graphite electrode impedance for aging

To estimate the graphite electrode impedance during aging, the same approach as the one presented in the chapter 3 is adopted. Considering the Fourrier-transformed variables [87] [88] [84] with the steady state solution, the graphite electrode impedance can be defined as follows:

$$Z = \frac{d\Delta\widetilde{U}_{OCV} + d\Delta\tilde{\eta} + R_{SEI} d\Delta\tilde{\imath}_{int}}{d\Delta\tilde{\imath}_{tot}} + R_{ohm} \quad (\text{IV. 9})$$

In the following, the interfacial impedances of the electrode presented in the equation (IV. 29) related to the over potential and the equilibrium potential will be detailed.

IV.2.1.2 **Local interface impedance**

As shown in equation (IV. 8), the total current, i_{tot}, between the electrolyte and the active material can be expressed as the sum of the interfacial current (presented in the chapter 3), i_{int}. and the double layer current density due to the SEI film presence, i_{dl}^{fSEI}. The capacitive SEI film current is resulting from the separation of charge across the dielectric of the SEI film. It can be modeled as [29]:

$$i_{dl}^{fSEI} = C_{dl}^{fSEI} \frac{\partial(\varphi_{int}^{-} - \psi_{int}^{SEI})}{\partial t} \quad \text{(IV. 10)}$$

Therefore, considering the Fourrier-transformed variables and the different potential definitions, $\tilde{\imath}_{dl}^{fSEI}$ can be defined as:

$$\tilde{\imath}_{dl}^{fSEI} = j\omega C_{dl}^{fSEI}(\Delta\tilde{\eta} + \Delta\tilde{U}_{OCV} + R_{SEI}\Delta\tilde{\imath}_{int}) \quad \text{(IV. 11)}$$

Thus, using the previous equation and Eq. (IV. 8), the graphite electrode impedance (Eq.(IV. 9)) can be expressed as:

$$Z = \frac{1}{j\omega C_{dl}^{fSEI} + \frac{1}{R_{SEI} + \frac{d\Delta\tilde{U}_{OCV} + d\Delta\tilde{\eta}}{d\Delta\tilde{\imath}_{int}}}} + R_{ohm} \quad \text{(IV. 12)}$$

Where $\frac{d\Delta\tilde{U}_{OCV}+d\Delta\tilde{\eta}}{d\Delta\tilde{\imath}_{int}}$ represents the interfacial impedance detailed in the scope of the BOL chapter. The expression, Eq.(IV. 12), is similar to the one presented by Sikha and White [29]. Assuming that the concentration of lithium ions in the SEI film, $\tilde{C}_l$, depends on $\Delta\tilde{\imath}_{int}$, and neglecting the quantity consumed by the SEI formation, the partial derivative can be expressed as follows:

$$\frac{d\Delta\tilde{U}_{OCV} + d\Delta\tilde{\eta}}{d\Delta\tilde{\imath}_{int}} = \left.\frac{\partial\Delta\tilde{U}_{OCV} + \partial\Delta\tilde{\eta}}{\partial\Delta\tilde{\imath}_{int}}\right|_{\tilde{C}_l} + \left.\frac{\partial\Delta\tilde{U}_{OCV} + \partial\Delta\tilde{\eta}}{\partial\Delta\tilde{C}_l}\right|_{\tilde{\imath}_{int}} \frac{d\Delta\tilde{C}_l}{d\Delta\tilde{\imath}_{int}} \quad \text{(IV. 13)}$$

Considering the result of the partial derivate of $\Delta\tilde{U}_{OCV}$ and $\Delta\tilde{\eta}$ with respect to the faradaic current and the capacitive one detailed in the previous chapter and applied to the first term, Eq. (IV. 13) can be simplified as follows:

$$\frac{d\Delta\widetilde{U}_{OCV}+d\Delta\tilde{\eta}}{d\Delta\tilde{\imath}_{int}}=\frac{1}{j\tilde{\omega}C_{dl}+\frac{1}{Z_f}}+\underbrace{\frac{\partial\Delta\widetilde{U}_{OCV}+\partial\Delta\tilde{\eta}}{\partial\Delta\tilde{C}_l}\Big|_{\tilde{\imath}_{int}}\frac{d\Delta\tilde{C}_l}{d\Delta\tilde{\imath}_{int}}}_{Z_W^{SEI}} \quad \text{(IV. 14)}$$

Where Z_W^{SEI} represents the diffusion impedance of the lithium ions through the SEI film. To get the general form of this diffusion impedance, the lithium ion concentration should be determined by studying the diffusion of the lithium ion through the SEI film (see next section). Therefore, considering Eq. (IV. 14), the graphite electrode impedance given by Eq. (IV. 9) can be presented as:

$$Z=\frac{1}{j\omega C_{dl}^{fSEI}+\frac{1}{R_{SEI}+Z_W^{SEI}+\frac{1}{j\tilde{\omega}C_{dl}+\frac{1}{Z_f}}}}+R_{ohm} \quad \text{(IV.15)}$$

At beginning of life, the SEI film thickness is very small and can be neglected. Hence, all the terms presented in the previous expression and related to the SEI film can be simplified. This simplification leads to the same impedance expression as the one presented in the BOL chapter (Eq. (III.52)).

IV.2.1.3 **Diffusion impedance through the SEI for the negative electrode**

The diffusion impedance through the SEI film is determined by considering a diffusion within a planar geometry of thickness L_{SEI} representing the SEI film. Indeed, $\frac{L_{SEI}}{r_s}$ ratio of SEI film thickness and particle radius is very small, around 1,5E-03. Furthermore, the lithium flux density at the electrolyte/SEI interface is equals to the one at the AM/SEI one. Using the general Fick law for the concentration perturbation in a planar geometry, the Li^+concentration can be expressed as:

$$j\omega_{SEI}\Delta\tilde{c}_l=D_{l_{SEI}}\frac{d^2\Delta\tilde{c}_l(x,t)}{dx^2} \quad \text{(IV. 16)}$$

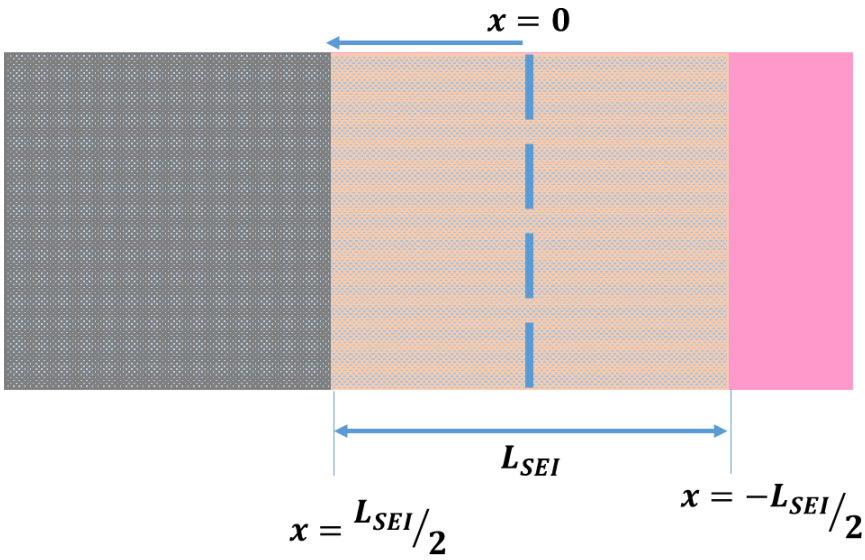

Figure IV-3*: Schematic presentation of the diffusion boundary notations within the SEI film.*

Following the boundary notations presented in Figure IV-3, the boundary conditions of the diffusion within the SEI film are:

$$\left.\frac{d\widetilde{\Delta c}_l}{dx}\right|_{x=\frac{L_{SEI}}{2}} = -\frac{\Delta\tilde{\imath}_{int}}{D_{l_{SEI}}F} \qquad (IV.\ 17)$$

$$\left.\frac{d\widetilde{\Delta c}_l}{dx}\right|_{x=-\frac{L_{SEI}}{2}} = \frac{\Delta\tilde{\imath}_{int}}{D_{l_{SEI}}F} \qquad (IV.\ 18)$$

These boundary conditions result from the lithium molar flux density associated to the diffusion through the planar film, assuming no consumption and using an argument of symmetry. The differential equation is solved and allows to express the Li^+concentration perturbation at the surface of the active material particle surface as function of the interfacial current:

$$\Delta\tilde{c}_l\left(x=\frac{L_{SEI}}{2}\right) = \frac{\Delta\tilde{\imath}_{int}\,L_{SEI}}{2FC_lD_{l_{SEI}}\sqrt{j\widetilde{\omega}_{SEI}}}\,tanh\left(\sqrt{j\widetilde{\omega}_{SEI}}\right) \qquad (IV.\ 19)$$

Where $\tilde{\omega}_{SEI} = \omega \frac{{L_{SEI}}^2}{4D_{Li,SEI}}$ is the reduced pulsation associated to the SEI and ω the pulsation.

Therefore, Z_W^{SEI} impedance, defined in Eq. (IV. 14), can be rewritten considering the equation (IV. 19):

$$Z_W^{SEI} = A \frac{L_{SEI}/2}{F C_l D_{l_{SEI}} \sqrt{j\tilde{\omega}_{SEI}}} tanh(\sqrt{j\tilde{\omega}_{SEI}}) \qquad \text{(IV. 20)}$$

Where $A = \frac{\partial \Delta \tilde{U}_{OCV} + \partial \Delta \tilde{\eta}}{\partial \Delta \tilde{C}_l}\Big|_{\tilde{\imath}_{int}}$ represents an empirical parameter fitted from experimental results. It corresponds the Warburg factor presented in the previous chapter.

IV.2.2 NMC 622 electrode

I.4.1.2 Model configuration for aging

As we have mentioned in chapter II, for the NMC622 active material studied in the scope of this thesis, the degradation phenomenon seems to be limited to the presence of a surface reconstruction layer (SRL) inside the active material at the AM/electrolyte interface.

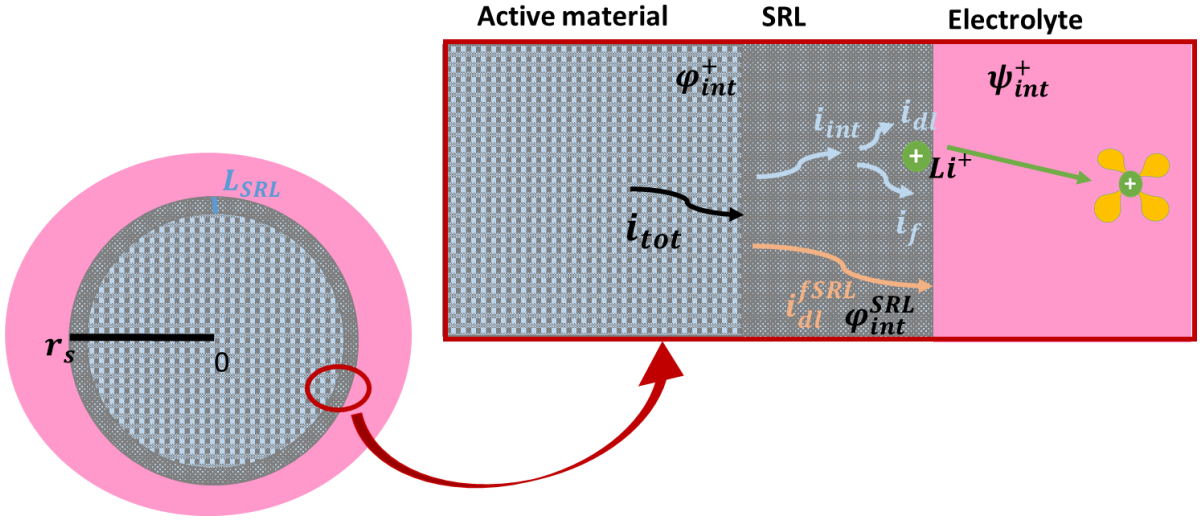

Figure IV-4 *: Transfer phenomena at the surface of a NMC622 active material at the positive electrode.*

Thus, we have chosen to model the positive electrode *via* three domains (Figure IV-4). The first domain is for AM, the second one contains the SRL film inside the AM and the third one is associated to the electrolyte. The different transfer phenomena in the AM and electrolyte domains are detailed and discussed in the BOL chapter. The SRL domain is added to take in consideration the aging effects in the NMC622 electrode *via* the presence of this layer at the surface of the active particles. It is worth mentioning that this layer is an electronic conductor. To determine the impedance model, the electrode potential is divided as follows:

$$U_{half\ cell} = (\varphi_{cc}^{+} - \varphi_{int}^{+}) + \left(\varphi_{int}^{+} - \varphi_{int}^{SRL}\right) + \left(\varphi_{int}^{SRL} - \psi_{int}^{+}\right) + (\psi_{int}^{+} - \psi_{int}^{sep}) \qquad (\text{IV. 21})$$

Where:

φ_{cc}^{+}: Electric potential of the current collector.

φ_{int}^{+}: Electronic potential of the positive electrode at the active material/SRL interface.

ψ_{int}^{+}: Ionic potential of the positive electrode at the active material SRL/electrolyte interface .

φ_{int}^{SRL}: Electronic potential of the SRL layer at the SRL/electrolyte interface

ψ_{int}^{sep}: Ionic potential of the electrolyte in the separator away from the SRL surface.

Note that $(\varphi_{cc}^{+} - \varphi_{int}^{+})$ and $\left(\psi_{int}^{+} - \psi_{int}^{sep}\right)$ are defined in the previous chapter and can be expressed as following:

$$\varphi_{cc}^{+} - \varphi_{int}^{+} = R_{ohm,electronic}^{+} i_{tot} \qquad (\text{IV. 22})$$

$$\psi_{int}^{+} - \psi_{int}^{sep} = R_{ohm,ionic}^{+} i_{tot} \qquad (\text{IV. 23})$$

$R_{ohm,electronic}^{+}$ and $R_{ohm,ionic}^{+}$, are the ohmic resistances resulting from the electrons and ions transports.

The electronic potential difference between the NMC active material and the SRL layer is related to the SRL electronic resistance, R_{SRL}, as follows:

$$\varphi_{int}^{+} - \varphi_{int}^{SRL} = \ R_{SRL} i_{int} \quad \text{(IV. 24)}$$

i_{int} being the total interfacial current passing through the cell. It is defined as the sum of the capacitive and the faradic one (Figure IV-4):

$$i_{int} = i_{dl} + i_f \quad \text{(IV. 25)}$$

The electrochemical reaction occurs at the SRL/electrolyte interface. Thus $\left(\varphi_{int}^{SRL} - \psi_{int}^{+}\right)$ takes the following form as defined in the previous chapter:

$$\varphi_{int}^{SRL} - \psi_{int}^{+} = \eta_P + E_{eq}^{P} \quad \text{(IV. 26)}$$

Thus, considering the previous definitions, the positive electrode potential can be presented as:

$$U_{NMC} = E_{eq}^{p} + \ \eta_p + \ R_{SRL} i_{int} + R_{ohm} i_{tot} \quad \text{(IV. 27)}$$

Where i_{tot} is divided on two paths as detailed on Figure IV-4:

$$i_{tot} = i_{int} + i_{dl}^{fSRL} \quad \text{(IV. 28)}$$

The first current density corresponds to the interfacial current presented in the previous chapter, i_{int} similar to the graphite while the second one represents the double layer current density due to the SRL film presence, i_{dl}^{fSRL}.

IV.2.2.1 **NMC622 electrode impedance for aging**

Similar to the graphite electrode, the approach presented in the previous section is applied to the NMC622 electrode. Therefore, considering Fourrier-transformed [88] [87] [84] variables with the steady state solution, the NMC electrode impedance can be defined as follows:

$$Z = \frac{d\Delta\widetilde{U}_{OCV} + d\Delta\tilde{\eta} + R_{SRL} d\Delta\tilde{\imath}_{int}}{d\Delta\tilde{\imath}_{tot}} + R_{ohm} \quad (\text{IV. 29})$$

In the following section, the interfacial impedance of the NMC degraded electrode will be detailed.

IV.2.2.2 **Local interface impedance**

In the NMC electrode, the total current, i_{tot}, between the electrolyte and the active material can be expressed as function of two currents paths. The first current path corresponds to the interfacial current, i_{int}. The second one represents the double layer current density due to the SRL film presence, i_{dl}^{fSRL}. This current is related to the separation of charge across the dielectric of the SRL of capacity C_{dl}^{fSRL}. It can be expressed as follows:

$$i_{dl}^{fSRL} = C_{dl}^{fSRL} \frac{\partial(\varphi_{int}^{+} - \psi_{int}^{+})}{\partial t} \quad (\text{IV. 30})$$

Considering the Fourrier-transformed variables, $\tilde{\imath}_{dl}^{fSRL}$ can be defined as:

$$\tilde{\imath}_{dl}^{fSRL} = j\omega C_{dl}^{fSRL}(\Delta\tilde{\eta} + \Delta\widetilde{U}_{OCV} + R_{SRL}\Delta\tilde{\imath}_{int}) \quad (\text{IV. 31})$$

Thus, using the previous equation, the positive electrode impedance (Eq.(IV. 29)) can be expressed as:

$$Z = \frac{1}{j\omega C_{dl}^{fSRL} + \frac{1}{R_{SRL} + \frac{d\Delta\widetilde{U}_{OCV} + d\Delta\tilde{\eta}}{d\Delta\tilde{\imath}_{int}}}} + R_{ohm} \quad \text{(IV. 32)}$$

Where $\frac{d\Delta\widetilde{U}_{OCV}+d\Delta\tilde{\eta}}{d\Delta\tilde{\imath}_{int}}$ represents the interfacial impedance detailed in the chapter III.

Pursuing the same approach applied in the graphite case (IV.2.1.2), the NMC electrode impedance becomes:

$$Z = \frac{1}{j\omega C_{dl}^{fSRL} + \frac{1}{R_{SRL} + Z_W^{SRL} + \frac{1}{j\tilde{\omega}C_{dl} + \frac{1}{Z_f}}}} + R_{ohm} \quad \text{(IV. 33)}$$

Where

$$Z_W^{SRL} = \left.\frac{\partial\Delta\widetilde{U}_{OCV} + \partial\Delta\tilde{\eta}}{\partial\Delta\tilde{C}_s}\right|_{\tilde{\imath}_{int}} \frac{d\Delta\tilde{C}_s}{d\Delta\tilde{\imath}_{int}} \quad \text{(IV. 34)}$$

It represents the diffusion impedance of the lithium within the SRL film. To get the general form of this impedance, the lithium concentration should be deduced by modelling the diffusion through the SRL film.

IV.2.2.3 **Diffusion impedance through the SRL for the positive electrode**

To calculate the diffusion impedance through the SRL, we follow the same steps as those used to determine Z_W^{SEI} in the graphite case. Since the SRL film is smaller than the NMC radius ($\frac{L_{SRL}}{r_s} \simeq$1E-05), the diffusion can be molded considering a planar geometry. Assuming a Fick diffusion with a constant concentration of the lithium in all the SRL film, Z_W^{SRL} can be defined as:

$$Z_W^{SRL} = A\frac{L_{SRL}}{2FC_sD_{S_{SRL}}\sqrt{j\widetilde{\omega}_{SRL}}}tanh(\sqrt{j\widetilde{\omega}_{SRL}}) \quad (\text{IV. 35})$$

Where $A = \frac{\partial\Delta\tilde{U}_{OCV}+\partial\Delta\tilde{\eta}}{\partial\Delta\tilde{C}_s}\Big|_{\tilde{i}_{int}}$ represents an empirical parameter fitted by the experimental results.

IV.2.3 Cell impedance: Results and discussion

In the previous sections, the different contribution of an impedance model of aged electrodes have been determined from a physics-based description. To summarize, the assumptions taken into consideration for the positive and the negative electrodes are:

- For the negative particles, the hypothesis considered in the chapter III are employed: the active material has a spherical geometry, the Fick law for diffusion inside the active material has been considered, the diffusion in the electrolyte is neglected, a kinetic reaction of insertion and de-insertion is considered at the active material surface. As we have mentioned in the previous chapter, CPE approximation will be considered for the non-ideal behavior of the double layer capacity. The effect of the ionic path through the electrode thickness described with the TLM will be neglected. Indeed, regarding the EIS performed at different cycling times, we have decided to take into account the contribution of the SEI layer in the high frequency domain. Therefore, in the present aging model, we have added the presence of a non-negligible SEI layer at the graphite interface, through which the lithium ion will diffuse, and which has a dielectric behavior leading to separation of charge.
- For the positive electrode, similarly to the negative electrode, the assumptions used in the chapter 3 have been considered with a CPE approximation. In addition to that, for the aging study, the presence of the SRL film inside the active material at the interface of the NMC was considered. As the different EIS spectra in the high frequency domain do not show any additional semicircle contribution (see chapter II), the passivation layer will be neglected.

In the following sections the impedance models for the graphite (Eq.(IV.15)) and the NMC (Eq.(IV. 33) will be compared to the aging experimental results presented in chapter 2. The

different physical parameters of both aged electrode models are identified by fitting the experimental Nyquist and Bode diagrams. In addition to that, the evolution of the characteristic times and frequencies of both electrodes during their entire life is calculated.

IV.2.3.1 **Negative electrode**

For the graphite, the electrical representation of the Eq. (IV.15) is presented in *Figure IV-5*. The physical phenomena related to the SEI occur in a frequency domain usually higher than the other phenomena and can therefore be separated mathematically in the impedance model from the other physics inside the electrode, using the following approximated expression:

$$Z_{Gr,CPE} = R_{ohm} + \frac{1}{j\omega C_{dl}^{fSEI} + \frac{1}{R_{SEI} + Z_W^{SEI}}} + \frac{1}{\frac{1}{Z_{c,CPE}} + \frac{1}{Z_f}} \qquad \text{(IV. 36)}$$

This mathematical simplification leads to a modified EEC model which is presented schematically in the right part of the *Figure IV-5*.

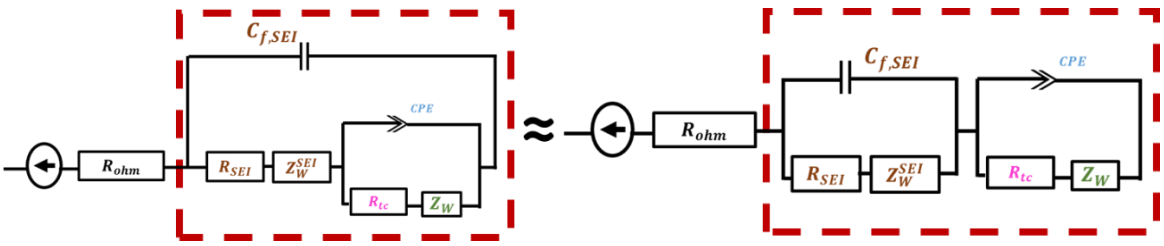

Figure IV-5: *Schematic EEC representation for the impedance of the negative aged electrode. Left: Full expression, Right: Approximated expression.*

In the right of the *Figure IV-5*, the first block corresponds to the aging phenomena and more specifically to the SEI formed at the surface of the graphite while the second one corresponds to the interfacial impedance developed in the previous chapter. This lattter block has been developed assuming a single particle model with the CPE approximation.

In order to check the relevancy of the proposed EEC structure in the frequency domain, a comparison with the experimental measurements is proposed in Figure IV-6 and *Figure IV-7*for the cells aged at 25°C and 45°C respectively. The comparison is performed at beginning of life, mid cycling (200 or 250 cycles) and at the end of life (600 cycles) for a SOC of 100%.

Note that the different EIS measurements had been performed at 25°C. The simulated impedance spectra presented in these figures have been obtained using the Eq.(IV. 36) and the parameters of the graphite summed-up in for the two temperature (25°C and 45°C). The different parameters related to the graphite active material presented in this table are identified via fitting the experimental impedance spectra in the mid to low frequency domains or using parameters measured via the specific experiments detailed in chapter II. Bode plots are used to limit the degree of freedom of the fitted parameters and the number of solutions of the different fitted parameters. A similar approach has been adopted to identify the SEI physical parameters presented in *Table IV-2*. For the SEI, all the presented parameters are fitted. For the graphite active material, radius of particles, electrode thickness, electrode area and the exchange current are fixed during the cell lifetime.

The two figures show a very good agreement between the experimental data and the model for both the Nyquist and the Bode representations. Therefore, for the graphite, a single particle model with a CPE approximation is a good alternative to fit and to present the predominant physics from the middle to the extremely low frequency domain. For the high frequency domain, considering an SEI layer, including lithium diffusion through it , is enough to fit this zone. In addition to that, these results confirm that the presence of the SEI controls this frequency domain.

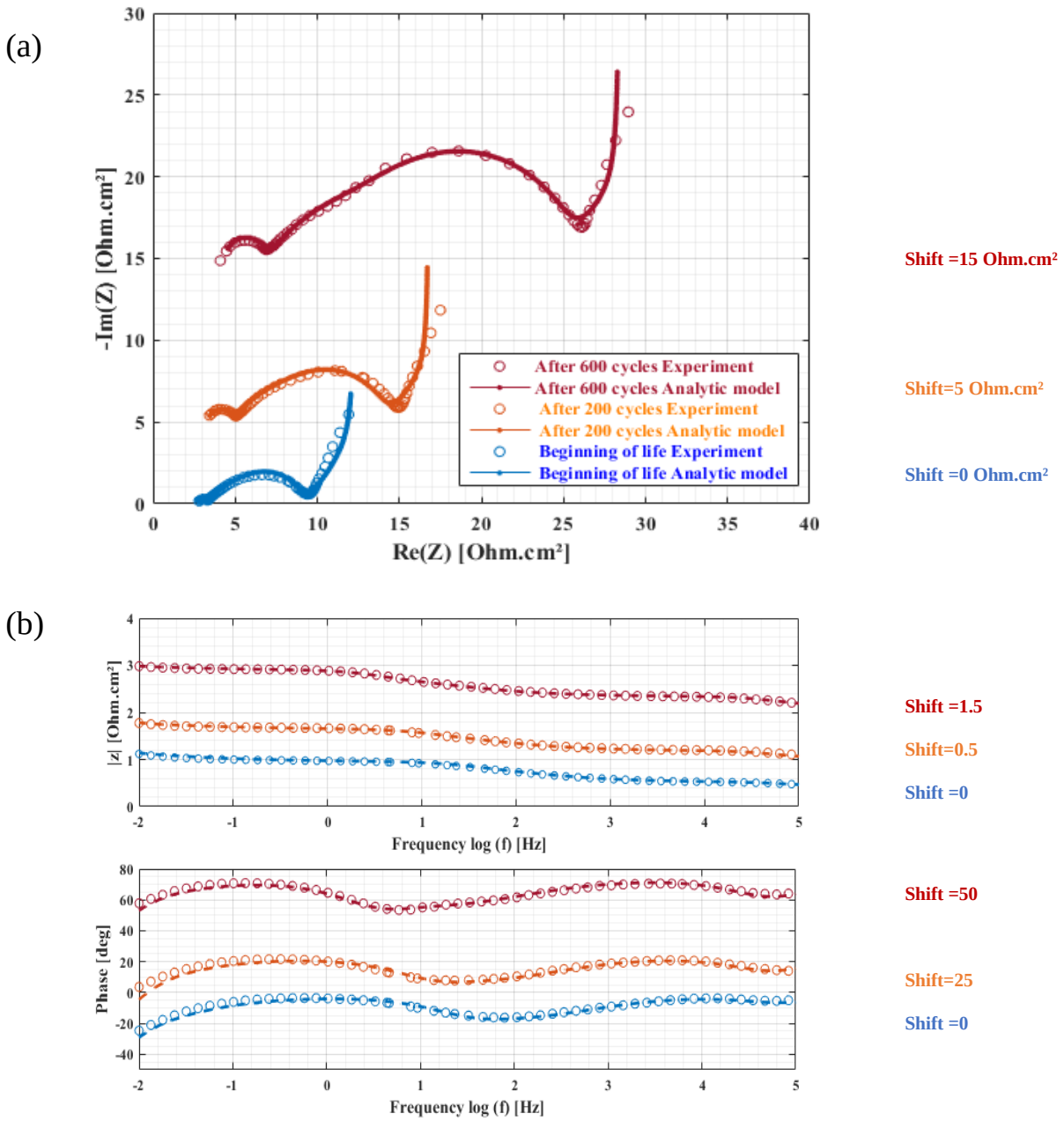

Figure IV-6 : A comparison between experiment measurements and analytic model result for the graphite electrode at full cell SOC=100% cycled at 25°C (a) EIS spectra in Nyquist, representation for: 0 cycles, 200 cycles and 600 cycles (b) EIS spectra in BODE representation: 0 cycles, 200 cycles and 600 cycles, log10 scale for the magnitude plot and linear scale for the phase plot.

(a)

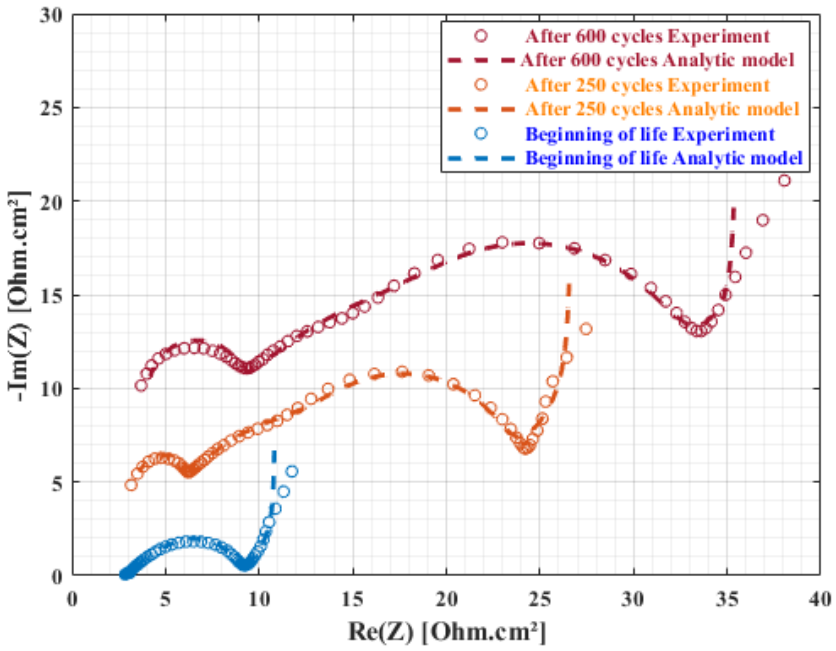

(b)

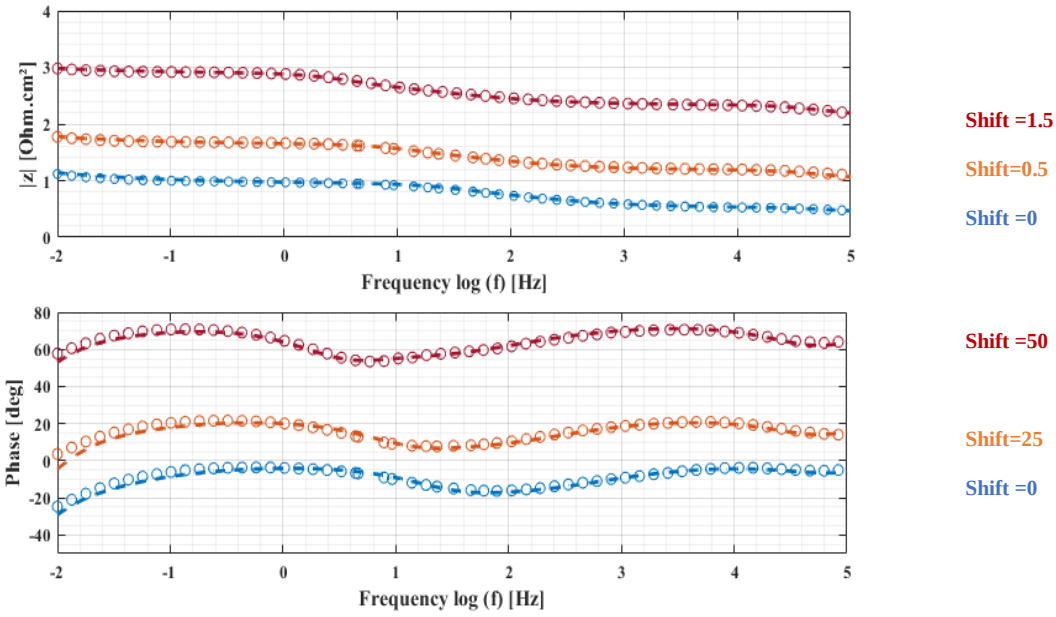

Figure IV-7 : *A comparison between experiment measurements and analytic model result for the graphite electrode at full cell SOC=100% cycled at 45°C (a) EIS spectra in Nyquist representation for: 0 cycles, 250 cycles and 600 cycles (b) EIS spectra in BODE representation for: 0 cycles, 250 cycles and 600 cycles, log10 scale for the magnitude plot and linear scale for the phase plot, log10 scale for the magnitude plot and linear scale for the phase plot.*

Table IV-1: Parameters used in developed model for the cells cycled at 25°C and 45°C: Graphite electrode

Parameter graphite	T= 25°C			T=45°C		
Cycle number	**0**	**200**	**600**	**0**	**250**	**600**
R_p *(m)*	8.00E-06	8.00E-06	8.00E-06	8.00E-06	8.00E-06	8.00E-06
L (m) **electrode thickness**	7.20E-05	7.20E-05	7.20E-05	7.20E-05	7.20E-05	7.20E-05
$D_s(m^2.s^{-1})$	5.20E-13	9.00E-13	8.00E-13	9.20E-13	6.90E-13	6.00E-13
$i_0(A.m^{-2})$	5.00E+00	5.00E+00	5.00E+00	5.00E+00	5.00E+00	5.00E+00
$S_{AM}(m^2)$	1.80E-02	1.10E-02	1.00E-02	1.70E-02	1.10E-02	7.80E-03
$S_g(m^2)$	12.25E-04	12.25E-04	12.25E-04	12.25E-04	12.25E-04	12.25E-04
S_{AM}/S_g	1.47E+01	8.98E+00	8.16E+00	1.39E+01	8.98E+00	6.37E+00
$C_{dl}(F.cm^{-2})$	4.69E-03	5.47E-03	7.35E-03	4.69E-03	5.31E-03	5.31E-03
$\alpha(-)$	6.80E-01	6.80E-01	6.80E-01	6.80E-01	6.80E-01	5.70E-01
$R_{tc}(\Omega.cm^2)$	3.49E+00	5.24E+00	6.29E+00	3.70E+00	5.20E+00	8.07E+00

Table IV-2 : Parameters used in developed model for the cells cycled at 25°C and 45°C: SEI

Parameter SEI	T= 25°C			T=45°C		
Cycle number	**0**	**200**	**600**	**0**	**250**	**600**
$C_{dl}^{fSEI}(F.cm^{-2})$	4.08E-06	2.40E-06	1.38E-06	4.08E-06	1.63E-06	1.39E-06
$R_{SEI}(\Omega.cm^2)$	6.10E-01	1.47E+00	2.45E+00	3.70E-01	2.69E+00	4.90E+00
$L_{SEI}(m)$	2.50E-08	5.00E-08	8.00E-08	2.50E-08	9.00E-08	1.12E-07
$D_{l_{SEI}}(m^2.s^{-1})$	1.06E-14	1.06E-14	1.10E-14	1.10E-14	1.20E-14	1.60E-14
$A(\Omega.A.cm^{-2})$	1.57E-06	2.33E-06	2.50E-06	1.51E-06	2.33E-06	3.29E-06

During aging, the charge transfer resistance increases. It is multiplied by a factor of 1.8 for T=25°C and 2 for T=45°C during the electrode cycling. Assuming a constant exchange current density (i_0), the AM exchange area has been divided per 2 for the two cycling temperatures conditions. The CPE factor remains constant during 600 at 25°C. However, it increases after 600 cycles at T=45°C. For the diffusion coefficient,

in the two cycling conditions, it does not change and remains around an average value of 7.40 E-13$m^2.s^{-1}$.

For the SEI parameters, the diffusion coefficient of Li^+ within the SEI film is around $10^{-14}\ m^2 s^{-1}$ in the same order of magnitude as the value suggested by Huang *et al* [30], who reported a value of 3.2 $10^{-14} m^2 s^{-1}$. The SEI resistance increases with aging. This increase is more significant for cycling at higher temperature. In fact, it is multiplied by a factor of 4 for T=25°C and 13 for T=45°C. Similarly, the SEI thickness has been multiplied by a factor of 3 for T=25°C and 4.5 for T=45°C. For the parameter A, it increases with the aging for the two temperatures. In fact, this parameter is a function of the OCP which contains non-ideal interaction energies. Therefore, we can conclude that with the aging, the non-ideal energies become more important.

In *Table IV-3*, the characteristic times and frequencies of transport phenomena in the active material and the SEI are listed for the different cycling conditions. They have been presented to highlight the evolution of each characteristic phenomena during cell lifetime. For the SEI, the characteristic times and frequencies are defined as:

$$\tau_{SEI\ Warbug} = \frac{{L_{SEI}}^2}{4D_{l_{SEI}}} \quad (\text{IV. } 37)$$

$$\tau_{SEI} = R_{SEI} C_{dl}^{fSEI} \quad (\text{IV. } 38)$$

$$f_i = \frac{1}{2\pi\tau_i} \quad (\text{IV. } 39)$$

Where i corresponds to SEI or SEI Warburg.

For the active material, these characteristic parameters are calculated using the following

$$\tau_{Warbug} = \frac{L^2}{D_s} \quad (\text{IV. } 40)$$

$$\tau_{Gr\ tc} = R_{tc} C_{dl} \quad (\text{IV. } 41)$$

$$f_i = \frac{1}{2\pi\tau_i} \quad (\text{IV. } 42)$$

For each cycling condition (i.e. same temperature, same cycle number) SEI frequency, $\boldsymbol{f_{SEI}}$, has the highest value, followed by the frequency of the SEI Warburg, $\boldsymbol{f_{SEI\ Warbug}}$. Then, active material characteristic

frequencies, charge transfer, $f_{Gr\,tc}$, and Warburg diffusion $f_{Gr\,Warbug}$ appear. $f_{Gr\,Warbug}$ reflecting the diffusion inside active material has the lowest value and presents the slowest physical process.

During the cycling, the characteristic times corresponding to the AM and the SEI parameters increase. Indeed, the transport phenomena in these two domains become slower with the aging. For the SEI transport, this behavior is exacerbated with temperature rise.

Table IV-3: Characteristic time and frequency of transport phenomena inside the graphite and SEI film

Parameter graphite & SEI	**T= 25°C**			**T=45°C**		
Cycle number	**0**	**200**	**600**	**0**	**250**	**600**
$\tau_{Gr\,tc}$ **(s)**	1.64E-02	2.87E-01	4.62E-01	1.74E-02	2.76E-01	4.28E-01
$f_{Gr\,tc}$ **(Hz)**	9.73E+00	5.56E-01	3.44E-01	9.18E+00	5.77E-01	3.72E-01
$\tau_{Gr\,Warbug}$ **(s)**	1.23E+02	7.11E+01	8.00E+01	6.96E+01	9.28E+01	1.07E+02
$f_{Gr\,Warbug}$ **(Hz)**	1.29E-03	2.24E-03	1.99E-03	2.29E-03	1.72E-03	1.49E-03
τ_{SEI} **(s)**	2.49E-06	3.53E-06	3.38E-06	1.51E-06	4.38E-06	6.37E-06
f_{SEI} **(Hz)**	6.40E+04	4.51E+04	4.71E+04	1.05E+05	3.63E+04	2.50E+04
$\tau_{SEI\,Warbug}$ **(s)**	1.47E-02	5.90E-02	1.45E-01	1.42E-02	1.69E-01	1.96E-01
$f_{SEI\,Warbug}$ **(Hz)**	1.08E+01	2.70E+00	1.09E+00	1.12E+01	9.44E-01	8.12E-01

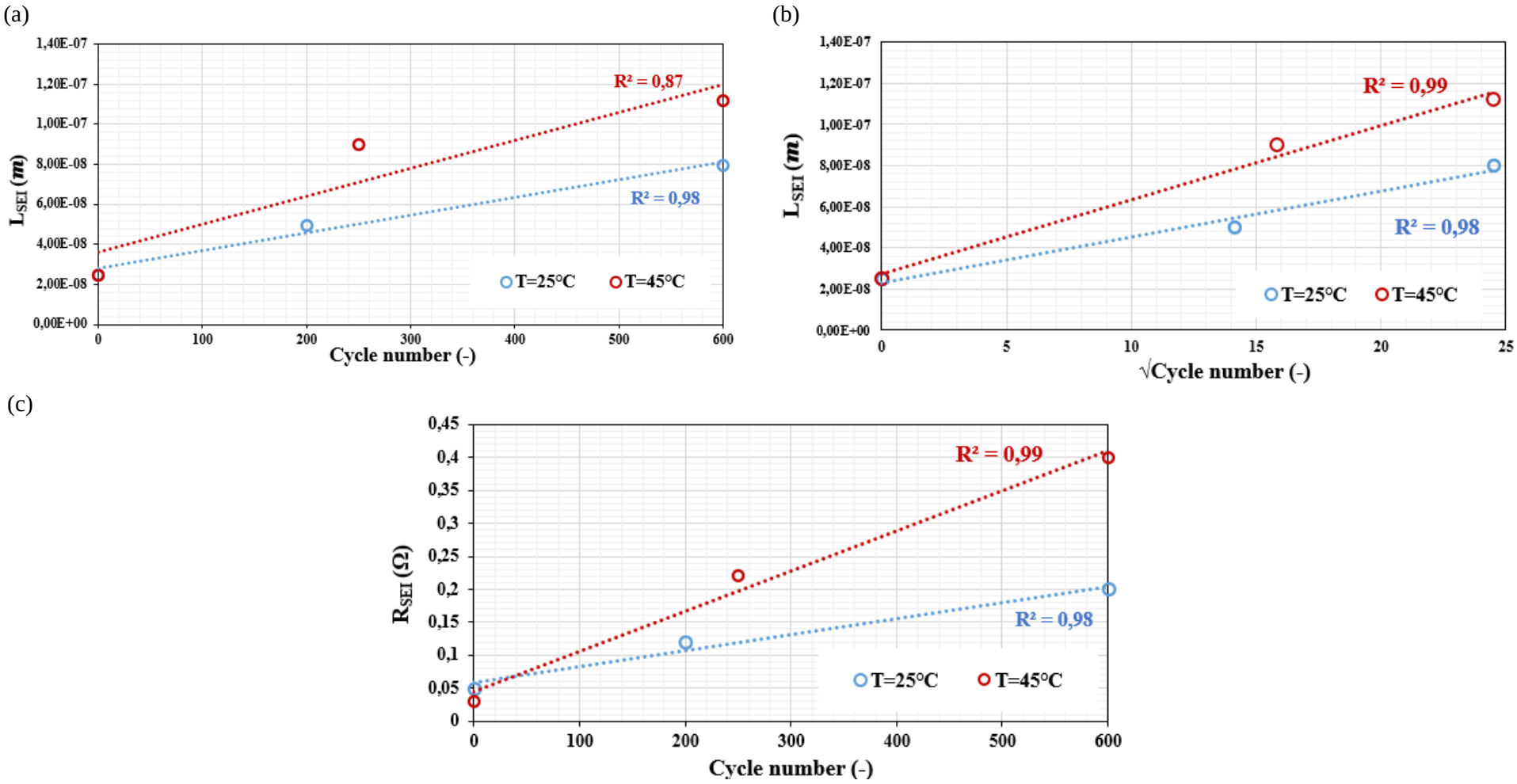

Figure IV-8 *: SEI layer growth and its resistance increase during graphite electrode cycling: (a) SEI thickness vs cycle (b) SEI thickness vs square root of cycle number (c) SEI resistance vs cycle.*

The evolutions of the SEI resistance and the corresponding thickness during cycling at T=25°C and T=45°C are presented in *Figure IV-8*. In the literature, the SEI thickness obeys aparabolic growth law [116]. In the present study, the coefficient of determination (R^2) for the L_{SEI} variation with cycle number (n) and the square root of (n) are remarkably close. In fact, for temperature of 45°C, R^2 is higher for the parabolic fit equation. This fact can be observed in *Figure IV-8*.a when the experimental curve starts to bend over. In general, the bends over is remarkable when the transport limitation is reached. This limit can be reached when the highest SEI thickness is observed and the growth rate became slower. For the SEI resistance, a linear behavior is observed. Therefore, we can deduce that the maximum SEI thickness is not reached for T=25°C and a linear regression is enough to explain R_{SEI} and L_{SEI} as function of the cycle number n. For T=45°C, the SEI thickness is a function of the square root of (n). However, the SEI resistance obeys a linear law with cycle number.

Another important relation is the dependency between the SEI resistance and thickness. Indeed, the SEI resistance is often assumed proportional to the SEI thickness [117] [118]. As presented in *Figure II-9*, the SEI resistance varies rather linearly with the SEI thickness. This linear behavior is much better for t=25°C than T=45°C. The slopes of these two curves give an idea about the resistance of the SEI formed at 25°C and 45°C cycling. For the 25°C cycling condition, this value is around 2.00E+06 giving a conductivity of 5.00E-07 $S.m^{-1}$. For the temperature cycling condition of 45°C, the slope is about 3.00E+06 corresponding to a conductivity of 3.33E-07 $S.m^{-1}$.

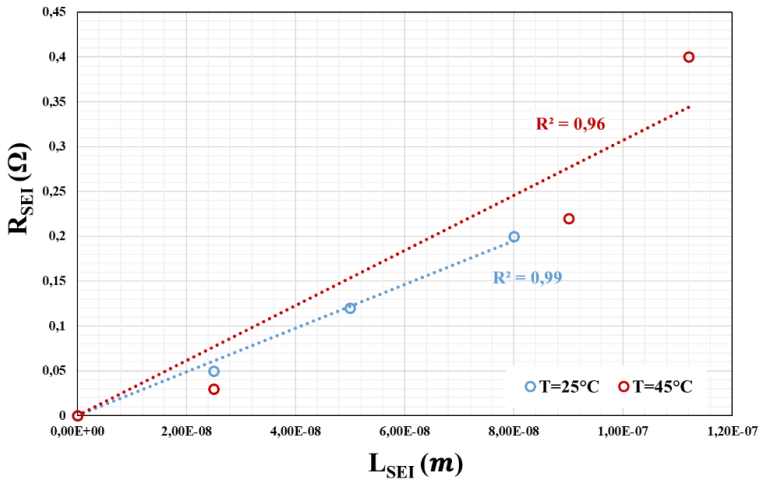

Figure IV-9 *: SEI resistance evolution with the SEI layer thickness.*

IV.2.3.2 **Positive electrode:**

For the positive electrode, the EEC model representing Eq. (IV. 33) is proposed in Figure IV-10. The diffusion through the SRL is supposed to be between the charge transfer physic and the diffusion inside the AM. We suppose that the two process can be separated leading to the following simplified EEC model:

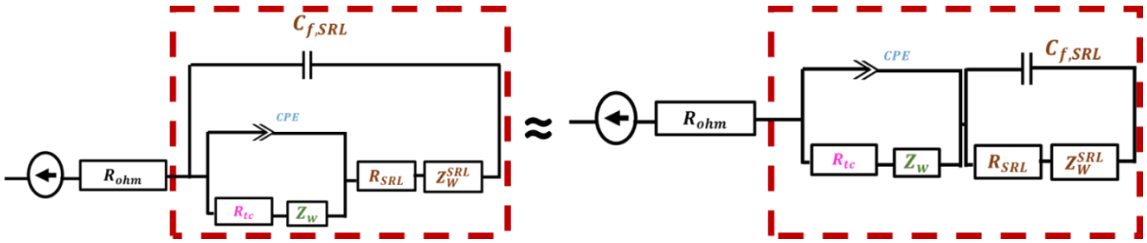

Figure IV-10*: Analytic EEC representation for the impedance of the positive aged electrode.*

The first block presented in Figure IV-10 is related to the interfacial electrode/electrolyte impedance developed in the BOL chapter. Similarly, to the graphite, this impedance is provided assuming a single particle model with the CPE approximation. However, the second one is related to aging contribution in the NMC622 with the SRL formation and the diffusion within it. In the same way as for the graphite, a comparison with experimental measurements is proposed in Figure IV-11 and Figure IV-12 (for cells aged at 25°C and 45°C respectively) with the analytic EEC model at a SOC of 100%. The analytic results have been performed using the parameters summarized in *Table IV-4* and *Table IV-5* for NMC622 and SRL layer, respectively. The same approach used in the graphite has been applied in the NMC case to identify the physical parameters. The two figures show a very good agreement with the experiments. Therefore, for the positive electrode (NMC622) considering an SRL layer diffusion contribution fit very well the second semicircle appearing in the moderate frequency domain. For the remaining frequencies parts, a single particle model with a CPE approximation is a good alternative to fit and present the predominant physics.

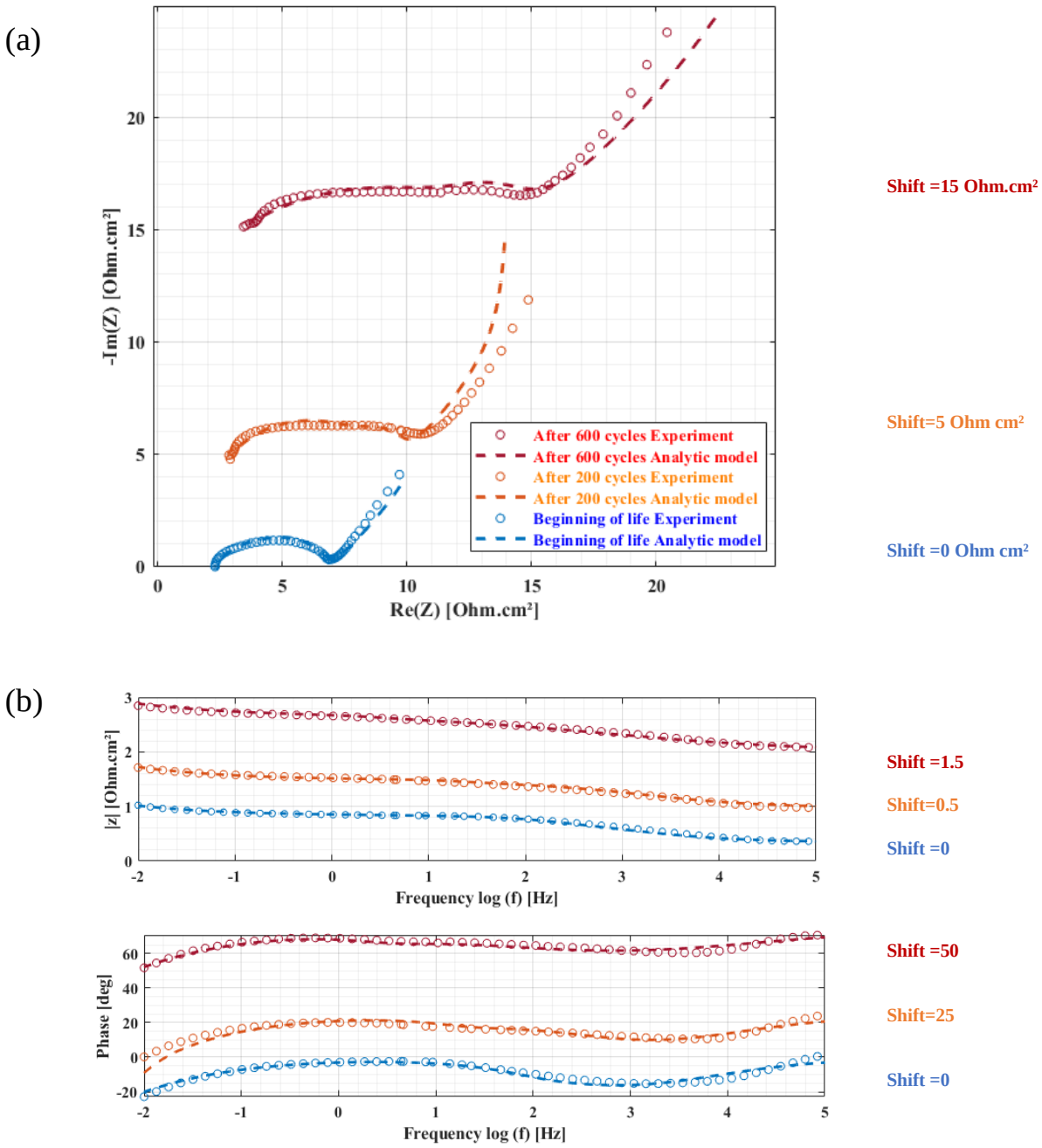

Figure IV-11 *: A comparison between experiment measurements and analytic model result for the NMC622 electrode at full cell SOC=100% cycled at 25°C (a) EIS spectra in Nyquist representation for: 0 cycles, 200 cycles and 600 cycles (b) EIS spectra in BODE representation for: 0 cycles, 200 cycles and 600 cycles, log10 scale for the magnitude plot and linear scale for the phase plot.*

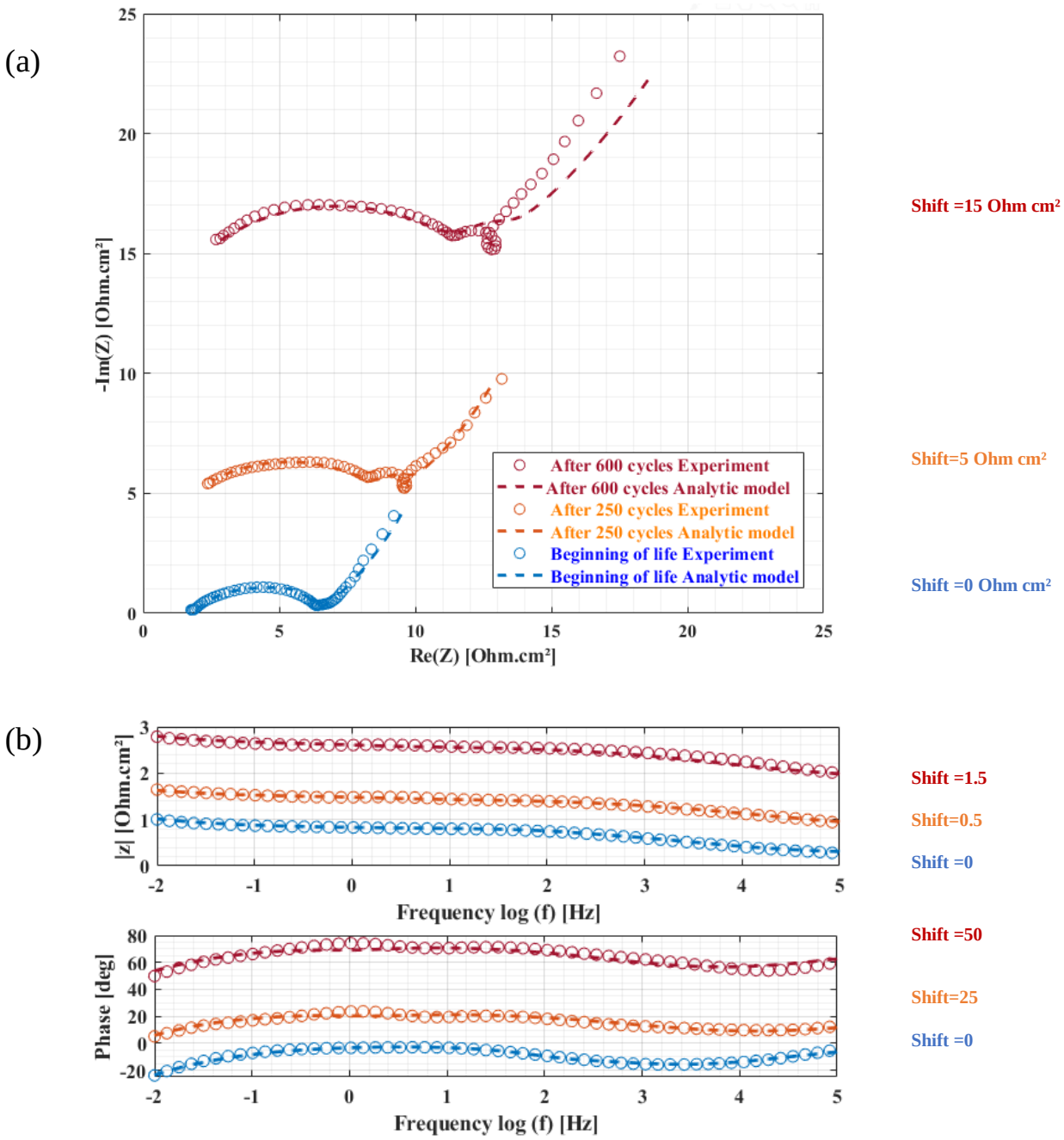

Figure IV-12 : *A comparison between experiment measurements and analytic model result for the NMC622 electrode at full cell SOC=100% cycled at 45°C (a) EIS spectra in Nyquist representation for: 0 cycles, 250 cycles and 600 cycles (b) EIS spectra in BODE representation for: 0 cycles, 250 cycles and 600 cycles, log10 scale for the magnitude plot and linear scale for the phase plot.*

Table IV-4: Parameters used in developed model for the cells cycled at 25°C and 45°C: NMC622 electrode

Parameter NMC622	T= 25°C			T=45°C		
Cycle number	**0**	**200**	**600**	**0**	**250**	**600**
R_p *(m)*	6.00E-06	6.00E-06	6.00E-06	6.00E-06	6.00E-06	6.00E-06
L (m)	6.00E-05	6.00E-05	6.00E-05	6.00E-05	6.00E-05	6.00E-05
$D_s(m^2.s^{-1})$	8.00E-14	2.00E-14	2.00E-14	9.00E-14	8.00E-14	5.00E-14
$i_0(A.m^{-2})$	2.10E+00	2.10E+00	2.10E+00	2.10E+00	2.10E+00	2.10E+00
$S_{AM}(m^2)$	3.28E-02	2.30E-02	1.70E-02	3.30E-02	2.00E-02	1.45E-02
$S_g(m^2)$	10.24E-04	10.24E-04	10.24E-04	10.24E-04	10.24E-04	10.24E-04
S_{AM}/S_g	3.20E+01	2.25E+01	1.66E+01	3.22E+01	1.95E+01	1.42E+01
C_{dl}(F.cm^{-2})	2.08E-03	2.35E-03	7.41E-03	1.91E-03	1.83E-03	1.46E-03
$\alpha(-)$	5.50E-01	5.50E-01	4.50E-01	5.50E-01	4.50E-01	4.90E-01
$R_{tc}(\Omega.cm^2)$	4.04E+00	6.15E+00	8.73E+00	4.12E+00	7.07E+00	9.69E+00

Table IV-5 : Parameters used in developed model for the cells cycled at 25°C and 45°C: SRL

Parameter SRL	T= 25°C			T=45°C		
Cycle number	**0**	**200**	**600**	**0**	**250**	**600**
C_{dl}^{fSRL}(F.cm^{-2})	1.73E-03	8.65E-03	3.26 E-3	1.73E-03	8.65E-03	1.38 E-3
$R_{SRL}(\Omega.cm^2)$	6.90E-01	1.04E+00	1.35E+00	6.90E-01	1.04E+00	1.04E+00
$L_{SRL}(m)$	1.50E-09	6.00E-09	1.50E-08	2.00E-09	8.00E-09	1.50E-08
$D_{SRL}(m^2.s^{-1})$	5.00E-14	1.00E-14	1.00E-14	1.00E-14	1.00E-14	1.00E-14
$A(\Omega.A.cm^{-2})$	7.34E-05	1 .11E-4	1.51E-04	7.84E-05	1.28E-04	1.75E-04

As presented in *Table IV-4*, the charge transfer resistance and the exchange area vary together with the cycling. In fact, R_{tc} increases along with aging while the exchange area decreases.

For the SRL, *Table IV-5*, The parameter A increases with the aging due to the increasement of the non-ideal interactions inside the active material. The diffusion coefficient of Li through the SRL is around $10^{-14}m^2.s^{-1}$ in same order of magnitude of the diffusion coefficient of Li inside

NMC622 active material. This result confirms the hypothesis of having SRL film inside the active material. It causes a deformation in the shape of charge-transfer semicircle because of the appearance of a second semicircle corresponding to the SRL. In the literature, it is noted that SRL induces an increase in the charge transfer impedance [119] similar to the obtained result. It has been mentioned that the SRL thickness is around 1nm to 3nm after formation [120] in the same order of the obtained values at 0 cycle.

To get a deeper view of transport and transfer processes for NMC 622 and SRL layer, characteristic times and frequencies are presented in *Table IV-6*. They have been calculated using the same general definitions used for SEI and graphite in the previous section (Eq ((IV. 37)- (IV. 42)).

Similar to the graphite, the diffusion inside the active material is the slowest phenomenon. For the first 200-250 cycles (depending on the temperature) the contribution of the diffusion in the SRL is negligible compared to the charge transfer resistance. This can be explained by the fact that the thickness of this film is too small. For the 600 cycles, this process becomes no more negligible and appears after the charge transfer contribution in the Nyquist plan.

Table IV-6 : Characteristic time of transport phenomena inside the NMC622 and SRL film

Parameter NMC&SRL	**T= 25°C**			**T=45°C**		
Cycle number	**0**	**200**	**600**	**0**	**250**	**600**
$\tau_{NMC\,tc}$ **(s)**	6.87E-04	1.18E-03	5.28E-04	6.40E-04	1.06E-03	6.78E-04
f_{tc} **(Hz)**	1.46E+03	8.47E+02	1.89E+03	1.56E+03	9.46E+02	1.48E+03
$\tau_{NMC\ Warbug}$ **(s)**	4.50E+02	1.80E+03	1.80E+03	4.00E+02	4.50E+02	7.20E+02
$f_{NMC\,Warbug}$ **(Hz)**	3.54E-04	8.85E-05	8.85E-05	3.98E-04	3.54E-04	2.21E-04
τ_{SRL} **(s)**	1.19E-03	9.00E-03	4.40E-03	1.19E-03	9.00E-03	1.44E-03
f_{SRL} **(s)**	1.33E+02	1.77E+01	3.62E+01	1.33E+02	1.77E+01	1.11E+02
$\tau_{SRL\,Warbug}$ **(s)**	4.50E-05	3.60E-03	2.25E-02	4.00E-04	6.40E-03	2.25E-02
$f_{SRL\,Warbug}$ **(Hz)**	3.54E+03	4.42E+01	7.08E+00	3.98E+02	2.49E+01	7.08E+00

For the SRL layer, linear R_{SRL} and L_{SRL}evolutions during cycling at T=25°C and T=45°C are presented in Figure IV-13. These parameters are more important at higher temperature during cycling. As the coefficient of determination of these expressions is around 0,99, therefore, a linear model to express the evolution of this SRL film parameters with the cycle number is enough.

(a)

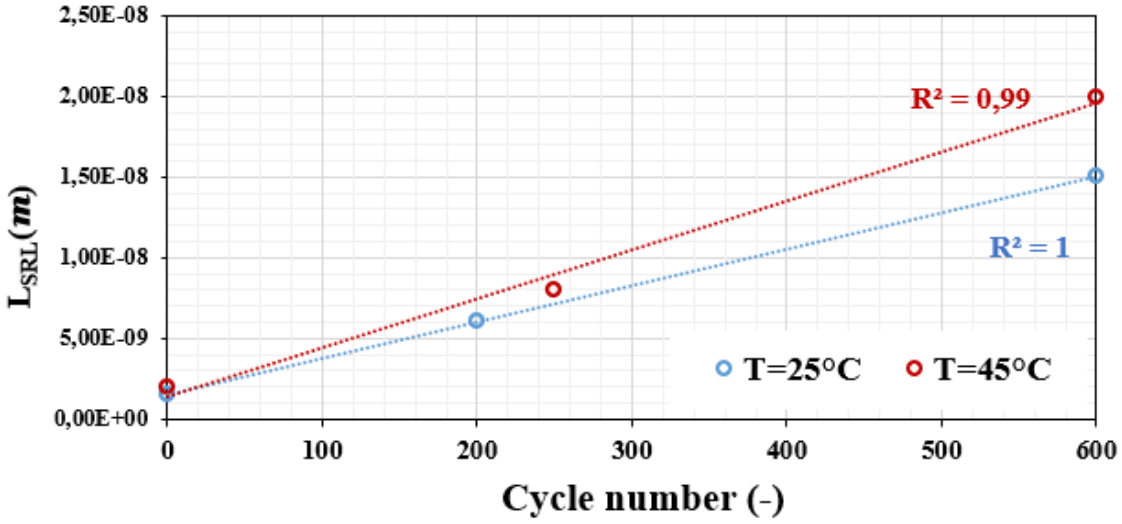

(b)

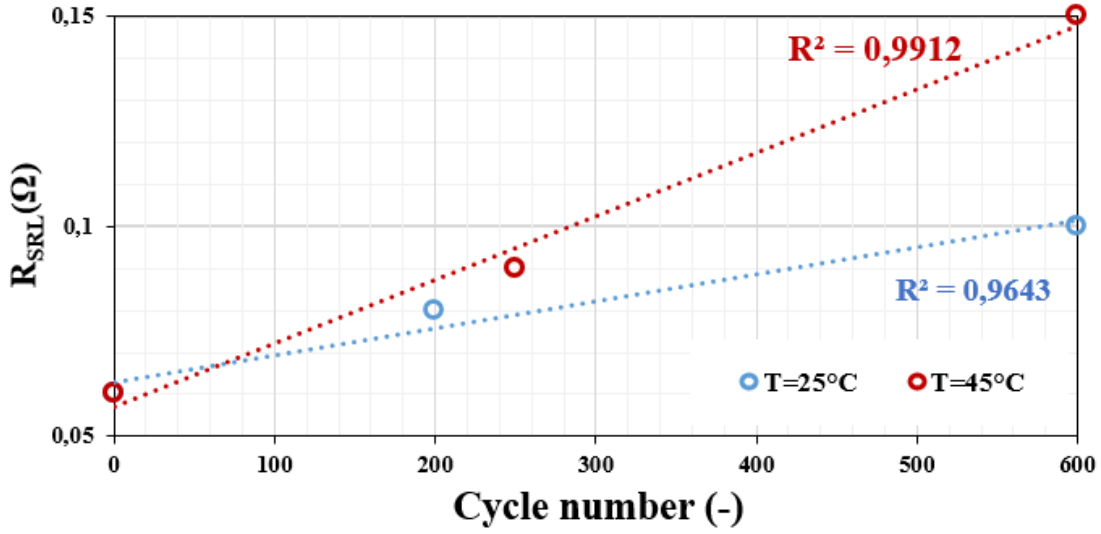

Figure IV-13 SRL layer growth and its resistance increase during NMC622 electrode cycling: (a) SRL thickness vs cycle number (b) SRL resistance vs cycle number.

IV.3 Up-scaling methodology: From the analytical impedance models to the temporal EEC models

In the previous section, the expression of the analytic model for the battery at different moment of its lifetime has been developed in the frequency domain. Two different models have been proposed depending on the electrode type. In this section, a temporal EEC model corresponding to this common mathematical structure has been developed for the positive and the negative electrodes based on the analytic one to describe the SRL and SEI Warburg contributions. A comparison with the experimental results for the two aging conditions, namely cycling at T= 25°C and T=45°C, is also presented to highlight the pertinence of the developed approach.

IV.3.1 Cell EEC temporal model with aging

In the framework of the proposed upscaling methodology from the analytic to the temporal EEC model, presenting the Warburg impedance in series is mandatory. This method based on the Mittag Leffer expansion has been detailed in the previous chapter. This mathematical development allows to identify any Warburg function with an equivalent impedance composed of series of capacities and resistances in parallel known as Foster structure. In this chapter, the same strategy is applied to simplify the Warburg functions related to the diffusion through the SEI for the graphite electrode (Eq.(IV. 20)) and the diffusion through the SRL for the NMC622 electrode (Eq.(IV. 35)). For the Warburg impedance related to the diffusion inside the active material, the solution demonstrated in the previous chapter is considered.

IV.3.1.1 **Negative electrode:**

For the graphite, Z_W^{SEI}, the Warburg impedance related to the diffusion within the SEI layer can be presented as:

$$Z_W^{SEI} = P_{SEI}\frac{tanh(s)}{s} \quad \text{(IV. 43)}$$

Where $s = \sqrt{j\tilde{\omega}_{SEI}}$ and P_{SEI} is a constant given by:

$$P_{SEI} = A\frac{L_{SEI}/2}{FC_l D_{l_{SEI}}} \quad \text{(IV. 44)}$$

The partial decomposition of the previous function is based on Mittag-Leffer's theorem and similar to the one detailed by Khun *et al* [31]. The analytic development in series of the previous equation leads to:

$$Z_W^{SEI} = \sum_{n=1}^{\infty}\frac{1}{\frac{s}{2P_{SEI}} + \frac{(n\pi - \frac{\pi}{2})^2}{2P_{SEI}}} \quad \text{(IV. 45)}$$

Considering the Foster structure, Z_W^{SEI} can be presented as function of series of admittances $Y_{n,SEI}$ and impedances $Z_{n,SEI}$:

$$Z_W^{SEI} = \sum_{n=1}^{\infty}\frac{1}{Y_{n,SEI} + \frac{1}{Z_{n,SEI}}} \quad \text{(IV. 46)}$$

expressed by capacitor and resistance respectively:

$$Y_{n,SEI} = C_{n,SEI}s^2 \quad \text{(IV. 47)}$$

And $Z_{n,SEI}$ is the resistance of each RC element of the series used to model the diffusion within the SEI:

$$Z_{n,SEI} = R_{n,SEI} \tag{IV. 48}$$

Within this representation, the SEI Warburg impedance can be presented as a series of RC elements in parallel. Indeed, the admittance is associated to the capacity, and the impedance denotes the resistance value. By identification with Eq. (IV. 45), the capacitor, $C_{n,SEI}$, is a function of P factor and is the same for all the RC elements of the series, as it does not depend on n RC elements, n, as:

$$C_{n,SEI} = \frac{1}{2P_{SEI}} \tag{IV. 49}$$

In the other hand, the SEI resistances in the series, will depend on the element number, n and it can be defined by identification as:

$$R_{n,SEI} = \frac{2P_{SEI}}{(n\pi - \frac{\pi}{2})^2} \tag{IV. 50}$$

Figure IV-14a illustrates the corresponding EEC model in the temporal domain for the graphite including SEI. This representation is based on the EEC model shown in *Figure IV-5* on the right. The Warburg impedance of the diffusion inside the active material Z_W has the same structure as the one developed in the previous chapter. We have chosen to limit ourselves to 3RC elements to express the diffusion through the SEI. Thus, the number of RC to be implemented in a BMS will be limited. With this result, we can demonstrate that having access to the value of P_{SEI} is enough to determine the different values of the RC elements.

IV.3.1.2 **Positive electrode:**

For the SRL film, the Warburg impedance of the diffusion through it has the same general form as the one for the SEI film. Therefore, following the same steps, the Foster structure of the SRL can be presented as:

$$Z_W^{SRL} = \sum_{n=1}^{\infty} \frac{1}{Y_{n,SRL} + \frac{1}{Z_{n,SRL}}} \quad \text{(IV. 51)}$$

Therefore, the SRL Warburg impedance can be presented as a series of RC elements in the same way as Z_W^{SEI} and Z_W. The admittance denotes a constant capacity for all the RC elements as follows:

$$C_{n,SRL} = \frac{1}{2P_{SRL}} \quad \text{(IV. 52)}$$

And the impedance denotes the resistance value which depends on the RC elements number similarly to the SEI film:

$$R_{n,SRL} = \frac{2P_{SRL}}{(n\pi - \frac{\pi}{2})^2} \quad \text{(IV. 53)}$$

Therefore, Figure IV-14b shows the final EEC model in the temporal domain for the NMC. This representation is based on EEC model given in *Figure IV-10*. Similarly, to the graphite, Warburg impedance of the diffusion inside the active material Z_W has the same structure developed in the previous chapter. Similar to the SEI for the graphite, to identify the different values of the RC elements, we have to know the value of P_{SRL}.

(a)

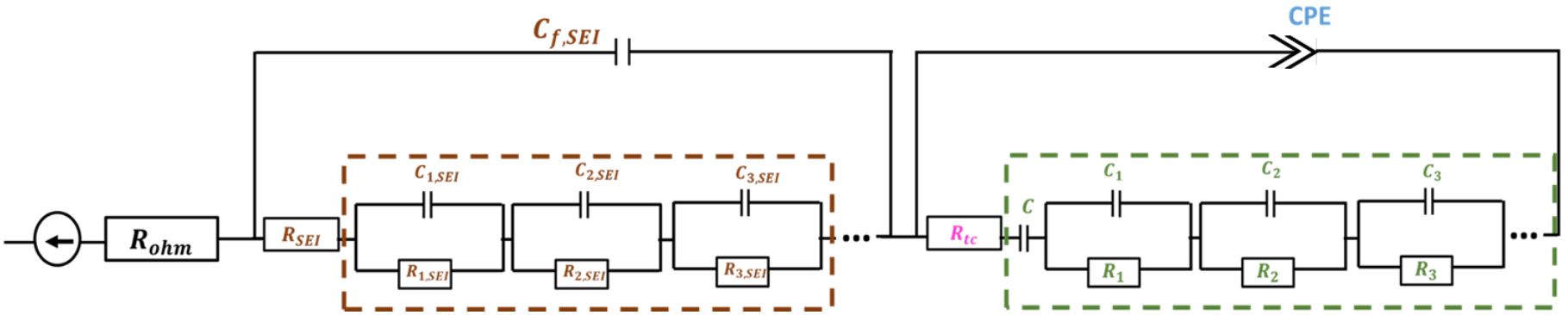

(b)

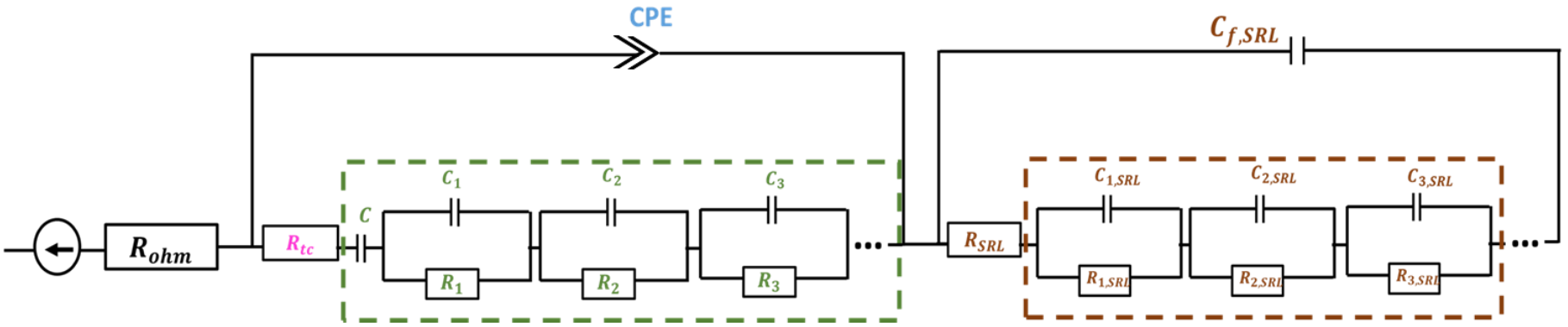

Figure IV-14 *: Representation of the EEC model in temporal domain for aged battery: (a) for the negative electrode, (b) for the positive electrode.*

IV.3.2 Results and discussions

In order to verify the relevance of the different approximations used to determine the final temporal EEC model for the graphite and NMC622 electrodes, a comparison with the experimental results is important. This comparison has been performed for the two aged conditions, namely cycling at temperature of 25°C and 45°C.

For the graphite, Figure IV-15 and Figure IV-16 show a good agreement between the simulated results and the experimental ones for the cells aged at 25°C and 45°C, respectively. The obtained values for each electric component used to fit the impedance spectra for the graphite active material and the SEI film is summarized in Table IV-7 and Table IV-8 respectively. For the diffusion phenomenon corresponding to active material and the SEI film, the characteristic times of each RC element does not change a lot during the cycling. However, for the charge transfer characteristic time of the graphite increases with cycling. This can be related to the fact that the charge transfer process become more difficult with the aging.

The EEC model developed for the NMC622 shows a good agreement with the experimental measurements for the two temperatures. *Table IV-9* and *Table IV-10* represent the values of the different electric components used to model the NMC622 and the SRL, respectively. The characteristic time of diffusion processes inside the active material and through the SRL remain stable. However, the resistance of Warburg RC elements increases with the charge transfer resistances increase with aging. The charge transfer characteristic time containing the transfer process become more significant with cycling.

In sum, independently to the electrode type, the charge transfer process is the most influenced physic inside the electrode during aging. It can be considered as the limited physic in the battery. For the two electrodes in presented EEC model, all the resistances describing the diffusion phenomena and charge transfer increase. The characteristic times of the different Warburg remain constant. However, the charge transfer, SEI and SRL characteristic time increase with the aging.

(a)

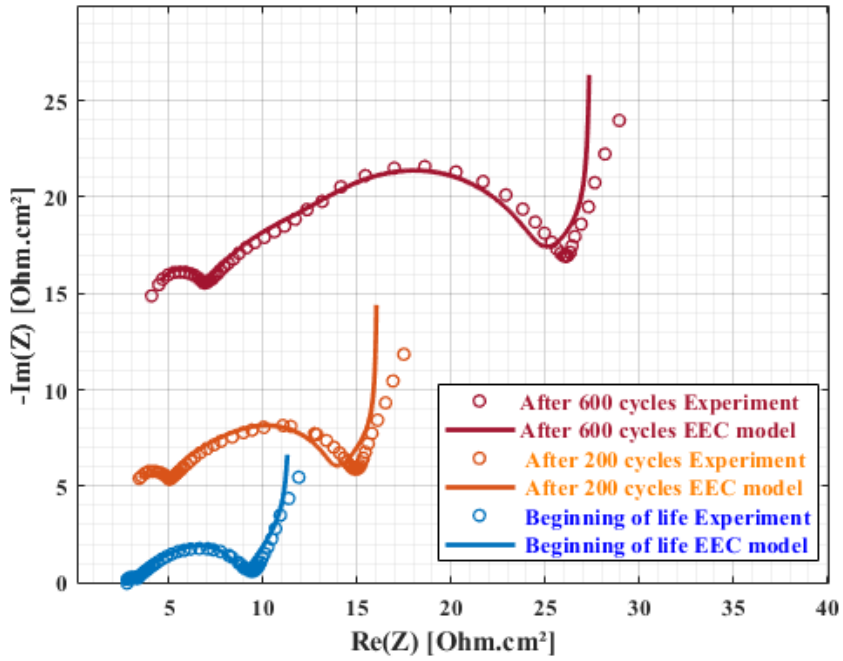

(b)

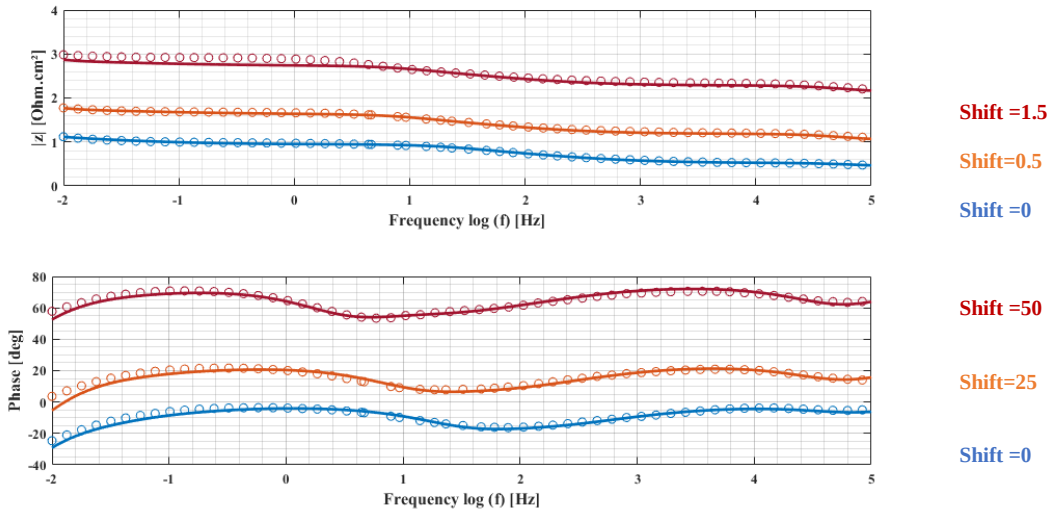

Figure IV-15 *: A comparison between experiment measurements and temporal EEC model result for the graphite electrode at full cell SOC=100% cycled at 25°C (a) EIS spectra in Nyquist representation for: 0 cycles, 200 cycles and 600 cycles (b) EIS spectra in BODE representation for: 0 cycles, 200 cycles and 600 cycles, log10 scale for the magnitude plot and linear scale for the phase plot.*

(a)

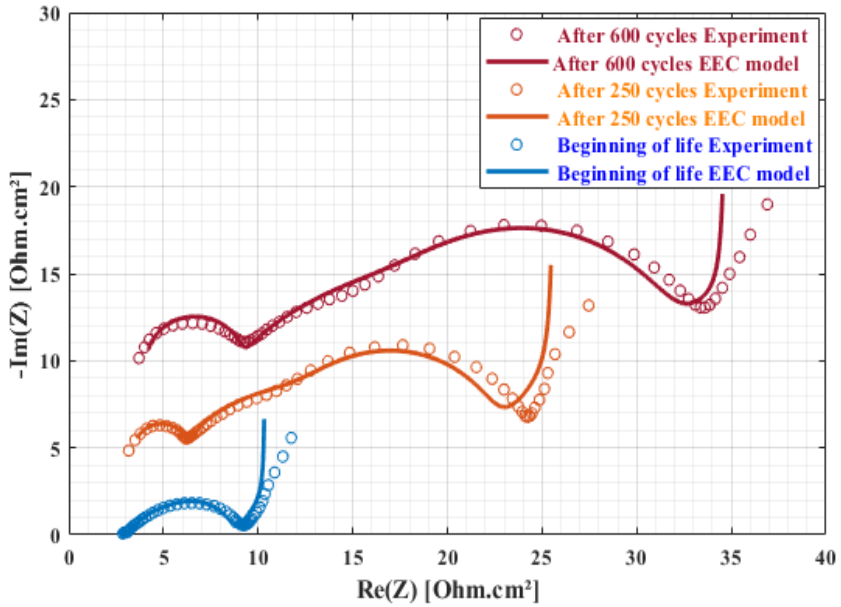

(b)

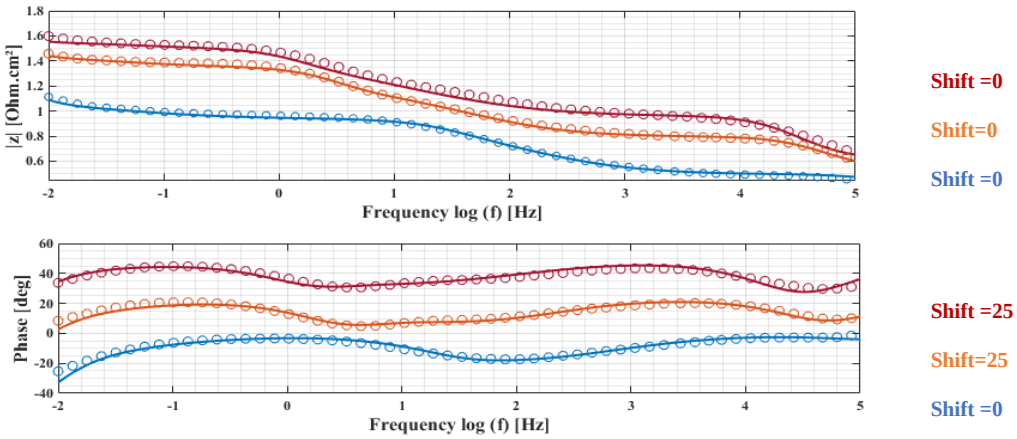

Figure IV-16 *: A comparison between experiment measurements and temporal EEC model result for the graphite electrode at full cell SOC=100% cycled at 45°C (a) EIS spectra in Nyquist representation for: 0 cycles, 250 cycles and 600 cycles (b) EIS spectra in BODE representation for: 0 cycles, 250 cycles and 600 cycles, log10 scale for the magnitude plot and linear scale for the phase plot.*

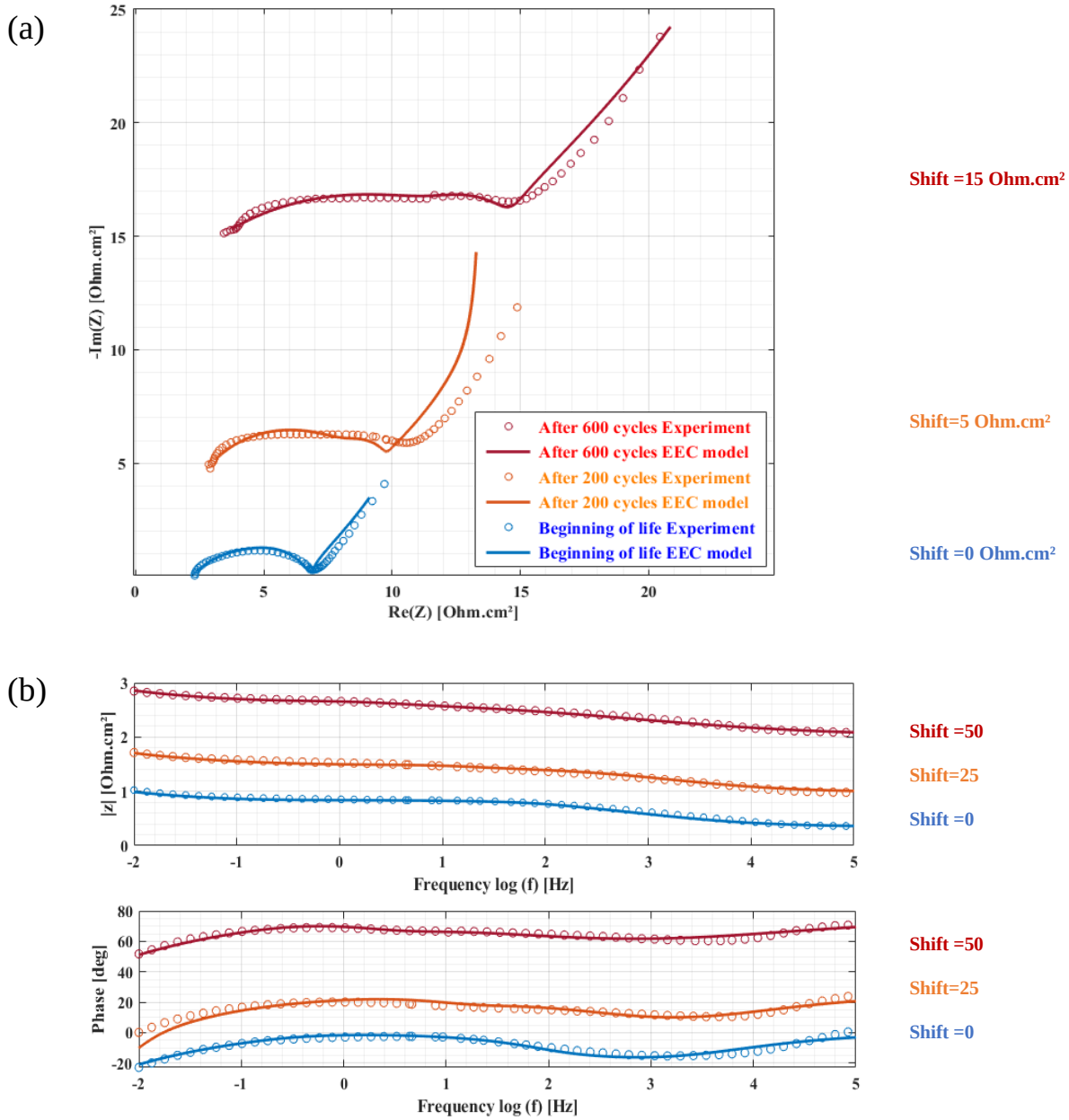

Figure IV-17 *: A comparison between experiment measurements and temporal EEC model result for the NMC622 electrode at full cell SOC=100% cycled at 25°C (a) EIS spectra in Nyquist representation for: 0 cycles, 200 cycles and 600 cycles (b) EIS spectra in BODE representation for: 0 cycles, 200 cycles and 600 cycles, log10 scale for the magnitude plot and linear scale for the phase plot.*

(a)

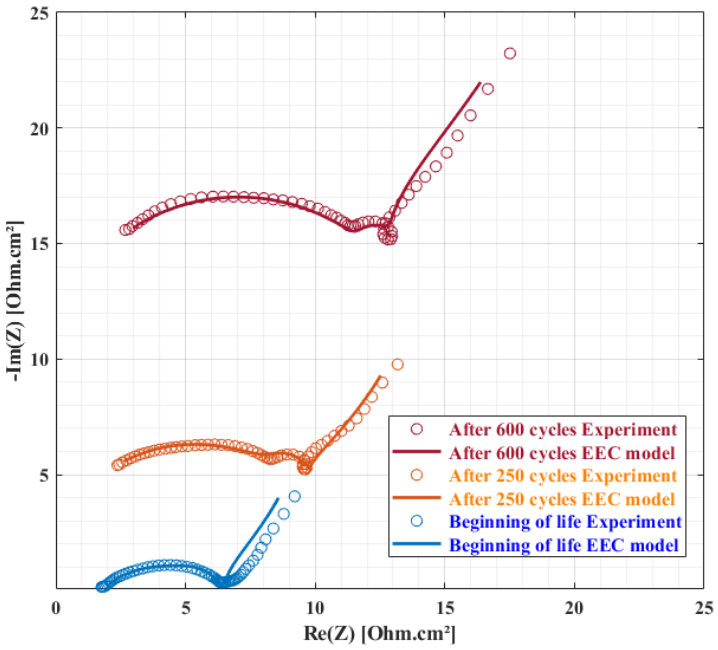

(b)

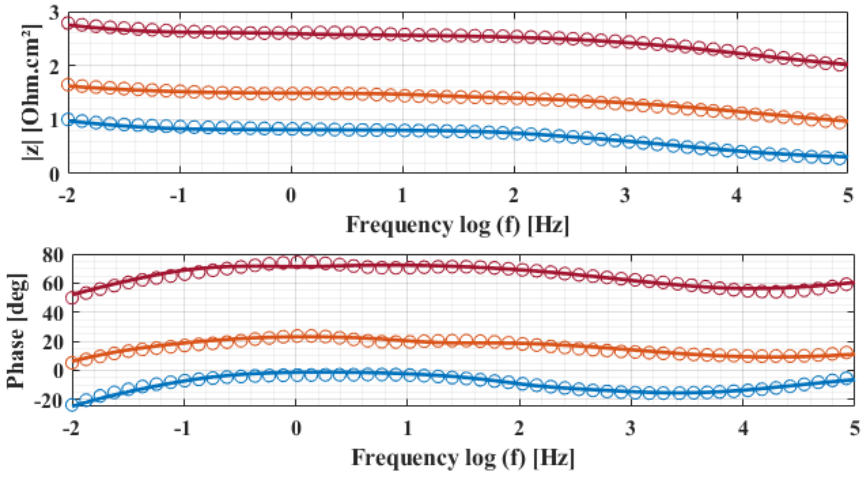

Figure IV-18 : *A comparison between experiment measurements and temporal EEC model result for the NMC622 electrode at full cell SOC=100% cycled at 45°C (a) EIS spectra in Nyquist representation for: 0 cycles, 250 cycles and 600 cycles (b) EIS spectra in BODE representation for: 0 cycles, 250 cycles and 600 cycles, log10 scale for the magnitude plot and linear scale for the phase plot.*

Table IV-7: Resulting values for components used with Foster structure to represent the EEC model for the negative electrode during its lifetime

Parameter graphite	T= 25°C			T=45°C		
Cycle number	**0**	**200**	**600**	**0**	**250**	**600**
CPE (F.cm^{-2})	4.69E-03	5.47E-02	7.35E-02	4.69E-03	5.31E-02	5.30E-02
R_{tc}(Ω.cm^2)	3.49E+00	5.24E+00	6.29E+00	3.70E+00	5.20E+00	8.07E+00
τ_{tc} (s)	1.64E-02	2.87E-01	4.62E-01	1.74E-02	2.76E-01	4.28E-01
C(F.cm^{-2})	2.10E-02	2.27E-02	1.80E-02	3.50E-02	1.71E-02	1.26E-02
$C_{i=1.2.3}$(F.cm^{-2})	3.16E-02	3.40E-02	2.79E-02	5.28E-02	2.56E-02	1.89E-02
R_1(Ω.cm^2)	1.24E+00	1.30E+00	1.60E+00	8.50E-01	1.76E+00	2.37E+00
τ_1 (s)	3.92E-02	4.42E-02	4.46E-02	4.49E-02	4.51E-02	4.48E-02
R_2(Ω.cm^2)	5.13E-01	4.70E-01	5.70E-01	3.10E-01	6.30E-01	8.50E-01
τ_2 (s)	1.62E-02	1.60E-02	1.59E-02	1.64E-02	1.61E-02	1.61E-02
R_3(Ω.cm^2)	2.62E-01	2.40E-01	2.95E-01	1.57E-01	3.20E-01	4.40E-01
τ_3 (s)	8.20E-03	8.20E-03	8.20E-03	8.30E-03	8.20E-03	8.20E-03
P(Ω.cm^2)	1.58E+01	1.60E+01	1.80E+01	9.41E+00	1.95E+01	2.64E+01

Table IV-8 : Resulting values for components used with Foster structure to represent the EEC model for the SEI film during its lifetime

Parameter SEI	T= 25°C			T=45°C		
Cycle number	**0**	**200**	**600**	**0**	**250**	**600**
P_{SEI} (Ω.cm^2)	2.33E+00	6.99E+00	1.19E+01	2.18E+00	1.10E+01	1.57E+01
C_{dl}^{fSEI}(F.cm^{-2})	4.08E-06	2.40E-06	1.38E-06	4.08E-06	1.63E-06	1.39E-06
R_{SEI}(Ω.cm^2)	6.10E-01	1.47E+00	2.45E+00	3.70E-01	2.69E+00	4.90E+00
τ_{SEI} (s)	2.49E-06	3.53E-06	3.38E-06	1.51E-06	4.38E-06	6.81E-06
$C_{i=1.2.3....SEI}$(F.cm^{-2})	2.10E-01	7.10E-02	4.20E-02	2.30E-01	4.10E-02	3.00E-02
$R_{1.SEI}$(Ω.cm^2)	1.89E+00	5.67E+00	9.61E+00	1.77E+00	8.94E+00	1.27E+01
$\tau_{1.SEI}$ (s)	3.97E-01	4.00E-01	4.00E-01	4.10E-01	3.60E-01	3.80E-01
$R_{2.SEI}$(Ω.cm^2)	2.10E-01	6.29E-01	1.06E+00	1.90E-01	9.90E-01	1.41E+00
$\tau_{2.SEI}$ (s)	4.41E-02	4.47E-02	4.45E-02	4.37E-02	4.06E-02	4.23E-02
$R_{3.SEI}$(Ω.cm^2)	7.00E-02	2.30E-01	3.80E-01	7.00E-02	3.60E-01	5.10E-01
$\tau_{3.SEI}$ (s)	1.50E-03	1.63E-02	1.60E-02	1.61E-02	1.48E-02	1.53E-02

Table IV-9 : Resulting values for components used with Foster structure to represent the EEC model for the NMC622 active material during its lifetime

ParameterNMC622	**T= 25°C**			**T=45°C**		
Cycle number	**0**	**200**	**600**	**0**	**250**	**600**
CPE (F.cm^{-2})	2.08E-03	2.35E-03	7.40E-04	1.90E-03	1.83E-03	8.56E-04
R_{tc}(Ω.cm^2)	4.04E+00	6.15E+00	8.73E+00	4.12E+00	7.07E+00	9.69E+00
τ_{tc} (s)	8.40E-03	1.45E-02	6.46E-03	7.83E-03	1.29E-02	8.29E-03
C(F.cm^{-2})	1.20E-02	7.49E+05	2.35E-03	1.00E-02	1.00E-02	5.97E-03
$C_{i=1.2.3}$(F.cm^{-2})	2.00E-02	1.20E-02	3.53E-03	2.00E-02	1.96 E-2	8.95E-03
R_1(Ω.cm^2)	2.48E+00	4.01E+00	1.27E+01	2.61E+00	2.29E+00	5.03E+00
τ_1 (s)	4.96E-02	4.81E-02	4.50E-02	5.22E-02	4.50E-02	4.50E-03
R_2(Ω.cm^2)	8.90E-01	1.44E+00	4.59E+00	9.40E-01	8.30E-01	1.81E+00
τ_2 (s)	2.00E-02	1.73E-02	1.60E-02	1.88E-02	1.66E-02	1.61E-03
R_3(Ω.cm^2)	4.50E-01	7.40E-01	2.34E+00	4.80E-01	4.30E-01	9.20E-01
τ_3 (s)	1.00E-02	8.88E-03	8.26E-03	9.60E-03	8.64E-03	8.23 E-3
P(Ω.cm^2)	2.75E+01	4.45E+01	1.41E+02	2.90E+01	3.00E+01	5.58E+01

Table IV-10 : Resulting values for components used with Foster structure to represent the EEC model for the SRL film during its lifetime

Parameter SRL	**T= 25°C**			**T=45°C**		
Cycle number	**0**	**200**	**600**	**0**	**250**	**600**
P_{SRL}(Ω.cm^2)	1.16E-04	1.06E-03	2.39E-03	2 .13E-4	2.35E-03	3.22E-03
C_{dl}^{fSRL}(F.cm^{-2})	1.73E-03	8.65E-03	3.26 E-3	1.73E-03	8.65E-03	1.38 E-3
R_{SRL}(Ω.cm^2)	6.90E-01	1.04E+00	1.35E+00	6.90E-01	1.04E+00	1.04E+00
τ_{SRL} (s)	1.19E-03	9.00E-03	4.40E-03	1.19E-03	9.00E-03	1.44E-03
$C_{i=1.2.3....SRL}$(F.cm^{-2})	3.71E+03	4.07E+02	1.70E+02	2.34E+03	2.54E+02	1.55E+02
$R_{1.SRL}$(Ω.cm^2)	1.09E-04	9.96E-04	2.40E-03	1.73E-04	1.90E-03	2.60E-03
$\tau_{1.SRL}$ (s)	4.00E-01	4.10E-01	4.10E-01	4.00E-01	4.80E-01	4.00E-01
$R_{2.SRL}$(Ω.cm^2)	1.21E-05	1.11E-04	2.64E-04	1.92E-05	2.12E-04	2.91 E-4
$\tau_{2.SRL}$ (s)	4.49E-02	4.52E-02	4.49E-02	4.49E-02	5.30E-03	4.49E-02
$R_{3.SRL}$(Ω.cm^2)	4.36E-06	3.98E-05	9.52E-05	6.91E-06	6.64E-05	1.04 E-4
$\tau_{3.SRL}$ (s)	1.62E-02	1.62E-02	1.62E-02	1.62E-02	1.68E-02	1.62E-02

IV.4 Conclusion

In this chapter, an up-scaling methodology has been established and developed for aged graphite and NMC622 electrodes based on all the above literature study and the experimental results (chapter 2). For the graphite, the presence of SEI and the diffusion within has been selected to represent the aging factor observed during cell lifetime. For the NMC622, it has been decided to focus on the presence of SRL inside the active material and the diffusion within during cycling.

Similar to the previous chapter, the up-scaling methodology has been established in two steps. The first step consists in presenting the different electrode impedances taking into account the identified aging physics in the frequency domain. A comparison with experimental EIS spectra measurements allows to validate the model and to get access to the aging physical parameters. Therefore, the evolution of the SEI and SRL layers thickness and resistances is discussed for two aged conditions (i.e.. T=25°C and T=45°C).

The second step consists in developing the temporal EEC model of the analytic impedance model proposed for the frequency domain. For the diffusion inside the active material, the same model developed in the BOL chapter is used. However, for the aging phenomena, a 3RC elements with a resistance are implemented in series to describe the diffusion through either SRL or SEI and their electronic and ionic resistance contribution, respectively. The different electric elements of the EEC are defined as function of the physical parameters at the electrode scale for the two electrode materials at different cycling time and for two cycling temperature conditions.

At the end of this chapter, an EEC model with 3RC element to express the most significant physics the electrode active material and 3RC to describe the aging is sufficient. With the proposed model, the aging prediction of the electrodes during their lifetime is possible.

Chapter V : Conclusion and perspectives

In this work, an up-scaling methodology has been established in order to develop an EEC model based on the physics at the electrode scale. It is based on a mathematical development to bridge the gap between the physical and geometrical parameters of physical-based models at the electrode scale and the empirical parameters used in the Equivalent Electric Circuit (CEE) models. Therefore, the different components of the final EEC model are defined as function of the electrode physical parameters. The different steps of the methodology have been discussed and detailed both at the beginning of life of the battery and during its entire life. Experimental campaigns have been performed to characterize the battery, provide the model inputs and validate the different steps of the methodology.

In the first part of the work, an investigation of the different active materials properties of a graphite/NMC622 system and their evolution during lifetime of the batteries are presented. For that purpose, two battery designs have been assembled. The first one is a coin cell design with two half-cell configurations (i.e. NMC622 *vs* Li and graphite *vs* Li). This design has been employed to explore the available capacity, the equilibrium potential and the variation of lithium diffusion coefficient as function of the stoichiometry for the two active materials. The second one is a pouch cell design with two configurations, *i.e.*, with reference electrode and without reference electrode. The LFP reference electrode synthesized in the present work is a key ingredient to validate the developed model. It shows a good stability during the battery lifetime and gave us an access to both electrode's performances and characteristics separately inside the complete pouch cell design. The reference electrode allows extracting the available capacities of both electrodes inside a pouch design and the relation between the SOC of the cell and electrode's active material's stoichiometries. The insertion of the LFP reference electrode also gave us the access to the electrode's spectra inside a complete cell design and for a specific cell SOC and electrodes active materials stoichiometry. These electrodes EIS measurements are essential in this work to validate the present up-scaling methodology through a model/experiment comparison More precisely, the EIS measurements have been employed to

determine the exchange current densities of the two electrodes active materials at beginning of life. Besides, the different geometric parameters of the electrodes have been measured or calculated or extracted from the literature. To have a clear insight about the aging of the different electrodes inside a pouch cell design, cycling aging with check-up protocols have been performed. The check-up protocols have been followed by EIS measurement which is used to validate the up-scaling methodology for the end of life.

In order to propose a consistent up-scaling methodology, we decided to develop it and validate it first at the BOL, for each electrode. To get that, two different steps have been followed. The first one consists in presenting the most important physics and assumptions in terms of equations. These equations are then solved in the frequency domain to obtain the corresponding analytical impedance model. The second step is about determining an EEC model in the temporal domain. To get that, the analytical impedance model in the frequency domain is mathematically simplified in a series of RC elements. This simplification is rigorous, as it is based on a series development, the desired precision can be adapted by adding additional terms of the series, and it provide explicit expressions between the electrodes and material properties and the different resistances and capacities of the EEC model. Therefore, the obtained formulation is adapted to real-time application since it involves only RC type elements, while an explicit link with the physics of the battery.

In the present study we considered first a spherical single particle model. The diffusion of lithium inside the particle and the charge transfer are considered, while the lithium ions transport within the electrolyte is neglected. Besides, the variation of the active material equilibrium potential with stoichiometry is also considered. Using this up-scaling methodology, we show that an EEC model with 3RC elements in series is able to model the diffusion inside the active particles, diffusion which has a form of a Warburg element in the analytical impedance. An enhancement study has also been performed to consider to non-ideal behavior of the double-layer capacity and to optimize the number of RC in the EEC model. For the NMC622, we demonstrate that, a 3 RC model with CPE approximation is sufficient to perfectly illustrate the controlling physics at BOL. However, for the graphite, to have a better agreement in the high frequency domain, further adjustment is necessary. To that end, the TLM approximation has been added in the analytical impedance model to account for the ionic resistance through the thickness of this thick electrode at the beginning of life. The same up-scaling steps are applied rigorously giving a 9R-Z, representing TLM impedance in the temporal domain, implemented to fit the impedance spectra of the graphite. A comparison with

the experimental EIS spectra allows to validate the developed models. At the end, the characteristic times and frequencies related to each physic has been identified.

In order to have a better prediction of the battery aging, the up-scaling methodology has also been applied on the electrodes during their lifetime. To do this, the main degradation phenomena at the positive and the negative electrode have first been identified. This has been performed *via* a bibliographic study and an interpretation of the experimental results of the aging campaign, including the EIS spectra evolutions. For the graphite, the presence of an SEI with the diffusion of lithium within it has been considered, as the growth of this passivation layer appears as the dominant aging phenomena in our aging campaign. For the NMC622, the formation of an SRL at the surface of the particle and the diffusion through has been studied. Similar to the beginning of life chapter, the up-scaling methodology has been followed in two distinct steps. In the first step, the different analytical electrodes impedance corresponding to the identified aging physics and assumptions in the frequency domain have been determined mathematically. The identification of the corresponding aging parameters and the evolution of all the physical ones have been obtained by comparison with the experimental results. In fact, an increase in the transport resistances in the AM as well as the SRL and SEI layers have been highlighted. The impact of the temperature, aging factor, on the degradation mechanism of the electrode has been studied. Therefore, the evolution of the SEI and SRL thickness and resistances are proposed for two aged conditions (i.e., T=25°C and T=45°C). Finally, an EEC model with 3RC element to express the most significant physics the electrode active material and 3RC to describe the aging is sufficient. This model is compared to the experimental EIS impedances measured during the electrode lifetime. With the proposed model, the aging prediction of the electrodes during their lifetime is possible. It suggest an EEC model composed on electrical element expressed as function of the physical properties at the electrode scale.

The second step consists in developing the temporal EEC model of the analytic impedance model in the frequency domain. For the diffusion inside the active material, the same model developed in the BOL chapter is used. For the aging phenomenon, 3RC elements with a resistance are implemented in series to describe the diffusion in SRL or SEI layers and the ionic and their electronic resistance, respectively. The different electric elements of the EEC are expressed explicitly as function of the physics properties at the electrode scale for the two electrode materials. This has been performed at different cycling times and for the two cycling temperatures conditions. To conclude on this point, an EEC model with a structure including

3RC elements for the active material and 3RC to describe the aging is sufficient to predict the cell performance during the battery lifetime.

In addition to the work developed in the scope of this thesis, there are still some work to increase the predictability of the different proposed models. First, during this project a large investigation of the physical parameters' evolutions with the stoichiometry of the active materials has been performed. For the NMC, we have proposed stoichiometry dependent laws that go beyond the proposed empirical relations proposed in the literature. It has been the aim of our research article presented in Annex. For the future employing these models to express the material properties is a good solution to enhance the model accuracy and predictability in a larger range of conditions. Besides, a comparison between the calendar and cycling experiments is a good strategy to be confident about the different aging conditions of the electrodes. Besides, this comparative study helps to have a clear vision about the most impacting aging phenomena at the calendar and cycling conditions. In the present study, referring the experimental result, the lithium plating hasn't been considered. To go further on this aging mechanism, it's possible to perform fast charge cycling followed by EIS measurement. With the last measurement, the impact of the lithium plating on the EIS spectra can be identified with the characteristic frequency domain.

For the future, adding the transport in the electrolyte is recommended to understand the real limitations of this transport process. In general, this physical process can impact, with moderation, the low frequency domain. In the present work we have neglected it after sensitivity analysis based on electrochemical Newman model simulations developed in the CEA laboratory. This study shows a limited electrochemical influence of this phenomenon.

In a next step, to be confident about the reliability of the model, for transport application, integrating it in a BMS is essential. For that purpose, the developed EEC model with 3RC to model the diffusion inside the AM and 3RC for the aging must be implemented in a BMS with the corresponding characteristic times identified in the framework of this thesis.

Finally, it is a main factor to apply the developed up-scaling methodology on other AM types and battery generations such as solid-state batterie. In fact, although the physical equations can be different from a battery generation to another, we assume that the different steps of the present methodology should remain the same. To check that, a validation on solid state battery system is interesting.

References

[1] «LITEN-CEA,» [En ligne]. Available: https://liten.cea.fr/cea-tech/liten/Pages/Accueil.aspx.

[2] «FORSEE POWER,» [En ligne]. Available: https://www.forseepower.com/.

[3] M. Shivika, D. Hancheng, F. Shinichiro et M.Toshihiko, «Bridging greenhouse gas emissions and renewable energy deploymenttarget: Comparative assessment of China and India,» *journal of Applied Energy,* vol. 166, 2016.

[4] P.-E. Brockway, A. , L.-I. Brand-Correa et L. Hardt, «Estimation of global final-stage energy-returnon-investment for fossil fuels with comparison to renewable energy sources,» *journal of nature energy,* vol. 4, pp. 612-621, 2019.

[5] N.Omar, P. d. Bossche, M.Daowd, O. Hegazy, J. Smekens, T. Coosemans et J.Van, «Rechargeable Energy Storage Systems for Plug-In Hybrid Electric Vehicles - Assessment of Electrical Characteristicc,» *J. Energies,* vol. 5, pp. 2952-2988, 2012.

[6] M.-S. Whittingham et F-R.Gamble, «The Lithium Intercalates of the Transition Metal Dichalcogenides,» *journal of Materials research bulletin,* vol. 10, pp. 363-371, 1975.

[7] K.Mizushima, P.-C. Jones, P.-J. Wiseman et J.-B. Goodenough, «LixCoO2 (0<x<1): A new cathode material for batteries of high energy density,» *Journal of Materials Research Bulletin,* vol. 15, pp. 783-789, 1980.

[8] D. Gruet, B. Delobel, D. Sicsic, I. T. Lucas et V. Vivier, «On the electrochemical impedance response of composite insertion electrodes. Toward a better understanding of porous electrodes,» *Electrochimica Acta,* vol. 295, pp. 787-800, 2019.

[9] N. Dufour, «Modélisation multi-physique de l'électrode de graphite au sein d'une batterie lithium-ion : Etude des hétérogénéités et des mécanismes de vieillissement,» 2019.

[10] A. Chen et P. K. Sen, «Advancement in battery technology: A state-of-the-art review,» chez *2016-ESC-0713*, 2016.

[11] T.-B. Reddy et D. Linden, «Linden's Handbook of Batteries,» New York , 4th Edition McGraw-Hill, 2011, pp. 35.1-35.94.

[12] N. Nitta, F. Wu, J. T. Lee et G. Yushin, «Li-ion battery materials: present and future,» *Materials Today,* vol. 18, pp. 252-264, 2015.

[13] D. P. Abraham, T. Spila, M.-M. Furczon et E. Sammann, «Evidence of Transition-Metal Accumulation on Aged Graphite Anodes by SIMS,» *Journal of Electrochemical and Solid-State Letters,* vol. 11, pp. A226-A228, 2008.

[14] Y. Miao, P.Hynan, A.-v. Jouanne et A.Yokochi, «Current Li-Ion Battery Technologies in Electric Vehicles and Opportunities for Advancements,» *Journal of Energies* , vol. 12, 2019.

[15] D. Doughty et E. Rother, «A general discussion of Li Ion battery safety,» *Journal of Electrochem. Soc. Interface,* vol. 2, 2012.

[16] A. Van der Ven, Z. Deng, S. Banerjee et S. P. Ong, «Rechargeable Alkali-Ion Battery Materials: Theory and Computation,» *Chemical Reviews,* vol. 0, p. null, 2020.

[17] X. Su, Q. Wu, J. Li, X. Xiao, A. Lott, W. Lu, B. W. Sheldon et J. Wu, «Silicon-Based Nanomaterials for Lithium-Ion Batteries: A Review,» *Advanced Energy Materials,* vol. 4, p. 1300882, 10 2013.

[18] J. Randles, «Kenitics of rapid electrode reactions,» *Discussions of the faraday society,* vol. 1, pp. 11-19, 1947.

[19] M. Doyle, T. F. Fuller et J. Newman, «Modeling of Galvanostatic Charge and Discharge of the Lithium/Polymer/Insertion Cell,» *J. Electrochem. Soc.,* vol. 140, pp. 1526-1533, 1993.

[20] N. Dufour, M. Chandesris, S. Geniès, M. Cugnet et Y. Bultel, «Lithiation heterogeneities of graphite according to C-rate and mass-loading: A model study,» *Electrochimica Acta,* vol. 272, pp. 97-107, 2018.

[21] J. Newman et W. Tiedemann, «Porous-electrode theory with battery applications,» *AIChE J.,* vol. 21, pp. 25-41, 1975.

[22] R. Levie, «On porous electrodes in electrolyte solutions - IV,» *Electrochimica Acta,* vol. 9, pp. 1231-1245, 1964.

[23] I. A. J. Gordon, S. Grugeon, H. Takenouti, B. Tribollet, M. Armand, C. Davoisne, A. Débart et S. Laruelle, «Electrochemical Impedance Spectroscopy response study of a commercial graphite-based negative electrode for Li-ion batteries as function of the cell state of charge and ageing,» *Electrochimica Acta,* vol. 223, pp. 63-73, 2017.

[24] J. Illig, M. Ender, A. Weber et E. Ivers-Tiffée, «Modeling graphite anodes with serial and transmission line models,» *Journal of Power Sources,* vol. 282, pp. 335-347, 2015.

[25] A. Jokar, B. Rajabloo, M. D\'esilets et M. Lacroix, «Review of simplified Pseudo-two-Dimensional models of lithium-ion batteries,» *Journal of Power Sources,* vol. 327, pp. 44-55, 2016.

[26] J. Li, N. Lotfi, R. G. Landers et J. Park, «A Single Particle Model for Lithium-Ion Batteries with Electrolyte and Stress-Enhanced Diffusion Physics,» *Journal of The Electrochemical Society,* vol. 164, pp. A874-A883, 2017.

[27] J. P. Meyers, M. Doyle, R. M. Darling et J. Newman, «The Impedance Response of a Porous Electrode Composed of Intercalation Particles,» *Journal of The Electrochemical Society,* vol. 147, pp. 2930-2940, 2000.

[28] M.Doyle, J.-P. Meyers et J. Newman, «Computer simulations of the impedance response of lithium rechargeable batteries,» *Journal of the Electrochemical Society,* vol. 147, pp. 99-110, 2000.

[29] G. Sikha et R. E. White, «Analytical Expression for the Impedance Response of an Insertion Electrode Cell,» *Journal of The Electrochemical Society,* vol. 154, p. A43, 2007.

[30] J.Huang, H.Ge, Z. Li et J. Zhang, «An Agglomerate Model for the Impedance of Secondary Particle in Lithium-Ion Battery Electrode,» *Journal of The Electrochemical Society,* vol. 161, pp. E3202-E3215, 2014.

[31] E. Kuhn, C. Forgez, P. Lagonotte et G. Friedrich, «Modelling Ni-mH battery using Cauer and Foster structures,» *Journal of Power Sources,* vol. 158, p. 490–1497, 2006.

[32] Y. Reynier, C. Vincens, C. Leys, B. Amestoy, E. Mayousse, B. Chavillon, L. Blanc, E. Gutel, W. Porcher, T. Hirose et C. Matsui, «Practical implementation of Li doped SiO in high energy density 21700 cell,» *Journal of Power Sources,* vol. 450, p. 227699, 2020.

[33] D. M. Bernardi et J.-Y. Go, «Analysis of pulse and relaxation behavior in lithium-ion batteries,» *Journal of Power Sources,* vol. 196, pp. 412-427, 2011.

[34] M. Ender, A. Weber et I.-T. Ellen, «Analysis of Three-Electrode Setups for AC-Impedance Measurements on Lithium-Ion Cells by FEM simulations,» *Journal of The Electrochemical Society,* vol. 159, pp. A128-A136, 2011.

[35] R. Tatara, P. Karayaylali, Y. Yu, Y. Zhang et L. Giordano, «The effect of electrode-electrolyte interface on the electrochemical impedance spectra for positive electrode in Li-Ion Battery,» *Journal of The Electrochemical Society,*, vol. 166, pp. A5090-A5098, 2019.

[36] D. Juarez-Robles, C.-F. Chen, Y. Barsukov et P.-P. Mukherjeea, «Impedance Evolution Characteristics in Lithium-Ion Batteries,» *Journal of The Electrochemical Society,* vol. 164, pp. A837-A847, 2017.

[37] I.-J. Gordon, S. Grugeon, A. Débart, G.Pascaly et S.Laruelle, «Electrode contributions to the impedance of a high-energy density Li-ion cell designed for EV applications,» *Solid State Ionics,* vol. 237, pp. 50-55, 2013.

[38] M-D.Levi, V.Dargel, Y.Shilina, D. Aurbach et I.-C. Halalay, «Impedance Spectra of Energy-Storage Electrodes Obtained with Commercial Three-Electrode Cells: Some Sources of Measurement Artefacts,» *Electrochimica Acta,* vol. 149, pp. 126-135, 2014.

[39] J. Costard, M. Ender, M. Weiss et E. Ivers-Tiffée, «Three-Electrode Setups for Lithium-Ion Batteries: II. Experimental Study of Different Reference Electrode Designs and Their Implications for Half-Cell Impedance Spectra,» *Journal of The Electrochemical Society,* vol. 164, pp. A80-A87, 2017.

[40] R. Zeh, F. Kindermann, R. Karl, H. Gasteiger et A. Jossen, Écrivains, *Electrode optimization and behavior of LTO/LFP electrodes for applications in lithium ion batteries.* [Performance]. Technical University of Munich, 2019.

[41] D. P. Abraham, D. w. Dees et S. Kawauchi, «Modeling the impedance versus voltage characteristics of LiNi(0.8)Co(0.15)Al(0.005)O(2),» *Electrochimica Acta,* vol. 53, pp. 2121-2129, 2008.

[42] A. Zaban, E. Zinigrad et D. Aurbach, «Impedance Spectroscopy of Li Electrodes. A General Simple Model of the Li-Solution Interphase in Polar Aprotic Systems,» *J. Phys. Chem.,* vol. 100, pp. 3089-3101, 1 1996.

[43] D. Aurbach, «Impedance Spectroscopy of Nonactive Metal Electrodes at Low Potentials in Propylene Carbonate Solutions,» *J. Electrochem. Soc.,* vol. 141, p. 1808, 1994.

[44] J. Illig, J. P. Schmidt, M. Weiss, A. Weber et E. Ivers-Tiff\'ee, «Understanding the impedance spectrum of 18650 LiFePO4-cells,» *Journal of Power Sources,* vol. 239, pp. 670-679, 2013.

[45] A. Martinent, B. L. Gorrec, C. Montella et R. Yazami, «Three-electrode button cell for {EIS} investigation of graphite electrode,» *Journal of Power Sources,* vol. 97–98, pp. 83-86, 2001.

[46] J. G. Thevenin, «Impedance of Lithium Electrodes in a Propylene Carbonate Electrolyte,» *J. Electrochem. Soc.,* vol. 134, p. 273, 1987.

[47] H. Schranzhofer, J. Bugajski, H. J. Santner, C. Korepp, K.-C. Möller, J. O. Besenhard, M. Winter et W. Sitte, «Electrochemical impedance spectroscopy study of the SEI formation on graphite and metal electrodes,» *Journal of Power Sources,* vol. 153, pp. 391-395, 2006.

[48] J. Huang, H. Ge, Z. Li et J. Zhang, «An Agglomerate Model for the Impedance of Secondary Particle in Lithium-Ion Battery Electrode,» *Journal of The Electrochemical Society,* vol. 161, pp. E3202-E3215, 2014.

[49] P. Arora, B. N. Popov et R. E. White, «Electrochemical Investigations of Cobalt-Doped LiMn2O4 as Cathode Material for Lithium-Ion Batteries,» *Journal of The Electrochemical Society,* vol. 145, pp. 807-815, 1998.

[50] W. Weppner et R. A. Huggins, «Determination of the Kinetic Parameters of Mixed-Conducting Electrodes and Application to the System Li3Sb,» *Journal of The Electrochemical Society,* vol. 124, pp. 1569-1578, 1977.

[51] D. W. Dees, S. Kawauchi, D. P. Abraham et J. Prakash, «Analysis of the Galvanostatic Intermittent Titration Technique (GITT) as applied to a lithium-ion porous electrode,» *Journal of Power Sources,* vol. 189, pp. 263-268, 2009.

[52] E. Markevich, M. D. Levi et D. Aurbach, «Comparison between potentiostatic and galvanostatic intermittent titration techniques for determination of chemical diffusion coefficients in ion-insertion electrodes,» *Journal of Electroanalytical Chemistry,* vol. 580, pp. 231-237, 2005.

[53] C. J. Wen, B. A. Boukamp, R. A. Huggins et W. Weppner, «Thermodynamic and Mass Transport Properties of LiAl,» *J. Electrochem. Soc,* vol. 126, n° %112, pp. 2258-2266, 1979.

[54] J. R. Dahn, «Phase diagram of LiC6,» *Phys. Rev. B,* vol. 44, n° %117, pp. 9170-9177, 11 1991.

[55] H. S. CARSLAW et J. C. JAEGER, Conduction of heat in solids, Oxford: Clarendon Press, 1959.

[56] K. Smith et C. Wang, «Solid-state diffusion limitations on pulse operation of a lithium ion cell for hybrid electric vehicles,» *Journal of Power Sources*, vol. 161, p. 628–639, 2006.

[57] E. Allcorn, S. O. Kim et A. Manthiram, «Lithium diffusivity in antimony-based intermetallic and FeSb–TiC composite anodes as measured by GITT,» *Phys. Chem. Chem. Phys.,* vol. 17, n° %143, pp. 28837-28843, 2015.

[58] X. H. Rui, N. Ding, J. Liu, C. Li et C. H. Chen, «Analysis of the chemical diffusion coefficient of lithium ions in Li3V2(PO4)3 cathode material,» *Electrochimica Acta,* vol. 55, pp. 2384-2390, 2010.

[59] M. Ecker, T. K. D. Tran, P. Dechent, S. Katz, A. Warnecke et D. U. Sauer, «Parameterization of a Physico-Chemical Model of a Lithium-Ion Battery: I. Determination of Parameters,» *Journal of The Electrochemical Society,* vol. 162, pp. A1836-A1848, 2015.

[60] S. Malifarge, B. Delobel et C. Delacourt, «Guidelines for the Analysis of Data from the Potentiostatic Intermittent Titration Technique on Battery Electrodes,» *Journal of The Electrochemical Society,* vol. 164, pp. A3925-A3932, 2017.

[61] Q. Wang, C.-H. Shen, S.-Y. Shen, Y.-F. Xu, C.-G. Shi, L. Huang, J.-T. Li et S.-G. Sun, «Origin of Structural Evolution in Capacity Degradation for Overcharged NMC622 via Operando Coupled Investigation,» *ACS Applied Materials & Interfaces,* vol. 9, pp. 24731-24742, 7 2017.

[62] J. Xu, E. Hu, D. Nordlund, A. Mehta, S. Ehrlich, X. Yang et W. Tong, «Understanding the Degradation Mechanism of Lithium Nickel Oxide Cathodes for Li-Ion Batteries,» *ACS Applied Materials and Interfaces,* vol. 8, p. 31677−31683, 2016.

[63] S. Zheng, C. Hong, X. Guan, Y. Xiang, X. Liu, G. Xu, R. Liu, G. Zhong, F. Zheng, Y. Li, X. Zhang, Y. Ren, Z. Chen, K.Amine et Y. Yang, «Correlation between long range and local structural changes in Ni-rich layered materials during charge and discharge process,» *Journal of Power Sources,* vol. 412, pp. 336-343, 2019.

[64] J. Nielsen et J. Hjelm, «Impedance of SOFC electrodes: A review and a comprehensive case study on the impedance of LSM:YSZ cathodes,» *Electrochimica Acta,* vol. 115, pp. 31-45, 2014.

[65] R. Levie, «On the impedance of electrodes with rough interfaces,» *Journal of Electroanalytical Chemistry and Interfacial Electrochemistry,* vol. 261, pp. 1-9, 1989.

[66] A. M. Colclasure et R. J. Kee, «Thermodynamically consistent modeling of elementary electrochemistry in lithium-ion batteries,» *Electrochimica Acta,* vol. 55, pp. 8960-8973, 2010.

[67] E. Prada, D. Di Domenico, Y. Creff, J. Bernard, V. Sauvant-Moynot et F. Huet, «Simplified Electrochemical and Thermal Model of LiFePO4-Graphite Li-Ion Batteries for Fast Charge Applications,» *Journal of The Electrochemical Society,* vol. 159, pp. A1508-A1519, 2012.

[68] P. C. Tsai, B. Wen, M. Wolfman, M. Choe, M. S. Pan, Li.Su, K.Thornton, J. Cabana et Y. Chiang, «Single-particle measurements of electrochemical kinetics in NMC and NCA cathodes for Li-ionbatteries,» *Energy and Environmental Science,* vol. 11, pp. 860-871, 2018.

[69] M. Z. Bazant, «Thermodynamic stability of driven open systems and control of phase separation by electro-autocatalysis,» *Faraday Discussions,* vol. 199, pp. 423-463, 2017.

[70] T. R. Ferguson et M. Z. Bazant, «Nonequilibrium Thermodynamics of Porous Electrodes,» *Journal of The Electrochemical Society,* vol. 159, pp. A1967-A1985, 2012.

[71] M. Doyle et J. Newman, «Modeling the performance of rechargeable lithium-based cells: design correlations for limiting cases,» *Journal of Power Sources,* vol. 54, pp. 46-51, 1995.

[72] A. J. Bard et L. R. Faulkner, Electrochemical Methods : Fundamentals and Application, 2nd éd., John Wiley and Sons, 2001.

[73] P. Ramadass, B. Haran, R. White et B. N. Popov, «Capacity fade of Sony 18650 cells cycled at elevated temperatures: Part I. Cycling performance,» *Journal of Power Sources,* vol. 112, pp. 606-613, 2002.

[74] J.Zhu, S. S-Asl, J.-C. Garcia, H.-H. Iddir, J.-R. Croy, R. Shahbazian-Yassar et G. Chen, «Atomic-Level Understanding of Surface Reconstruction Based on Li[NixMnyCo1−x−y]O2 Single-Crystal Studies,» *ACS Appl. Energy Mater,* vol. 3, pp. 4799-4811, 2020.

[75] T.-P. Heins, N. Harms, L.-S. Schramm et U. Schrçder, «Development of a new Electrochemical Impedance Spectroscopy Approach for Monitoring the Solid Electrolyte Interphase Formation,» *Energy technology,* vol. 4, pp. 1509-1503, 2016.

[76] N. Ghanbari, T. Waldmann, M. Kasper, P. Axmann et M. Wohlfahrt-Mehrens, «Inhomogeneous Degradation of Graphite Anodes in Li-Ion Cells: A Postmortem Study Using Glow Discharge Optical Emission Spectroscopy (GD-OES),» *The Journal of Physical Chemistry C,* vol. 120, pp. 22225-22234, 2016.

[77] T. Li, X. Yuan, L. Zhang, D. Song, K. Shi et C. Bock, «Degradation Mechanisms and Mitigation Strategies of Nickel-Rich NMC-Based Lithium-Ion Batteries,» *Electrochemical Energy Reviews,* vol. 3, pp. 43-80, 2020.

[78] G. Ning, B. Haran et B. N. Popov, «Capacity fade study of lithium-ion batteries cycled at high discharge rates,» *Journal of Power Sources,* vol. 117, pp. 160-169, 5 2003.

[79] J. Randles, «Kinetics of rapid electrode reactions,» *Discussions of the Faraday Society,* 1947.

[80] T. R. Ferguson, «Lithium-Ion Battery Modeling using Nonequilibrium Thermodynamics,» 2014.

[81] L. Lavigne, J. Sabatier, J. M. Francisco, F. Guillemard et A. Noury, «Lithium-ion Open Circuit Voltage (OCV) curve modelling and its ageing adjustment,» *Journal of Power Sources,* vol. 324, pp. 694-703, 2016.

[82] D. K. Karthikeyan, G. Sikha et R. E. White, «Thermodynamic model development for lithium intercalation electrodes,» *Journal of Power Sources,* vol. 185, pp. 1398-1407, 2008.

[83] I. J. Ong et J. Newman, «Double-Layer Capacitance in a Dual Lithium Ion Insertion Cell,» *Journal of The Electrochemical Society,* vol. 146, pp. 4360-4365, 1999.

[84] D. Gruet, B. Delobel, D. Sicsic, I. T. Lucas et V. Vivier, «On the electrochemical impedance response of composite insertion electrodes. Toward a better understanding of porous electrodes,» *Electrochimica Acta,* vol. 295, pp. 787-800, 2019.

[85] A. Berrueta, A. Urtasun, A. Ursúa et P. Sanchis, «A comprehensive model for lithium-ion batteries: From the physical principles to an electrical model,» *Energy,* vol. 144, pp. 286-300, 2018.

[86] T. F. Fuller, M. Doyle et J. Newman, «Simulation and Optimization of the Dual Lithium Ion Insertion Cell,» *Journal of The Electrochemical Society,* vol. 141, pp. 1-10, 1994.

[87] J. Song et M. Z. Bazant, «Effects of Nanoparticle Geometry and Size Distribution on Diffusion Impedance of Battery Electrodes,» *ECS,* vol. 160, pp. A15-A24, 2013.

[88] M. chandesris, C. Robin, M. Gereard et Y. Bultel, «Investigation of the difference between the low frequency limit of impedance spectrum and the slope of the polarizationcurve,» *Electrochimica Acta,* vol. 180, pp. 581-590, 2018.

[89] M. Z. Bazant, «Theory of chemical kinetics and charge transfer based on nonequilibrium thermodynamics,» *Accountes of chemical research,* vol. 46, p. 1144, 2013.

[90] M. Schönleber, C. Uhlmann, P. Braun, A. Weber et E. Ivers-Tiffée, «A Consistent Derivation of the Impedance of a Lithium-Ion Battery Electrode and its Dependency on the State-of-Charge,» *Journal of Electrochimica Acta,* vol. 243, pp. 250-259, 2017.

[91] S. Cruz-Manzo et P. Greenwood, «Blocked-Diffusion with Frequency Dispersion for Study of EIS in NiMH Batteries,» *Journal of The Electrochemical Society,* vol. 166, pp. A1176-A1184, 2019.

[92] J. B. Jorcin, M. E. Orazem, N. P\'ebère et B. Tribollet, «CPE analysis by local electrochemical impedance spectroscopy,» *Electrochimica Acta,* vol. 51, n° %18-9, pp. 1473-1479, 2006.

[93] J. Illig, M. Ender, A. Weber et E. Ivers-Tiffee, «Modeling graphite anodes with serial and transmission line models,» *J. Power Sources,* vol. 282, pp. 335-347, 2015.

[94] T. Takamatsu et O. H, «Online Parameter Estimation for Lithium-Ion Battery by Using Adaptive Observer for Fractional-Order System,» *Electronics and Communications in Japan,*, vol. 101, pp. 80-89, 2018.

[95] R. M. Foster, «A Reactance Theorem,» *journal of Bell Syst. Tech.*, vol. 3, p. 259–267, 1924.

[96] J. Huang, Z. Li, J. Zhang, S. Song, Z. Lou et N. Wu, «An Analytical Three-Scale Impedance Model for Porous Electrode with Agglomerates in Lithium-Ion Batteries,» *Journal of The Electrochemical Society,* vol. 162, pp. A585-A595, 2015.

[97] J. Vetter, P. Novak, M. R. Wagner, C. Veit, K.-C. Moller, J. O. Besenhard, M. Winter, M. Wohlfahrt-Mehrens, C. Vogler et A. Hammouche, «Ageing mechanisms in lithium-ion batteries,» *Journal of Power Sources,* vol. 147, pp. 269-281, 2005.

[98] J. Christensen et J. Newman, «Cyclable Lithium and Capacity Loss in Li-Ion Cells,» *Journal of The Electrochemical Society,* vol. 152, pp. A818-A829, 2005.

[99] A. Barre, B. Deguilhem, S. Grolleau, M. Gerard, F. Suard et D. Riu, «A review on lithium-ion battery ageing mechanisms and estimations for automotive applications,» *Journal of Power Sources,* vol. 241, pp. 680-689, 2013.

[100] R. Xiong, Y.Pan, W.Shen, H.Li et F.Sun, «Lithium-ion battery aging mechanisms and diagnosis method for automotive applications: Recent advances and perspectives,» *journal of Renewable and Sustainable Energy Reviews,* vol. 131, 2020.

[101] C. R. Birkl, M. R. Roberts, E. McTurk, P. G. Bruce et D. A. Howey, «Degradation diagnostics for lithium ion cells,» *Journal of Power Sources,* vol. 341, pp. 373-386, 2017.

[102] O. Borodin, X. Ren, J. Vatamanu, A. v. Cresce, J. Knap et K. Xu., «Modeling insight into battery electrolyte electrochemical stability and interfacial structure,» *Accounts of Chemical Research,* vol. 12, p. 2886–2894, 2017.

[103] J.-P. Gabano, Lithium Stability and Film Formation in Organic and Inorganic Electrolytes for Lithium Battery Systems, in Lithium Batteries, London: Academic Press, 1983.

[104] H. Buqa, A. Würsig, J. Vetter, M. Spahr, F. Krumeich et P. Novák, «SEI film formation on highly crystalline graphitic materials in lithium-ion batteries,» *Journal of Power Sources,* vol. 153, pp. 385-390, 2006.

[105] Y. Zhao, S.-Y. Choe et J. Kee, «Modeling of degradation effects and its integration intoelectrochemical reduced order model for Li(MnNiCo)O2/Graphitepolymer battery for real time applications,» *journal of Electrochimica Acta,* vol. 270, pp. 440-452, 2018.

[106] J.-A. Gilbert, I.-A. Shkrob et D.-P. Abraham, «Transition Metal Dissolution, Ion Migration, Electrocatalytic Reduction and Capacity Loss in Lithium-Ion Full Cells,» *Journal of the Electrochemical Society,* vol. 164, pp. A389-A399, 2017.

[107] Z. Li, J. Huang, B. Y. Liaw, V. Metzler et J. Zhang, «A review of lithium deposition in lithium-ion and lithium metal secondary batteries,» *Journal of Power Sources,* vol. 254, pp. 168-182, 2014.

[108] J.-K. Stark, Y. Ding et P. Kohla, «Dendrite-Free Electrodeposition and Reoxidation of Lithium-Sodium Alloy for Metal-Anode Battery,» *Journal of The Electrochemical Society,* vol. 158, pp. A1100-A1105, 2011.

[109] R. Mogi, M.Inaba, S.-K. Jeong, Y.Iriyama, T. Abe et Z. Ogumia, «Effects of Some Organic Additives on Lithium Deposition in Propylene Carbonate,» *Journal of The Electrochemical Society,* vol. 149, pp. A1578-A1583, 2002.

[110] S-I.Tobishima, H. Yamamoto et M. Matsuda, «Study on the reduction species of sulfur by alkali metals in nonaqueous solvents,» *journal of Electrochimica Acta*, vol. 42, pp. 1019-1029, 1997.

[111] C. Delacourt, A. Kwong, X. Liu, R. Qiao, W. L. Yang, P. Lu, S. J. Harris et V. Srinivasan, «Effect of Manganese Contamination on the Solid-Electrolyte-Interphase Properties in Li-Ion Batteries,» *Journal of The Electrochemical Society*, vol. 160, pp. A1099-A1107 , 2013.

[112] M. Cugnet, M. Dubarry et B. Y. Liaw, «Modeling,» *Encyclopedia of Electrochemical Power Sources*, vol. 4, pp. 816-828, 2009.

[113] J. Xu, E. Hu, D. Nordlund, A. Mehta, S. N. Ehrlich, X.-Q. Yang et W. Tong, «Understanding the Degradation Mechanism of Lithium Nickel Oxide Cathodes for Li-Ion Batteries,» *ACS Applied Materials \& Interfaces*, vol. 8, pp. 31677-31683, 2016.

[114] D. Aurbach, B. Markovsky, G. Salitra et E. M. e. al., «Review on electrode–electrolyte solution interactions, related to cathode materials for Li-ion batteries,» *journal of Power Sources*, vol. 165, pp. 491-499, 2007.

[115] J.-H. Kim, S. C. Woo, M.-S. Park, K. J. Kim, T. Yim, J.-S. Kim et Y.-J. Kim, «Capacity fading mechanism of LiFePO4 based lithium secondary batteries for stationary energy storage,» *Journal of Power Sources*, vol. 229, pp. 190-197, 2013.

[116] J. Christensen et J. Newman, «A Mathematical Model for the Lithium-Ion Negative Electrode Solid Electrolyte Interphase,» *Journal of The Electrochemical Society*, vol. 151, pp. A1977-A1988, 2004.

[117] S. Das, P. M. Attia, W. C. Chueh et M. Z. Bazant, «Electrochemical kinetics of SEI growth on carbon black II: Modeling,» *Journal of the Electrochemical Society*, vol. 166, pp. E107-E118, 2019.

[118] L. Guangyu et L. Wei, «A Model of Concurrent Lithium Dendrite Growth, SEI Growth,SEI Penetration and Regrowth,» *Journal of The Electrochemical Society*, vol. 164, pp. A1826-A1833, 2017.

Annex

Experimental and theoretical investigation of Li-ion battery active materials properties: application to a graphite/ $Ni_{0.6}Mn_{0.2}Co_{0.2}O_2$ system

Oumaima Chaouachi[a,b], Jean-Michel Réty[a], Sylvie Génies[b], Marion Chandesris[b*],Yann Bultel[c]

[a]*Forsee Power, 1 Boulevard Hippolyte Marquès, 75013 Paris, France*

[b]*Univ Grenoble Alpes, CEA LITEN 17 Rue des Martyrs, F-38054 Grenoble Cedex 9, France*

[c]*Univ. Grenoble Alpes, Univ. Savoie Mont Blanc, CNRS, Grenoble INP, LEPMI, 38000 Grenoble, France*

*marion.chandesris@cea.fr

Keywords: Li-ion batteries, electrochemical impedance spectroscopy, Modeling, active material properties, Reference electrode

Abstract:

The knowledge of active materials properties and their evolution with aging is crucial to simulate and predict with a high reliability the electrochemical performance of lithium-ion batteries. In view of developing more accurate physics-based Lithium Ion Battery (LIB) models, this paper aims to present a consistent framework, including both experiments and theory, in order to retrieve the active material properties of commonly used electrodes made of graphite at the negative and $Ni_{0.6}Mn_{0.2}Co_{0.2}O_2$ (NMC 622) at the positive, as function of the active materials stoichiometry. To measure the equilibrium potential and the solid diffusion coefficient, Galvanostatic Intermittent Titration Technique (GITT) measurements were used. Electrochemical impedance spectroscopy (EIS) measurements with reference electrodes were performed to determine the exchange current density using the transmission line model. The measured stoichiometry dependence of these three active material properties has been further analyzed, based on thermodynamic considerations. For the positive material, a model is proposed highlighting the non-ideal behavior of lithium inside the host material. The thermodynamic relations available in the literature are not directly transposable to the $Ni_{0.6}Mn_{0.2}Co_{0.2}O_2$ material, suggesting the necessity to account for supplementary terms. Nevertheless, the proposed stoichiometry dependent laws determined with the same stoichiometry definition go already beyond most reported values for the $Ni_{0.6}Mn_{0.2}Co_{0.2}O_2$ and can be used to increase the predictability of multi-physics lithium-ion battery models.

1. Introduction

Lithium ion batteries (LIB) have been considered as a technological and commercial success since their first commercialization by SONY in 1991. Due to their advantageous characteristics such as their high energy density and power capabilities, this technology is equipping a growing number of applications ranging from small-scale electronic gadgets to automotive vehicles [8]. Optimization of LIB performances for various usages requires the understanding and the knowledge of the different physical mechanisms of the battery with a sound quantification. Mathematical models are a useful tool to decouple and to quantify these different mechanisms, and to understand their evolution along the lifetime of the battery. A huge research effort devoted to battery modeling started in the 60s with different approaches such as Equivalent Electric Circuit (EEC) models [18], but also electrochemical ones like the so called porous electrode model introduced by Newman and Tiedeman in 1975 [19, 20] and applied on LIB in the 90s [21]. On one hand, EEC models, considered as semi-empirical models, simplify the multi-physics behavior of the cell to obtain a representation with an electric circuit, which makes them easy to implement in a Battery Management System (BMS). On the other hand, electrochemical models, based on the computation of physical phenomena at the electrode scale, allow predicting the electrochemical behavior of the system, for various operating conditions and/or electrodes designs, which make them a powerful tool for optimization. These models however require an accurate description and a coupling of the different physics, to account for electrochemical reactions, mass and charge transports as well as thermal effects. In particular, the knowledge of the physical properties of the different components of the LIB is key in this approach to ensure a high level of predictability. Among these physical properties, it is crucial to determine accurately those related to the active materials, such as the equilibrium potential, the lithium solid diffusion or the exchange current density as these properties are affecting significantly the models results.

Up to day, many studies have been carried out to understand the physical and electrochemical mechanisms that take place in the different cell components, to determine the most important physical parameters and how they can be implemented in models. In the literature, many experimental protocols are proposed to measure geometric and physical parameters of the electrodes such as electronic conductivity, porosity, active material equilibrium potential or lithium diffusion coefficient [59]. Electrochemical Impedance Spectroscopy (EIS) has been considered as a standard method to estimate fundamental physical properties, to investigate

reaction mechanisms and to characterize batteries [8], [42], [43], [44]. It is an effective tool to follow concurrently the resistive, capacitive and the inductive behaviors of the system. The exploitation of the EIS results can help to figure out many physical phenomena such as solid phase diffusion, charge transfer kinetics and ion transport by using their frequency dependent characteristics. Moreover, in the literature, EIS measurements have been used to study electrode/electrolyte interface [45], electrolyte performance [46], and to evaluate the aging by following the SEI resistance [47], [48]. It has been also used to study the kinetics of charge transfer in Li-ion batteries and evaluate precisely the exchange current density i_0. Generally, a simple R-C element model is implemented to extract i_0 from an impedance spectrum [49]. However, this model assumes a semi-circle shape for the charge transfer resistance in the impedance spectra which is not always observed in the experiments with porous electrodes. Transmission line model (TLM) [64], [24] is more appropriate to take into account the non-semicircle shape of the impedance spectra in the middle to high frequency range that porous electrode may cause. Another central electrochemical technique to determine active material properties is the Galvanostatic Intermittent Titration Technique (GITT). Since the pioneering work of Weppner and Huggins [50], it has been used with a growing interest to retrieve the equilibrium potential and transport parameters of various active materials [50], [51], [52], [59].

Regarding active material properties, equilibrium potential curves with a dependence on the stoichiometry are most of the time implemented in multi-physics models, as this dependence is well recognized. Furthermore, to simplify their implementation in the different models, analytic expressions are sometimes suggested as the one proposed by Doyles (1995) [71] to model the equilibrium potential of the active material as function of the state of charge (SOC). However, this stoichiometry dependence is rarely transposed to the other active material properties. Indeed, many models use constant values for the solid diffusion D_s while the exchange current density i_0, is modeled with a stoichiometry dependence of the form $y^{\alpha}(1-y)^{1-\alpha}$ arising from the classical Butler-Volmer relation [121], [122]. Such an approach does not take into consideration the non-ideal interactions between ions in intercalation materials and does not take into account the interdependence between the active material properties. A more thermodynamically consistent approach has been proposed by Bazant studying the electrochemical kinetic of Li insertion in lithium iron phosphate ($LiFePO_4$) active materials [70]. This approach highlights the links between the active material properties toward the stoichiometry dependence and provides expressions that can be implemented in LIB models. If this thermodynamic approach exists for $LiFePO_4$ active materials, it is however missing for

other active materials currently used in commercial cells, such as graphite or transition metal oxides of the Ni-Mn-Co family.

In view of developing more accurate physics-based LIB models, this paper aims to present a consistent framework, including both experiments and theory, in order to retrieve the active material properties of commonly used electrodes made of graphite at the negative and $Ni_{0.6}Mn_{0.2}Co_{0.2}O_2$ at the positive, as function of the active materials stoichiometry. To measure the equilibrium potential and the solid diffusion coefficient, GITT measurements were used, while EIS measurements with reference electrodes were performed to determine the exchange current density and were analyzed using a TLM model [64], [24]. Then, the measured stoichiometry dependence of these three active material parameters is further analyzed, based on thermodynamic considerations. For the $Ni_{0.6}Mn_{0.2}Co_{0.2}O_2$ active material, a model is proposed to account for this observed stoichiometry dependence, highlighting the non-ideal molecular behavior of lithium inside the host material.

2. Experimental

2.1 Materials:

A NMC-based positive electrode (PE) was prepared by coating a dispersion of a polycristalline Li-$Ni_{0.6}Mn_{0.2}Co_{0.2}O_2$ (Umicore), Super P65 (Imerys) with an exchange surface area of 65m²/g and VGCF-H from Showa Denko as carbon conductive additive and PolyVinyliDene Fluoride (PVDF) as a binder with 92:2:2:4 weight ratio, on an aluminum foil. The graphite-based negative electrode (NE) was prepared similarly, by using a mixture of spherical graphite with CMC (Ashland) and SBR (BASF) binders (sodium carboxymethyl cellulose and styrene butadiene rubber) with 97.4:1.3:1.3 weight ratio, coated on a copper foil. The average particles sizes $\boldsymbol{r_{50}}$ have been measured by laser granulometry and are around 6.6µm for the $Ni_{0.6}Mn_{0.2}Co_{0.2}O_2$ and 7.88µm for the graphite.

The two electrodes were prepared using a laboratory in house process [32]. The components were mixed using a planetary mixer, using deionized water as solvent for the negative electrode and NMP solvent for the positive electrode. The slurry was then coated onto the current collectors. A custom reverse roll coater installed in dry room with 1.5 m drying oven was used for both electrodes which were then calendared to reach the desired porosity. They were manufactured considering a loading of 18.2 mg/cm² for the positive and 10.8 mg/cm² for the graphite with a porosity of 24% and 26% respectively. With the estimated reversible capacity, these loadings correspond to 3.43 mAh/cm² and 3.78 mAh/cm², which leads to a face to face

N/P ratio of 1.1. The separator is a 25 µm thick mono-layer (PP) Celgard 2400. The electrolyte (UBE) consists of 1M of lithium hexafluorophosphate (LiPF6) in 1:1:1 weight proportion of ethylene carbonate (EC), ethyl methyl carbonate (EMC), and dimethyl carbonate (DMC), whose purity limit is 5 ppm of H2O, 10 ppm of HF. For the different designs, the electrolyte is put in large excess to get a full wetting of the electrodes and avoid electrolyte starvation.

2.2 Designs:

The first design is a so-called half-cell design in coin cell (CC) format. It is a CR2032 coin cell format made of stainless steel and it consists of a top cover, bottom container spacer and spring. This design consists of the tested active materials electrode as working electrode (graphite in case of the NE and $Ni_{0.6}Mn_{0.2}Co_{0.2}O_2$ in case of the PE) with a 14mm diameter and a lithium foil as counter electrode, with a 16mm diameter. The exchange surface areas $\boldsymbol{S_{AM}}$ for this coin cell design are estimated from the knowledge of $\boldsymbol{r_{50}}$ and assuming that particles are spherical, giving a value around 3.31m² for the $Ni_{0.6}Mn_{0.2}Co_{0.2}O_2$ and 2.68m² for the graphite (Summary in table 1). This coin cell design will be used to perform GITT measurements in order to extract equilibrium potentials and diffusion coefficients of both active materials.

The second design is a pouch cell containing the two tested electrodes (graphite for the NE, $Ni_{0.6}Mn_{0.2}Co_{0.2}O_2$ for the PE) with a lithium foil reference electrode inserted between the PE and the separator an covered with an extra separator to avoid short circuit, as described Fig. 19a. An aluminum tab is ultrasonically welded to the positive electrode, while a nickel one is welded to the negative. The pouch cells are assembled in a dry room (-20°C dew point) and filled with electrolyte in an Argon filled glove box. The pouches are put under partial vacuum and the all sandwich is sealed using a heatsealer. The electrode surface areas $\boldsymbol{S_g}$ are for the positive electrode 10.24 cm² (3.2x3.2) and for the negative 12.25 cm² (3.5x3.5). These dimensions are chosen to ensure a good coverage of the positive electrode by the negative one, while trying to keep this mismatch as low as possible. Indeed, this mismatch implies an increase of the irreversible capacity with lithium consumed at the negative electrode during its first lithiation due to SEI formation. This area mismatch leads to a lower utilization of the cathode with, at the cell scale, an electrode capacity ratio N/P of 1.3 instead of the “face to face” N/P ratio of 1.1. The exchange surface areas $\boldsymbol{S_{AM}}$ for this pouch cell design are estimated from the knowledge of $\boldsymbol{r_{50}}$ giving a value around 22.03m² for the $Ni_{0.6}Mn_{0.2}Co_{0.2}O_2$ and 22.28m² for the graphite (Summary in table 1).

For EIS measurements, the choice of the reference electrode is a key issue. In the literature, lithium foil is often used as a reference electrode for electrochemical characterization in the conventional 3-electrode design (Fig. 1a) [123]. However, this kind of reference electrode suffers from a low stability [34] and can also cause artificial EIS response detected in Nyquist plots as a “spiral“ type behavior, leading to a lack of reproducibility [35]. These effects make them non-efficient for investigations during aging or involving impedance measurements. Alternative solutions are proposed in the literature to limit these effects. As reference electrodes must have a stable potential over a large SOC range, lithium titanate ($Li_4Ti_5O_{12}$) and $LiFePO_4$ have recently attracted considerable attentions as reference electrodes for EIS [36], [23], [37], [38], [39], [40]. For the present work, $LiFePO_4$ is used as a reference electrode. The electrode is prepared by mixing a commercial $LiFePO_4$ active material from BeLife with Super P65 as carbon conductive additive and PVDF as binder before a coating on an aluminum mesh. This reference electrode is inserted inside the 4-electrode pouch cell design presented Fig. 19b. The Li reference electrode is kept in the system to control the potential of the electrodes. A partial delithiation of $LiFePO_4$ is performed *in situ* once the cell is assembled and charged at a C/50 rate to reach the 3.48V *vs* Li^+/Li potential plateau and a stoichiometry of 0.5.

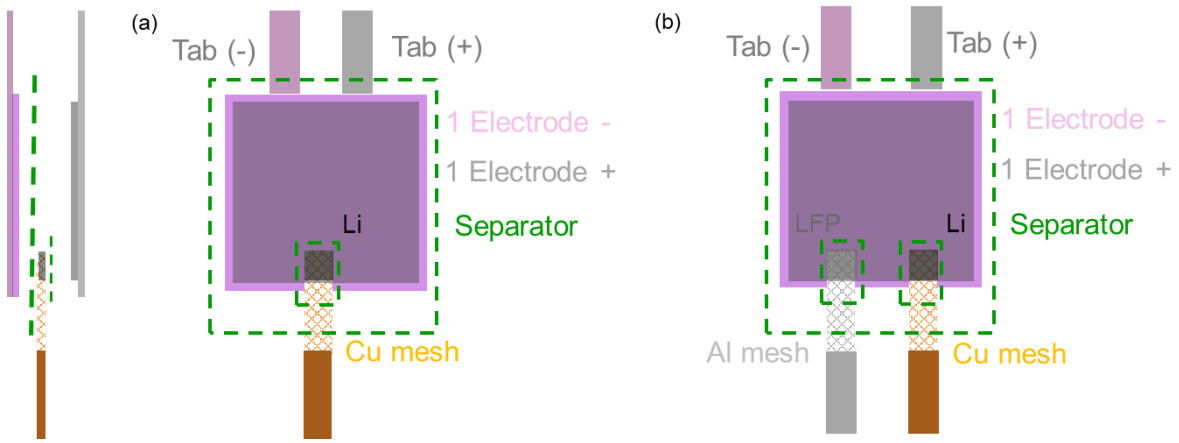

Fig. 19: Schematic description of (a) the 3-electrodes pouch cell design with (left) side view and (right) top view and (b) the 4- electrodes pouch cell design from top view.

The pouch cell design with one reference electrode has been used to perform a GITT measurement. The aim is to retrieve a relation between the SOC of the pouch cell design and the stoichiometries of the two active materials. The second design with two reference electrodes

has been used to perform EIS at different SOC and deduce the exchange current densities of the active materials as function of their stoichiometry.

2.3 Electrochemical measurements:

After assembly, pouchs are put in a mechanical homemade design, where a homogeneous force of roughly 100N is applied, which corresponds to a pressure of 1bar on the 10 cm² surface. A formation protocol at 25°C is applied to the coin and the pouch cells. For $Ni_{0.6}Mn_{0.2}Co_{0.2}O_2$ vs. Li coin cells, it consists of two full charge/discharge cycles between 2.6 and 4.3V at C/20. For graphite vs. Li coin cells and the pouch cell designs, it consists of one cycle at C/20 followed by 3 cycles at C/5 of full discharge/charge applied between 10mV and 1V and 2.5 and 4.2V respectively. This last protocol is performed to ensure the formation of a stable Solid Electrolyte Interphase (SEI) on the graphite particles. The C-rate for the formation cycles is estimated from the reversible capacity of the electrodes measured in dedicated experiments. For the subsequent C-rates, the capacity measured during the formation at C/20 is used to recompute the C-rate. All the electrochemical measurements on coin cells or pouch cells were performed using a modular potentiostat/galvanostat/EIS VMP3 from Bio-Logic, Seyssinet-Pariset, France.

GITT protocol: GITT experiment consists of series of current pulses at a fixed value followed by rest periods. This sequence is repeated until the battery is fully charged and discharged. This protocol is used to determine the equilibrium potential and lithium diffusion coefficient of active materials [50], [51], [52]. In this study, a series of pulses is applied to the cell at a fixed current of C/10 during 12 minutes, followed by a 4h relaxation time. The sequence is repeated 50 times until complete charge or discharge of the cell. GITT tests were performed on $Ni_{0.6}Mn_{0.2}Co_{0.2}O_2$ *vs.* Li and graphite *vs.* Li coin cells, as well as in the pouch cell design with a Li reference electrode. During the pulse period, data are recorded at every voltage increment/decrement of 1mV. The GITT protocol is applied after formation of the cells and is performed in both charge and discharge. It is started in charge for $Ni_{0.6}Mn_{0.2}Co_{0.2}O_2$ vs. Li and full cell configurations, and in discharge for graphite vs. Li.

Electrochemical Impedance Spectroscopy (EIS) protocol: During an EIS measurement, alternative sinusoidal potential excitations are applied to the electrochemical cell at various frequencies, while measuring the resulting currents. These current signals are analyzed at the different frequencies to obtain the cell impedance spectra. This measurement is performed by

using an excitation signal with a small amplitude to obtain the pseudo-linear response of the cell. In this study, Potentio-Electrochemical Impedance Spectroscopy (PEIS) measurements were performed at different SOC on the pouch cell with $LiFePO_4$ reference electrode. The measurements were done in potentiostatic mode with a voltage amplitude of 5mV. The frequency range was set to 200 kHz-0.1 mHz with 8 points per decade. Impedance spectra were measured at room temperature. To reach the desired SOC, a galvanostatic discharge at C/10 is applied during 1h, followed by a rest period of 1h to reach equilibrium before the PEIS measurement. This protocol is repeated 10 times to complete the lithiation process. It is applied in discharge after the cell formation protocol and a first charge of the cell until the cut off voltage of 4.2V.

3. Experimental results

In this section, we present the active material properties obtained from the electrochemical measurements. During the results analysis, special attention has been put on the stoichiometry determination to latter allow material properties comparison.

3.1 Equilibrium potential

Equilibrium potential, E_q of an active material inside an electrode is reached when the chemical potentials of lithium in both phases, *i.e.* at the interface between the active material and the electrolyte, are equal. Using GITT methods, E_q is identified at the end of each relaxation period [53]. For the coin cell designs, *i.e.* working electrode vs. Li, the measured open circuit potential (OCP) corresponds to the equilibrium potential of the studied material. The results obtained for $Ni_{0.6}Mn_{0.2}Co_{0.2}O_2$ and graphite in both lithiation and delithiation are shown Fig. 2 as function of the material stoichiometry, together with the averaged value.

For the graphite (Fig. 2a), the stoichiometry range is defined by assuming that, at the end of the first lithiation the material stoichiometry, $y_{max}^{CC,Gr}$ is equal to one, and by using the subsequent delithiation to determine the reversible capacity $Q_{rev}^{CC,Gr}$, which is reached in our case at 356 $\mathrm{mAh/g}$ with a first irreversible capacity ($Q_{irrev}^{CC,Gr}$) of 28 mAh/g. This value is slightly lower than the theoretical capacity Q_{th}^{Gr}equals to 372 $\mathrm{mAh/g}$. This theoretical capacity is used to calculate the minimum stoichiometry ($y_{min}^{CC,Gr}$) corresponding to the delithiated graphite, with the following equation, and we obtain a value of 0.045:

$$y_{min}^{CC,Gr} = \frac{Q_{th}^{Gr} - Q_{rev}^{CC,Gr}}{Q_{th}^{Gr}} \quad (20)$$

For the graphite (Fig. 2a), the three classical potential plateaus are observed with a slope close to zero and two transitions regions for stoichiometry around 0.17 and 0.5. A slight difference between the lithiation and delithiation curves is observed, but only during these transition regions. The potential plateaus correspond to coexistence of two-phases in the solid material, while only one phase exists in the transition regions [54]. The derivative of the equilibrium potential versus stoichiometry, obtained from the average value, is also presented and highlights the variation of the potential during the transition regions.

For the $Ni_{0.6}Mn_{0.2}Co_{0.2}O_2$, the stoichiometry range is calculated considering the theoretical value (Q_{th}^{NMC}) of 276.7 mAh/g and by assuming that the material is fully lithiated before formation. The measured reversible capacity ($Q_{rev}^{CC,NMC}$) of 184 mAh/g is determined from the lithiation step, by taking into account the first irreversible capacity ($Q_{irrev}^{CC,NMC}$) of 21 mAh/g. The maximum and minimum stoichiometries of $Ni_{0.6}Mn_{0.2}Co_{0.2}O_2$ in lithiation $y_{max}^{CC,NMC}$ and delithiation $y_{min}^{CC,NMC}$ are respectively given by:

$$y_{max}^{CC,NMC} = \frac{Q_{th}^{NMC} - Q_{irrev}^{CC,NMC}}{Q_{th}^{NMC}} \quad (21)$$

$$y_{min}^{CC,NMC} = \frac{Q_{th}^{NMC} - (Q_{rev}^{CC,NMC} + Q_{irrev}^{CC,NMC})}{Q_{th}^{NMC}} \quad (22)$$

Leading to a variation range of [0.259 – 0.92]

As presented in (Fig. 2b), there is almost no difference between lithiation and delithiation measurements, which confirm that the equilibrium state is reached at the end of the relaxation periods. The equilibrium potential for $Ni_{0.6}Mn_{0.2}Co_{0.2}O_2$ steadily decreases when the stoichiometry increases with a higher slope at low stoichiometry. It is highlighted on the derivative of the average equilibrium potential that the slope is almost constant for a stoichiometry above 0.65.

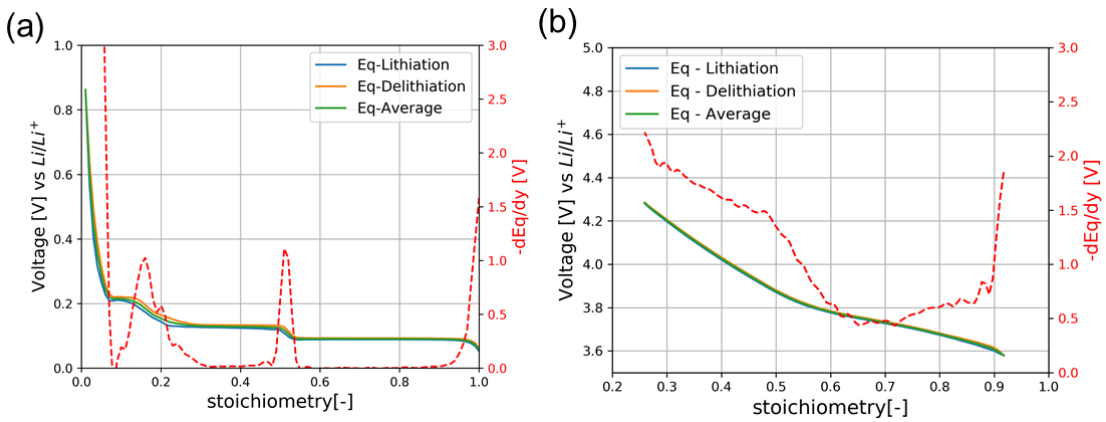

Fig. 20: Equilibrium potentials measured in half-cell configuration in lithiation and delithiation together with the average value and its derivative versus stoichiometry (a) Graphite vs Li (b) $Ni_{0.6}Mn_{0.2}Co_{0.2}O_2$ vs Li

For electrochemical experiments in full cell configuration, material properties are measured as function of the SOC of the cell. To get the active material properties as function of their own stoichiometry, a relation between the active materials stoichiometry and the SOC of the cell is required. In this work, we have used the GITT experiment in pouch cell format with a reference electrode to obtain these relations. Indeed, the lithium reference electrode gives access to the positive and negative equilibrium potentials within the full cell and allows following the stoichiometry variation range of both electrodes along the equilibrium curves.

Fig. 3a shows the cell OCP together with the electrode potentials extracted from the GITT experiment in the pouch cell format as function of the cell capacity. Computed OCP results of $Ni_{0.6}Mn_{0.2}Co_{0.2}O_2$ and graphite from the CC results are also presented as function of the pouch cell capacity Fig. 3a. To perform this comparison, the capacities of $Ni_{0.6}Mn_{0.2}Co_{0.2}O_2$ and graphite measured per masse of active material in the CC design, are multiplied by the masses of active material used in the pouch format. Furthermore, the computed CC results are then shifted so as to be superposed with the pouch cell results. A very good superposition is obtained. These operations allow to have a first overview of the stoichiometry ranges used for the two electrodes. We can notice that with the present design, only 56% of the negative electrode capacity is used. Indeed, as shown in Fig. 3a, the two upper plateaus of the graphite are used with the pouch format, and only a small portion of the lower one.

The maximum stoichiometry in the pouch design is calculated considering the theoretical capacity and the irreversible capacity of the pouch formation as:

$$y_{max}^{Pouch,NMC} = \frac{Q_{th}^{NMC} - Q_{irrev}^{pouchNMC}}{Q_{th}^{NMC}} \quad (23)$$

Since, the irreversible capacity $Q_{irrev}^{pouch,NMC}$ expressed as function of positive active material is higher in the pouch cell format due to SEI formation on the negative electrode and area mismatch, $Q_{irrev}^{pouch,NMC} = 42$ mAh/g, it leads to a maximum stoichiometry of 0.848, which is lower than in the coin cell format. The minimum stoichiometry $y_{min}^{Pouch,NMC}$ is determined considering the first delithiation step leading to a minimum stoichiometry of 0.259 equals to the value obtain in the coin cell format.

For the negative electrode, the amount of used capacity in the pouch format is only 29.8 mAh, much lower than the 53 mAh available capacity. It corresponds to a reversible capacity $Q_{rev}^{Pouch,Gr}$ equals to 205 mAh/g. By Assuming that the minimum stoichiometry for graphite in the pouch cell format is the same than in the coin cell format ($y_{min}^{Pouch,Gr} = 0.045$), the value of the full lithiation in the case of pouch system is expressed as:

$$y_{max}^{Pouch,Gr} = y_{min}^{Pouch,Gr} + \frac{Q_{rev}^{Pouch,Gr}}{Q_{th}^{Gr}} \quad (24)$$

It leads to a value of 0.598, lower than the one in CC format.

Finally, the stoichiometry of the active materials in each electrode can be related to every SOC of the cell (Fig. 3b) using the following relations:

$$y_{NMC} = -\left(y_{max}^{Pouch,NMC} - y_{min}^{Pouch,NMC}\right) SOC + y_{max}^{Pouch,NMC} \quad (25)$$

$$y_{Gr} = \left(y_{max}^{Pouch,Gr} - y_{min}^{Pouch,Gr}\right) SOC + y_{min}^{Pouch,Gr} \quad (26)$$

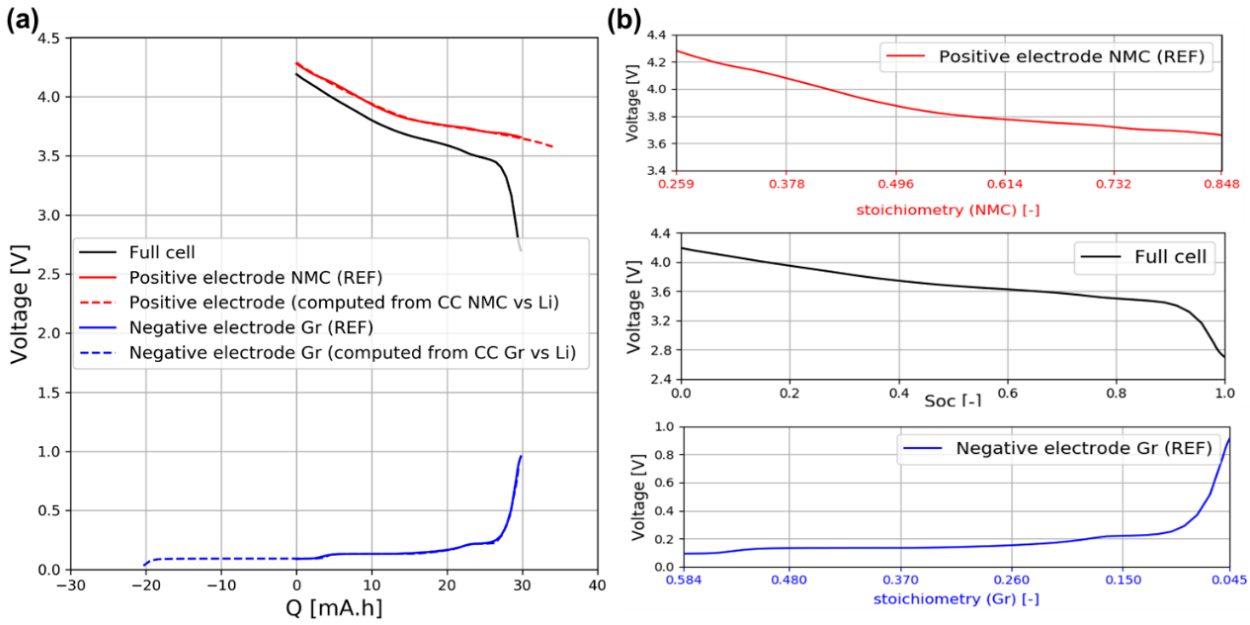

Fig. 21: (a) Pouch cell OCP curves as function of the cell capacity with the positive and the negative electrodes potentials measured with the reference electrode (labeled REF) compared to the positive and negative electrodes potentials computed from the coin cells (CC) measurements , (b) OCP curves of the full cell and positive and negative electrodes as function of the cell SOC and active materials stoichiometry

3.2 Diffusion coefficient in active materials

The chemical diffusion coefficient is determined from the transient voltage responses during the pulses at constant current of the GITT experiment in coin cell design. To that end we use Eq. (8) which has been developed in [53], [50], [8] from the analytical solution of diffusion processes in a planar geometry. For this geometry, the solution of the diffusion problem can be expressed as an infinite series of error functions. For the spherical geometry, the analytical solution is developed in the literature only in Fourier series [55], which do not converge rapidly for short times. Nevertheless, Smith et al. [56] have shown, by using an empirical development of the Fourier series at short time, that the development proposed to estimate the diffusion coefficient for the planar geometry is also valid for the spherical one.

$$D_s = \frac{4}{\pi}\left(\frac{V_M I_0}{S_{AM} F z_i}\right)^2 \left[\frac{dE_q}{dy} \Big/ \frac{dE}{d\sqrt{t}}\right]^2 \qquad t \ll {r_s}^2 / D_s \tag{27}$$

I_0 is the applied constant current during the pulse, V_M the active material molar volume, z_i the number of electron exchanged during the (de)-insertion reaction, and equals to 1, F the Faraday constant and S_{AM} the exchange area in CC design between the electrolyte and the active material

particles. $\frac{dE_q}{dy}$ is the slope of the equilibrium potential vs. the stoichiometry y. Equation 12 assumes a diffusion Fick's law, a small diffusion length compared to the dimension of the particle as well as a negligible volume changes.

$\frac{dE}{d\sqrt{t}}$ can be obtained from the plot of the transient voltage versus the square root of time during the constant current pulse. To choose the right time domain, the linearity of the transient voltage versus the square root of time has been checked for each pulse. For the positive electrode, Figure II-9a shows the typical transient voltage response obtained during one of the pulse at C/10 as function of time for the first 250s of the pulse. At beginning of the pulse, the voltage varies linearly with the square root of time, as illustrated Fig. 4b. A similar behavior is obtained for the negative electrode in the single-phase regions, as illustrated Fig. 5. This confirms that the GITT-obtained diffusion values for these stoichiometries are accurate and that the slope from the curve fit can be used in Eq.8 [57] [58] [53]. The physical parameters used in the data treatment are summarized TableV-1. The values obtained for the diffusion coefficients for both active materials are displayed Fig. 6 as function of the stoichiometry of each electrode.

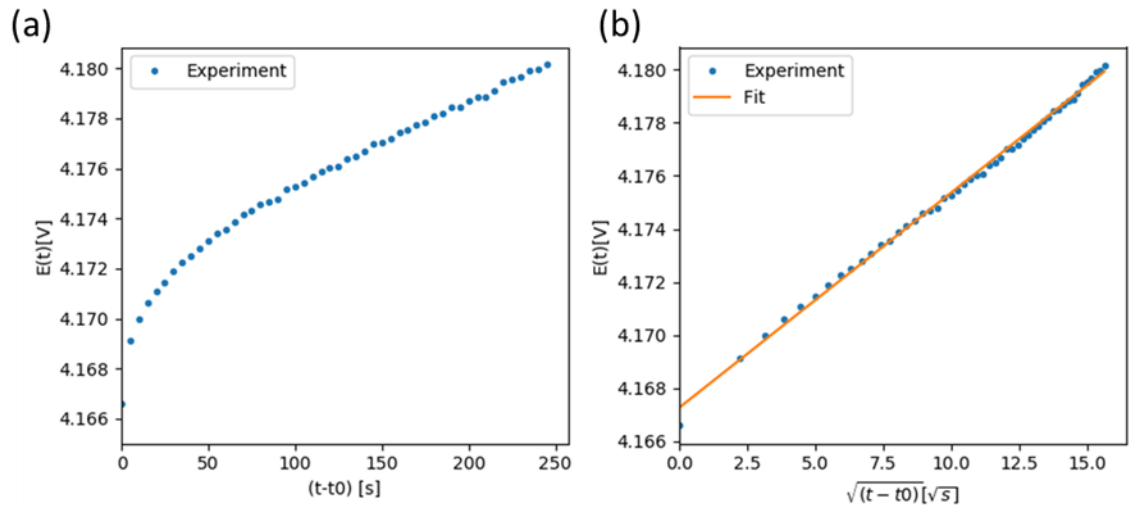

Fig. 22 : $Ni_{0.6}Mn_{0.2}Co_{0.2}O_2$ vs. Li GITT experiment (a) Cell voltage as a function of time during a charging current pulse (b) Cell voltage vs square root time for the same charging current pulse with the corresponding linear fit

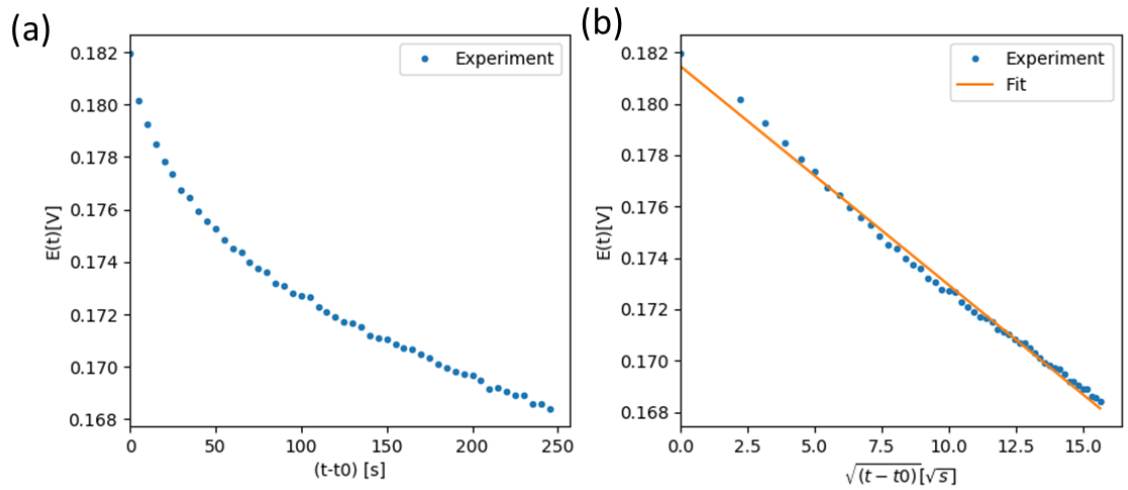

Fig. 23: Graphite vs. Li GITT experiment (a) Cell voltage as a function of time during a discharging current pulse (b) Cell voltage vs square root time for the same discharging current pulse with the corresponding linear fit

TableV-1: Parameters used to extract the graphite and $Ni_{0.6}Mn_{0.2}Co_{0.2}O_2$ diffusion coefficients (CC design) and exchange current densities (Pouch design)

Parameter	**Value**			
	Graphite	$Ni_{0.6}Mn_{0.2}Co_{0.2}O_2$	Source	Error
$\boldsymbol{I_0(A)}$ **during pulse**	5.5e-4	4.6e-4	calculated	-
$\boldsymbol{V_M(m^3.mol^{-1})}$	5.31e-6	12.35e-6	calculated	-
$\boldsymbol{r_{50}(m)}$	7.88e-6	6.6e-6	Measured	± 1.8µm
$\boldsymbol{L\ (m)}$	72e-6	66e-6	Measured	± 1µm
$\boldsymbol{S_g(m^2)}$ **in CC design**	1.5e-4	1.5e-4	calculated	-
$\boldsymbol{S_{AM}(m^2)}$ **in CC design**	2.68e-4	3.31e-4	calculated	-
$\boldsymbol{S_g(m^2)}$ **in pouch design**	12.25e-4	10.24e-4	calculated	-
$\boldsymbol{S_{AM}(m^2)}$ **in pouch design**	22.28e-4	22.03e-4	calculated	-

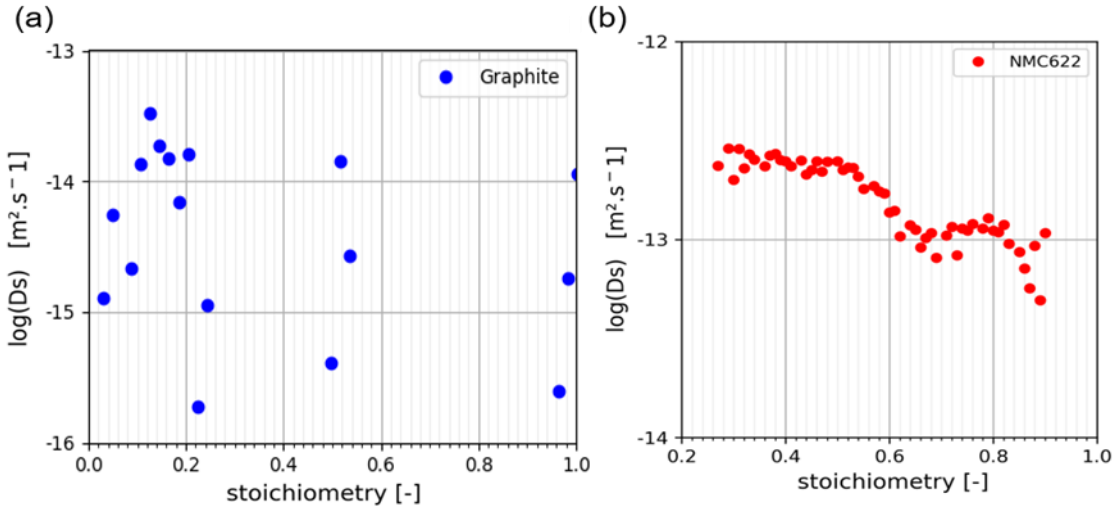

Fig. 24: Base 10 logarithm of the diffusion coefficient vs stoichiometry: (a) graphite, (b) $Ni_{0.6}Mn_{0.2}Co_{0.2}O_2$

The diffusion coefficient measured with this technique is a function of the derivative of the potential with respect to the stoichiometry, $\frac{dE_q}{dy}$. The interpretation of the measurement relies on Fick's law, which accounts for diffusion in one phase. For the graphite electrode, two phases can co-exist, which leads to a plateau in the equilibrium potential of graphite (See Fig. 2a) where $\frac{dE_q}{dy}$ is almost zero. As the present technique is not adequate to extract diffusion coefficients in these two-phase regions, we choose to not display the points obtained on the plateaus on Fig. 6a, but only those corresponding to the transition regions. For the three regions (stoichiometries below 0.25, stoichiometries around 0.5 and stoichiometries above 0.95), the values are between 1E-15 and 1E-14 $m^2\ s^{-1}$ without a clear tendency regarding the dependence on the stoichiometry. The order of magnitude and the overall tendencies are nevertheless coherent with results reported in the literature for graphite, whose values are in the range [1E-15 – 1E-13] $m^2\ s^{-1}$ in [59], or [3E-15 and 1.E-12] in [60].

For $Ni_{0.6}Mn_{0.2}Co_{0.2}O_2$, a regular monotone decrease of the diffusion coefficient can be observed in Fig. 6b. D_s values are varying between 1E-13 and 5E-13$m^2\ s^{-1}$ over the entire stoichiometry compared to the values proposed in the literature [1E-16 – 1E-11] $m^2\ s^{-1}$ [61]. An almost constant value around 5E-13$m^2\ s^{-1}$ is obtained for stoichiometry below 0.49, while a slight decrease is observed until stoichiometry of 0.64, with a subsequent stabilization at a value around 1E-13 $m^2\ s^{-1}$ for the highest stoichiometry values. These three domains might be related to the structure changes of the $Ni_{0.6}Mn_{0.2}Co_{0.2}O_2$ active material [62] [63]. This material

undergoes phase transition from pristine hexagonal H1 phase to subsequent hexagonal H2 and H3 phases. Although *ex-situ* and operando XRD measurements have been reported recently [63], the cognition of the structural difference between these phases and their precise stoichiometry range remains not fully understood. In our measurements, the domain of stoichiometry above 0.64 could related to the region where H1 and H2 structures coexist and the second domain [0.49 – 0.64] to a region where only the H2 structure is existing, while the last domain [0.26 – 0.49] to a region where a transition between H2 and H3 structures manifests.

3.3 Exchange current density

The aim of this section is to determine the exchange current densities of the two active materials from the EIS measurements carried out in the pouch cell design with two reference electrodes. Fig. 25 displays the Nyquist plots of the EIS obtained for the negative electrode (a), full cell (b) and positive electrode (c) at the different states of charge of the cell. Whatever the system, the Nyquist plots consist of an out-of-shaped semicircle alike in appearance of a half ellipse in high and intermediate frequency ranges and a straight line inclined at a constant angle to the real axis in the lower frequency range. The first capacitive arc is related for a part to the charge transfer phenomenon from where the i_0 values for the two electrodes can be fitted. The flattened shape can be observed in the case of porous electrodes with limited electronic or ionic conductivities [27]. The straight-line in the low frequency limit is due to diffusion phenomena which can be described with a Warburg contribution. For a better identification of the different physical domain in the spectra, a presentation of the imaginary part of the impedance vs. frequency is shown in Fig. 6 for the two electrodes. This figure allows to determine the characteristic frequency of the charge transfer (f_{max}), which corresponds to the highest point of the semi-circle in the Nyquist plots. The second identified characteristic frequency is the one corresponding to the minimum value of the imaginary part of the impedance while going to low frequency ($f_{\min}$). This frequency represents the limit between the interfacial phenomena (charge transfer resistance) and the bulk phenomena (lithium transports in particles and electrolyte).

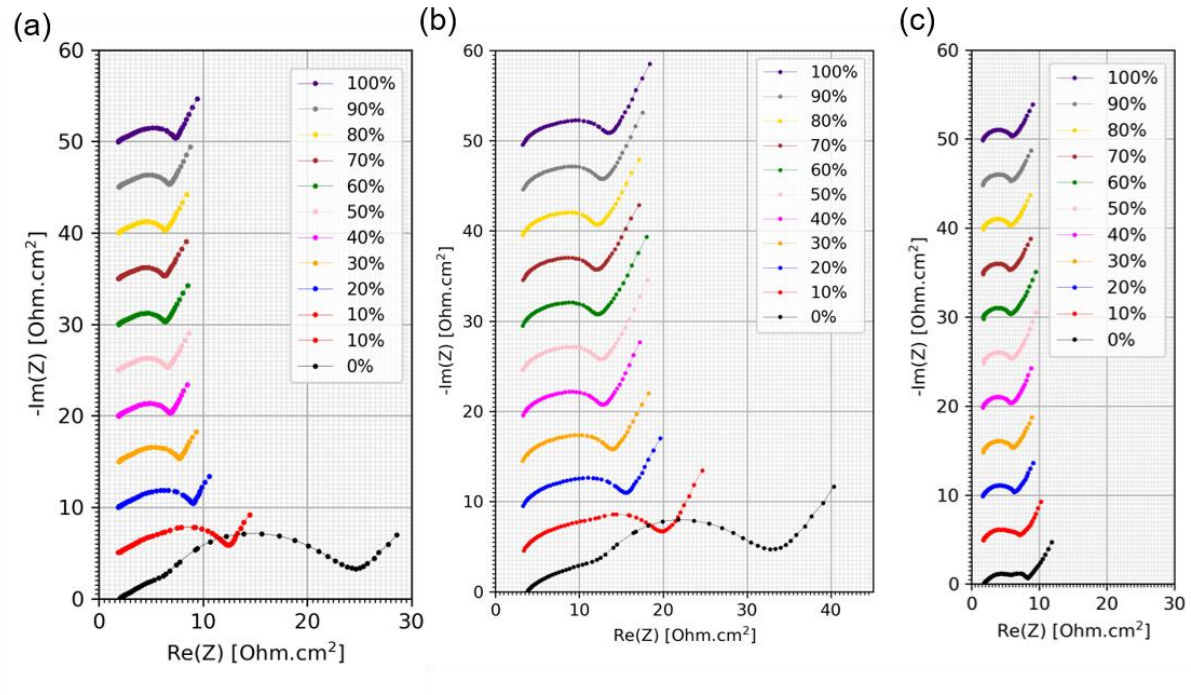

Fig. 25: EIS spectra of the 4-electrode pouch cell in Nyquist plot at different SOC: (a) negative electrode (graphite), (b) full cell and (c) positive electrode ($Ni_{0.6}Mn_{0.2}Co_{0.2}O_2$), with a shift of 5 ohm.cm² between two successive SOC

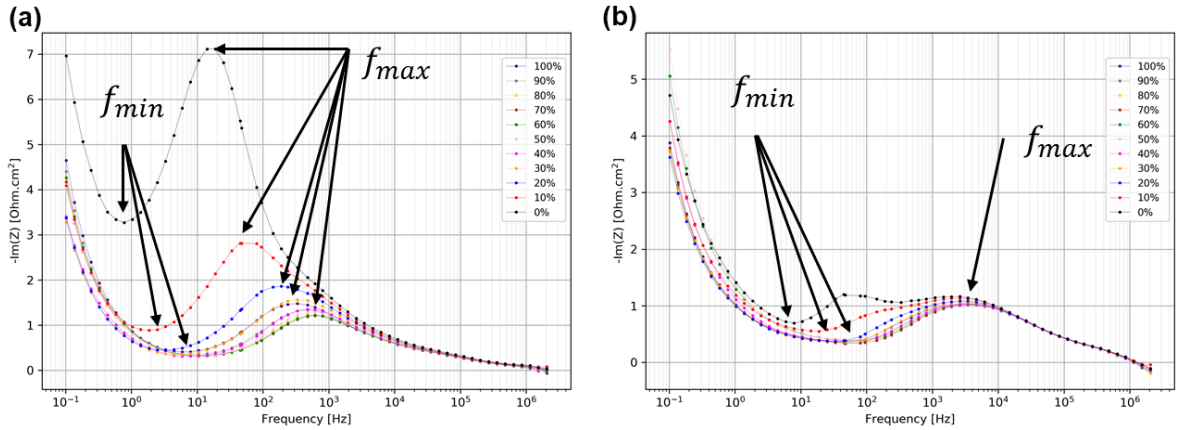

Fig. 26: EIS spectra of the 4-electrode pouch cell at different SOC represented with -Im(Z) vs frequency: (a) negative electrode (graphite), (b) positive electrode ($Ni_{0.6}Mn_{0.2}Co_{0.2}O_2$)

For the graphite, the physical phenomenon representing the AM/electrolyte interface in the EIS diagrams is in the intermediate to high frequency domain. As shown in fig. 5a, the magnitude of the flattened semi-circle corresponding to the charge transfer resistance decreases when the SOC of the cell increases. For a SOC higher than 20%, f_{max} and $f_{\min}$ are rather constant as can be seen Fig. 6a, which reflects a stable interface electrochemistry. However, for a SOC between 20% and 0%, $f_{\min}$ decreases a lot, going from values around 260 Hz for SOC of 100%

to values around 19 Hz at 0% SOC (Fig. 6a) suggesting a slower charge transfer for a lower SOC [37].

For $Ni_{0.6}Mn_{0.2}Co_{0.2}O_2$ (Fig. 5.c), EIS spectra are quite similar to the negative ones, but with an overall lower magnitude. For a SOC higher than 30%, all the diagrams have the same flattened semicircles shape with a constant width. Conversely, two flat semicircles shape can be distinguished with a width increase when the SOC decreases from 20% to 0%. As presented in fig. 6.b, f_{max} and $f_{\min}$ are the same over a large SOC range of [30%- 100%]. However, they increase from 20% to 0%. The same behavior, for a SOC below 30%, was reported for other materials similar to $Ni_{0.6}Mn_{0.2}Co_{0.2}O_2$, like $LiMn_2O_4$ [23] and $LiNi_{0.8}Co_{0.15}Al_{0.05}O_2$ [41]. In these works, the high frequency arc was associated to the Li^+ migration through the oxide layer film and the second one between the higher and middle frequency to the charge transfer resistance.

EIS measurements are fitted to extract the exchange current densities of both graphite and $Ni_{0.6}Mn_{0.2}Co_{0.2}O_2$ active materials. To reach this goal, the capacitive arc of the different spectra should be analyzed quantitatively by using EEC model. As mentioned before, simple R-C element model is usually implemented by assuming a semi-circle shape of the capacitive arc, which is not observed in the present case (see fig. 5). In fact, porous electrodes have a potential gradient along the electrode layer thickness. Thus, TLM model is employed in order to analyze EIS spectra, by considering electronic and ionic paths through the solid phase and the electrolyte in the pores respectively [23], [24]. For porous LIB electrodes, the electronic conductivity is much higher than the ionic one. Therefore, electronic resistance can be neglected, and the TLM [65] impedance is reduced to:

$$Z_{TLM} = \lambda\chi \coth\left(\frac{L}{\lambda}\right) \tag{28}$$

The resistance per unit length χ related to the ionic path is defined as:

$$\chi = \frac{1}{\sigma_e} \tag{29}$$

The ionic conductivity σ_e is equal to 1 mS/cm at 25°C for the studied electrolyte. This model takes into account the charge transfer at the interface between active materials and the

electrolyte, via the introduction of λ, the characteristic alternating current penetration depth in the electrode defined by:

$$\lambda = \sqrt{\frac{Z_{int}\, L}{\chi}} \tag{30}$$

The values of the electrode thickness L are provided in table 1 for the positive and negative electrodes respectively. The area-specific impedance Z_{int} of the electrochemical reaction taking place at the interface, is modeled as a simple parallel combination between the charge transfer R_{ct} and a constant phase element (CPE) [64]:

$$Z_{int} = \frac{R_{ct}}{1 + (i\omega R_{ct} C)^n} \tag{31}$$

with

$$R_{ct} = \frac{RTS_g}{Fi_0 S_{AM}} \tag{32}$$

S_g is the geometric area in the pouch design, S_{AM} is the AM exchange area in the pouch design, R is gas constant, T is the temperature, F is the Faraday's constant and i_0 is the exchange current density. A procedure was adopted to fit, with this TLM model, the capacitive arc of the experimental EIS spectra (Fig. 5a-c) corresponding to the charge transfer phenomenon for each value of the SOC in the frequency range between f_{min} and 200kHz. The used parameters are presented in Table 1. This method allows us to extract the values of i_0 for each stoichiometry value for both PE and NE, *via* Eq. (13).

The obtained results are presented Figure II-14a. as function of the active material stoichiometries. For the graphite, the experimental curve of exchange current density is asymmetric; with values ranging between 0.8 and 8.4 A/m², which is consistent with the values reported in the literature [66], [67] that show large variation: between 0.5 and 35 A/m². For the $Ni_{0.6}Mn_{0.2}Co_{0.2}O_2$, the experimental curve has a more symmetric shape compared to the graphite. The exchange current densities obtained as function of the stoichiometry are in the

range of 2.3-4.8 A/m², in agreement with the values proposed in the literature that are in the range [0.1-6] A/m² [59], [68].

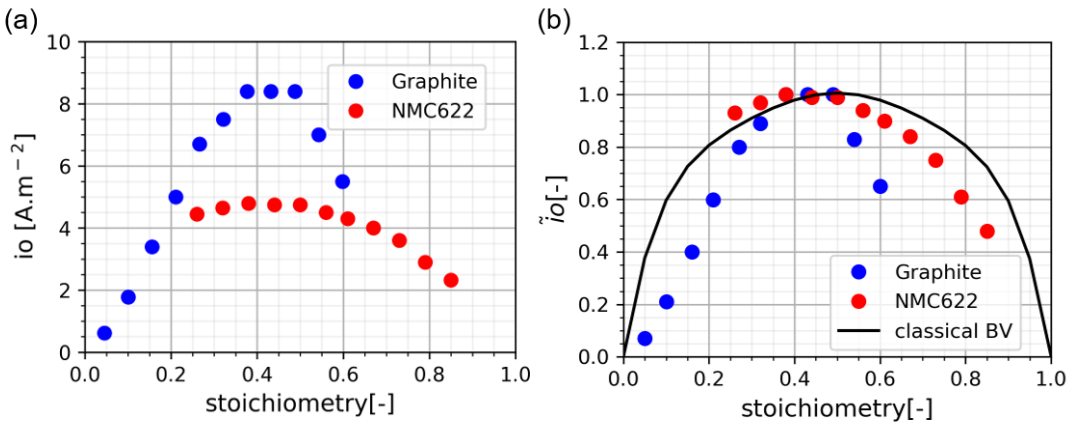

Fig. 27: Exchange current density vs. Stoichiometry: (a) for $Ni_{0.6}Mn_{0.2}Co_{0.2}O_2$ and graphite, (b) dimensionless version for comparison with the Butler-Volmer relation using $\alpha = 0.5$ (classical BV) *[72]*

4. Theoretical discussion

In earlier studies on lithium iron phosphate ($LiFePO_4$) [69], [70], it has been reported that the variation of the exchange current density with the stoichiometry is different from the Butler-Volmer approach classically used in porous electrode theory [71]. This discrepancy is also observed in the present study for the positive and the negative electrodes as shown in Fig. 7.b, where the dimensionless measured exchange current densities are compared to the Butler-Volmer results using $\alpha = 0.5$. Furthermore, in these works, the interdependence between the different active material properties is highlighted. In this study, we will follow a similar approach to analyze the link between the different material properties focusing on the molecular interactions (repulsive or attractive forces) and their impact on the active material properties. Indeed, these interactions are usually traduced in solid activity coefficients, which are used to express either the equilibrium potential or the solid diffusion. In the following, a methodology is applied to extract the values of the non-ideal interactions' energies for the positive active material, *i.e.* $Ni_{0.6}Mn_{0.2}Co_{0.2}O_2$, and we present an analytic model for the three active material properties, namely the equilibrium potential, the diffusion coefficient, as well as the exchange current density.

4.1 Theoretical framework

To express the equilibrium potential (E_q) of a Li-ion intercalation electrode, experimental profiles are usually fitted with an empirical expression due to the lack of understanding of the solid-state redox reactions. In this study, a modified Nernst equation is used [124], which is function of liquid and solid activity coefficients respectively (γ_l, γ_s) and of the insertion rate $\theta = C_s/C_s^{max}$.

$$E_q = \frac{RT}{F} ln\left(\frac{\gamma_l}{\gamma_s \theta}\right) + E_0 \tag{33}$$

where E_0 includes the reference potential, as well as all terms which are not stoichiometry dependent. Since for the studied materials, the insertion rate and the stoichiometry are equals, we will only refer to the stoichiometry in the following. From a thermodynamic point of view, the solid coefficient activity, γ_s, accounts for lithium ion interactions with the vacant sites and the intra-molecular interactions between the lithium ions and maybe to other non-ideal interactions with the host structure. Considering a regular solution model [124], [125], the solid coefficient activity can be expressed as follows:

$$\gamma_s = \frac{1}{1-y} \exp\left(\frac{1}{RT}(e_s + e_1 y + e_2 y^2)\right) \tag{34}$$

The term in the exponential accounts for the non-ideal interactions. A quadratic expression was chosen for the intercalation energy factor to account for both lithium-vacant site and lithium-lithium interactions. e_s is the interaction energy between lithium and the solid host materials, which is an attractive interaction and should be negative [126]. Note that e_1 and e_2 are the coefficients of a polynomial function of the interaction energy representing the lithium-lithium interactions in the same layer and between the neighboring layers. To simplify the up-coming demonstrations, the non-dimensional form of these energies is introduced ($\varepsilon_i = e_i/RT$). By using the solid activity coefficient definition (Eq. (34)), the equilibrium potential can be expressed as follows:

$$E_q = \frac{RT}{F}\left[\ln(\frac{1-y}{y}) - (\varepsilon_s + \varepsilon_1 y + \varepsilon_2 y^2)\right] + E_0' \tag{35}$$

Where E_0' is a constant. The driven force for the diffusion flux can be defined using either the chemical potential gradient or the concentration gradient. Considering these two latter definitions, the chemical solid diffusion coefficient can be obtained as shown in [50] as:

$$\frac{D_s}{D_0} = \frac{\partial \ln(\gamma_s y)}{\partial \ln(y)} \tag{36}$$

D_0 is the tracer diffusivity deduced from the chemical potential gradient used to express the flow. By using the expression of the equilibrium potential E_q (Eq. (35)), it is possible to explicit the link between these two parameters:

$$\frac{D_s}{D_0} = -y\frac{F}{RT}\frac{dE_q}{dy} \tag{37}$$

and the dependence of the diffusion coefficient on the stoichiometry, can be made explicit:

$$\frac{D_s}{D_0} = y\left[\frac{1}{y} + \frac{1}{(1-y)} + \varepsilon_1 + 2\varepsilon_2 y\right] \tag{38}$$

Similarly, the exchange current density (i_0) for intercalation electrodes can be expressed as function of the solid coefficient activity (Eq. (34)). This expression is derived from the general expression of the Butler-Volmer equation for concentrated solution proposed by Bazant [124]:

$$i_0 = \frac{i_{00}}{\gamma_a}(\gamma_s y)^{\alpha} \tag{39}$$

α is the symmetry factor of the charge transfer, i_{00} is a kinetic constant which is stoichiometry independent and γ_a is the activity coefficient of the transition state. Considering a fixed number n, of excluded sites, during the intercalation process, the activity coefficient can be modeled as:

$$\gamma_a = \frac{1}{(1-y)^n}\exp(\varepsilon_a) \tag{40}$$

ε_a is the intercalation energy factor of the transition state, which does not depend on the stoichiometry. These developments lead to the following expression of i_0 as function of the intercalation energies (e_s, e_1, e_2) or to simplify ($\varepsilon_s, \varepsilon_1, \varepsilon_2$):

$$i_0 = {i_{00}}' y^{\alpha}(1-y)^{(n-\alpha)} \exp\left(\alpha\,(\varepsilon_s + \varepsilon_1 y + \varepsilon_2 y^2)\right) \quad (41)$$

The non-stoichiometry dependent terms have been gathered in the pre-factor ${i_{00}}'$.

4.2 Theoretical results

$\varepsilon_s, \varepsilon_1$ and ε_2 are determined from the experimental results. The simulated E_q (Eq. (35)), D_s (Eq. (12)) and i_0 (Eq. (41)) are compared to the experimental measurements. We have limited our study to the positive electrode active material, *i.e.* the $Ni_{0.6}Mn_{0.2}Co_{0.2}O_2$, as the multi-phase behavior of graphite is more complex to apprehend without resorting to multi-phasic theories.

The interactions energy factors have been determined from the equilibrium potential of the $Ni_{0.6}Mn_{0.2}Co_{0.2}O_2$ material by using Eq. (35). To obtain a good fit over the whole stoichiometry range, we have distinguished three stoichiometry zones in which each intercalation factor has a constant value that changes from one zone to another. These three different zones could account for the host material structure modification upon intercalation as reported in [62], [63]. The obtained values for the coefficient of the second order polynomial are given table 2, by using an empirical value for ${E_0}'$ equals to 3.798 V.

Table 2: Fitted values of interaction energies

Stoichiometry zone	$\boldsymbol{\varepsilon_s}\,[-]$	$\boldsymbol{e_s}\,[\boldsymbol{eV}]$	$\boldsymbol{\varepsilon_1}[-]$	$\boldsymbol{e_1}[\boldsymbol{eV}]$	$\boldsymbol{\varepsilon_2}\,[-]$	$\boldsymbol{e_2}[\boldsymbol{eV}]$
zone 1(0,26 <y < 0,49)	-38.09	-0.98	91.13	2.34	-38.94	-1
zone 2 (0,49 <y< 0,64)	-59.17	-1.52	177.89	4.57	-129.81	-3.34
zone 3 (0,64 <y< 0,9)	-4.95	-0.13	3.89	0.1	8.76	0.23

The result of the fit is displayed Fig. 28a, which shows an excellent agreement between the experimental result and the analytic expression for the equilibrium potential, the average deviation being below 2 mV. Therefore, Eq. (35) can be implemented to express the equilibrium

potential of the $Ni_{0.6}Mn_{0.2}Co_{0.2}O_2$ instead of using empirical data. To get a global view of the interactions inside the solid active material, the sum of the interaction energies, $-(\varepsilon_s + \varepsilon_1 y + \varepsilon_2 y^2)$ is displayed Fig. 28b. Even though we have used a second order polynomial, the dependence remains rather linear in two regions, at low and high stoichiometries. Such linear dependency was also reported for Li_xTiS_2 [127] with an interaction energy modeled as A.y with A=220meV.

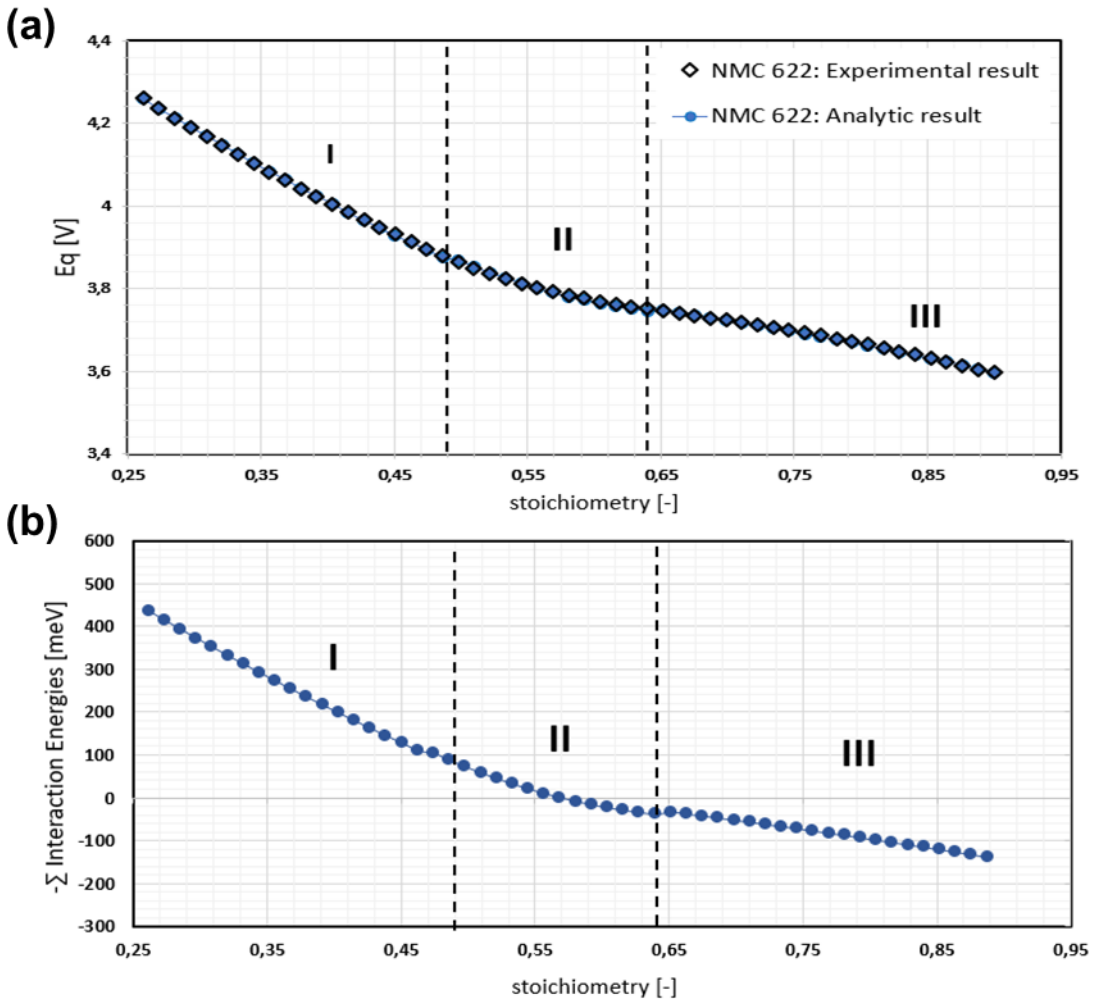

Fig. 28: (a) $Ni_{0.6}Mn_{0.2}Co_{0.2}O_2$ equilibrium potential. Validation of the analytic expression by comparison to the experimental results. (b) Sum of the interaction energies for the $Ni_{0.6}Mn_{0.2}Co_{0.2}O_2$ active material as function of the stoichiometry

For the diffusion coefficient D_s, Eq. (12) is implemented using the values of the intercalation energies factors determined previously (table 2). A good agreement with the experimental data throughout the entire stoichiometry (Fig. 29a) is achieved when D_0 is defined as a function of the square root of the stoichiometry:

$$D_0 = \frac{A}{\sqrt{y}} \tag{42}$$

considering a parameter A equal to 6.25 $10^{-15} m^2\ s^{-1}$.

More precisely, two different zones can be distinguished. In the first one, for a stoichiometry lower than 0.64, the analytic model matches very well the experimental data. Conversely, for higher stoichiometry, the analytical equation for D_s does not fit well with experimental data. This difference for high stoichiometry between [0.64-0.9] may be due to non-ideal behavior of the active material and other interactions than the intra-molecular interactions. To get a better result (Fig. 29.b), D_0 was modified for this part of stoichiometry and expressed as:

$$D_0 = \frac{A'}{\sqrt{y}}(1-y)^{0.3} \tag{43}$$

Where the parameter A' is equal to 8.99 $10^{-15} m^2.s^{-1}$.

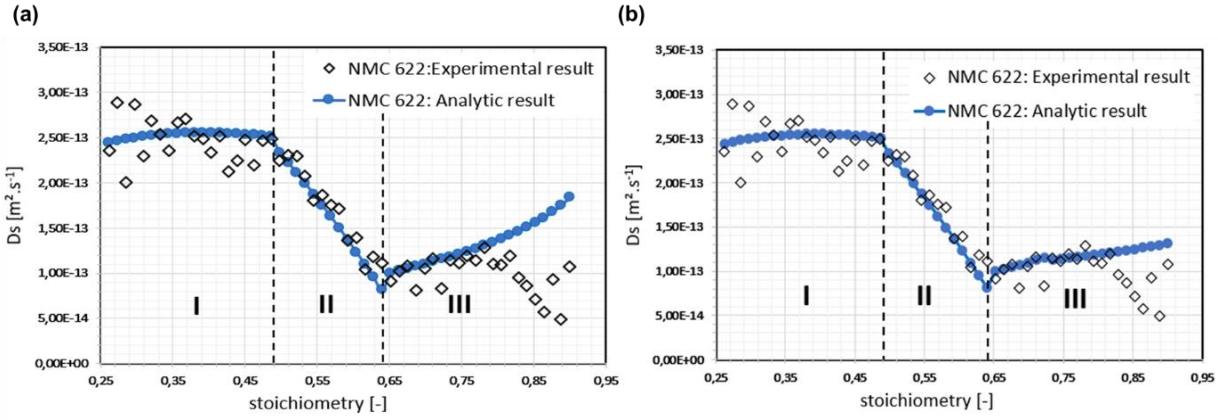

Fig. 29: Validation of the model equation of the $Ni_{0.6}Mn_{0.2}Co_{0.2}O_2$ D_s

Regarding the exchange current density, Eq. (41) has been implemented using the intercalation energies factors presented in table 2. The analytic curve was fitted with n=0.75, $\alpha = 0.023$ and $i'_{00} = 8.5\ A.m^{-2}$ with an average deviation of 0.073 $A.m^{-2}$. A visual inspection of the plots (Fig. 30) reveals a very good agreement for all the stoichiometry range. Therefore, Eq. (41) leads to a better agreement than the one obtained with the classical Butler-Volmer expression (Figure II-14.b), for which an average deviation of 0.39 $A.m^{-2}$ from the experimental result was obtained. Thus, taking into consideration the impact of the non-ideal interactions reduces

three times the average deviation. However, the fitted value for the symmetry factor α is very small, in order to limit the impact of the interaction energies on the exchange current density. Since the reported value for α is much lower than expected, compared to the one proposed with classical BV equals to 0.5, we report for comparison another solution based on the modified Butler-Volmer relation without taking into account the non-ideal interaction energies. In this case Eq. (41) reduces to:

$$i_0 = i_{00}{}' y^{\alpha}(1-y)^{(n-\alpha)} \tag{44}$$

The best fit is obtained considering that the number of excluded sites, n, is equal to 2, and α is equal to 0.9. The corresponding result is displayed Fig. 30. This analytic model is also very close from the experimental data, an average deviation of 0.129 $A.m^{-2}$ being achieved.

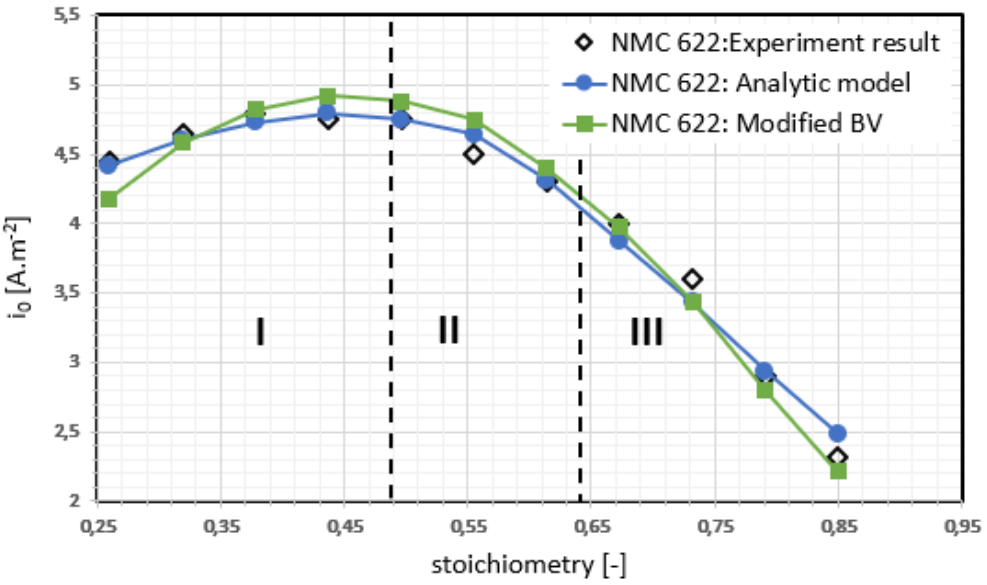

Fig. 30: Validation of the model equation of the $Ni_{0.6}Mn_{0.2}Co_{0.2}O_2$ i_0

In this part, an effort has been made to explicit the link between the three active material properties (the equilibrium potential, E_q, the diffusion coefficient, D_s and the exchange current density, i_0) using thermodynamic relations available in the literature. Based on these relations, we find some unexpected results. For example, for the solid diffusion coefficient, generally, it is related to the derivative of the equilibrium potential via the stoichiometry and not the square root of the stoichiometry, as reported here. Likewise, the analytic expression of the exchange current density developed in this work leads to assign a very small value to the symmetry factor to limit the impact of the interaction energies and to be able to match the experimental results. This result is rather unexpected and leads to think about another significant interaction energy

which should be taken into account. This supplementary term might arise from a concentration gradient of the lithium at the active particle surface [124] due to very localized structural modifications. Indeed, spinel and rocksalt phases often form as thin layered on the surface of layered intercalation compounds, which might modify very locally the interaction energies [128]. This type of development, taking into consideration the heterogeneities inside the active material, goes however beyond the scope of this work, but seems crucial if we wish to keep a thermodynamic consistency to describe the different active material physical parameters.

5. Conclusion

In this paper, we have presented a consistent route to measure and extract the values of three of the most significant active material physical properties, namely the equilibrium potential, the diffusion coefficient and the exchange current density, as function of the stoichiometry of the active materials. The *de Levie*'s model has been used to retrieve the exchange current densities of the two porous electrodes from EIS spectra measured using $LiFePO_4$ as a reference electrode. The link between the three measured properties has been then further discussed using a general thermodynamic approach. Focusing on the $Ni_{0.6}Mn_{0.2}Co_{0.2}O_2$ positive material, the interaction energies have been determined and analytical expressions for the diffusion coefficient and exchange current densities have been suggested. The thermodynamic relations available in the literature are not directly transposable to the $Ni_{0.6}Mn_{0.2}Co_{0.2}O_2$ material, suggesting the necessity to account for supplementary terms. Nevertheless, the proposed stoichiometry dependent laws determined with the same stoichiometry definition go already beyond most reported values for the $Ni_{0.6}Mn_{0.2}Co_{0.2}O_2$ and can be used to increase the predictability of multi-physics lithium-ion battery models.

Acknowledgements

This work has received funding from the French National Association of Research and Technology (CIFRE 2017/0705). We are grateful to Yvan Reynier for the manufacturing of the electrodes.

List of Symbols

Parameter	Symbol
Stoichiometry (-)	y
coefficient activity of the transition state (-)	γ_l
solid coefficient activity (-)	γ_s
Symmetry factor of the charge transfer (-)	α
Intercalation energy factors of the lithium- vacant site (-)	ε_s
Ionic resistance ($ohm\ m$)	χ
Characteristic alternating current penetration depth in the electrode (m)	λ
Electronic conductivity ($S\ m^{-1}$)	σ_e
Polynomial coefficient of intercalation energy factors of the lithium- vacant site and lithium-lithium (-)	ε_1
Polynomial coefficient of intercalation energy factors of the lithium- vacant site and lithium-lithium (-)	ε_2
Capacitance (F m^{-2})	C
Diffusion coefficient of Lithium in the active material ($m^{2}\ s^{-1}$)	D_s
Polynomial coefficient of intercalation energy of the lithium- vacant site and lithium-lithium (meV)	e_1
Polynomial coefficient of intercalation energy of the lithium- vacant site and lithium-lithium (meV)	e_2
Intercalation energy of the lithium- vacant site (meV)	e_s
Equilibrium potential (V)	E_q
Faraday's constant (96487$C\ mol^{-1}$)	F
Applied constant current during the pulse (A)	I_0
Exchange current density ($A\ m^{-2}$)	i_0
Electrode's thickness (m)	L
Capacity (mAh)	Q
Gas constant (8.314 $J\ mol^{-1}K^{-1}$)	R
Charge transfer resistance ($ohm\ m^2$)	R_{ct}
Exchange area (m^2)	S_{AM}
Geometric area (m^2)	S_g
state of charge of the cell (-)	Soc
Transmission line model ($ohm\ m^2$)	TLM
Temperature (K)	T
Molar volume($m^3\ mol^{-1}$)	V_M
Area-specific impedance of the electrochemical reaction taking place at the interface ($ohm\ m^2$)	Z_{int}
TLM impedance ($ohm\ m^2$)	Z_{TLM}
Number of electron exchanged during the (de)-insertion reaction (-)	z_i

[1] D. Gruet, B. Delobel, D. Sicsic, I. T. Lucas and V. Vivier, "On the electrochemical impedance response of composite insertion electrodes. Toward a better understanding of porous electrodes," *Electrochimica Acta,* vol. 295, pp. 787-800, 2019.

[2] J. Randles, "Kenitics of rapid electrode reactions," *Discussions of the faraday society,* vol. 1, pp. 11-19, 1947.

[3] M. Doyle, T. F. Fuller and J. Newman, "Modeling of Galvanostatic Charge and Discharge of the Lithium/Polymer/Insertion Cell," *J. Electrochem. Soc.,* vol. 140, pp. 1526-1533, 1993.

[4] N. Dufour, M. Chandesris, S. Geniès, M. Cugnet and Y. Bultel, "Lithiation heterogeneities of graphite according to C-rate and mass-loading: A model study," *Electrochimica Acta,* vol. 272, pp. 97-107, 2018.

[5] J. Newman and W. Tiedemann, "Porous-electrode theory with battery applications," *AIChE J.,* vol. 21, pp. 25-41, 1975.

[6] M. Ecker, T. K. D. Tran, P. Dechent, S. Katz, A. Warnecke and D. U. Sauer, "Parameterization of a Physico-Chemical Model of a Lithium-Ion Battery: I. Determination of Parameters," *Journal of The Electrochemical Society,* vol. 162, pp. A1836-A1848, 2015.

[7] A. Zaban, E. Zinigrad and D. Aurbach, "Impedance Spectroscopy of Li Electrodes. A General Simple Model of the Li-Solution Interphase in Polar Aprotic Systems," *J. Phys. Chem.,* vol. 100, pp. 3089-3101, 1 1996.

[8] D. Aurbach, "Impedance Spectroscopy of Nonactive Metal Electrodes at Low Potentials in Propylene Carbonate Solutions," *J. Electrochem. Soc.,* vol. 141, p. 1808, 1994.

[9] J. Illig, J. P. Schmidt, M. Weiss, A. Weber and E. Ivers-Tiff\'ee, "Understanding the impedance spectrum of 18650 LiFePO4-cells," *Journal of Power Sources,* vol. 239, pp. 670-679, 2013.

[10] A. Martinent, B. L. Gorrec, C. Montella and R. Yazami, "Three-electrode button cell for {EIS} investigation of graphite electrode," *Journal of Power Sources,* vol. 97–98, pp. 83-86, 2001.

[11] J. G. Thevenin, "Impedance of Lithium Electrodes in a Propylene Carbonate Electrolyte," *J. Electrochem. Soc.,* vol. 134, p. 273, 1987.

[12] H. Schranzhofer, J. Bugajski, H. J. Santner, C. Korepp, K.-C. Möller, J. O. Besenhard, M. Winter and W. Sitte, "Electrochemical impedance spectroscopy study of the SEI formation on graphite and metal electrodes," *Journal of Power Sources,* vol. 153, pp. 391-395, 2006.

[13] J. Huang, H. Ge, Z. Li and J. Zhang, "An Agglomerate Model for the Impedance of Secondary Particle in Lithium-Ion Battery Electrode," *Journal of The Electrochemical Society,* vol. 161, pp. E3202-E3215, 2014.

[14] P. Arora, B. N. Popov and R. E. White, "Electrochemical Investigations of Cobalt-Doped LiMn2O4 as Cathode Material for Lithium-Ion Batteries," *Journal of The Electrochemical Society,* vol. 145, pp. 807-815, 1998.

[15] J. Nielsen and J. Hjelm, "Impedance of SOFC electrodes: A review and a comprehensive case study on the impedance of LSM:YSZ cathodes," *Electrochimica Acta,* vol. 115, pp. 31-45, 2014.

[16] J. Illig, M. Ender, A. Weber and E. Ivers-Tiffée, "Modeling graphite anodes with serial and transmission line models," *Journal of Power Sources,* vol. 282, pp. 335-347, 2015.

[17] W. Weppner and R. A. Huggins, "Determination of the Kinetic Parameters of Mixed-Conducting Electrodes and Application to the System Li3Sb," *Journal of The Electrochemical Society,* vol. 124, pp. 1569-1578, 1977.

[18] D. W. Dees, S. Kawauchi, D. P. Abraham and J. Prakash, "Analysis of the Galvanostatic Intermittent Titration Technique (GITT) as applied to a lithium-ion porous electrode," *Journal of Power Sources,* vol. 189, pp. 263-268, 2009.

[19] E. Markevich, M. D. Levi and D. Aurbach, "Comparison between potentiostatic and galvanostatic intermittent titration techniques for determination of chemical diffusion coefficients in ion-insertion electrodes," *Journal of Electroanalytical Chemistry,* vol. 580, pp. 231-237, 2005.

[20] M. Doyle and J. Newman, "Modeling the performance of rechargeable lithium-based cells: design correlations for limiting cases," *Journal of Power Sources,* vol. 54, pp. 46-51, 1995.

[21] T. Danner, M. Singh, S. Hein, J. Kaiser, H. Hahn and A. Latz, "Thick electrodes for Li-ion batteries: A model based analysis," *Journal of Power Sources,* vol. 334, pp. 191-201, 2016.

[22] J. Sturm, S. Ludwig, J. Zwirner, C. Ramirez-Garcia, B. Heinrich, M. F. Horsche and A. Jossen, "Suitability of physicochemical models for embedded systems regarding a nickel-rich, silicon-graphite lithium-ion battery," *Journal of Power Sources,* vol. 436, p. 226834, 2019.

[23] T. R. Ferguson and M. Z. Bazant, "Nonequilibrium Thermodynamics of Porous Electrodes," *Journal of The Electrochemical Society,* vol. 159, pp. A1967-A1985, 2012.

[24] Y. Reynier, C. Vincens, C. Leys, B. Amestoy, E. Mayousse, B. Chavillon, L. Blanc, E. Gutel, W. Porcher, T. Hirose and C. Matsui, "Practical implementation of Li doped SiO in high energy density 21700 cell," *Journal of Power Sources,* vol. 450, p. 227699, 2020.

[25] M.-D. Levi, K. Gamolsky, D. Aurbach, U. Heider and R. Oesten, "Determination of the Li ion chemical diffusion coefficient for the topotactic solid-state reactions occurring via a two-phase or single-phase solid solution pathway," *Journal of Electroanalytical Chemistry,* vol. 477, pp. 32-40, 1999.

[26] M. Ender, A. Weber and I.-T. Ellen, "Analysis of Three-Electrode Setups for AC-Impedance Measurements on Lithium-Ion Cells by FEM simulations," *Journal of The Electrochemical Society,* vol. 159, pp. A128-A136, 2011.

[27] R. Tatara, P. Karayaylali, Y. Yu, Y. Zhang and L. Giordano, "The effect of electrode-electrolyte interface on the electrochemical impedance spectra for positive electrode in Li-Ion Battery," *Journal of The Electrochemical Society,,* vol. 166, pp. A5090-A5098, 2019.

[28] D. Juarez-Robles, C.-F. Chen, Y. Barsukov and P.-P. Mukherjeea, "Impedance Evolution Characteristics in Lithium-Ion Batteries," *Journal of The Electrochemical Society,* vol. 164, pp. A837-A847, 2017.

[29] I. A. J. Gordon, S. Grugeon, H. Takenouti, B. Tribollet, M. Armand, C. Davoisne, A. Débart and S. Laruelle, "Electrochemical Impedance Spectroscopy response study of a commercial graphite-based negative electrode for Li-ion batteries as function of the cell state of charge and ageing," *Electrochimica Acta,* vol. 223, pp. 63-73, 2017.

[30] I.-J. Gordon, S. Grugeon, A. Débart, G.Pascaly and S.Laruelle, "Electrode contributions to the impedance of a high-energy density Li-ion cell designed for EV applications," *Solid State Ionics,* vol. 237, pp. 50-55, 2013.

[31] M-D.Levi, V.Dargel, Y.Shilina, D. Aurbach and I.-C. Halalay, "Impedance Spectra of Energy-Storage Electrodes Obtained with Commercial Three-Electrode Cells: Some Sources of Measurement Artefacts," *Electrochimica Acta,* vol. 149, pp. 126-135, 2014.

[32] J. Costard, M. Ender, M. Weiss and E. Ivers-Tiffée, "Three-Electrode Setups for Lithium-Ion Batteries: II. Experimental Study of Different Reference Electrode Designs and Their Implications for Half-Cell Impedance Spectra," *Journal of The Electrochemical Society,* vol. 164, pp. A80-A87, 2017.

[33] R. Zeh, F. Kindermann, R. Karl, H. Gasteiger and A. Jossen, Writers, *Electrode optimization and behavior of LTO/LFP electrodes for applications in lithium ion batteries.* [Performance]. Technical University of Munich, 2019.

[34] C. J. Wen, B. A. Boukamp, R. A. Huggins and W. Weppner, "Thermodynamic and Mass Transport Properties of LiAl," *J. Electrochem. Soc,* vol. 126, no. 12, pp. 2258-2266, 1979.

[35] J. R. Dahn, "Phase diagram of LiC6," *Phys. Rev. B,* vol. 44, no. 17, pp. 9170-9177, 11 1991.

[36] H. S. CARSLAW and J. C. JAEGER, Conduction of heat in solids, Oxford: Clarendon Press, 1959.

[37] K. Smith and C. Wang, "Solid-state diffusion limitations on pulse operation of a lithium ion cell for hybrid electric vehicles," *Journal of Power Sources,* vol. 161, p. 628–639, 2006.

[38] E. Allcorn, S. O. Kim and A. Manthiram, "Lithium diffusivity in antimony-based intermetallic and FeSb–TiC composite anodes as measured by GITT," *Phys. Chem. Chem. Phys.,* vol. 17, no. 43, pp. 28837-28843, 2015.

[39] X. H. Rui, N. Ding, J. Liu, C. Li and C. H. Chen, "Analysis of the chemical diffusion coefficient of lithium ions in Li3V2(PO4)3 cathode material," *Electrochimica Acta,* vol. 55, pp. 2384-2390, 2010.

[40] S. Malifarge, B. Delobel and C. Delacourt, "Guidelines for the Analysis of Data from the Potentiostatic Intermittent Titration Technique on Battery Electrodes," *Journal of The Electrochemical Society,* vol. 164, pp. A3925-A3932, 2017.

[41] Q. Wang, C.-H. Shen, S.-Y. Shen, Y.-F. Xu, C.-G. Shi, L. Huang, J.-T. Li and S.-G. Sun, "Origin of Structural Evolution in Capacity Degradation for Overcharged NMC622 via Operando Coupled Investigation," *ACS Applied Materials & Interfaces,* vol. 9, pp. 24731-24742, 7 2017.

[42] J. Xu, E. Hu, D. Nordlund, A. Mehta, S. Ehrlich, X. Yang and W. Tong, "Understanding the Degradation Mechanism of Lithium Nickel Oxide Cathodes for Li-Ion Batteries," *ACS Applied Materials and Interfaces,* vol. 8, p. 31677−31683, 2016.

[43] S. Zheng, C. Hong, X. Guan, Y. Xiang, X. Liu, G. Xu, R. Liu, G. Zhong, F. Zheng, Y. Li, X. Zhang, Y. Ren, Z. Chen, K.Amine and Y. Yang, "Correlation between long range and local structural changes in Ni-rich layered materials during charge and discharge process," *Journal of Power Sources,* vol. 412, pp. 336-343, 2019.

[44] J. P. Meyers, M. Doyle, R. M. Darling and J. Newman, "The Impedance Response of a Porous Electrode Composed of Intercalation Particles," *Journal of The Electrochemical Society,* vol. 147, pp. 2930-2940, 2000.

[45] D. P. Abraham, D. w. Dees and S. Kawauchi, "Modeling the impedance versus voltage characteristics of LiNi(0.8)Co(0.15)Al(0.005)O(2)," *Electrochimica Acta,* vol. 53, pp. 2121-2129, 2008.

[46] R. Levie, "On the impedance of electrodes with rough interfaces," *Journal of Electroanalytical Chemistry and Interfacial Electrochemistry,* vol. 261, pp. 1-9, 1989.

[47] A. M. Colclasure and R. J. Kee, "Thermodynamically consistent modeling of elementary electrochemistry in lithium-ion batteries," *Electrochimica Acta,* vol. 55, pp. 8960-8973, 2010.

[48] E. Prada, D. Di Domenico, Y. Creff, J. Bernard, V. Sauvant-Moynot and F. Huet, "Simplified Electrochemical and Thermal Model of LiFePO4-Graphite Li-Ion Batteries for Fast Charge Applications," *Journal of The Electrochemical Society,* vol. 159, pp. A1508-A1519, 2012.

[49] P. C. Tsai, B. Wen, M. Wolfman, M. Choe, M. S. Pan, Li.Su, K.Thornton, J. Cabana and Y. Chiang, "Single-particle measurements of electrochemical kinetics in NMC and NCA cathodes for Li-ionbatteries," *Energy and Environmental Science,* vol. 11, pp. 860-871, 2018.

[50] A. J. Bard and L. R. Faulkner, Electrochemical Methods : Fundamentals and Application, 2nd ed., John Wiley and Sons, 2001.

[51] M. Z. Bazant, "Thermodynamic stability of driven open systems and control of phase separation by electro-autocatalysis," *Faraday Discussions,* vol. 199, pp. 423-463, 2017.

[52] M. Z. Bazant, "Theory of Electrochemical Kinetics based on Nonequilibrium Thermodynamics," MIT, Cambridge, USA, 2012.

[53] M. Chandesris, D. Caliste, D. Jamet and P. Pochet, "Thermodynamics and Related Kinetics of Staging in Intercalation Compounds," *The Journal of Physical Chemistry C,* vol. 123, pp. 23711-23720, 2019.

[54] P. Derosa and P. Balbuena, "A Lattice-Gas Model Study of Lithium Intercalation in Graphite," *Journal of The Electrochemical Society,* vol. 146, pp. 3630-3638, 1999.

[55] C. Déportes, M. Duclot, P. Fabry, J. Fouletier, A. Hammou, M. Kleitz, E. Siebert and J. Souquet, Electrochimie des Solides, 1994.

[56] M. Radin, S. Hy, M. Sina, C. Fang, H. Liu, J. Vinckeviciute, M. Zhang, M. S. Whittingham, Y. S. Meng and A. V. d. Ven, "Narrowing the Gap between Theoretical and Practical Capacities in Li-Ion Layered Oxide Cathode Materials," *Advanced Energy Materials,* Vols. 7, 1602888, 2017.

Résumé

La technologie des batteries Lithium-ion est vrai succès qui est largement utilisée dans diverses technologies portatives, pour le transport et les réseaux. Néanmoins, au vue de la diversité des chimies des batteries Lithium-ion et des nombreux mécanismes de vieillissement, il est primordial pour les concepteurs de modules de batterie d'avoir recours à la modélisation des performances et du vieillissement afin de satisfaire le cahier des charges des modules développés. Les cellules Lithium-ion sont des systèmes multi-physiques par essence, où des modifications aux échelles microscopiques impactent fortement les caractéristiques globales de la cellule. Les modèles mathématiques de ces systèmes doivent donc être capables de lier ces caractéristiques globales à la description des phénomènes physiques aux échelles microscopiques. Dans cette thèse une méthodologie de remontée d'échelle est proposée afin de concevoir un modèle de type circuit électrique équivalent qui se base sur les physiques à l'échelle de l'électrode pour les batteries lithium-ion. Cette méthodologie est développée en début de vie et au cours du vieillissement d'une cellule de type graphite vs NMC622. Elle est établie en deux temps. Premièrement, les équations physiques sont résolues dans le domaine fréquentiel pour obtenir le modèle d'impédance analytique correspondant. Ensuite, pour avoir un modèle simple à intégrer dans des applications à temps réel, ce modèle d'impédance analytique est mathématiquement simplifié en une série d'éléments RC (en parallèle). Pour valider la démarche et les différentes étapes de la méthodologie, des campagnes expérimentales ont été réalisées au cours du vieillissement de la batterie. De plus, ces expériences ont permis de caractériser les différentes composantes de la cellule et d'alimenter les modèles avec les paramètres caractéristiques des matériaux actifs utilisés.

Mots clés : Batteries Lithium-ion, modèles circuits électriques équivalents, NMC622 *vs* graphite, vieillissement.

Abstract

Li-ion battery technology has a great success and is widely used in various portable technologies. for transport and stationary applications. However, given the diversity of battery chemistries and the numerous aging phenomena, it remains critical for battery pack designers to resort to simulation of battery performance and aging in order to optimize the module design. Li-ion batteries are multiscale systems where modifications at microscopic length scales have a large impact on global cell characteristics. Mathematical models of these systems must therefore be able to link the global cell characteristics to the description of the physical phenomena at microscopic scales. In the scope of this work, an up-scaling methodology is developed to bridge the gap between the physical and geometrical parameters from physics-based models at the electrode scale, and the empirical parameters from EEC models used for batteries. It is applied in the beginning of life and during lifetime of graphite vs NMC622 cell type. Our methodology is established in two stages. First, the physical equations are solved in the frequency domain to obtain the corresponding analytical impedance model. Then, this impedance model is mathematically simplified in a series of RC elements (in parallel), using a mathematical development. The obtained formulation is adapted to real-time application since it involves only RC type elements. An experimental study has been performed to validate the different steps of the methodology during its entire life. Besides, it has been used to measure and deduce the physical parameters of the different active materials employed.

Keywords: Lithium-ion batteries, Equivalent Electric Circuit models, NMC622 *vs* graphite, aging